UNIVERSITÀ
DEGLI STUDI
FIRENZE

Università degli Studi di Firenze &
European Laboratory for Non-Linear Spectroscopy

PhD in Atomic and Molecular Photonics

CYCLE XXXV

COORDINATOR Prof. Diederik Wiersma

# Towards an Entangled Atom Interferometer Operating on the Clock Transition in Strontium

Academic Discipline (SSD) FIS/03 Fisica della Materia


**Doctoral Candidate**
Joep Assendelft

**Supervisor**
Prof. Guglielmo M. Tino

**PhD Coordinator**
Prof. Diederik Wiersma

**Co-Supervisor**
Dr. Leonardo Salvi


Years 2020/2022

# Abstract

## Towards an Entangled Atom Interferometer Operating on the Clock Transition in Strontium

by J. Assendelft

Most atom interferometer experiments are performed in laboratory environments, but their potential for inertial sensing in real-world applications ranges from geophysics, navigation and natural resource exploration to next-generation space missions for Earth observation, tests of the equivalence principle, the observation of gravitational waves and the search for dark matter. The sensitivity of atom interferometers increases by using larger ensembles of atoms that achieve larger separations during operation. Instead of increasing the size of the instrument there is another way to gaining sensitivity. Creating correlations between atoms, i.e. quantum entanglement, allows for operation beyond the standard quantum limit. In this work an experimental setup is constructed working towards an entangled atom interferometer operating on the clock transition in strontium. A home-built narrow-linewidth clock laser system is realised to generate the interferometer pulses. An optical ring cavity is constructed for performing quantum non-demolition (QND) measurements by cavity-aided probing. A balanced homodyne detection system is realised in order to detect the weak probe light. A QND measurement sequence for entangling strontium atoms is proposed, surpassing the standard quantum limit. Two schemes are proposed for injecting entangled atoms into an atom interferometer that operates on the clock transition. Finally a roadmap is laid out towards a future gravity mission in space using an entangled atom interferometer operating on the clock transition.

# Acknowledgements

I would like to express my deepest appreciation for my supervisors Guglielmo Tino and Leonardo Salvi, your world class expertise in atom interferometry was the reasons for coming to Florence. You enriched my knowledge in order to gain all the skills needed to become an experimental physicist in atomic physics. Your attitude to have everything in the lab home-built thought me not just physics, but also how to construct lasers, optical cavities, photodetectors, control electronics and much more. For me this led to a deeper understanding of the experimental setup that I have been working on over the course of my PhD. Some highlights that I will never forget are the successful baking of the vacuum system, the first time creating a blue MOT, reaching the hertz level linewidth with the clock laser, finally getting the homodyne detection system to work and the two conferences in Vilnius (ECAMP14) and Toronto (ICAP2022). The entangled atom interferometer setup is not yet completed, but I am proud of all that we have achieved so far, I hope you are too. I am confident that under your supervision the realisation of a metrologically useful entangled interferometer is imminent.

I am grateful to Olivier Carraz and Eamonn Murphy for sparking my interest in atom interferometry during my internship at the European Space Agency (ESA). I want to thank ESA for co-funding my PhD in order to continue exploring the possibilities of enhancing the sensitivity of atom interferometers for a future gravity mission in space. I would like to thank you both for supervising me during my five month stay at ESTEC in the first year of my PhD, I learned a great deal about atom interferometry in microgravity and about space missions in general. Ever since I was a small kid I was fascinated by space, but I could only dream about the spaceships, rockets and satellites. However, sometimes the dreams of a small kid come true.

I would like to thank Jakob Reichel and Klemens Hammerer for reviewing my thesis. I hope that it was of interest to you.

Durante il mio tempo in Italia non ho imparato solo fisica atomica, ma anche essere italiano. Voglio ringraziare tutti i miei amici in Italia per i bei momenti insieme! Abbiamo condiviso tanti piatti italiani, ora sono dipendente da pizza, pasta, risotto, gelato e pasticcini. Ho giocato a calcio con i più bravi. Ma soprattutto voglio ringraziarvi per l'ospitalità e la condivisione della cultura italiana. Il mio tempo in Italia è uno da ricordare e tornerò molte volte!

Mijn PhD was niet altijd rozengeur en maneschijn, vooral het eerste jaar tijdens de COVID-19 pandemie was niet makkelijk. Gelukkig kan ik altijd vertrouwen op de steun van mijn familie en vrienden in Nederland. Als ik er even doorheen zat was dat altijd snel opgelost na een belletje met één van jullie, bedankt daar voor! Ik vond het ook erg leuk jullie gids te zijn tijdens de diverse bezoeken, ik hoop dat jullie tijdens een kort bezoek net zo van Florence hebben kunnen genieten als ik de laatste jaren.

# Contents

**Abstract** i

**Acknowledgements** ii

**1 Introduction** 1
- 1.1 Atom Interferometer Concept . . . 2
- 1.2 How do Entangled Atoms Improve the Sensitivity of an Atom Interferometer? . . . 6
  - 1.2.1 Entangled Atom Picture . . . 7
- 1.3 Thesis Outline . . . 10

**2 Experimental Setup** 12
- 2.1 Strontium Atom . . . 12
- 2.2 Experimental Optical Ring Cavity . . . 15
  - 2.2.1 Cavity Mode Profile . . . 16
- 2.3 Vacuum System . . . 18
  - 2.3.1 Assembly and Baking of the Vacuum System . . . 18
  - 2.3.2 Generating an Atomic Beam of Strontium Atoms from the Oven . . . 20
  - 2.3.3 Zeeman Slower . . . 21
  - 2.3.4 Optical Layout around the Vacuum System . . . 22
  - 2.3.5 Cavity Temperature Controller . . . 25
- 2.4 Realisation of a Home-Built Narrow-Linewidth Clock Laser . . . 28
  - 2.4.1 External-Cavity Diode Lasers . . . 28
  - 2.4.2 Clock Laser System at 698 nm . . . 30
- 2.5 Magneto-Optical Trap of Strontium Atoms . . . 35
  - 2.5.1 Blue MOT . . . 35
  - 2.5.2 Blue Laser System at 461 nm . . . 38
  - 2.5.3 Repumping Laser System at 497 nm . . . 39
  - 2.5.4 Red MOT . . . 40
- 2.6 Loading the Optical Lattice . . . 44
  - 2.6.1 Lattice Laser System at 813 nm . . . 44
- 2.7 Red Laser System at 689 nm for Cooling and Squeezing . . . 46
- 2.8 Homodyne Detection System . . . 50
  - 2.8.1 Balanced Homodyne Detection . . . 50
  - 2.8.2 Optical Layout to Stabilise the Phase Difference between the Probe and Local Oscillator . . . 51
  - 2.8.3 Low-Frequency Noise Leaking into the Homodyne Signal . . . 53
  - 2.8.4 Phase-Locked Loop between the Probe and Local Oscillator . . . 54
  - 2.8.5 Photon Shot Noise Limited Detection . . . 59
  - 2.8.6 Stabilising the Local Oscillator Intensity . . . 59
  - 2.8.7 Optically Balanced Homodyne Detection System Improvement . . . 62

**3 Using Atom-Cavity Interactions for Entanglement Generation** 63
- 3.1 Cavity-Enhanced Atom-Light Interactions . . . 63
- 3.2 Probing the Ground State Population . . . 67

3.2.1 Frequency Scan across Cavity Resonance . . . 70
3.2.2 Bare Cavity Resonance Frequency Measurement . . . 71
3.2.3 Shifted Cavity Resonance Frequency Measurement . . . 72
3.3 Quantum Non-Demolition Measurement Sequence . . . 73
3.3.1 State Preparation . . . 73
3.3.2 Spin Echo Sequence . . . 73
3.3.3 Applying Feedback to the Squeezed State . . . 74
3.4 Estimates of the Attainable Squeezing . . . 75

**4 Using Entangled Atoms in Interferometry on the Clock Transition** **77**
4.1 Advantage of Operating on the Clock Transition . . . 77
4.2 Transferring Entanglement to a Momentum State Superposition . . . 78
4.3 Generating Entanglement with Free-Falling Atoms . . . 80
4.4 Entangled Gradiometer . . . 81

**5 Roadmap towards a Future Space Mission** **83**
5.1 Next-Generation Gravity Mission . . . 83
5.2 Terrestrial Mission with a Second-Generation Device . . . 84
5.3 Entangled Gradiometer Space Mission Concept . . . 85
5.3.1 Quantum Non-Demolition Measurements in Space . . . 85
5.3.2 On-Board Readout using a Dual Species Gradiometer . . . 87

**6 Conclusions and Outlook** **88**

**A Experimentally Useful Strontium Transition Frequencies** **90**

**B Printed Circuit Board Designs** **92**
B.1 Cavity Temperature Controller Schematic . . . 92
B.2 SWAP Controller Schematic . . . 99
B.3 Homodyne Detector Schematic . . . 101

**Bibliography** **103**

# Chapter 1

# Introduction

The main goal of physics is to perform experiments and develop theories to describe the behaviour of the world around us. Successfully describing a physical phenomenon brings about a deeper level of understanding, that is why I love physics so much. Physicists are dreaming big when exploring the Universe, but they also investigate the tiniest of elementary particles. New theories on quantum mechanics have been developed in order to describe the microscopic world of the atom, which has led to many advances in technology like lasers, the diode and the transistor, which have led to the modern world full of computers, telecommunication devices and other electronic systems. Today physicists are working towards the second quantum revolution [1], which will shape the 21$^{st}$ century [2].

Quantum technologies are constantly evolving and have the potential to deliver accurate results faster than their classical counterparts. For example quantum metrology is used to define the second [3, 4] or to measure the gravitational constant [5]. However, the second will likely be redefined in the near future by the current most accurate timekeeper on the planet: the optical lattice clock [6]. Another promising technology is the quantum computer [7, 8], which is able to solve specific problems exponentially faster compared to a classical computer. Quantum computation can lead to new discoveries in medicine, more efficient batteries and solar cells, traffic optimisation and many new to discover applications. Different hardware platforms are being pursued in order to build the best quantum computer, one of them being cold atoms [9, 10, 11].

The field of quantum metrology [12] is constantly developing and improving the accuracy of various measurement techniques, like atomic clocks [13], interferometers [14] and magnetometers [15]. These devices are used to study fundamental constants [5, 6], the equivalence principle [16, 17], the gravitational redshift [18, 19] and gravitational waves [20] just to name a few.

While most experiments are performed in laboratories there is a push to use quantum sensors in real-world applications [21], like transportable optical lattice clocks [22] and transportable gravimeters [23]. Especially gravimeters are of interest, because precise knowledge of the gravity field can be related to the mass distribution of the Earth, which is important to many fields such as geophysics [24, 25, 26, 27, 28, 29, 30], navigation [31], natural resource exploration [32, 33, 34, 35] and in redefining the kilogram [36]. Precise gravity measurements can have a significant impact on society, such as monitoring the global sea level rise [29] due to melting of ice worldwide [25] caused by global warming, provide early warning signals by observing seismic activity that could result in earthquakes and volcanism [26], monitoring of groundwater storage [34] in areas facing droughts [33] and/or (drinking) water shortages.

Gravity measurements can be performed locally with a transportable gravimeter on land [37], sea [28, 38] or in the air [39, 40, 41], while global coverage was achieved by going to space with the GRACE [42] and GOCE [43] missions. Studies have been performed for a new gravity mission in space with cold atoms [44, 45, 46] in order to determine the system requirements.

An atom interferometer is a device that measures accelerations with atoms [47]. It uses laser pulses

to split an atom into two wave packets, which travel along two separated paths in space. More laser pulses are used to recombine the paths and to create an interference pattern between the matter waves at the interferometer output. The phase of the interference pattern holds the information of the measured acceleration. The sensitivity of an atom interferometer is proportional to the number of atoms and to the separation between the wave packets during operation. Atom number $N$ is limited by technical matters and the achievable separation is limited by the size of the instrument. Large interferometers have been constructed as 10 m towers [48, 49], but due to the dimensions their operation in the field is problematic.

Another way to improve the sensitivity of atom interferometers and gravimeters is by creating correlations between the atoms, i.e. quantum entanglement. Entangling the atoms may reduce the uncertainty of a given observable at the cost of an increased uncertainty in another observable: these are squeezed atomic states. Squeezing the atomic state can improve the uncertainty scaling beyond the standard quantum limit of $1/\sqrt{N}$ for uncorrelated atoms, up to the Heisenberg limited scaling of $1/N$. Note that not every entangled state is useful for metrology, but a certain type of squeezed states can be created that improves the phase estimation during the final state readout [12, 50, 51, 52]. For a given sensitivity the size and weight of the instrument can be reduced by using entangled atoms with respect to using uncorrelated atoms. Furthermore, smaller averaging times are possible when using entangled atoms, which improves the sensor bandwidth.

Squeezing has been used successfully with light in order to improve the sensitivity of the laser interferometer gravitational wave observatories (LIGO and VIRGO), which operate beyond the standard quantum limit [53] in order to improve the sensitivity to gravitational waves [54]. Entangled atom interferometers have been demonstrated [55, 56, 57], but either the atom number or the achievable separation was limited due to the fragility of the phase-sensitive squeezed states. The technology needs to be developed further in order to become metrologically useful. This involves being able to entangle larger atomic ensembles and the entanglement needs to persist for a longer period of time, such that future atom interferometers and gravimeters benefit from operating with entangled atoms compared to just increasing the size of the instrument.

The apparatus described in this work is still under construction, it aims at performing proof-of-principle atom interferometry experiments using entangled strontium atoms. The optical clock transition in strontium gives access to a metastable excited state, this enables atom interferometry using single-photon transitions [58, 59], which leads to the cancellation of common laser phase noise in the gradiometer scheme. The proposed entanglement generation scheme [60] uses cavity-enhanced matter-light interactions to entangle strontium atoms at the cavity focal point by probing through a high-finesse cavity on an intercombination transition.

## 1.1 Atom Interferometer Concept

An atom interferometer [61, 62, 63, 64, 65, 66] uses matter waves, but it shares many similarities with interferometers that use light [67, 68]. Ultimately this comes from the wave-particle duality of matter. An ensemble of particles of mass $M$ at temperature $T_{DB}$ has an associated de Broglie wavelength [69]

$$\lambda_{DB} = \frac{h}{\sqrt{2\pi M k_B T_{DB}}}, \tag{1.1}$$

with $h$ the Planck constant and $k_B$ the Boltzmann constant. In daily life the wavelike nature of matter is not observed due to the de Broglie wavelength $\lambda_{DB}$ being very short, because the particles are simply 'too hot'. But when cooling down to extremely low temperatures the wavelike nature starts to play a role, for example $^{87}$Sr atoms cooled down to $T_{DB} = 1$ $\mu$K have a de Broglie wavelength of $\lambda_{DB} = 187$ nm, which leads to the interference of the wavefunctions of neighbouring atoms. The atom interferometer splits and reflects matter waves similarly to how a Mach-Zehnder interferometer operates with light (Fig. 1.1). However, laser pulses are used to manipulate the matter waves instead of the beam splitters and mirrors that are used to manipulate light.

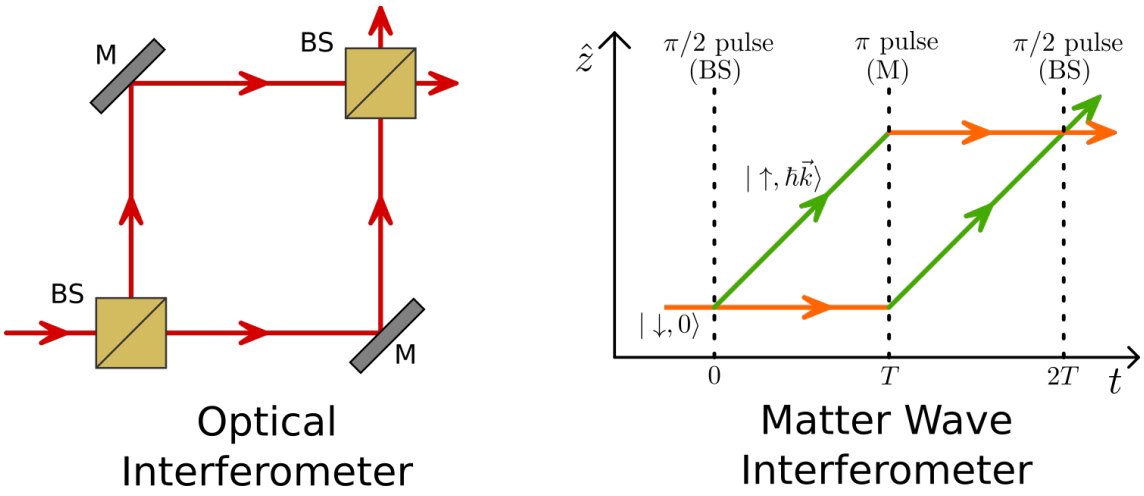


Figure 1.1: Mach-Zehnder type interferometers using light (left) or matter waves (right) are very similar. The wave is split into two equal wave packets by the first beamsplitter (BS). A mirror (M) is used to redirect the trajectories. The wave packets are split again at the recombination point by the second beamsplitter, this creates an interference pattern at the interferometer output.

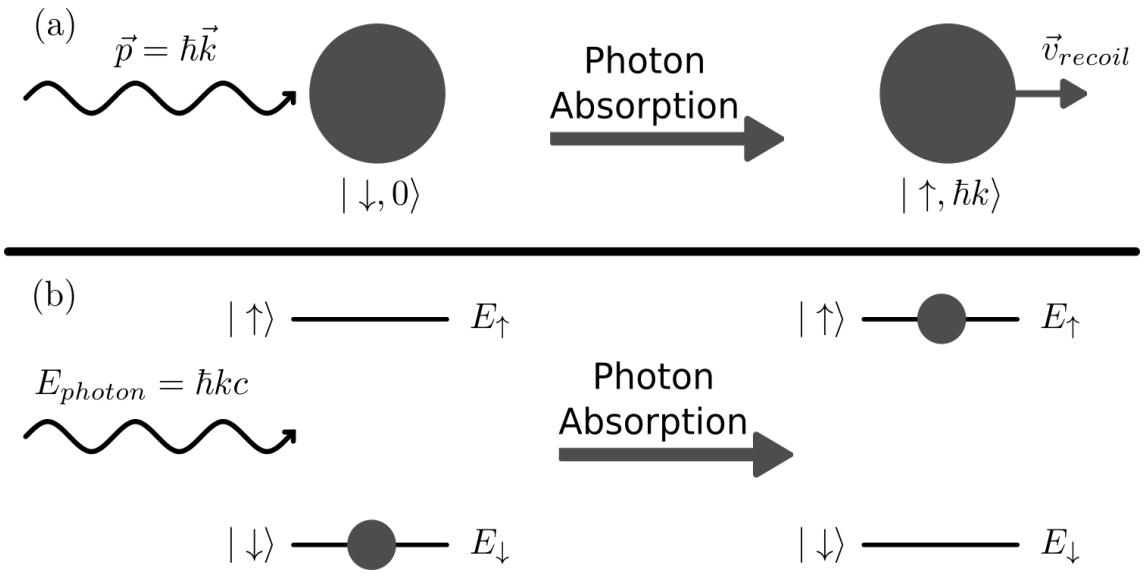


Figure 1.2: The photon absorption event causing an atomic transition from state $|\downarrow\rangle$ to state $|\uparrow\rangle$ is depicted in the inertial frame (a) and in an energy level diagram (b). The absorption occurs when the photon is on resonance: $E_{photon} = E_\uparrow - E_\downarrow + \hbar^2k^2/(2M)$. Momentum $\vec{p} = \hbar\vec{k}$ is transferred from the photon to the atom at the absorption event, causing the atom to gain a velocity of $\vec{v}_{recoil} = \hbar\vec{k}/M$. Note that the total energy and momentum are conserved for the complete system (photon + atom) during the single-photon transition.

### Manipulating Matter Waves with Laser Pulses

The laser pulses act as mirrors and beam splitters for matter waves by driving transitions between the internal atomic states. Consider an atom with two (meta)stable states $|\uparrow\rangle$ and $|\downarrow\rangle$, with the corresponding energy levels $E_\uparrow$ and $E_\downarrow$. If the photons of the laser pulse are on resonance ($E_{photon} = \hbar kc = E_\uparrow - E_\downarrow + \hbar^2k^2/(2M)$, with $c$ the speed of light and $\vec{k}$ the wavevector of the photon), then the atom can absorb a photon, which will cause an atomic transition from state $|\downarrow\rangle$ to state $|\uparrow\rangle$ (Fig. 1.2). At the single-photon transition not only the internal state of the atom is

changed, but the atom also changes its momentum by absorbing the photon momentum $\vec{p} = \hbar\vec{k}$, where $k = 2\pi/\lambda$ with $\lambda$ the wavelength of the photon. Absorption of a photon increases the velocity of the atom by the photon recoil velocity $\vec{v}_{recoil} = \hbar\vec{k}/M$. Due to the transfer of momentum it is possible for the laser pulses to mimic beam splitters and mirrors for matter waves. By adjusting the pulse time or intensity it is possible to split or to reflect a matter wave. The mirror pulse is known as a $\pi$ pulse and the beamsplitter pulse is known as a $\pi/2$ pulse. Atom interferometers do not solely operate using single-photon transitions. It is more common to make use of an excited intermediate state $|e\rangle$, in order to make a two-photon transition, like for Bragg [70] and Raman [65] pulses. Any closed two-photon transition can be used, since there is no requirement on the excited state lifetime.

### The Interferometer Pulse Sequence

At the start of the interferometer sequence the matter wave is split into an equal superposition of two wave packets by the first $\pi/2$ pulse (Fig. 1.3), thus the atom is at two places at once in the form of two matter wave packets. The $\pi$ pulse is applied after an interrogation time $T$, which acts as a mirror for the two matter wave packets in order to recombine their trajectories. After an additional interrogation time $T$ the final $\pi/2$ pulse is applied, which splits the two matter wave packets into four matter wave packets. After the final pulse the wave packets that occupy the same state interfere due to their wavelike nature. Note that at the recombination point the separation between the wave packets should be small compared to the de Broglie wavelength ($\Delta z < \lambda_{DB}/2$) in order to resolve the interference fringes [45]. The trajectories of the wave packets are affected by gravity due to the non-zero atomic mass.

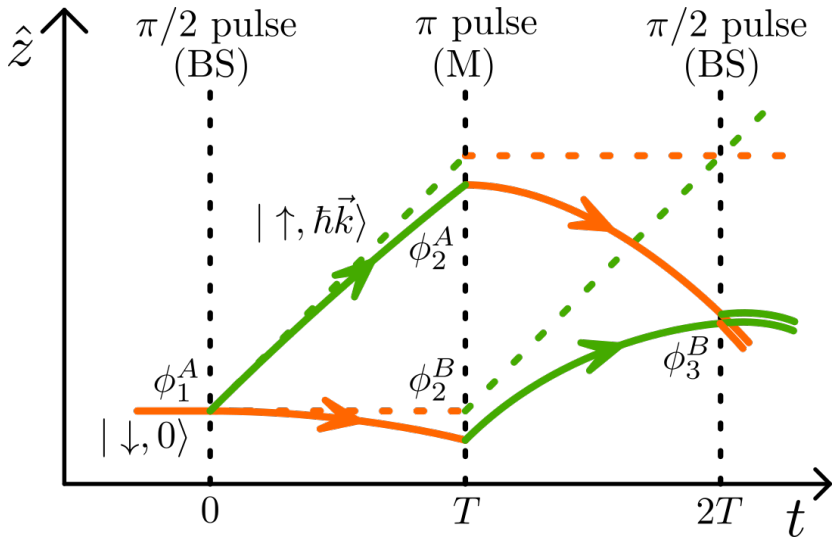


Figure 1.3: Mach-Zehnder matter wave interferometer with (solid) and without (dashed) gravity. The phase of the laser $\phi_i^j$ at pulse $i = 1, 2, 3$ along path $j = A, B$ is imprinted onto the matter wave packet only when a single-photon transition occurs. Figure adapted from [65].

### Gravity Field Information Encoded into the Interferometer Phase

The phase of the laser is imprinted onto the wave packet when a single-photon transition occurs, this encodes information about the gravitational field into the phase $\phi_{AI}$ of the atom interferometer interference pattern [64, 65, 66]

$$\begin{aligned} \phi_{AI} &= \left(\phi_1^A(t_1) - \phi_2^A(t_2)\right) - \left(\phi_2^B(t_2) - \phi_3^B(t_3)\right) \\ &= kgT^2, \end{aligned} \tag{1.2}$$

with $g$ the gravitational acceleration and $\phi_i^j(t_i) = kz_i - \omega t_i$ is the phase of the laser light at angular frequency $\omega$, position $z_i$ and time $t_i$ at pulse $i = 1, 2, 3$ along path $j = A, B$. Increasing the size of

the interferometer allows for longer interrogation times $T$, which leads to a stronger gravity signal, because the phase $\phi_{AI}$ scales quadratically with the interrogation time $T$.

It is interesting to measure the gravity field gradient $\gamma_g$ instead of measuring the gravitational acceleration $g$, because a gravity field model can be created from the gravity gradient data [71], the equivalence principle can be tested [16] or the gravitational constant $G$ can be measured [5]. An atom gradiometer [45, 46, 72], which consists of two atom interferometers interacting with the same laser while displaced by an initial vertical distance $d_0$ at pulse $i = 1$, cancels many common noise effects. Increasing the initial vertical displacement $d_0$ between the two interferometers leads to a stronger gravity gradient signal, but also increases the size of the instrument.

### Population State Readout to Estimate the Phase Shift

The interferometer phase $\phi_{AI}$ [Eq. (1.2)] cannot be measured directly. Instead it is estimated by measuring the state populations $N_\uparrow$ and $N_\downarrow$ of the states $|\uparrow\rangle$ and $|\downarrow\rangle$ respectively at the output ports of the atom interferometer. In order to illustrate this point it is convenient to think of the quantum state as a spin vector on the Bloch sphere (Fig. 1.4). The collective quantum state of $N$ atoms can be described by a spin-$N/2$ particle by extending the spin-1/2 model of a single two-level system (atom) to $N$ atoms. The collective spin is described by the collective Bloch vector

$$\vec{J} = \sum_{i=1}^{N} \vec{j}_i, \tag{1.3}$$

and the projection of the collective Bloch vector along the $\hat{z}$-axis is

$$J_z = \sum_{i=1}^{N} (j_z)_i = N\frac{P_\uparrow - P_\downarrow}{2} = \frac{N_\uparrow - N_\downarrow}{2}, \tag{1.4}$$

with $(j_z)_i$ the projection along the $\hat{z}$-axis of the Bloch vector of atom $i$, $P_\uparrow = (1 - \cos(\phi_{AI}))/2$ the probability to measure $\vec{j}_i$ as spin up and $P_\downarrow = (1 + \cos(\phi_{AI}))/2$ the probability to measure $\vec{j}_i$ as spin down. The probabilities are the same for all atoms, because they gain the same phase $\phi_{AI}$ during the interferometer sequence. For example, if no phase is acquired $\phi_{AI} = 0$, then all atoms end up in state $|\downarrow, 0\rangle$. Or if a phase of $\phi_{AI} = \pi$ is acquired, then all atoms end up in $|\uparrow, \hbar\vec{k}\rangle$.

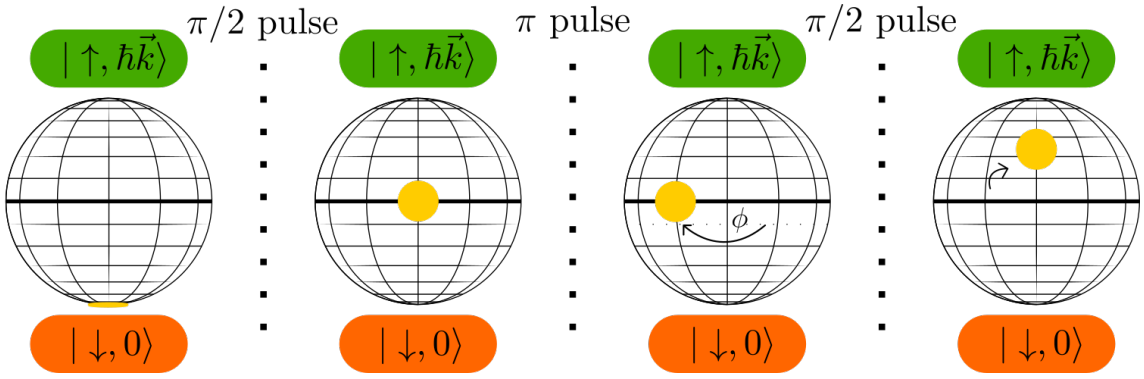


Figure 1.4: Quantum state evolution of $N$ atoms during the interferometer pulse sequence visualised as a spin-$N/2$ particle on the Bloch sphere, where the yellow circle denotes the uncertainty distribution of Bloch vector $\vec{J}$. All $N$ atoms start in the spin down state $|\downarrow, 0\rangle$. The first $\pi/2$ pulse creates an equal superposition between spin up $|\uparrow, \hbar\vec{k}\rangle$ and spin down $|\downarrow, 0\rangle$, thus the Bloch vector points along the equator. The quantum state starts to gain a phase $\phi$ due to gravity. The $\pi$ pulse recombines the trajectories, this flips the Bloch vector. The Bloch vector stays on the equator, but now gains phase in the opposite direction. The final $\pi/2$ pulse projects the acquired phase onto the polar angle of the Bloch vector, such that the interferometer phase $\phi_{AI}$ can be determined by reading out the state populations $N_\downarrow$ and $N_\uparrow$ of the states $|\downarrow, 0\rangle$ and $|\uparrow, \hbar\vec{k}\rangle$ respectively.

**Uncertainty in the Phase Estimation**

Every atom inside the interferometer acquires the same phase $\phi_{AI}$, which is determined by measuring the state populations:

$$-\cos(\phi_{AI}) = P_\uparrow - P_\downarrow = \frac{N_\uparrow - N_\downarrow}{N} = \frac{N - 2N_\downarrow}{N} = 1 - \frac{2N_\downarrow}{N}, \tag{1.5}$$

which is non-linear in phase. The atom interferometer is most sensitive to changes in phase $\delta\phi_{AI}$ close to the equator of the Bloch sphere, where it operates in the linear regime. Note that when moving away from the equator the signal-to-noise ratio of the phase readout remains constant, however as soon as other technical noises emerge the signal-to-noise ratio decreases when moving away from the equator [60], thus the optimal point for phase readout is on the equator. For phases close to the equator $\phi_{AI} = (n + 1/2)\,\pi + \delta\phi_{AI}$ the small angle approximation can be made:

$$-\cos(\phi_{AI}) = -\cos((n + 1/2)\,\pi + \delta\phi_{AI}) = \sin(n\pi + \delta\phi_{AI}) \approx (-1)^n\,\delta\phi_{AI}.$$

In the small angle approximation the variance of the atom interferometer phase is equal to the variance of the fluctuations:

$$\mathrm{Var}(\phi_{AI}) = \mathrm{Var}(\delta\phi_{AI}) = \mathrm{Var}\left(1 - \frac{2N_\downarrow}{N}\right) = \frac{4}{N^2}\mathrm{Var}(N_\downarrow).$$

The phase uncertainty $\sigma_{\phi_{AI}}$ in the small angle approximation is [50, 51, 52]

$$\sigma_{\phi_{AI}} = \sqrt{\mathrm{Var}(\phi_{AI})} \approx \frac{2}{N}\sqrt{\mathrm{Var}(N_\downarrow)} \approx \frac{2}{N}\sqrt{\frac{N}{4}} = \frac{1}{\sqrt{N}}, \tag{1.6}$$

where in the final approximation $N_\downarrow \approx N/2$ is assumed for a phase $\phi_{AI}$ close to the equator, see section 1.2 for a more detailed explanation and an intuitive example. The relation $\sigma_{\phi_{AI}} = 1/\sqrt{N}$ is known as the standard quantum limit (SQL), which is the lowest achievable uncertainty for an atom interferometer using $N$ uncorrelated atoms. This expression also shows that the uncertainty $\sigma_{\phi_{AI}}$ of the phase estimation reduces when measuring with an increased atom number $N$, therefore the instrument gains sensitivity by operating with larger atom numbers.

## 1.2 How do Entangled Atoms Improve the Sensitivity of an Atom Interferometer?

The sensitivity of an atom interferometer depends on how well the phase $\phi_{AI}$ can be estimated by measuring the state populations $N_\uparrow$ and $N_\downarrow$ of the states $|\uparrow\rangle$ and $|\downarrow\rangle$ respectively. In order to explain the concept of uncertainty with a nice analogy imagine that the state populations are determined after a single $\pi/2$ pulse, such that the Bloch vector points along the equator. The uncorrelated atoms are represented by a coherent spin state (CSS), they are put into an equal superposition of $|\uparrow\rangle$ and $|\downarrow\rangle$ by the $\pi/2$ pulse:

$$|\psi_{CSS}\rangle = \prod_{i=1}^{N} |\psi\rangle_i = \prod_{i=1}^{N} \frac{|\uparrow\rangle_i + |\downarrow\rangle_i}{\sqrt{2}}, \tag{1.7}$$

which is a product of $N$ uncorrelated atoms, where every atom (spin-1/2 system $i$) is in an equal superposition between the spin states $|\uparrow\rangle_i$ and $|\downarrow\rangle_i$. This means that every atom is in two different states at two different locations at the same time, it is simultaneously in state $|\uparrow\rangle$ on path $A$ and in state $|\downarrow\rangle$ on path $B$. By measuring the state of the atoms they are forced to choose a state (and location), the quantum state collapses and is projected onto one of the two spin states $|\uparrow\rangle$ or $|\downarrow\rangle$ with equal probability $P_\uparrow = P_\downarrow = 1/2$. Measuring the state of $N$ uncorrelated atoms in an equal superposition is analogous to flipping $N$ coins, where each coin ends up heads (analogous to $|\uparrow\rangle$) or tails (analogous to $|\downarrow\rangle$) with equal probability $P_{heads} = P_{tails} = 1/2$. From coin flipping experience it is clear that the number of heads $N_{heads}$ (analogous to $N_\uparrow$)

and the number of tails $N_{tails}$ (analogous to $N_\downarrow$) vary with each trial. $N_\uparrow$ and $N_\downarrow$ vary the same way between measurement cycles, when preparing a new equal superposition of $N$ atoms every cycle. The coins and the atoms both follow a binomial distribution [51], with expected values $\mathrm{E}[N_{heads}] = NP_{heads} = N/2$, $\mathrm{E}[N_{tails}] = NP_{tails} = N/2$, $\mathrm{E}[N_\uparrow] = NP_\uparrow = N/2$, $\mathrm{E}[N_\downarrow] = NP_\downarrow = N/2$ and variances $\mathrm{Var}(N_{heads}) = \mathrm{Var}(N_{tails}) = NP_{heads}P_{tails} = N/4$ and $\mathrm{Var}(N_\uparrow) = \mathrm{Var}(N_\downarrow) = NP_\uparrow P_\downarrow = N/4$. This is the reason that at the SQL $\mathrm{Var}(N_\downarrow) = N/4$ for $\sigma_{\phi_{AI}}$ [Eq. (1.6)], with $E[N_\downarrow] = N/2 \Leftrightarrow N_\downarrow \approx N/2$.

Next the full atom interferometer sequence is revisited, where the state probabilities $P_\uparrow$ and $P_\downarrow$ are unequal and depend on the acquired interferometer phase. This is analogous to an unfair coin, with probability $P_\downarrow$ for tails and $P_\uparrow = 1 - P_\downarrow$ for heads. For unequal probabilities the variance $\mathrm{Var}(N_\downarrow) = NP_\uparrow P_\downarrow < N/4$ is lower than when the probabilities are equal. The phase uncertainty $\sigma_{\phi_{AI}}$ reduces when the Bloch vector is in the polar regions, here the phase estimation is more precise. However, in this region the readout of the interferometer state populations is less sensitive to the acquired phase compared to readout along the equator [Eq. 1.5]. As stated previously the signal-to-noise ratio is constant with interferometer phase if only shot noise is considered [60]. Unfortunately added technical noise sources are present during readout, which reduce the signal-to-noise ratio when moving away from the equator. Therefore the interferometer phase is ideally read out on the equator, which could be realised with a phase feedback protocol [73].

### 1.2.1 Entangled Atom Picture

Think again of the coin flip analogy when measuring the state populations of atoms in an equal superposition, but consider a situation with only two coins/atoms. Flipping two uncorrelated coins has four possible outcomes: heads+heads, heads+tails, tails+heads and tails+tails. Now imagine I give you two special coins that are perfectly anticorrelated, flip both coins simultaneously, one ends heads up and the other ends tails up due to the anticorrelation. Now imagine flipping both coins with your eyes closed, then cover one coin with your hand and open your eyes. The uncovered coin landed either heads or tails, for this example consider it landed tails. Now my question to you is: Do you know the face of the coin covered by your hand? An obvious answer would be no, from experience with flipping uncorrelated coins you would say that it is a 50/50 percent chance between heads and tails. But remember, these are special entangled coins, they are anticorrelated and therefore the coin covered by your hand is heads up. Lift up your hand if you do not believe me, see it is heads up. Try it multiple times if you wish, but when you lift your hand the second coin will always be anticorrelated with the first coin. Please take good care of these two entangled coins, because they are very fragile! These entangled coins were not just lying around, instead they have been created by generating entanglement between two regular coins.

To some entanglement might seem like magic and it has led to the famous thought experiment the Einstein-Podolsky-Rosen (EPR) paradox [74]. The Bell test [75] has been developed in order to show that entanglement really exists, it is not just some "spooky action at a distance". Passing the Bell test proves the existence of entanglement, it has been demonstrated for example by entangling two electron spins in diamond nitrogen-vacancy centers separated by 1.3 km [76].

#### Squeezed Spin States

The picture of two entangled coins/atoms is extended to $N$ coins/atoms. The quantum state describing $N$ perfectly anticorrelated atoms is hard to create. Instead this work aims to create squeezed states, which are not maximally entangled, but still provide useful benefits. The squeezed states are easy to visualise on the Bloch sphere (Fig. 1.5). By visualising the states on the Bloch sphere it is clear why these states are called squeezed states, because their uncertainty distribution is a squeezed version of the circular uncertainty distribution of the coherent spin state (CSS). The spin state uncertainty distribution follows Heisenberg's uncertainty principle [77, 50, 51, 52]

$$\sigma_\phi \sigma_\theta \geq \frac{1}{N}, \tag{1.8}$$

with $\sigma_\phi$ the uncertainty of the azimuthal angle and $\sigma_\theta$ the uncertainty of the polar angle of the Bloch vector. For a CSS the uncertainties are equal in both directions $\sigma_\phi = \sigma_\theta = 1\sqrt{N}$, the

uncertainty distribution is represented by a circle. The goal of using squeezed states is to reduce the uncertainty in one direction with respect to the CSS, which means that the uncertainty in the other (anti-squeezed) direction increases due to the Heisenberg relation. The two squeezed states that are of most interest are the population squeezed and phase squeezed states, but any rotation of the uncertainty distribution is possible, for example by the use of laser pulses. The population squeezed state has an uncertainty $\sigma_\theta < 1/\sqrt{N}$ in the polar angle below the SQL, which increases the precision of the population state readout with respect to a CSS. The phase squeezed state has an uncertainty $\sigma_\phi < 1/\sqrt{N}$ in the azimuthal angle below the SQL, which leads to a more precise gain in phase during the interferometer sequence with respect to a CSS. The size of the uncertainty distribution of squeezed states $\sigma_\phi\sigma_\theta > 1/N$ is larger than the size of the uncertainty distribution of a CSS $\sigma_\phi\sigma_\theta = 1/N$, because the operations that generate the squeezing introduce extra uncertainty in the anti-squeezed direction [78].

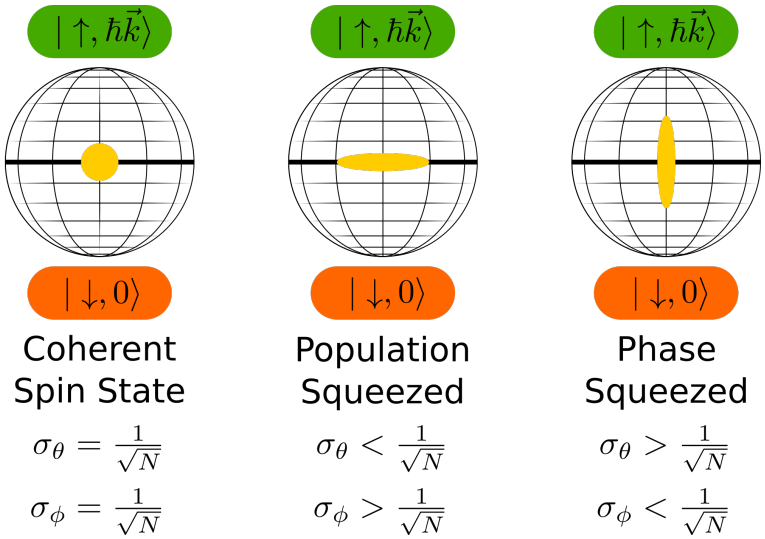


Figure 1.5: Squeezed and coherent spin state comparison for a spin-$N/2$ system depicted on Bloch spheres, where the yellow shape denotes the uncertainty distribution of the Bloch vector. The coherent spin state (CSS) has equal uncertainty in both directions/angles. A squeezed state has reduced uncertainty in one direction, but an increased uncertainty in the other direction. The population squeezed spin state has minimal uncertainty in the polar angle $\sigma_\theta$, which increases the precision of the population state readout with respect to a CSS. The phase squeezed state has minimal uncertainty in the azimuthal angle $\sigma_\phi$, which leads to a more precise gain in phase during the interferometer sequence with respect to a CSS.

An entangled interferometer operates with a phase squeezed state during the interferometer sequence in order to gain phase with an increased sensitivity. Then for state readout a population squeezed state is desired, therefore the state is rotated from phase squeezed to population squeezed by the final interferometer pulse (Fig. 1.6). Optical clocks and atom interferometers that use squeezed states are affected by the increased anti-squeezed uncertainty. The precision of the measurement is reduced, because the anti-squeezed direction leaks into the measurement due to the curvature of the Bloch sphere [79, 78], even if anti-squeezing is minimal.

It is challenging to create entanglement between atoms and then preparing the state in such a way that an equal superposition squeezed in the phase direction is created after the first $\pi/2$ pulse. But the real challenge lies in creating such a phase sensitive state that has a long lifetime [80] in order to complete the full interferometer sequence. However, the interferometer sequence has an advantage over the Ramsey sequence of the optical clock, the central $\pi$ pulse of the interferometer effectively creates a spin-echo sequence. This has been demonstrated to extend the lifetime of a phase squeezed state from 600 $\mu$s to 2 ms [80].

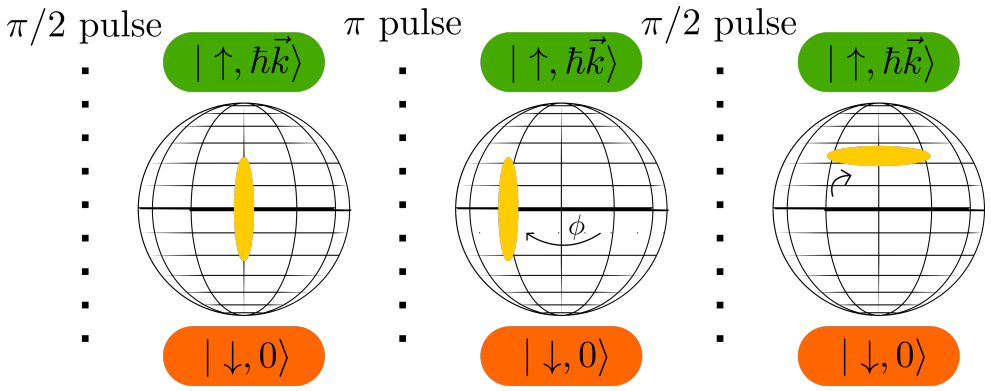


Figure 1.6: Quantum state evolution of $N$ entangled atoms during the interferometer pulse sequence visualised as a spin-$N/2$ system on the Bloch sphere. The uncertainty of Bloch vector $\vec{J}$ is represented by the yellow oval. The goal is to have an equal superposition between spin up $|\uparrow, \hbar\vec{k}\rangle$ and spin down $|\downarrow, 0\rangle$ squeezed in the phase direction after first $\pi/2$ pulse. The quantum state starts to gain a phase $\phi$ due to gravity with an increased sensitivity due to the squeezing. The $\pi$ pulse recombines the trajectories, this flips the Bloch sphere. The Bloch vector stays on the equator, but now gains phase in opposite direction. The final $\pi/2$ pulse projects the acquired phase onto the polar angle of the Bloch vector. This rotates the phase squeezed state into a population squeezed state, such that the state populations $N_\downarrow$ and $N_\uparrow$ of the states $|\downarrow, 0\rangle$ and $|\uparrow, \hbar\vec{k}\rangle$ can be determined with increased precision.

**Entanglement Generation through Quantum Non-Demolition Measurements**

In this work the entanglement will be created through quantum non-demolition (QND) measurements [81] by making use of an optical cavity [82, 83, 84, 85]. The atomic state populations are the observable of interest, but the cavity resonance frequency is the observable that will be measured. The atom-cavity interactions cause the atomic state populations to induce a shift in the cavity resonance frequency. The concept of the QND measurement is to measure the shift in cavity resonance frequency in order to determine the state populations of the quantum state non-destructively, therefore gaining knowledge about the state without disturbing it. The knowledge of the quantum state populations reduces the uncertainty $\sigma_\theta$, effectively creating a population squeezed quantum state. The final step is transforming the quantum state such that it becomes phase squeezed at the start of the interferometer sequence.

Maximally entangled atoms would lead to an atom interferometer phase scaling of $\sigma_{\phi_{AI}} = 1/N$, which is the Heisenberg limited scaling. For large atom numbers $N$ this would be a massive improvement to the sensitivity of the quantum sensor with respect to the SQL for uncorrelated atoms, where the phase scales as $\sigma_{\phi_{AI}} = 1/\sqrt{N}$. It is hard to generate maximally entangled states for large atom numbers due to technical limitations of the entanglement creation process and also their fragility is a factor. Squeezed states are not maximally entangled, therefore it is not possible to reach Heisenberg limited scaling for the entangled atom interferometer. However, squeezed states have been used in a time-reversal protocol [55] in order to demonstrate Heisenberg scaling $\sigma_{\phi_{AI}} = b/N$ with $b > 1$, but the entanglement in this protocol was generated using a one-axis twisting (OAT) approach. For entanglement generation using QND measurements it is also possible to reach Heisenberg scaling $\sigma_{\phi_{AI}} \propto 1/N$ but only at lower atom numbers, because at a certain atom number $N$ the phase scaling reduces to $\sigma_{\phi_{AI}} \propto 1/N^{3/4}$, where the atom number switching point depends on the cavity parameters and loss channels [86]. Still the phase uncertainty atom number scaling improves using QND measurements (either $\sim 1/N$ or $\sim 1/N^{3/4}$) compared to the SQL scaling of $1/\sqrt{N}$. An entangled atom interferometer operating with a large number of entangled atoms $N$ and an interrogation time $T$ surpassing a few milliseconds has not yet been demonstrated, because a large amount of entanglement is fragile, but the prospect of the massive increase in sensitivity is promising.

## 1.3 Thesis Outline

The goal of this thesis is to describe the construction of an experimental setup for performing proof of principle atom interferometry experiments operating on the clock transition using entangled strontium atoms. The experimental sequence can be divided into three main parts: first a sample of cold strontium atoms needs to be prepared, then entanglement needs to be generated between the atoms and finally the entangled atoms will be used in a Mach-Zehnder interferometer.

Chapter 1 motivated the work, which is aimed at improving the sensitivity of atom interferometers through the use of entangled atoms for precision gravity measurements. The concept of an atom interferometer was explained (Sec. 1.1), which described how gravity is measured by manipulating matter waves with laser pulses. The concept of entanglement was explained by making an intuitive analogy between entangled atoms in a momentum state superposition and flipping special anticorrelated coins (Sec. 1.2.1). The entangled atoms were represented on the Bloch sphere as squeezed spin states, with their corresponding uncertainty distribution. Quantum non-demolition measurements will be used to generate the entanglement, which leads to an improved atom number scaling in the phase estimation compared to the standard quantum limit for uncorrelated atoms.

Chapter 2 describes the constructed experimental setup. The strontium atom is introduced (Sec. 2.1) and its most important transitions are highlighted. An experimental optical ring cavity (Sec. 2.2) was constructed for performing quantum non-demolition measurements. A vacuum system (Sec. 2.3) has been constructed from scratch for interferometry experiments. A home-built narrow-linewidth clock laser system at 698 nm (Sec. 2.4) has been realised in order generate the interferometer pulses. A magneto-optical trap (Sec. 2.5) of strontium atoms was created, the system requirements are highlighted in order to provide effective cooling and trapping. An optical lattice (Sec. 2.6) was realised in order to trap the atoms at the focus of the optical ring cavity, which enhances the atom-light interaction. A red laser system at 689 nm (Sec. 2.7) was realised for the cooling and squeezing processes. A homodyne detection system (Sec. 2.8) was constructed and characterised, its purpose is to amplify the weak optical signal obtained from probing the optical ring cavity resonance frequency. A weak probe beam is necessary in order to preserve the non-demolition character of the probing measurement.

Chapter 3 describes the generation of entanglement by performing quantum non-demolition (QND) measurements using atom-cavity interactions. The model of an atom located at the focus of an optical cavity is explored, in order to derive the cavity-enhanced atom-light interactions (Sec. 3.1). The principle of the ground state population measurement is explained (Sec. 3.2). The atoms located at the focus of the optical ring cavity are prepared in a single state, followed by the QND measurement sequence (Sec. 3.3) that generates the entanglement between the atoms. The attainable levels of squeezing are estimated (Sec. 3.4).

Chapter 4 describes how to inject entangled atoms into an atom interferometer that operates on the clock transition. The advantage of using the clock transition for interferometry is highlighted (Sec. 4.1). Two schemes are discussed to create an entangled interferometer, one scheme transfers entanglement from an internal state superposition to a momentum state superposition (Sec. 4.2) and the other scheme generates entanglement between free-falling atoms in a momentum state superposition (Sec. 4.3). Both schemes can be extended to an entangled gradiometer configuration (Sec. 4.4).

Chapter 5 discusses space applications for atom interferometry. The European Space Agency is considering atom interferometry for a future gravity mission (Sec. 5.1). A roadmap towards a future gravity mission using an entangled atom interferometer operating on the clock transition is presented. A terrestrial mission (Sec. 5.2) should be performed first, but a preliminary design for a future space instrument is presented in section 5.3.

Chapter 6 concludes the work and provides a brief outlook on the future of the experimental setup.

Appendix A lists the transition frequencies in $^{87}$Sr and $^{88}$Sr that are useful in the experiment for cooling, trapping, probing and interferometer pulses.

Appendix B describes the design considerations based on experimental requirements for the cavity

temperature controller (Sec. B.1), the sawtooth-wave adiabatic passage controller (Sec. B.2) and the homodyne detector (Sec. B.3). The schematics are explained step by step, the function and component requirements are highlighted.

# Chapter 2

# Experimental Setup

The majority of my work was spent on designing and constructing various parts of the experimental setup, working towards an entangled interferometer operating on the clock transition in strontium. The underlying principle in generating squeezed states is the interaction between the strontium atoms and the light inside the experimental ring cavity. Therefore it is crucial to be able to prepare and trap a sample of ultra-cold strontium atoms at the focus of the ring cavity where the atom-light interaction strength is maximal. The strontium atom is introduced (Sec. 2.1) and its most important transitions are highlighted. An experimental optical ring cavity (Sec. 2.2) was constructed for performing quantum non-demolition measurements. A vacuum system (Sec. 2.3) has been constructed from scratch for interferometry experiments. A home-built narrow-linewidth clock laser system at 698 nm (Sec. 2.4) has been realised in order generate the interferometer pulses. A magneto-optical trap (Sec. 2.5) of strontium atoms was created, the system requirements are highlighted in order to provide effective cooling and trapping. An optical lattice (Sec. 2.6) was realised in order to trap the atoms at the focus of the optical ring cavity, which enhances the atom-light interaction. A red laser system at 689 nm (Sec. 2.7) was realised for the cooling and squeezing processes. A homodyne detection system (Sec. 2.8) was constructed and characterised, its purpose is to amplify the weak optical signal obtained from probing the optical ring cavity resonance frequency. A weak probe beam is necessary in order to preserve the non-demolition character of the probing measurement.

## 2.1 Strontium Atom

Strontium is an alkaline earth metal with two valence electrons, which leads to a singlet-triplet energy level structure that allows for many experimentally interesting transitions that are used in metrology and quantum simulators. Especially the optical clock transition in strontium is of great interest. Strontium is used in the world's most accurate atomic clocks [6] that can operate even outside of the laboratory [22]. The energy level structure allows for high-fidelity entanglement between strontium Rydberg atoms which opens up the route to the next-generation of quantum simulators in alkaline earth atoms [87, 88]. The narrow optical transitions are of interest for atom interferometry to transfer a large momentum [70, 89] or to operate using single-photon transitions [59].

Transitions between the strontium energy levels (Fig. 2.1) are in the visible domain, which coincides well with the availability of lasers at these wavelengths. The strong transition at 461 nm excites the atom from the ground state $\left(5s^2\right)\,{}^1S_0$ to the excited state $5s5p\ {}^1P_1$, which has a lifetime of $\tau = 5.263(4)$ ns or a transition linewidth of $\gamma = 1/\tau = 2\pi \cdot 30.24(2)$ MHz [90]. The large atomic linewidth allows for transitions to be driven by a $\lambda = 461$ nm laser for a large range of velocity classes, this motivates the choice for using the ${}^1S_0 \leftrightarrow {}^1P_1$ transition to image cold atomic clouds. The ${}^1S_0 \leftrightarrow {}^1P_1$ transition is also used for the first cooling stages, because it has the largest linewidth available out of all transitions from the ground state and therefore the largest possible

photon scattering rate $R_{scatt} \propto \gamma$, which allows for fast deceleration, cooling and trapping of the atoms [91, 92, 93].

Unfortunately the $^1S_0 \leftrightarrow {}^1P_1$ transition is not a closed transition, because an atom in the excited state $5s5p\ ^1P_1$ does not always decay to the ground state $(5s^2)\ ^1S_0$, it can also decay to the $5s4d\ ^1D_2$ state with a very small probability $(1 : 50\ 000)$. The $^1P_1 \leftrightarrow {}^1D_2$ transition has a linewidth of $\gamma = 2\pi \cdot (613 \pm 234)$ Hz [94]. The $^1D_2$ level has a lifetime of 0.49(4) ms [95], the atom decays either into the $5s5p\ ^3P_2$ state (branching ratio 33%, $\gamma = 2\pi \cdot (108 \pm 10)$ Hz) or into the $5s5p\ ^3P_1$ state (branching ratio 67%, $\gamma = 2\pi \cdot (216 \pm 20)$ Hz). Atoms in the $^3P_1$ level decay back to the ground state $^1S_0$, so they re-enter the cooling cycle and are therefore recovered. The $^3P_2$ level on the other hand is meta-stable with a measured lifetime of $\tau = 520^{+310}_{-140}$s [96], therefore roughly one atom gets lost every 150 000 photon scattering events. In order to recover the atoms from the $^3P_2$ level back into the ground state various repumping schemes can be employed via the $5s6s\ ^3S_1$ level [97, 98], the $5s5d\ ^3D_2$ level [99, 100] or the $5s6d\ ^3D_2$ level [101], such that the atoms can continue their cooling cycle.

The repumping scheme of choice uses the $5s5d\ ^3D_2$ level, because a only a single laser at $\lambda = 497$ nm is needed that drives the $^3P_2 \leftrightarrow {}^3D_2$ transition. The lifetime of the $^3D_2$ level $\tau = 16.34(13)$ ns [102], the atom decays either into $5s5p\ ^3P_1$ or back into $5s5p\ ^3P_2$. The atom is therefore optically pumped into $5s5p\ ^3P_1$, from which the atom decays back to the ground state $^1S_0$.

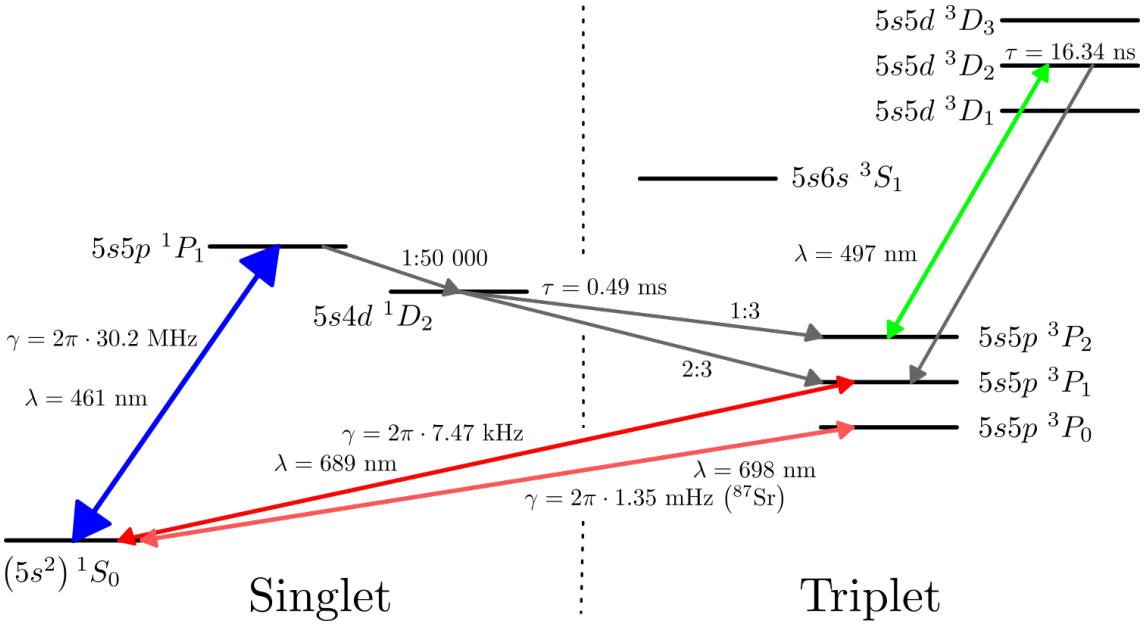


Figure 2.1: Energy level structure of strontium using the LS-coupling notation. The transitions used for cooling, trapping, repumping, imaging, sensing and interferometry are highlighted with double-sided arrows, including their wavelength $\lambda$ with corresponding colour and their atomic linewidth $\gamma$. Decay channels are highlighted with single grey arrows and include their decay probability. Lifetimes $\tau$ are reported for two levels involved in the repumping scheme. Figure adapted from [100].

Intercombination transitions between singlet and triplet states change the spin of the atom, which is forbidden in the LS-coupling scheme according to selection rules for electric dipole transitions. However, in the intermediate coupling regime state mixing occurs between states with a similar $J$ due to the spin-orbit interaction. In the case of strontium a small part of the $^1P_1$ level is mixed into the $^3P_1$ level, which makes it possible to drive an electric dipole transition at $\lambda = 689$ nm between the ground state $(5s^2)\ ^1S_0$ and the excited state $5s5p\ ^3P_1$. The lifetime of the $^3P_1$ level $\tau = 21.3(5)\ \mu$s [103, 104], which makes the transition narrow ($\gamma = 2\pi \cdot 7.47(18)$ kHz) compared to common dipole-allowed transitions. The narrow red transition at $\lambda = 689$ nm is used to cool and

trap atoms at microkelvin temperatures in the second cooling stage [105, 106], after precooling and trapping using the $\lambda = 461$ nm transition for the first stage. Furthermore, the narrow transition is used to probe atoms that are in a superposition using a cavity in order to generate entanglement between the atoms [82].

Arguably the most interesting transition in strontium is the optical clock transition at $\lambda = 698$ nm between the ground state$\left(5s^2\right)\,{}^1S_0$ and the excited state $5s5p\ {}^3P_0$, because it is doubly forbidden according to selection rules for electric dipole transitions. This transition is naturally allowed in $^{87}$Sr due to the hyperfine interaction mixing the $5s5p\ {}^3P_1$ and $5s5p\ {}^3P_0$ levels, therefore a tiny fraction of ${}^1P_1$ is mixed into ${}^3P_0$, since ${}^3P_1$ is a mixture of ${}^3P_1$ and ${}^1P_1$. All the state mixing leads to an extremely narrow natural linewidth $\gamma = 1.35\,(3)$ mHz and it also means that the $5s5p\ {}^3P_0$ state is metastable with a lifetime $\tau = 118(3)$ s [107]. The optical clock transition can also be induced in the bosonic isotopes by applying a static magnetic field that couples the $5s5p\ {}^3P_1$ and $5s5p\ {}^3P_0$ levels [108]. The clock transition is used for state preparation during the squeezing sequence and in interferometry [59]. During state preparation the atoms are trapped in an optical lattice at $\lambda = 813$ nm. This wavelength is specifically chosen, because it is the magic wavelength for strontium [109, 110, 111], which produces equal light shifts on the two clock states ${}^1S_0$ and ${}^3P_0$.

| | ${}^1S_0 \leftrightarrow {}^1P_1$ | ${}^1S_0 \leftrightarrow {}^3P_1$ | ${}^1S_0 \leftrightarrow {}^3P_0$ |
|---|---|---|---|
| $\lambda$ | 460.862 nm | 689.449 nm | 698.446 nm |
| $\omega$ | $2\pi \cdot 650.506$ THz | $2\pi \cdot 434.829$ THz | $2\pi \cdot 429.228$ THz |
| $\gamma$ | $2\pi \cdot 30.2$ MHz | $2\pi \cdot 7.47$ kHz | $2\pi \cdot 1.35$ mHz |
| $I_{sat}$ | 40.3 mW/cm$^2$ | 2.98 $\mu$W/cm$^2$ | 0.518 pW/cm$^2$ |
| $v_{recoil}$ | 9.96 mm/s | 6.66 mm/s | 6.57 mm/s |
| $a_{max}$ | $9.45 \cdot 10^5$ m/s$^2$ | 156 m/s$^2$ | $2.79 \cdot 10^{-5}$ m/s$^2$ |

Table 2.1: Properties of the three main transitions in $^{87}$Sr for $F = 9/2 \leftrightarrow F' = 9/2$: wavelength $\lambda$, angular frequency $\omega$, linewidth $\gamma$, saturation intensity $I_{sat} = \hbar\omega^3\gamma/\left(12\pi c^2\right)$ [69], recoil velocity $v_{recoil}$ and maximum deceleration $a_{max} = v_{recoil}\gamma/2$ [69].

### Strontium Isotopes

There are four stable strontium isotopes (Tab. 2.2), one fermionic isotope $^{87}$Sr and three bosonic isotopes $^{84}$Sr, $^{86}$Sr and $^{88}$Sr. The desired isotope can be targeted in experiments due to small differences in transition frequencies between isotopes. Transition frequencies useful for experiments with $^{87}$Sr (Tab. A.2) and $^{88}$Sr (Tab. A.1) are listed in the appendix.

| Isotope | Atomic mass | Isotopic abundance | Nuclear spin | Nuclear magnetic dipole moment |
|---|---|---|---|---|
| $^{84}$Sr | 83.913 426 (4) u | 0.56(1)% | $I = 0$ | - |
| $^{86}$Sr | 85.909 260 730 9 (91) u | 9.86(1)% | $I = 0$ | - |
| $^{87}$Sr | 86.908 877 497 0 (91) u | 7.00(1)% | $I = 9/2$ | $\mu_{nuc} = -1.09316(11)\mu_N$ |
| $^{88}$Sr | 87.905 612 257 1 (97) u | 82.58(1)% | $I = 0$ | - |

Table 2.2: Stable strontium isotopes with their respective atomic mass [112, 113], isotopic abundance [113, 114], nuclear spin [115, 116] and nuclear magnetic dipole moment in terms of the nuclear magneton $\mu_N$ [117].

## 2.2 Experimental Optical Ring Cavity

In this work an optical ring cavity is used to enhance the atom-light interaction in order to generate squeezed states. The optical ring cavity is also referred to as the experimental cavity, because it interacts with the atoms during the experiment. The cavity consists of four mirrors placed in a ring configuration, the cavity design is described in [60]: the main geometry design considerations of the ring configuration are having homogenous atom-light coupling, allowing for atomic access to enter and exit the cavity mode volume during loading of the sample and the interferometry sequence respectively and allowing for optical access for the lasers that provide cooling, trapping, probing and interferometry pulses to the atoms. The cavity parameters like mode waist size and position, cavity finesse $\mathcal{F}$ and mirror transmissions depends on the specifications of the mirrors. The construction process in which I participated is described in [118].

The intracavity intensity and other cavity properties are derived using input-output theory [119]. There are four cavity mirrors with reflection and transmission coefficients $r_i$ and $t_i$ respectively. The input field $E_0$ gets transmitted into the cavity after which it performs multiple round trips, after the $n^{\text{th}}$ round trip the field amplitude is $t_1 E_0 \left(r_1 r_2 r_3 r_4 \mathrm{e}^{ikL}\right)^n$, where $kL$ is the phase shift acquired by making a round trip through the ring cavity of length $L$. The electric field amplitude inside the cavity $E_c$ is a superposition of all round trip field amplitudes [119]

$$E_c = t_1 E_0 \sum_{n=0}^{\infty} \left(r_1 r_2 r_3 r_4 \mathrm{e}^{ikL}\right)^n = \frac{t_1 E_0}{1 - r_1 r_2 r_3 r_4 \mathrm{e}^{ikL}}.$$

The ratio between the input intensity $I_0$ (input power $P_0$) and intracavity intensity $I_c$ (intracavity power $P_c$) is [119]

$$\frac{P_c}{P_0} = \frac{I_c}{I_0} = \left|\frac{E_c}{E_0}\right|^2 = \frac{T_1}{(1-r)^2 + 4r\sin^2\left(\frac{kL}{2}\right)},$$

with $r = r_1 r_2 r_3 r_4$ the amplitude reflectivity product and $T_1 = t_1^2$ the power transmission coefficient of mirror 1. The light inside the cavity constructively interferes when the resonance condition $kL/2 = \pi n$ is met for $n \in \mathbb{Z}$. This leads to the ring cavity free spectral range (FSR) [119]

$$f_{\text{FSR}} = \frac{c}{L}, \tag{2.1}$$

with resonance condition $f = n f_{\text{FSR}}$ in terms of frequency. The cavity finesse is defined as [119]

$$\mathcal{F} = \frac{\pi\sqrt{r}}{1-r}. \tag{2.2}$$

The maximum circulating intensity inside the ring cavity is defined as [119]

$$I_{max} = \frac{T_1 \mathcal{F}^2}{\pi^2 r} I_0 \approx \frac{T_1 \mathcal{F}^2}{\pi^2} I_0, \tag{2.3}$$

assuming high-reflectivity mirrors $r \approx 1$ in the last step. This means that the intracavity intensity $I_c$ of a high-finesse cavity far exceeds the input intensity $I_0$ when on resonance. The intracavity intensity (Fig. 2.2) is rewritten as [119]

$$I_c(f) = \frac{I_{max}}{1 + \left(\frac{2\mathcal{F}}{\pi}\right)^2 \sin^2\left(\frac{\pi f}{f_{\text{FSR}}}\right)}, \tag{2.4}$$

which has a Lorentzian line shape with full-width at half maximum (FWHM) [119]

$$\kappa/(2\pi) = \frac{f_{\text{FSR}}}{\mathcal{F}} \tag{2.5}$$

with $\kappa$ representing the cavity linewidth.

The optical ring cavity has a measured finesse of $\mathcal{F} = 24(2)\cdot 10^3$, an FSR of $f_{\mathrm{FSR}} = 1.43136(3)$ GHz and a linewidth of $\kappa = 2\pi \cdot 57.6(1)$kHz [120].

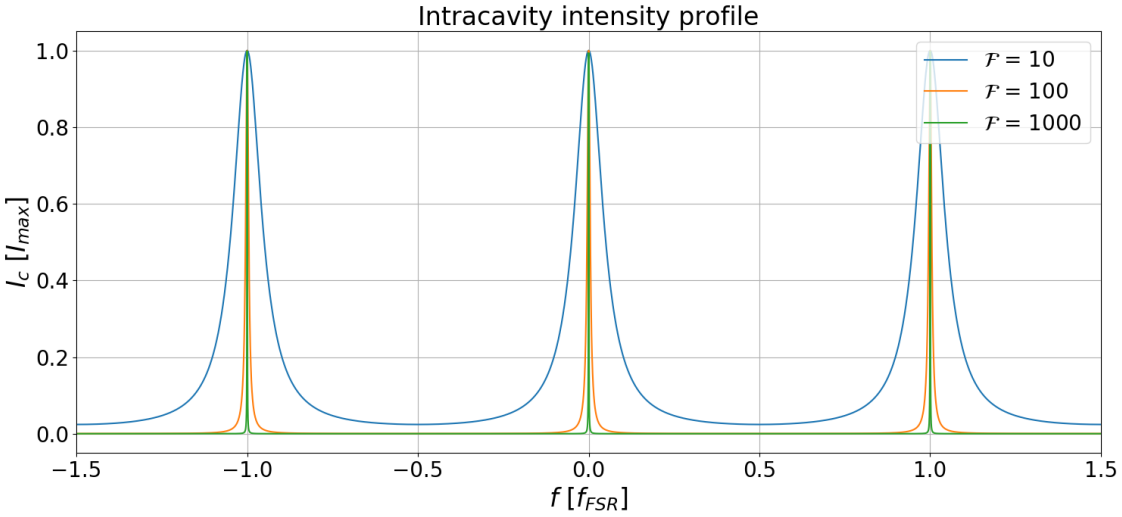


Figure 2.2: Intracavity intensity profile $I_c$ [Eq. (2.4)] in terms of free spectral range (FSR) for a cavity with a finesse of $\mathcal{F} = 10$ (blue), $\mathcal{F} = 100$ (orange) and $\mathcal{F} = 1000$ (green).

### 2.2.1 Cavity Mode Profile

The intracavity electric field mode operator is described by [121]

$$\vec{E}_c(\vec{r},t) = i\mathcal{E}_0\left(\hat{\epsilon}_c f(\vec{r})\, a e^{-i\omega_c t} - \hat{\epsilon}_c^* f^*(\vec{r})\, a^\dagger e^{i\omega_c t}\right), \tag{2.6}$$

with $\mathcal{E}_0$ the normalisation factor, $\hat{\epsilon}_c$ the cavity unit vector, $f(\vec{r})$ the dimensionless function that describes the spatial structure of the mode, $\omega_c$ the angular frequency of the cavity, $a^\dagger$ and $a$ the photon creation and annihilation operators, with commutation relation $[a, a^\dagger] = 1$. The effective mode volume $\mathcal{V}$ is defined as [121]

$$\mathcal{V} = \int \left|\vec{f}(\vec{r})\right|^2 d^3\vec{r}, \tag{2.7}$$

where $\vec{f}(\vec{r}) = f(\vec{r})\,\hat{\epsilon}_c$, with $f(\vec{r})$ a scalar function that has a maximum value of 1. The cavity n-photon state $|n\rangle$ (when $n$ photons are inside the cavity) has an energy of $\hbar\omega_c(n+1/2)$, which is equivalent to the energy stored in the electric field [121]

$$\begin{aligned}\left\langle n\left|\int \epsilon_0\left|\vec{E}_c\right|^2 d^3\vec{r}\right|n\right\rangle &= \hbar\omega_c\left(n+\frac{1}{2}\right)\\ \Leftrightarrow 2\epsilon_0\mathcal{V}(2n+1)\,\mathcal{E}_0^2 &= \hbar\omega_c(2n+1),\end{aligned}$$

thus the normalisation factor [121]

$$\mathcal{E}_0 = \sqrt{\frac{\hbar\omega_c}{2\epsilon_0\mathcal{V}}}. \tag{2.8}$$

The intracavity field is described by transverse electromagnetic (TEM) Gaussian modes. Consider the $\hat{z}$-direction along the cavity axis, such that the cavity $\mathrm{TEM}_{00}$ mode propagates with wave vector $\vec{k} = k\hat{z}$, such that the spatial structure of the cavity mode is described by [119]

$$f(\vec{r}) = f(x,y,z) = \frac{\sqrt{w_{0x}}}{\sqrt{w_x(z)}} e^{-\frac{x^2}{w_x(z)^2}} \frac{\sqrt{w_{0y}}}{\sqrt{w_y(z)}} e^{-\frac{y^2}{w_y(z)^2}} e^{i\left(kz+\frac{kx^2}{2R_x(z)}+\frac{ky^2}{2R_y(z)}-\phi_G(z)\right)}, \tag{2.9}$$

where $x$ is the tangential direction and $y$ the sagittal direction. The mode waists $w_x(z)$ and $w_y(z)$ propagate along the cavity axis as [119]

$$w_j(z) = w_{0j}\sqrt{1+\left(\frac{(z-z_{0j})\,\lambda}{\pi w_{0j}^2}\right)^2}, \tag{2.10}$$

with $w_{0j}$ the waist at focal point $z_{0j}$ for $j = x, y$. The wavefront curvatures $R_x(z)$ and $R_y(z)$ propagate along the cavity axis as [119]

$$R_i(z) = (z-z_{0j})\left(1+\left(\frac{\pi w_{0j}^2}{\lambda\,(z-z_{0j})}\right)^2\right), \tag{2.11}$$

for $j = x, y$. The Gouy phase is given by [119]

$$\phi_G(z) = \left(\arctan\left(\frac{\lambda\,(z-z_{0x})}{\pi w_{0x}^2}\right)+\arctan\left(\frac{\lambda\,(z-z_{0y})}{\pi w_{0y}^2}\right)\right)/2. \tag{2.12}$$

The spatial structure of the Gaussian mode is used to calculate the effective cavity mode volume

$$\mathcal{V} = \int_0^L\int_{-\infty}^{\infty}\int_{-\infty}^{\infty}\left|\vec{f}(x,y,z)\right|^2 dxdydz = \frac{\pi L w_{0x} w_{0y}}{2} \tag{2.13}$$

with $L$ the length of the cavity mode volume, which is equal to the cavity length.

The optical ring cavity is designed [60] with two flat (M1 and M4) and two curved (M2 and M3) mirrors, which creates two focal points along the cavity mode profile at $z_{0x} = z_{0y} = 76.4$ mm and at $z_{0x} = z_{0y} = 179.6$ mm (Fig. 2.3). The waist of the focal point on arm 2 ($z_0 = 76.4$ mm) between the flat mirrors (M1 and M4) is targeted at $w_{0x} = 149.8$ $\mu$m in the tangential plane and $w_{0y} = 179.8$ $\mu$m in the sagittal plane for $\lambda = 689.4$ nm. The waist of the focal point on arm 4 ($z_0 = 179.6$ mm) between the curved mirrors (M2 and M3) is targeted at $w_{0x} = 32.0$ $\mu$m in the tangential plane and $w_{0y} = 29.4$ $\mu$m in the sagittal plane for $\lambda = 689.4$ nm. The ring cavity has a targeted length of $L = 206.5$ mm. The chosen waist locations are at the most convenient position to load and probe the atoms during the experiment, while avoiding the exact crossing where a standing wave pattern is formed due to interference. The two different mode waist sizes allow for homogeneous coupling to smaller and larger atomic clouds.

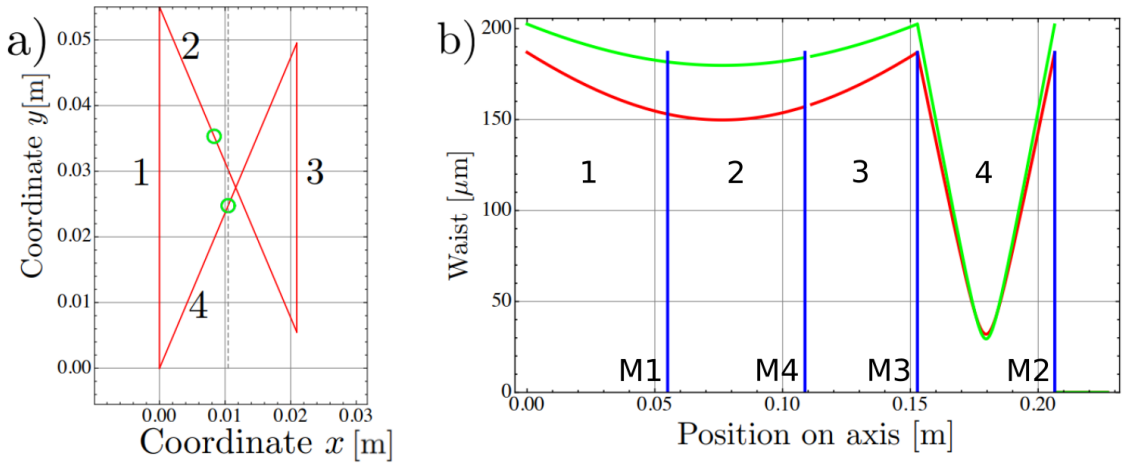


Figure 2.3: Optical ring cavity mode profile. (a) The ring cavity geometry is shown, where the numbers indicate the arms of the cavity mode. The upper focal point (green circle) located on arm 2 has a larger waist than the lower focal point (green circle) located on arm 4. The dotted vertical line depicts the interferometry axis. (b) Cavity waist along the optical axis in the tangential plane (red) and sagittal plane (green). The cavity mirrors (M1, M2, M3 and M4) are indicated by the vertical blue lines. Figure adapted from [60].

## 2.3 Vacuum System

The vacuum system provides a controllable environment for the atoms with enough optical access points used for cooling, trapping, sensing and imaging the atoms. The vacuum system (Fig. 2.4) consists of an oven, a cube, a Zeeman slower, a science chamber and two pumps, which are all connected by various valves, crosses and other vacuum components. A differential pumping tube is located at the entrance of the Zeeman slower, such that a differential pressure is created in the system. The oven and science chamber each have a dedicated vacuum pump, such that a lower pressure is reached in the science chamber($< 1.0 \cdot 10^{-10}$ mbar) compared to the oven pressure ($7.7 \cdot 10^{-10}$ mbar).

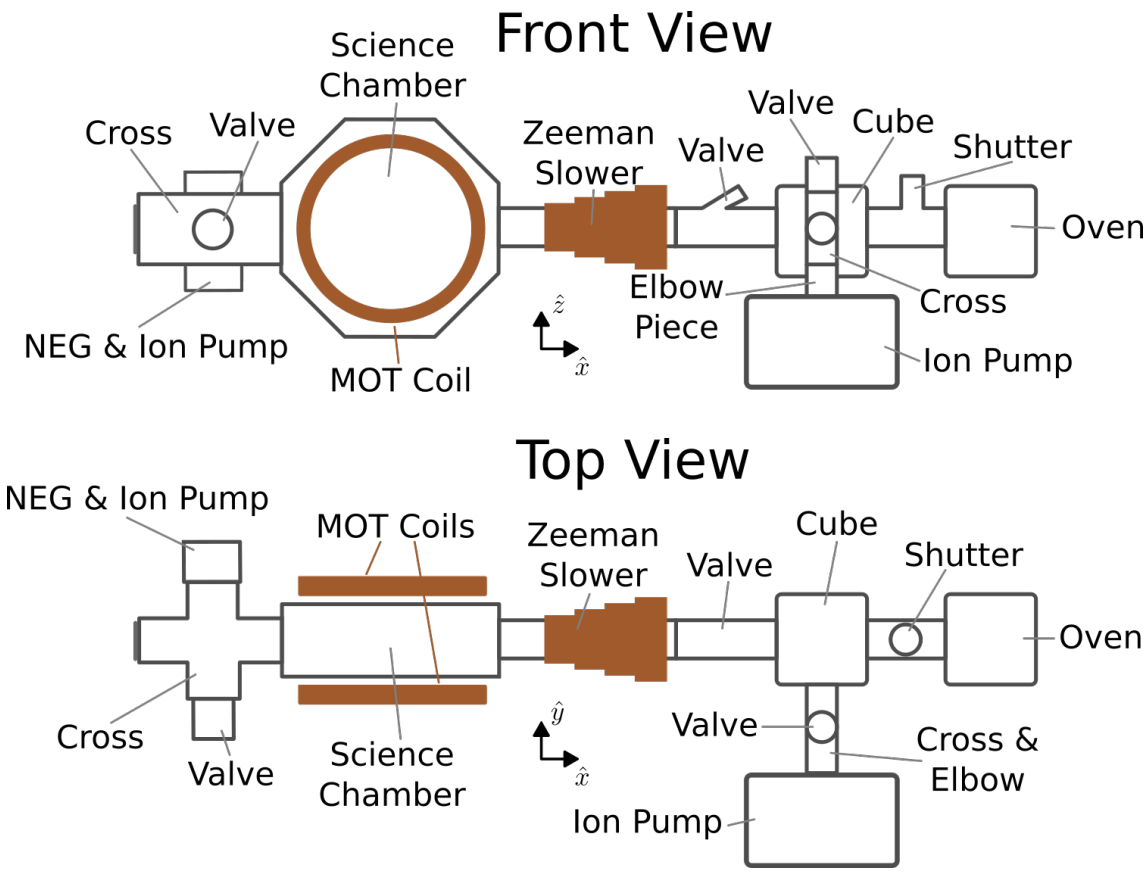


Figure 2.4: Schematic representation of the vacuum system. The oven holds the strontium source that generates the atomic beam. The beam can be blocked by turning the mechanical shutter. The cube has optical access to allow for transverse cooling of the atomic beam. The beam can be blocked from the rest of the system by closing the valve towards the Zeeman slower. The atoms reach the science chamber after getting decelerated inside the Zeeman slower, where the tapered solenoid generates the required magnetic field profile. Two coils are placed outside the science chamber to generate a quadrupole field for the magneto-optical trap (MOT). The system has two vacuum pumps in order to reach a lower pressure in the science chamber compared to the oven.

### 2.3.1 Assembly and Baking of the Vacuum System

The vacuum system has been built from scratch. Before the assembly started all parts have been thoroughly cleaned with acetone and methanol in order to remove oxidised strontium atoms and other dirt from a previous experiment. When connecting the vacuum parts it is important to evenly distribute the pressure by tightening opposite bolts over multiple rounds while following a star configuration. In the final step the flange that holds the optical ring cavity (Fig. 2.5) was attached to the science chamber, which completed the assembly.

After completing the vacuum system it was wrapped with fibre glass heating tapes and covered with insulating layers of aluminum foil in preparation of the baking procedure. The temperature of the vacuum system was increased in a stepwise fashion up to a temperature of $\sim 130$ °C while maintaining a small temperature gradient across the system. The vacuum system is heated, such that the metal outgasses more material. A turbomolecular pump was connected in order to remove all outgassed particles. The pressure stabilised after, but above the limit of the turbomolecular pump, which indicated that we had a leak in the system.

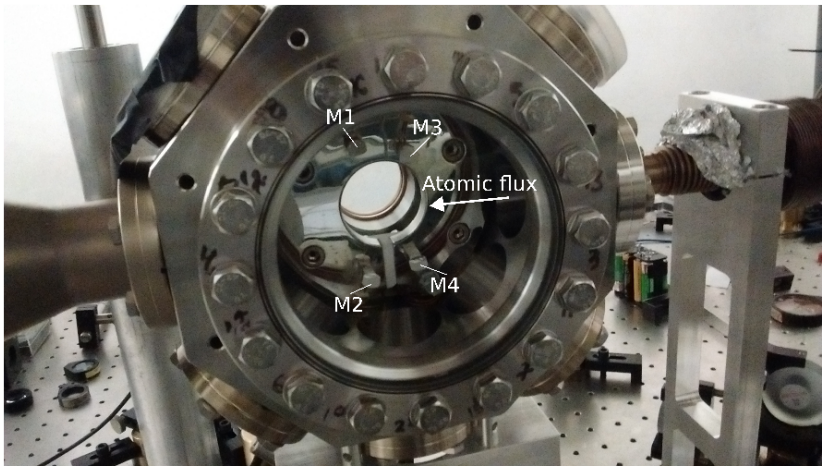


Figure 2.5: The optical ring cavity, consisting of mirrors 1 through 4 (M1, M2, M3 and M4), is mounted vertically inside the science chamber. The atomic flux enters the science chamber from the Zeeman slower, which is connected through a bellow.

The temperature was ramped down to $\sim 70$ °C in order to activate the residual gas analyser (RGA), which shows the partial pressure per atomic mass number. We found that the water level decreased, but nitrogen, air and $CO_2$ levels not so much when comparing an RGA trace to one taken at the start of the baking. We tested for leaks by flowing helium on certain parts of the vacuum system, because it permeates easily through the leaks and it is naturally absent. A large helium spike was visible on the RGA when flowing the helium gas close to the flange on the back of the science chamber, the flange that holds the optical ring cavity. On this flange are pins that provides an electrical connection to the heaters and piezoelectric transducers located on the cavity flange side that is under vacuum. We could identify that one of these pins was loose and caused the leak. The pin was glued with Torr Seal epoxy and the next day no helium showed up on the RGA traces when flowing helium.

With the leak fixed the second baking round started, again heating to $\sim 130$ °C. Now the pressure stabilised after some days to $7.1 \cdot 10^{-8}$ mbar by only using the turbomolecular pump. The non-evaporative getter (NEG) pump was conditioned and afterwards the temperature was ramped down to $\sim 70$ °C. The NEG was activated to bring the pressure down even further. The system was cooled down to room temperature, which enabled us to active the ion pump. All pumps working together brought the pressure down to $< 1.0 \cdot 10^{-10}$ mbar indicated by the ion pump. The final step was closing the valve to the turbomolecular pump and disconnecting it while keeping the vacuum intact. The whole assembly and baking procedure was completed in three months.

The oven section was baked separately, because the atomic source needed to be refilled. Before refilling the oven all parts were cleaned with acetone and methanol to remove the white strontium oxide layer. This reduces black body radiation losses from the oven, which is crucial to reach high temperatures at a relatively low power consumption. The shield covering the atomic source was heavily oxidised, the strontium oxide layer was machined away, afterwards the shield was cleaned with the chemicals. The oven was reassembled with the cleaned parts. Before closing the oven it needed to be refilled, which can not be done in air, because it will oxidise the strontium. The whole oven was covered in a plastic bag which was then filled with nitrogen. The oven was

successfully refilled in the nitrogen environment and then closed off. The oven section was baked with heating tapes in a similar fashion to the rest of the experimental setup, but it could be done at a much faster pace due to the smaller volume. During the baking we had another leak, which was discovered in a similar manner using the RGA while flowing helium. The thermistor port from which we readout the oven temperature was leaking, some more Torr Seal epoxy fixed the leak. At the end of the baking the oven was cooled down and the ion pump connected to this section was activated. The valve to the turbomolecular pump was closed, such that it could be removed. The final oven pressure reaches $7.7 \cdot 10^{-10}$ mbar.

### 2.3.2 Generating an Atomic Beam of Strontium Atoms from the Oven

A steady flux of strontium atoms is needed such that short loading times of an atomic sample can be achieved, which allows for quick repetitions of experiments. The vapor pressure of strontium (and other alkaline earth metals) at room temperature is low compared to alkali metals [122], therefore a high temperature is needed to create a strontium atomic beam source. The compact and efficient strontium oven operates at a temperature of 450 °C, which generates an atomic flux of $1.0 \cdot 10^{13}$ $s^{-1}cm^{-1}$ [123]. The atomic beam is collimated by a nozzle made of steel capillaries. The oven is constantly in operation, but the atomic beam can be blocked by turning the mechanical shutter and by closing the valve connecting the oven to the Zeeman slower (Fig. 2.4). The velocity distribution of the atomic beam follows a Maxwell-Boltzmann distribution, with the most probable velocity

$$v_{beam} = \sqrt{3k_B T/m} \tag{2.14}$$

with $k_B$ the Boltzmann constant, $T$ the (absolute) temperature of the atoms exiting the oven and $m$ the atomic mass. The most probable velocity of the strontium beam $v_{beam} \approx 454$ m/s for an oven temperature of 450 °C and atomic mass $m = 87.62(1)$ u. It is possible to operate the oven at a higher temperature $T$ in order to increase the atomic flux, which could be beneficial when working with a less abundant isotope, but this also increases the velocity of the beam $v_{beam}$, which means that more slowing would be needed in future steps. Another way of accumulating more atoms of a less abundant isotope is using the metastable $5s5p\ ^3P_2$ level as a reservoir. The atoms load the reservoir and are only repumped back to the ground state when the desired number of atoms in the reservoir is reached [124].

#### Aligning the Atomic Beam

The goal is to prepare a sample of strontium atoms at the focus of the optical ring cavity that is located inside the science chamber, therefore it is crucial to align the atomic beam as close to the final destination as possible. The Zeeman slower is connected to the science chamber by a flexible bellow, such that the orientation of the atomic beam can be changed with respect to the science chamber. Changing the path of the atomic beam requires careful translation of the complete first section of the vacuum chamber (the oven, cube and Zeeman slower) relative to the science chamber, without creating leaks. The alignment procedure starts by aligning the Zeeman slower beam, such that it crosses the cavity plane at the focal points, while passing through the Zeeman slower and ultimately reaching the oven. The frequency of the Zeeman slower beam is tuned to resonance on the $^1S_0 \leftrightarrow {}^1P_1$ transition, taking into account the Doppler shift due to the velocity of the beam $v_{beam}$. The atomic fluorescence can be observed by looking through one of the windows of the cube or the science chamber. The atomic beam resembles a narrow streak of blue light inside the Zeeman slower beam, it looks like a tiny blue lightsaber. The goal is to have this tiny blue lightsaber cross the cavity plane at the focal points, thus the complete first section of the vacuum chamber is carefully moved in order to translate the beam path relative to the optical ring cavity. The beam crosses the cavity plane after the first alignment step, but it crosses below the focal points of the cavity. Therefore the height of the pillars supporting the oven, the cube and the Zeeman slower is adjusted in order to raise the atomic beam, such that it crosses the focal points of the cavity. The Zeeman slower beam is realigned during the translation of the atomic beam, such that it keeps crossing the focal points of the cavity, while reaching through the Zeeman slower all the way to the oven.

The cube has optical access to the atomic beam in order to implement transverse cooling, which increases the atomic flux by reducing the transverse velocity distribution. Due to a lack of laser power at $\lambda = 461$ nm this is currently not yet implemented. The transverse velocity distribution of the atomic beam exciting the oven has been observed by shining light perpendicular to the atomic beam through the windows of the cube, while scanning the laser frequency. The Zeeman slower beam is roughly aligned with the center of the cone of atoms exiting the oven, therefore the majority of the atoms inside the atomic beam reach the focus of the optical ring cavity, but transverse cooling would certainly improve the atomic flux of the system.

### 2.3.3 Zeeman Slower

The Zeeman slower can slow down a wide velocity class of atoms [125], such that a large flux of cold atoms reaches the science chamber. The goal is to slow down the atoms inside the atomic beam to a final velocity $v_{final} \approx 50$ m/s, which corresponds to the capture velocity of the successive cooling stage i.e. the magneto-optical trap. The 30 cm long tapered solenoid of the Zeeman slower creates a magnetic field profile in order to compensate for the Doppler effect of the slowing atoms, such that the atomic beam remains on resonance with the Zeeman slower beam ($\lambda = 461$ nm, with $\sigma_+$ polarisation) while the atoms decelerate over the full length of the Zeeman slower. A closed transition is required for efficient cooling using the Zeeman slower, for $^{88}$Sr the Zeeman slower operates on the $(5s)^2\,{}^1S_0\ (J=0,\ M_J=0) \leftrightarrow 5s5p\,{}^1P_1\ (J'=1,\ M_{J'}=+1)$ transition and it operates on the $(5s)^2\,{}^1S_0\ (F=9/2,\ M_F=9/2) \leftrightarrow 5s5p\,{}^1P_1\ (F'=11/2,\ M_{F'}=11/2)$ transition for $^{87}$Sr. The atomic flux of $^{87}$Sr is limited due to undesired transitions to the hyperfine levels $F'=7/2$ and $F'=9/2$ of the ${}^1P_1$ state that lie 43 MHz above and 17 MHz below $F'=11/2$ respectively (Fig. A.1). The undesired transitions occur due to the large linewidth of the blue transition ($\gamma = 2\pi \cdot 30.2$ MHz) in combination with imperfect polarisation of the Zeeman slower beam, angular divergence or misalignment of the laser with the magnetic field axis.

The ${}^1P_1$ level has $g_{J'} = 1$ and the ${}^1S_0$ level has $g_J = 0$, thus $g_{J'}M_{J'} - g_J M_J = 1\cdot 1 - 0\cdot 0 = 1$ for $^{88}$Sr. The hyperfine level ${}^1P_1\ (F'=11/2)$ of $^{87}$Sr has $g_{F'} = 2/11$, the ground state ${}^1S_0\ (F=9/2)$ has $g_F = g_I\mu_N/\mu_B$, thus $g_{F'}M_{F'} - g_F M_F = 2/11 \cdot 11/2 - g_I\mu_N/\mu_B \cdot 9/2 \approx 1$. Thus changing between isotopes only requires tuning of the Zeeman slower beam frequency to account for the isotope shift, because the closed transitions to cool $^{87}$Sr and $^{88}$Sr require the same magnetic field profile to satisfy the resonance condition along the complete length of the tapered solenoid.

The blue lasers system [126] is able to generate an optical power of $P = 33$ mW in the Zeeman slower beam, which has a waist of $w_0 = 5$ mm and is slightly focussed towards the oven. Therefore the intensity at the axis of the beam $I_0 = 2P/\left(\pi w_0^2\right) = 84$ mW/cm$^2$, thus reaching a saturation parameter of $s = I/I_{sat} = 2$. This means that the scattering force [69]

$$\vec{F}_{scatt}(\delta) = \hbar\vec{k}R_{scatt}(\delta) = \hbar\vec{k}\frac{\gamma}{2}\frac{s}{1+s+4\delta^2/\gamma^2}, \tag{2.15}$$

with $\delta = \omega - \omega_0$ the detuning form atomic resonance, produces a deceleration of $a = 2a_{max}/3$ on resonance. The stopping distance for a strontium beam with most probable velocity $v_{beam} = 454$ m/s is $L_0 = v_{beam}^2/a_{max} = 22.0$ cm [69]. However, the system operates with a saturation parameter of $s = 2$, thus a Zeeman slower length of $3L_0/2 = 33.0$ cm is needed to completely stop the atoms. The atoms are not brought to a complete stop, instead they exit the Zeeman slower with a final velocity of [69]

$$v_{final} = \frac{1}{k}\left(-\delta + \frac{\left(g_{F'}M_{F'} - g_F M_F\right)\mu_B B_{bias}}{\hbar}\right) \approx 50 \text{ m/s}, \tag{2.16}$$

due to Zeeman slower beam operating at the chosen detuning of $\delta = -481$ MHz and the choice of bias field $B_{bias}$.

The achievable slowing with the Zeeman slower can be increased, which will allow for operation at higher oven temperatures $T$ that will increase the atomic flux. The laser power in the Zeeman slower beam can be increased through the expansion of the blue laser system with a second slave laser, which is then dedicated to generate the Zeeman slower beam. The system will therefore operate

with a saturation parameter of $s \gg 1$, thus reaching close to the maximum deceleration $a_{max}$ produced by the scattering force. Which would mean that the system could decelerate an atomic beam with a higher most probable velocity of $v_{beam}$, which is generated at higher oven temperatures. (Note the melting point for strontium $T_{melt} = 777$ °C.) Together with the implementation of transverse cooling it is therefore possible to increase the atomic flux drastically in the future.

### 2.3.4 Optical Layout around the Vacuum System

The optical system is built around the optical ring cavity, which acts as the heart of the experiment for performing interferometry with squeezed states. The optical ring cavity is mounted vertically in the science chamber (Fig. 2.5), the ring cavity configuration allows optical access for the final cooling stages, entanglement creation and for interferometry along the gravitational axis (Fig. 2.6).

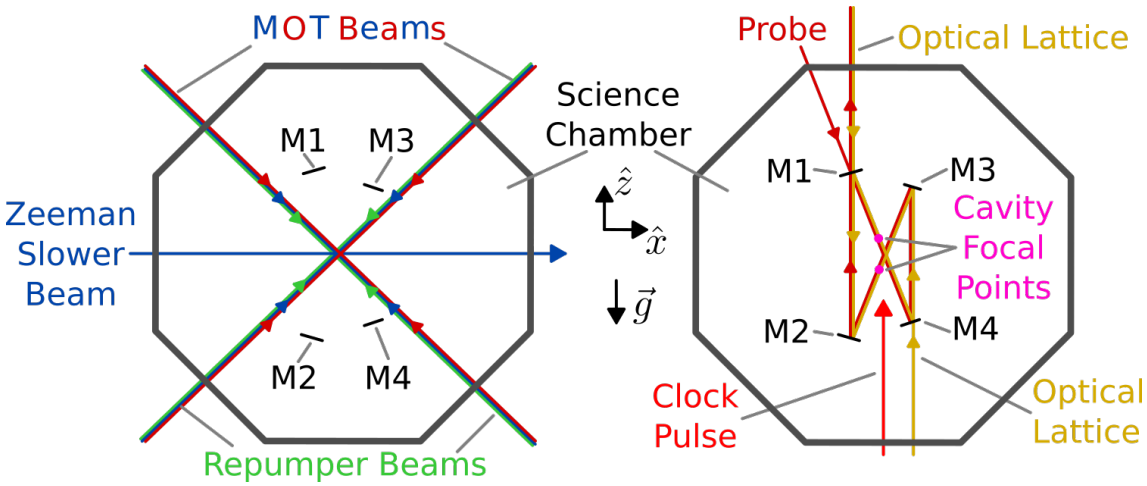


Figure 2.6: Schematic representation of the laser beams that enter the science chamber. On the left the beams that facilitate the cooling are shown. On the right the beams used in interferometry and to create entanglement are shown. The Zeeman slower beam ($\lambda = 461$ nm) decelerates the atoms inside the Zeeman slower. The magneto-optical trap (MOT) beams cool and trap the decelerated atoms at the center of three perpendicular counter-propagating beam pairs, the repumper beams recover the atoms lost to the $^3P_2$ level. The axial MOT beams and repumper beams along $\hat{y}$ are not shown. Two different stages are used, the first stage at $\lambda = 461$ nm (blue) with the repumper at $\lambda = 497$ nm (green) is followed by the second stage at $\lambda = 689$ nm (red). The beams for the two MOT stages are superimposed to efficiently transfer the atoms from the first to the second stage. The probe beam ($\lambda = 689$ nm) is coupled to mirror 1 (M1) of the cavity, it is used to create entanglement. Two beams at $\lambda = 813$ nm are coupled to mirror 1 (M1) and mirror 4 (M4) of the cavity, they are counter-propagating which generates an optical lattice inside the cavity plane. The goal is to trap the atoms inside the optical lattice at one of the focal points of the cavity for maximum atom-light interaction with the probe beam. The probe and optical lattice are superimposed. The clock pulse ($\lambda = 698$ nm) along the gravitational axis is in free space, it drives state transitions during the entanglement and interferometry sequences.

#### Full Optical Layout for the Two-Stage MOT

Light from the blue (Sec. 2.5.2), repumping (Sec. 2.5.3) and red (Sec. 2.7) laser systems is transported towards the science chamber (Fig. 2.7) in order to create a two-stage magneto-optical trap (MOT). The Zeeman slower beam decelerates the atoms inside the Zeeman slower (Sec. 2.3.3). The MOT beams cool and trap the decelerated atoms at the center of three perpendicular counter-propagating beam pairs in two stages: first the blue MOT stage (Subec. 2.5.1) which is followed by the red MOT stage (Subsec. 2.5.4)]. The repumper beams recover the atoms lost to the $^3P_2$ level during the blue MOT stage. The axial MOT beams and repumper beams along $\hat{y}$ are not shown. The MOT center is located inside the plane of the optical ring cavity (M1, M2, M3 and M4).

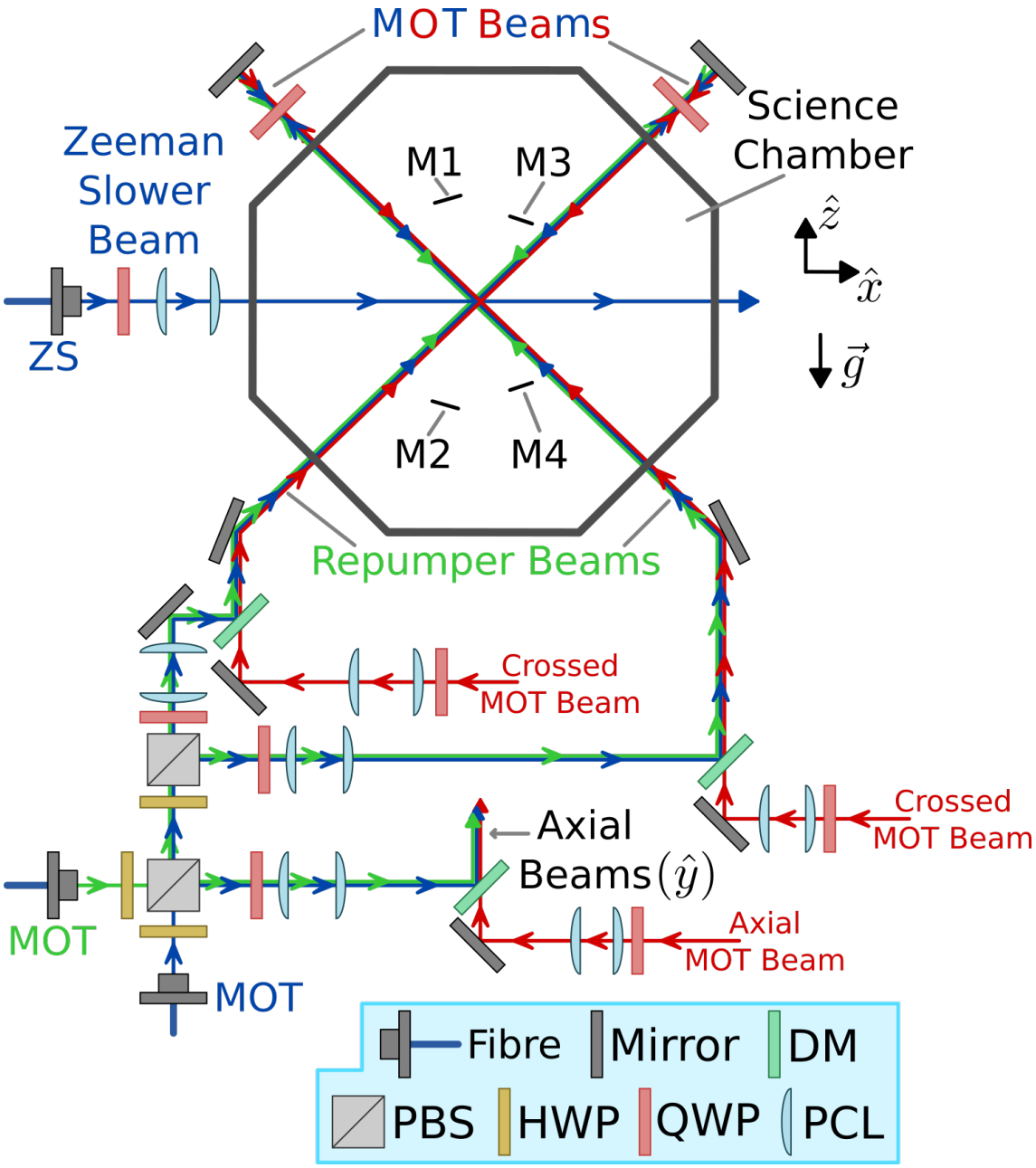


Figure 2.7: Schematic representation of the Zeeman slower beam and the two-stage magneto-optical trap (MOT) beams. The beams propagating close to each other represent superimposed beams. The abbreviated symbols indicate a dichroic mirror (DM), polarising beamsplitter cube (PBS), half waveplate (HWP), quarter waveplate (QWP) and a plano convex lens (PCL). The QWPs are used to create the required circular polarisations, which depends on the orientation of the magnetic fields. The PCL pairs are used to create collimated beams with a waist of $w_0 = 5$ mm. The red MOT beams are created on the same optical table, therefore they do not exit from an optical fiber.

### Full Optical Layout for Probing and Clock Pulses

Light from the red (Sec. 2.7), clock (Sec. 2.4.2) and lattice (Sec. 2.6.1) laser systems is transported towards the science chamber (Fig. 2.8) in order to trap, probe and pulse the atoms.

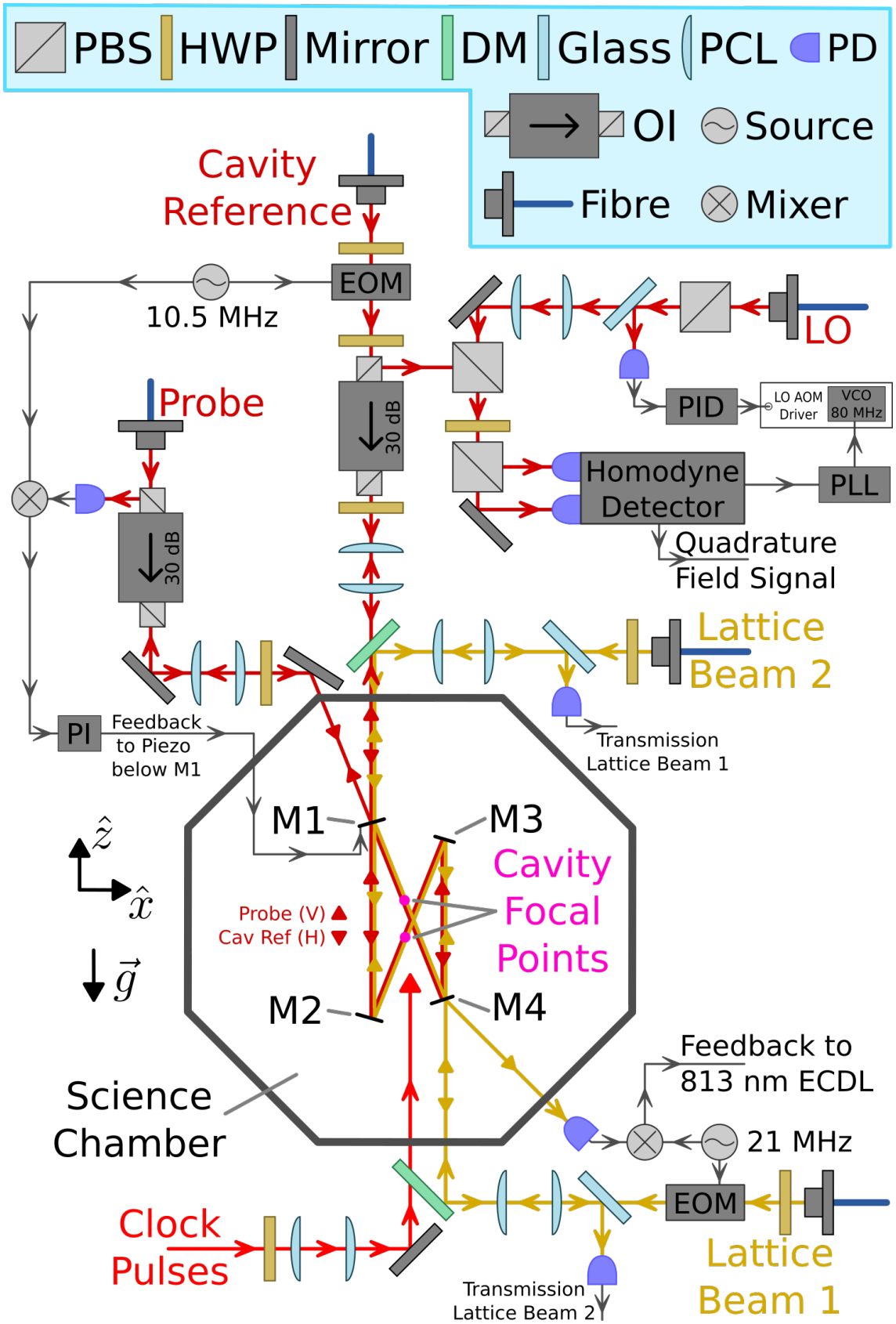


Figure 2.8: Schematic representation of the optical setup for probing the atoms and for applying clock pulses. The full caption is shown on the next page.

Caption figure 2.8: Schematic representation of the optical setup for probing the atoms and for applying clock pulses. The beams propagating close to each other represent superimposed beams. The abbreviated symbols indicate a polarising beamsplitter cube (PBS), half waveplate (HWP), dichroic mirror (DM), plano convex lens (PCL), photodiode (PD) and an optical isolator (OI). The mirrors of the optical ring cavity are abbreviated with M1, M2, M3 and M4. Dichroic mirrors are used to split the different beams based on wavelength. Two optical isolators are used to split the counter-propagating probe beam (vertical polarisation) and cavity reference beam (horizontal polarisation) based on polarisation.

Two lattice beams (Fig. 2.8) are mode matched to the cavity using a PCL pair on each beam. Lattice beam 1 is locked to the cavity using the Pound-Drever-Hall (PDH) technique [127, 128, 129]. Sidebands are generated at ±21 MHz by the electro-optic modulator (EOM), the beat note is measured with a photodiode in reflection of M4. The generated PDH error signal is used as a feedback to the 813 nm ECDL in order to lock the laser to the cavity. A single PDH scheme is necessary to lock both lattice beams, since the two lattice beams are generated by splitting the 813 nm light into two beams (Sec. 2.6.1). The transmission of both lattice beams is observed on individual photodiodes by picking of a small portion of the transmitted light with a piece of glass, this signal can be used to stabilise the intracavity intensity of the individual lattice beams. The purpose of the optical lattice is to trap strontium atoms at one of the cavity focal points.

The cavity reference beam (Fig. 2.8) is mode matched to the cavity using a PCL pair. The cavity frequency is stabilised by locking it to the cavity reference beam using the PDH technique. The cavity reference beam propagates inside the cavity with a horizontal polarisation. The EOM generates sidebands at ±10.5 MHz, the beat note is measured with a photodiode in reflection of M1. The generated error signal is fed to a PI-controller, which provides feedback to the piezoelectric transducer below the pillar holding M1 in order to stabilise the cavity length.

The probe beam (Fig. 2.8) is mode matched to the cavity using a PCL pair. The +1 sideband of the probe (Fig. 2.30) scans the cavity resonance frequency (Subsec. 3.2.1), the carrier of the probe is reflected of M1. The probe beam propagates inside the cavity with a vertical polarisation. The probe is optically amplified by the homodyne detection system (Sec. 2.8).

The local oscillator (LO) beam (Fig. 2.8) is mode matched to the probe beam using a PCL pair. The polarisation maintaining fiber head is rotated such that the LO exits with a horizontal polarisation. A small part of the beam is picked of using a piece of glass to stabilise intensity and polarisation fluctuations, the signal measured by the photodiode is fed to a PID-controller, which provides an error signal to the LO AOM driver. The probe beam and LO beam are superimposed based on polarisation using a PBS, such that no signal from the probe is lost compared to using a 50/50 beamsplitter cube. The superimposed signal is split 50/50 using a HWP in combination with a PBS, such that a balanced homodyne detector is created. The phase between the probe beam and LO beam is stabilised by the phase-locked loop (PLL), see figure 2.39. The quadrature field signal gives the information about the cavity reference frequency.

The clock pulses propagate in free space (Fig. 2.8), the beam is collimated with a waist of $w_0 = 5$ mm using a PCL pair. The $\lambda/2$ waveplate is used to rotate the polarisation for maximal coupling to the atoms. The fiber noise cancellation setup (Fig. 2.15) will transport the light to the optical table hosting the vacuum system, therefore the clock pulses do not exit from an optical fiber.

### 2.3.5 Cavity Temperature Controller

The atomic induced shift in cavity resonance frequency is measured during the quantum non-demolition measurement, which means that any change in cavity resonance frequency not caused by the atoms leads to an error. The four cavity mirrors (M1, M2, M3 and M4) are mounted on pillars, which are connected to the cavity flange (Fig. 2.9). Temperature fluctuations cause thermal expansion and contraction of the cavity flange, which effectively changes the cavity length and thus the cavity frequency. Inside the cavity flange there is a PT100 resistor to measure the temperature of the cavity flange and four high power resistors ($R_{heater} = 25\ \Omega$ each) that dissipate energy acting as heaters. The designed cavity temperature controller (CTC) reads out the PT100

sensor and supplies a current $I_{heat}$ to the four heaters connected in series (100 Ω total resistance) in order to stabilise the temperature of the cavity flange.

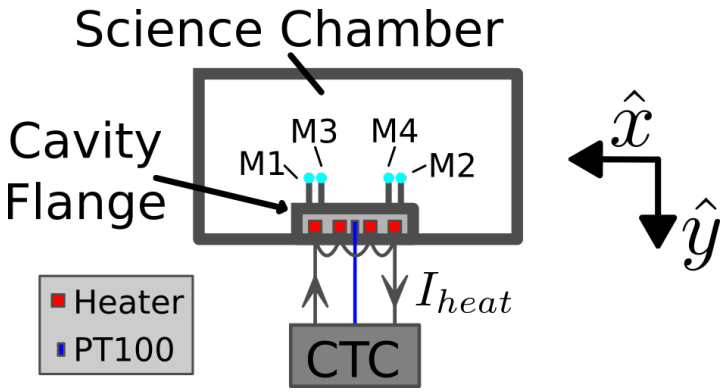


Figure 2.9: Schematic representation of the cavity temperature stabilisation loop. The resistance of the PT100 resistor is read out (blue line) by the cavity temperature controller (CTC) in order to determine the temperature of the cavity flange. The CTC generates a current $I_{heat}$, which is supplied to the four heaters connected in series. The high power resistors (heaters) dissipate the electrical power in the form of heat. The CTC controls the current $I_{heat}$ in order to stabilise the cavity temperature in this heating only feedback loop.

The cavity temperature feedback loop is a heating only circuit. The cavity flange relies on dissipating its heat to the environment for 'cooling'. The heating and cooling response are measured by supplying a heating impulse of two minutes while observing the voltage over the PT100 resistor mounted in a voltage divider (Fig. 2.10). The heating and cooling data is fitted with an exponential, the heating timescale $\tau_{heat} = 59.3$ s and the cooling timescale $\tau_{cool} = 165$ min. The large timescales are caused by the large volume of the cavity flange (CF100). Due to the long timescales it is convenient to use a digital PID-controller instead of the analog PID-controllers that are normally used in the lab to stabilise the laser temperature. An Arduino DUE microcontroller is chosen to act as the digital PID-controller. The printed circuit board (PCB) is designed (Sec. B.1) to act as an Arduino shield, such that it can easily be inserted.

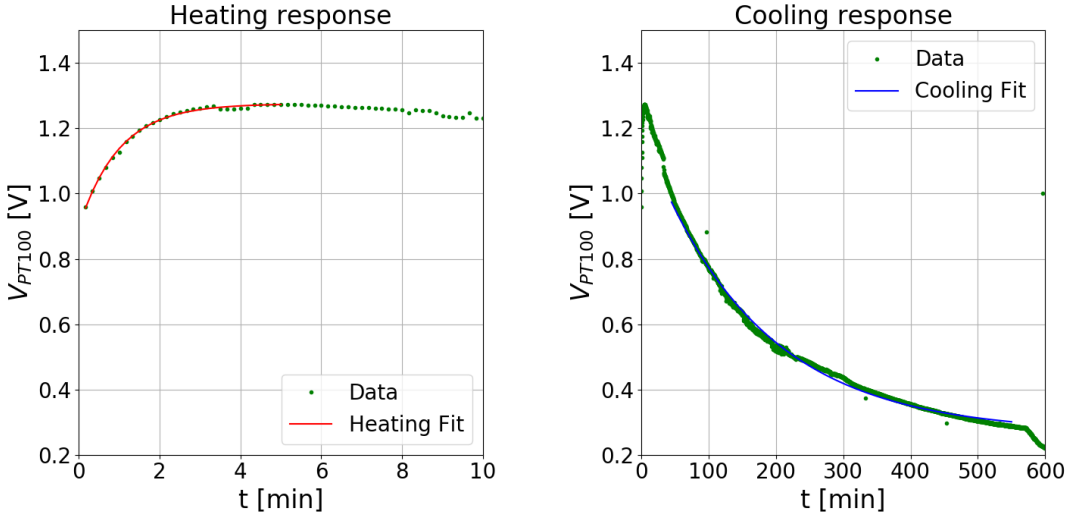


Figure 2.10: The cavity flange is heated for two minutes, the heating response (left) and cooling response (right) are measured by observing the voltage over the PT100 sensor. The heating and cooling data is fitted with an exponential, the heating timescale $\tau_{heat} = 59.3$ s and the cooling timescale $\tau_{cool} = 165$ min.

The resistance $R_{PT100}$ of the PT100 is measured (Fig. 2.11) at various heating currents $I_{heat}$ in order to get an idea of the cavity temperatures that can be reached. After setting the heating current there is a wait time of at least 3 to 4 hours in order to give the cavity time to reach a stable temperature. The PT100 has a resistance of $R_{PT100} = 100\ \Omega$ at $T = 0\ °C$, the resistance increases linearly with 0.39 Ω/°C. The cavity can be heated from room temperature up to 45°C at $I_{heat} = 90$ mA, which is a reasonable temperature range. The cavity temperature scales linearly with heater current.

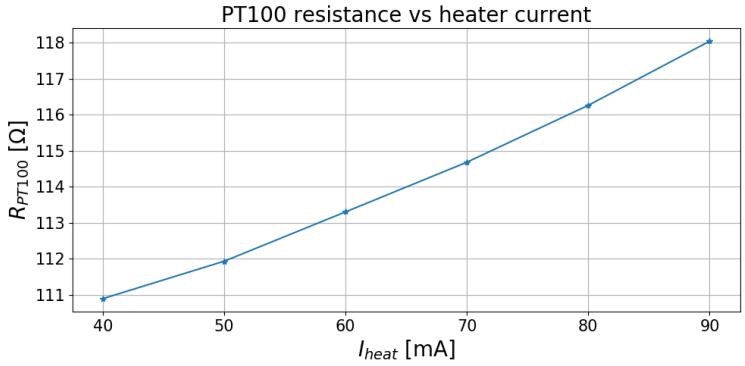


Figure 2.11: PT100 resistance vs heater current. The measured PT100 resistances $R_{PT100}$ (blue stars) are connected by line segments. The resistance $R_{PT100}$ scales linearly with heater current $I_{heat}$.

The CTC is designed to stabilise the cavity temperature at the chosen temperature set point, which has a range of 25°C to 45°C. The heating current $I_{heat}$ is updated every 100 ms by the digital PID-controller. The error signal has a sensitivity of 56.3 $\mu$K/bit, see section B.1 for more details.

## 2.4 Realisation of a Home-Built Narrow-Linewidth Clock Laser

A home-built narrow-linewidth clock laser was realised in order to drive the $^1S_0 \leftrightarrow {}^3P_0$ clock transition, I nicknamed him Daniel after my watch. The linewidth requirement for this laser is very strict, because the clock transition in $^{87}$Sr has a natural linewidth of $\gamma = 1.35$ mHz [107]. But driving the clock transition at high intensities (i.e. large $s$) broadens the linewidth to $\gamma_s = \gamma\sqrt{1+s}$ [69]. Ideally the laser linewidth is smaller than the power broadened linewidth $\gamma_{laser} < \gamma_s$, such that the full intensity of the beam is used to drive the desired transition. Therefore the target for the clock laser linewidth is on the order of 1 Hz. Ideally the interferometer pulses on the clock transition are driven at a Rabi frequency on the order of kilohertz, with quite a large saturation parameter $s = I/I_{sat} = 2\Omega^2/\gamma^2 \sim 10^{12}$ [69]. Driving the clock transition at such high Rabi frequencies results in a broad clock transition, but a narrow-linewidth clock laser is still desired in order to imprint minimal phase noise onto the wave packets during the interferometer sequence.

### 2.4.1 External-Cavity Diode Lasers

All master lasers in the experimental setup are home-built, they are external-cavity diode lasers (ECDLs) [130, 131, 132], which use a grating to provide optical feedback in an external-cavity configuration in order to narrow the linewidth and to emit into a single mode. All ECDL master lasers are built in the Littrow configuration (Fig. 2.12). The laser light hits a grating, which creates an angle-dependent diffraction pattern based on constructive interference [119]

$$\sin(\theta_n) = \frac{n\lambda}{d}, \tag{2.17}$$

with $\theta_n$ the angle of the $n^{\text{th}}$ diffraction order, $\lambda$ the wavelength of the light and $d$ the line spacing of the grating. Most of the home-built ECDLs use a GH13-18V grating (1800 lines/mm) such that $d = 10^{-3}/1800$ m. The wavelength $\lambda$ of the ECDL is selected by tuning the angle of the grating to $2\theta_1$, such that the first diffraction order ($n = 1$) at the chosen wavelength $\lambda$ is back reflected towards the laser diode in order to provide optical feedback. The angle of the grating is tuned with a piezoelectric transducer, which is mounted on the back of the grating.

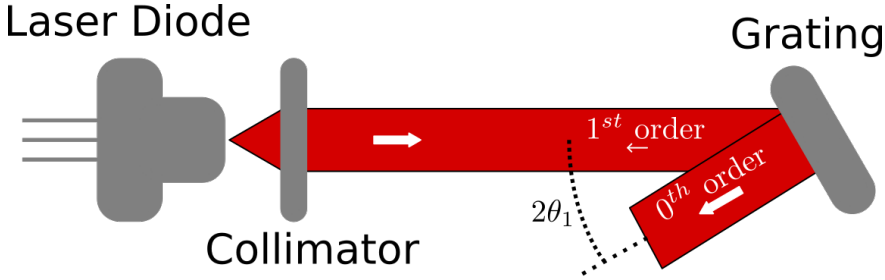


Figure 2.12: Schematic representation of an external-cavity diode laser (ECDL) in Littrow configuration. The laser diode emission is collected by an aspheric lens (the collimator) with focal length $f = 4.51$ mm (C230TMD-A or B), which collimates the light into a collimated beam. The collimated beam hits the grating angled at $2\theta_1$, such that the $1^{\text{st}}$ order is reflected back towards the laser diode. The wavelength-dependent back reflected light provides optical feedback for the laser diode.

The laser linewidth reduces when the ECDL cavity length $L$ (the distance between the diode and grating) is increased. A longer external-cavity leads to a larger dispersion of the first diffraction order and to the selection of modes that have a long coherence length. This narrows down the amount of modes that can be selected to provide optical feedback. A downside of using a long external cavity is the laser becoming more sensitive to mode hops, due to the reduced free spectral range $f_{FSR} = c/(2L)$. The 'old' ECDLs (blue, red and repumper) in the experimental setup have a cavity length of $L = 2$ cm. Two new ECDLs (clock and lattice) have been realised with a

cavity length of $L = 25$ cm. The long ECDL configuration is one of the ingredients for creating a narrow-linewidth clock laser.

Another control knob to tune the lasing wavelength is temperature, because the emission pattern of the laser diode increases in wavelength when temperature goes up. The diode is placed in a holder mounted on a Peltier element and thermistor, which are used in a feedback loop to stabilise the temperature with an external controller.

New laser designs are based on a cat eye configuration [133, 134], where an interference filter is used to select the wavelength instead of using a grating. An advantage of the cat eye design is that the beam exits in a straight line, there is no angle dependence as is the case for an ECDL in Littrow configuration. Recently a cat eye laser has been demonstrated with a small intracavity lithium niobate electro-optic modulator as the output coupler [134], which was able to reduce the linewidth of the laser to 1 Hz. This would be a nice future upgrade for the master lasers in the experimental setup.

### Constructing an ECDL

The construction process of our home-built ECDLs is briefly described. The laser box is assembled including peltier elements and thermistor, enough thermal paste is applied for proper heat transfer. All electronics (modulation circuit, diode protection, safety switch) are connected and finally the laser diode is installed. The temperature control system is engaged, the feedback system needs some time to stabilise the temperature of the laser. For AR-coated diodes the laser current is tuned above the laser threshold current in order to have enough light to work with.

The first step in alignment is collimating the beam, the collimator is placed in a translation stage and lowered in front of the diode. The position of the collimator is tuned such that the beam is collimated along the complete distance up to infinity (which is usually the wall of the laboratory). The beam path can be prolonged by using a mirror, this makes it easier to check for a collimated beam at far away distances.

The second step is placing the grating, which is glued on a "bendable" metal piece, such that the grating angle can be changed with the help of a piezoelectric transducer. The laser current is tuned just below the threshold current. The horizontal angle of the grating is adjusted such that the first diffraction order is sent back towards the laser diode at the desired wavelength. The vertical angle of the grating is adjusted in order to achieve optical feedback, the laser will start lasing due to the ECDL configuration lowering the threshold current. Achieving lasing due to proper optical feedback is easy to notice, because the beam will become very intense.

The third step is reducing the threshold current. A properly aligned ECDL has a lower threshold current compared to when the laser would be free running. This is achieved by optimising the position of the collimator by carefully tuning the translation stage. The vertical angle of the grating is only tuned slightly to get the laser back to lasing, the majority of the work is done by tuning the collimator. The distance between the laser diode and the collimator is the most sensitive to tuning, but also the most important direction to tune. In order to perform this task properly it is convenient to modulate the laser current with a triangle wave via the modulation port of the laser diode driver. The current is set close to the threshold current. The emitted light is observed with a photodiode that is connected to an oscilloscope. (Note that other methods are possible, but this is how we check the lasing threshold.) The laser current is reduced, such that half of the current modulation is below the threshold and half is above, the oscilloscope shows a pattern of a flat line alternating with a triangle. The position of the collimator is improved, this will reduce the laser threshold and therefore increase the laser output power. The signal observed with the photodiode will rise and shows a triangular wave pattern. The laser current is reduced to have the triangular modulation halfway the threshold again and the process is repeated. Eventually it is no longer possible to improve and the lasing mode will be lost. The laser current is increased a bit and the previously found optimal conditions are restored.

The wavelength is measured again after aligning the laser, if everything is according to plan then it is time to glue the collimator. Araldite glue is prepared and the height of the translation stage is

written down. The collimator is raised and the surface of the laser base piece is glued. The glueing is performed carefully, such that no glue is accidentally put on the diode. The collimator is lowered into the Araldite glue until it is at the noted height. The technique for ECDL alignment using the photodiode and oscilloscope as described in the previous paragraph is used again to find the lasing threshold. While the Araldite glue dries for 24 hours the lasing threshold is checked in the first few hours, because when the Araldite glue dries it will "shrink" a bit, i.e. loose volume pulling down on the collimator. The translation stage is not touched when the glue is drying, instead the threshold is recovered by tuning the vertical angle of the grating. Usually this is enough, only in "extreme" cases the collimator position needs to be adjusted during the drying of the glue. After 24 hours the collimator is carefully loosened from the translation stage. A final check of the lasing threshold and the wavelength is performed. If everything is fine, then the home-built ECDL has been constructed successfully. A power versus current and wavelength versus current measurement is performed to characterise the newly constructed laser.

### 2.4.2 Clock Laser System at 698 nm

The clock laser system (Fig. 2.13) produces 698 nm light in order to drive $\pi/2$ and $\pi$ pulses on the ${}^1S_0 \leftrightarrow {}^3P_0$ clock transition. The master ECDL is frequency stabilised to a high-finesse ultra-low expansion (ULE) Fabry-Pérot cavity using the Pound-Drever-Hall (PDH) technique [127, 128, 129] in order to narrow the laser linewidth. The high-finesse ULE cavity is shielded against black body radiation by a gold shield, has a linewidth of $\kappa = 2\pi \cdot 3.75\,(0.15)$ kHz, a finesse of $\mathcal{F} = 4.09\,(15) \cdot 10^5$ and a day to day drift in cavity resonance frequency on the order of 100 kHz [135, 136]. The master laser is isolated with a 60 dB optical isolator, because the narrow-linewidth laser is highly sensitive to optical feedback. During the construction of the setup a 30 dB optical isolator was first used, but optical feedback from the ULE cavity was observed. The 30 dB optical isolator was therefore replaced by a 60 dB optical isolator. Optical feedback is no longer observed with 60 dB of isolation.

An older generation clock laser [136] was locked to the ULE cavity in two steps: first the master was locked to an intermediate-finesse cavity to narrow the laser linewidth $< 1$ kHz, then it was locked to the high-finesse ULE cavity in the second step by providing feedback on the intermediate-finesse cavity length and on an acousto-optic modulator. In this system (Fig. 2.13) the newly constructed long ECDL is locked directly to the high-finesse ULE cavity, which is possible due to the narrow linewidth provided by the ECDL cavity length of 25 cm (Sec. 2.4.1). Even though there is no estimate of the long ECDL linewidth in similar systems it was on the order of a few 10 kHz.

The output power of the laser system is increased by using a slave laser and a tapered amplifier (TA). The master laser injects the slave, both lasers use the same diode (HL7001MG). The slave laser is necessary in order to reach the appropriate power to inject the TA (EYA-TPA-0690-00500-2003-CMT02-0000). An additional cylindrical lens pair is used before the TA in order match the spatial mode of the slave laser with the spatial mode of the TA. Unfortunately the spatial mode of the TA is split into two thin rectangles, furthermore the TA has its peak wavelength typically somewhere between 685 nm and 690 nm. Heating the TA to 30 °C and very careful mode matching enabled the injection of the TA at 698 nm despite these difficulties. The light is amplified to 151 mW at the TA output when sourcing 800 mA to the TA. These TAs (EYA-TPA-0690-00500-2003-CMT02-0000) are known to degrade rapidly [59], therefore alternative solutions will be explored to attain the required laser power.

#### Narrowing the Clock Laser Linewidth

A sideband of the master laser (see inset of fig. 2.13) is frequency stabilised to the ULE Fabry-Pérot cavity with the PDH method by using double phase modulation through the fiber EOM. Locking to the sideband is necessary to bridge the frequency gap between the resonance frequency of the ${}^1S_0 \leftrightarrow {}^3P_0$ clock transition and the frequency of the ULE cavity. The generated PDH error signal is used to narrow the linewidth of the laser by providing feedback directly to the laser current (compensating high-frequency current noise), to the laser diode driver (compensating low-frequency current noise) and to the piezoelectric transducer controlling the ECDL grating (compensating low-frequency noise and drift).

The frequency noise (Fig. 2.14) of the home-built clock laser is determined by measuring the voltage noise power spectral density $S_V$ of the PDH error signal, which is converted to a frequency noise power spectral density $S_f$ using

$$S_f = \left(\frac{\kappa}{V_{pp}}\right)^2 S_V,$$

with $\kappa = 2\pi \cdot 3.75$ kHz the linewidth of the ULE cavity and $V_{pp} = 728$ mV the peak to peak voltage of the PDH error signal around cavity resonance.

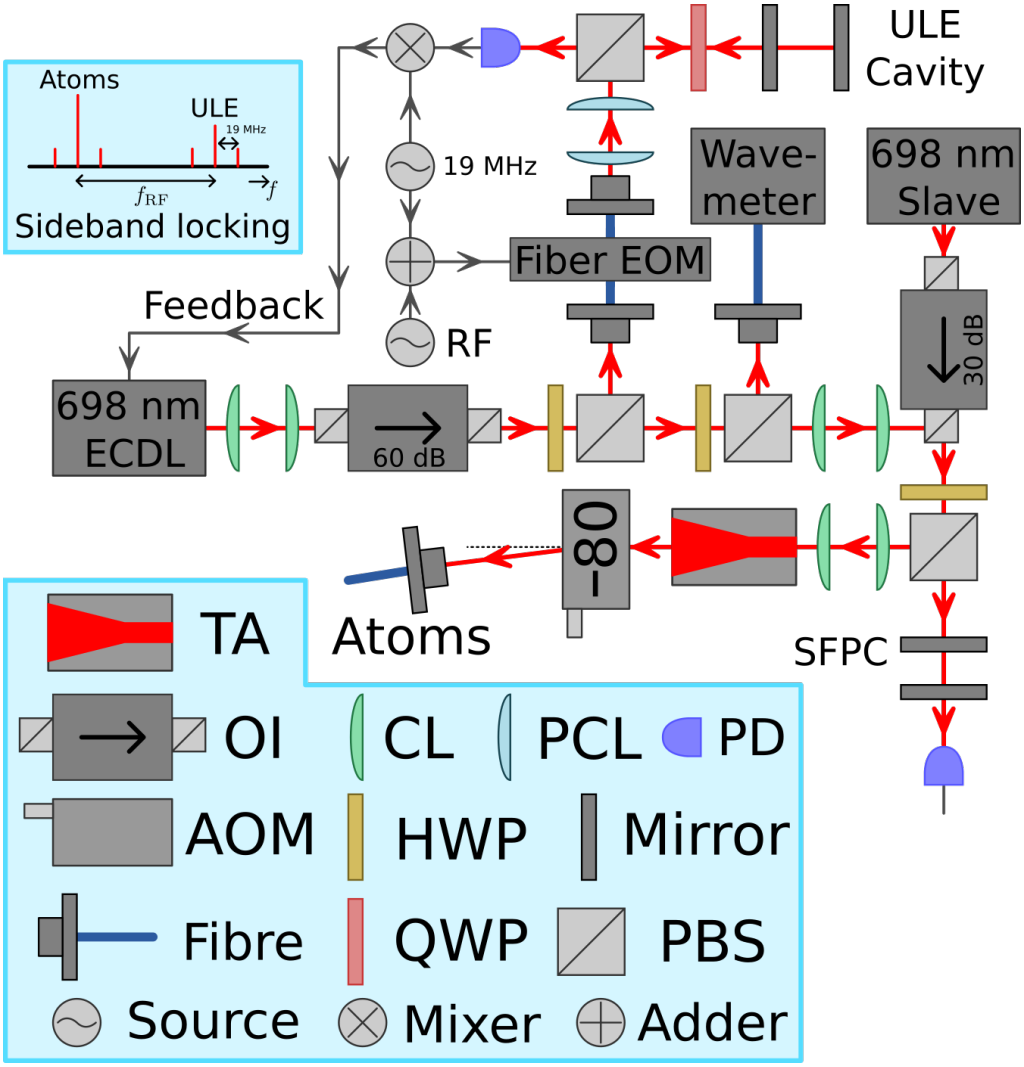


Figure 2.13: Schematic representation of the clock laser system in master-slave configuration. The abbreviated symbols indicate a tapered amplifier (TA), optical isolator (OI), acousto-optic modulator (AOM), cylindrical lens (CL), plano convex lens (PLC), half waveplate (HWP), quarter waveplate (QWP), photodiode (PD) and a polarising beamsplitter cube (PBS). A sideband of the master laser is frequency stabilised to an ultra-low expansion (ULE) Fabry-Pérot cavity using the Pound-Drever-Hall technique [127, 128, 129] by double phase modulation through the fiber EOM. The frequency diagram inset shows the frequency spectrum of the master laser for sideband locking. The master injects the slave via the output port of an optical isolator. The transmission of the scanning Fabry-Pérot cavity (SFPC) is observed with a photodiode to check if the slave laser is injected. The light is amplified by a tapered amplifier and transported to the vacuum chamber through an optical fibre. The AOM generates the clock pulses by diffracting the light into the $-1^{\text{st}}$ order.

The linewidth of the laser is estimated by $\pi$ times the white noise level of the frequency noise power spectral density [138, 139], which leads to an estimated laser linewidth of $\sim 1$ Hz (Fig. 2.14). Note that the white noise spectrum is not flat above 10 kHz due to the limited bandwidth of the lock. Also note that this estimate using the white noise level is considered as an underestimate for the laser linewidth, creating a beat note with another clock laser would be a better measurement. Furthermore, the noise at low frequencies is still large and will require further optimisation, however the main point is that high-frequency noise reduction can be achieved by stabilising to a single cavity.

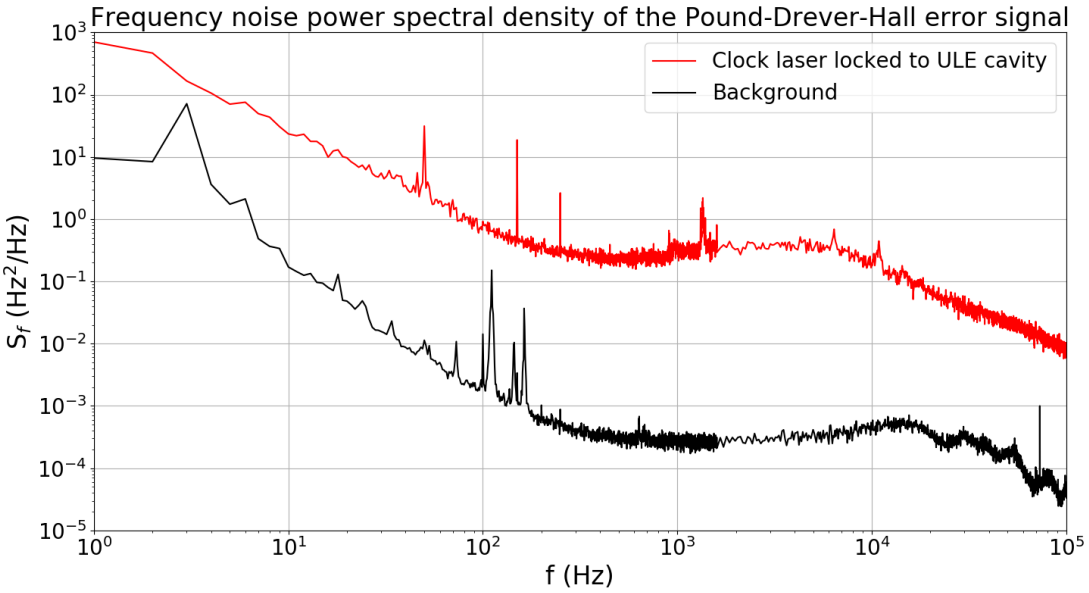


Figure 2.14: Frequency noise power spectral density of the clock laser Pound-Drever-Hall error signal when locked to the ultra-low expansion (ULE) cavity (red). The background signal (black) is measured with the clock laser unlocked and far from cavity resonance. The spectrum shows a $1/f$ behaviour until 20 Hz, then the spectrum is flat due to white noise up to roughly 10 kHz. Above 10 kHz the noise reduces again, because higher frequencies are outside the bandwidth of the lock.

### Clock Laser System Improvements

A very powerful clock laser system is desired, such that short interferometry pulses can be realised in free space. A $\pi$ pulse lasts $\tau_\pi = 100$ $\mu$s with a Rabi frequency of $\Omega = 2\pi \cdot 5$ kHz. Generating pulses with a beam waist of $w_0 = 5$ mm at a Rabi frequency of $\Omega = 2\pi \cdot 5$ kHz requires an optical power of

$$P = \frac{\pi w_0^2}{2} I = \frac{\pi w_0^2}{2} \frac{2\Omega^2}{\gamma^2} I_{sat} = \frac{\pi w_0^2 \Omega^2}{\gamma^2} I_{sat} = 5.58 \text{ W}.$$

The required power is almost two orders of magnitude more than the 151 mW of the current system setup. Previous results of an interferometer operating on the clock transition [59] show that increasing the waist of the clock pulses from $w_0 = 0.9$ mm to $w_0 = 1.8$ mm increases the sensitivity threefold, due to an increase in visibility by a factor of three. The observations are attributed to the thermal expansion of the wave packets, the effects are lessened the larger the beam is compared to the cloud size. This motivates the choice of increasing the beam waist to $w_0 = 5$ mm. Furthermore the expansion of the cloud can be limited by cooling the atoms to lower temperatures and/or using a more narrow velocity selection.

Note that high Rabi frequencies can be achieved with the current setup during the quantum non-demolition measurement sequence by using a smaller beam waist $w_0$, because then the atoms are

confined inside the optical lattice. A Rabi frequency of $\Omega = 2\pi \cdot 5$ kHz can be achieved with a beam waist of $w_0 = 0.5$ mm for a power of $P = 55.8$ mW. This power is achievable with the current system when factoring in the losses due to the AOM efficiency (67 %) and the fiber coupling efficiency (55 %). ($P = 151$ mW $\cdot\, 67\% \cdot 55\% = 55.6$ mW.)

High power 698 nm clock pulses can be generated by a titanium:sapphire laser [140]. The creation of a home-made injection-locked titanium:sapphire laser [141] will be explored in order to increase the laser power of the clock laser system. The injection locked setup is advantageous because the realised narrow-linewidth master laser (Fig. 2.14) can be used as a seed.

### Fiber Phase Noise Cancellation Scheme

The narrow linewidth of the laser is lost when transporting the clock laser light trough an optical fiber, due to fiber-induced phase noise. This can be compensated using a fiber noise cancellation scheme [142, 143]. The idea is that a bit of light will be sent back through the fiber, such that double the phase noise will be measured at the beat note of twice the AOM frequency (Fig. 2.15). A phase-locked loop (PLL) will be created to lock a voltage controlled oscillator (VCO) to double the phase noise. The frequency and phase will be halved by a frequency divider ($f/2$), such that the AOM will be driven by a signal that will compensate the phase noise of a single pass through the optical fiber. With the PLL engaged the light exciting the fiber will maintain its narrow linewidth.

Note that the phase noise compensation will be active all the time by sending back the $0^{\text{th}}$ order through the fiber, but less light will be sent back through the fiber when part of the light will be pulsed into the $1^{\text{st}}$ diffraction order towards the atoms. Therefore it is recommended to test the phase noise cancellation scheme with light diffracted into the $1^{\text{st}}$ order, such that the scheme will be characterised well while sending interferometer pulses towards the atoms.

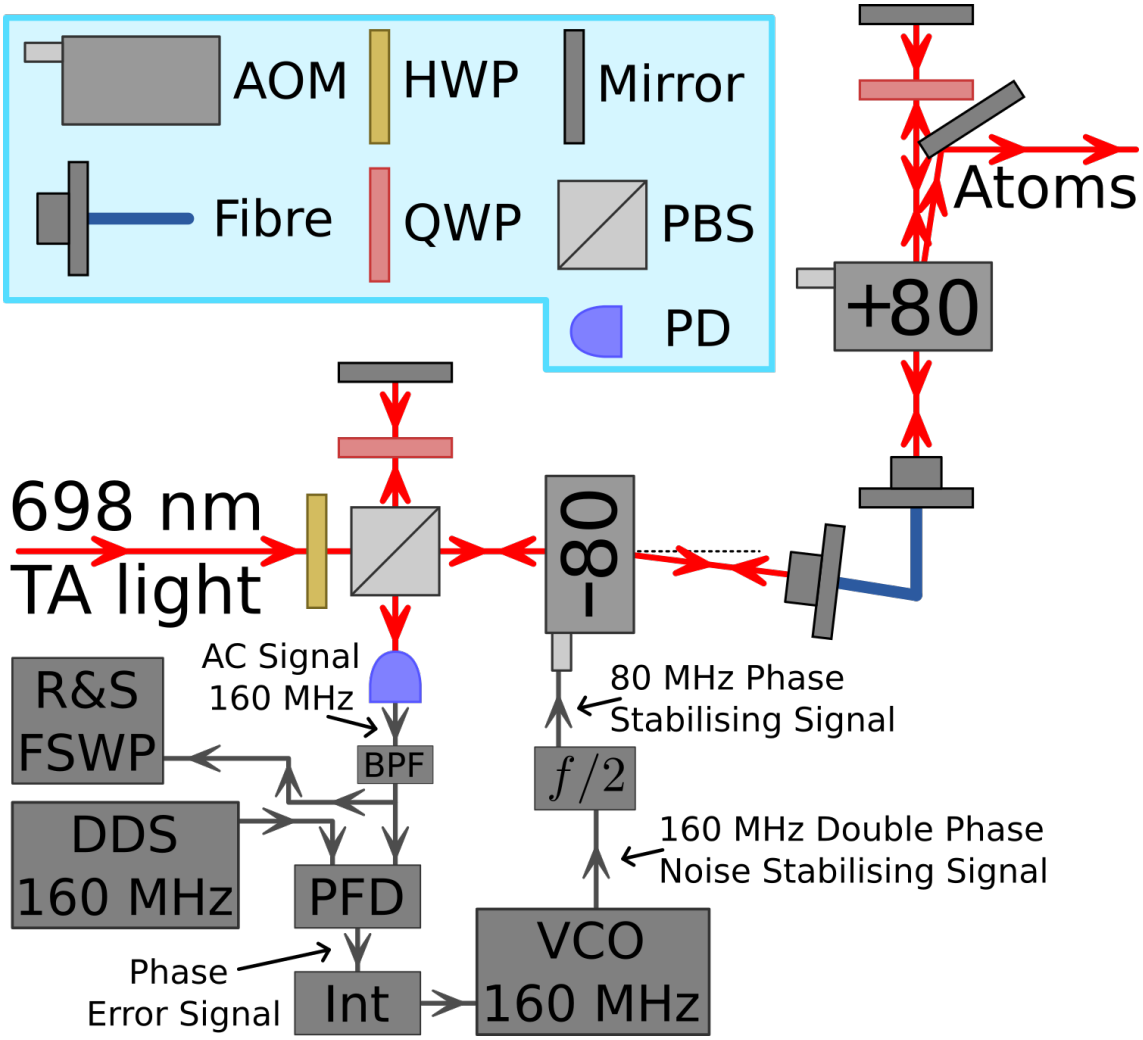


Figure 2.15: Schematic representation of the fiber noise cancellation setup for the clock laser. The abbreviated symbols indicate an acousto-optic modulator (AOM), half waveplate (HWP), quarter waveplate (QWP), polarising beamsplitter cube (PBS) and a photodiode (PD). The first AOM (-80 MHz) is used to compensate the phase noise that gets introduced by transport through the optical fiber. The second AOM (+80 MHz) is used to generate the interferometer pulses, the $1^{st}$ diffraction order goes to the atoms inside the vacuum chamber. The $0^{th}$ order is sent back through the optical fiber accumulating the phase noise from the fiber for a second time. The light from the two arms of the PBS interferes, which creates a beat note at 160 MHz that is measured by the photodiode. The AC signal is filtered by a bandpass filter (BPF), the phase noise of the signal can be observed by a Rohde&Schwartz phase noise analyser (R&S FSWP). The phase frequency detector (PFD) generates a phase error signal by comparing the frequency and phase of the 160 MHz beat note and the 160 MHz reference signal from the DDS source. The phase error signal is integrated by an integrator circuit (Int), which is then used to porivide feedback to the voltage controlled oscillator (VCO) at 160 MHz. The VCO generates a 160 MHz signal that compensates double the phase noise, because the light used in the feedback system passed the optical fiber twice, therefore accumulating double the phase noise. The frequency and phase are halved by a frequency divider ($f/2$), such that the AOM is driven by a signal at 80 MHz, which compensates the phase noise of a single pass through the optical fiber. The light that is used for feedback not only passes the optical fiber twice, but it also passes the phase noise compensating AOM twice. Thus the phase noise of the beat note reduces with the phase-locked loop (PLL) engaged, this indicates successful compensation of the fiber phase noise.

## 2.5 Magneto-Optical Trap of Strontium Atoms

The magneto-optical trap (MOT) cools and traps atoms due to radiation pressure in combination with a quadrupole magnetic field [144]. The MOT is formed by three perpendicular counter-propagating beam pairs that intersect at the center of the quadrupole field, which ideally is located near the focus of the cavity (Fig. 2.6). A restoring force towards the center of the trap is created due to the applied magnetic field in combination with using the correct circular polarisation of the light beams. Two magnetic coils of radius $R = 12$ cm and $N = 80$ windings are placed alongside the science chamber (Fig. 2.4) a distance $2a = 12$ cm apart in the anti-Helmholtz configuration. The coils generate a quadrupole field, which near the origin is given by

$$\begin{aligned} \vec{B}(x,y,z) &= \frac{d\vec{B}_x}{dx}x + \frac{d\vec{B}_y}{dy}y + \frac{d\vec{B}_z}{dz}z \\ &= \frac{3\mu_0 N I_{coils} a R^2}{\left(R^2+a^2\right)^{5/2}}\left(-\frac{x}{2}, y, -\frac{z}{2}\right), \end{aligned} \tag{2.18}$$

with $\mu_0$ the vacuum permeability and $I_{coils}$ the current running through the magnetic coils, which are connected in series. The coils are positioned such that the center of the quadrupole field is in close vicinity to the focus of the optical ring cavity. Compensation coils are wrapped around the science chamber in all three dimensions in order to adjust the center of the field, such that it coincides with the focus of the cavity and the intersection of the three counter-propagating beam pairs of the MOT.

There are two stages in the MOT, the first stage uses blue light at $\lambda = 461$ nm to cool and trap atoms in combination with green light at $\lambda = 497$ nm to repump lost atoms, the second stage uses red light at $\lambda = 689$ nm for cooling and trapping. The first MOT stage operating on the blue ${}^1S_0 \leftrightarrow {}^1P_1$ transition provides strong trapping and cooling due to the large linewidth. Using two MOT stages enables cooling down to microkelvin temperatures [105], because the linewidth of the ${}^1S_0 \leftrightarrow {}^3P_1$ transition is narrower compared to the ${}^1S_0 \leftrightarrow {}^1P_1$ transition, therefore a lower Doppler cooling limit can be reached.

### 2.5.1 Blue MOT

The Doppler cooling limit [69] of the blue MOT is $T_D = \hbar\gamma_s/(2k_B) = 725$ $\mu$K, which is higher than the recoil temperature $T_{recoil} = \hbar^2k^2/(mk_B) = 1.04$ $\mu$K. The maximal deceleration $a_{max}$ is five orders of magnitude larger than the acceleration due to gravity, therefore the atoms will not fall/sag out of the MOT. The ${}^1S_0 \leftrightarrow {}^1P_1$ transition is not a closed transition, atoms are lost to the metastable ${}^3P_2$ state roughly once every 150 000 photon scattering events. The atoms are recovered by superimposing a repumping laser at 497 nm onto the MOT beams, which recovers the atoms using the ${}^3D_2$ level.

The MOT coils in anti-Helmholtz configuration generate a magnetic field gradient of 45 G/cm by running a current of $I_{coils} = 75$ A through the coils [Eq. (2.18)], which are water cooled in order to dissipate heat. The crossed MOT beams operate with a power of $P_{crossed} = 6$ mW per beam and the axial MOT beam operates with a power of $P_{axial} = 4$ mW [126], which leads to a total power of $P_{center} = 32$ mW at the center of the MOT where the three counter-propagating beam pairs intersect. The MOT beams have a waist of $w_0 = 5$ mm, therefore the atoms experience an intensity of $I = 2P/(\pi w_0^2) = 81.5$ mW/cm$^2$ at the center of the MOT, thus reaching a saturation parameter of $s = I/I_{sat} = 2$. The capture velocity of the MOT $v_{capture} \approx 56$ m/s [69] for a beam waist of $w_0 = 5$ mm. Thus the MOT is efficiently loaded, because the atoms exit the Zeeman slower with a final velocity $v_{final} \approx 50$ m/s. Roughly 2 mW of $\lambda = 497$ nm light is used for the superimposed repumping beams in order to recover atoms lost to the ${}^3P_2$ level. Experimentally it was observed that the MOT performs at its best when it is operated with a detuning of $\delta = -2\pi \cdot 30$ MHz. Under the mentioned conditions the setup generates a ${}^{88}$Sr MOT of $1.4 \cdot 10^7$ atoms with a loading time of $\tau = 106.6$ ms and a temperature of $T = 9.7 \pm 1.3$ mK [126], which is about a factor 10 higher than the theoretical Doppler limit. Lower temperatures can be achieved if the blue laser power is reduced [92].

### MOT Operation with Nuclear Spin $I \neq 0$ and $J_{ground} = 0$ in $^{87}$Sr

Operating a MOT for $^{87}$Sr differs from many other elements that have a hyperfine structure, because the ground state $^1S_0$ only has a nuclear magnetic moment $\vec{\mu}_{nuc}$. The magnetic sublevels of the ground state are therefore subjected to a smaller Zeeman shift, because $\vec{\mu}_{nuc}$ is a lot weaker than the electronic contributions by about a factor $\mu_B/\mu_N \approx 1836$, with $\mu_B$ the Bohr magneton and $\mu_N$ the nuclear magneton. This means that $g_F \ll g_{F'}$, which leads to a restoring force for only a part of the magnetic sublevels (Fig. 2.16). The other magnetic sublevels are off-resonance or experience a repulsive force from the center.

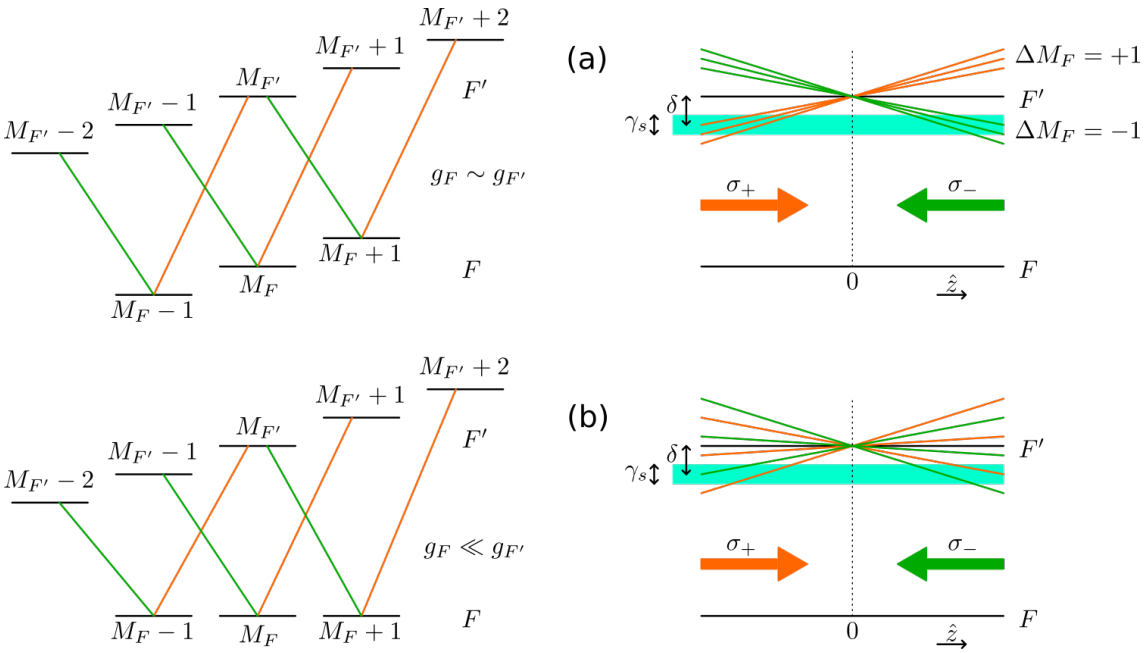


Figure 2.16: The energy levels in these examples are assumed to have positive g-factors and they experience a positive field gradient. (a) Example of the MOT mechanism for hyperfine structure with g-factors of similar magnitude ($g_F \sim g_{F'}$) for the ground state hyperfine level $F$ and excited state hyperfine level $F'$, which is the case for the alkali atoms. The MOT produces a restoring force for all magnetic sublevels by operating with a negative detuning $\delta$. (b) Example of the MOT mechanism for hyperfine structure where $g_F \ll g_{F'}$, like in $^{87}$Sr. The MOT operates at a negative detuning $\delta$ on a transition with a power broadened linewidth $\gamma_s$, which provides a restoring force for only a part of the magnetic sublevels. The other magnetic sublevels are off-resonance or experience a repulsive force from the center. Figure adapted from [145].

The position-dependent resonance condition alone is not enough to achieve a restoring force to the center, the $^{87}$Sr MOT mechanism also relies on the relative transition probabilities between the magnetic sublevels, which has been used to trap atoms (with $J_{ground} \neq 0$) relying on optical pumping only [146]. For $\sigma_\pm$ polarised light the $M_F \rightarrow M_{F'} = M_F \pm 1$ transition probability is the largest for the magnetic sublevel $M_F = \pm F$ and it decreases monotonically when moving towards the opposite sublevel $M_F = \mp F$ [106]. Stable trapping can be achieved when the strontium atom at $z < 0$ is in magnetic sublevel $M_F = 9/2$. For $z > 0$ the strontium atom has to be in magnetic sublevel $M_F = -9/2$ to generate a net restoring force towards the center (Fig. 2.17). If the atom is not in the correct sublevel to satisfy the trapping condition, then it will be optically pumped to this sublevel after a few cycles of absorption and stimulated emission. Hyperfine level $^1P_1$ ($F' = 9/2$) is used to optically pump the magnetic sublevels due to the broad linewidth of the blue transition and the close proximity of $^1P_1$ ($F' = 9/2$) to the cooling and trapping level $^1P_1$ ($F' = 11/2$) (Fig. 2.18). The recoil frequency of the optical pumping process $\omega_{recoil} = kv_{recoil} = 2\pi \cdot 21.6$ kHz is a lot smaller than the transition linewidth $\gamma = 2\pi \cdot 30.2$ MHz, thus the resonance conditions are still satisfied after a few pumping cycles. It is also important that the optical pumping does not provide any

additional heating. The optical pumping process consists of absorption and stimulated emission, because both beams are on resonance with all magnetic sublevels at all positions due to the smaller g-factor of $g_{F'} = 4/99$ for ${}^1P_1\,(F' = 9/2)$ with respect to $g_{F'} = 2/11$ for ${}^1P_1\,(F' = 11/2)$. Due to the transition probabilities it is more likely to have stimulated emission along the same beam as the absorption process, which means there is no net change in momentum, thus there is no additional heating.

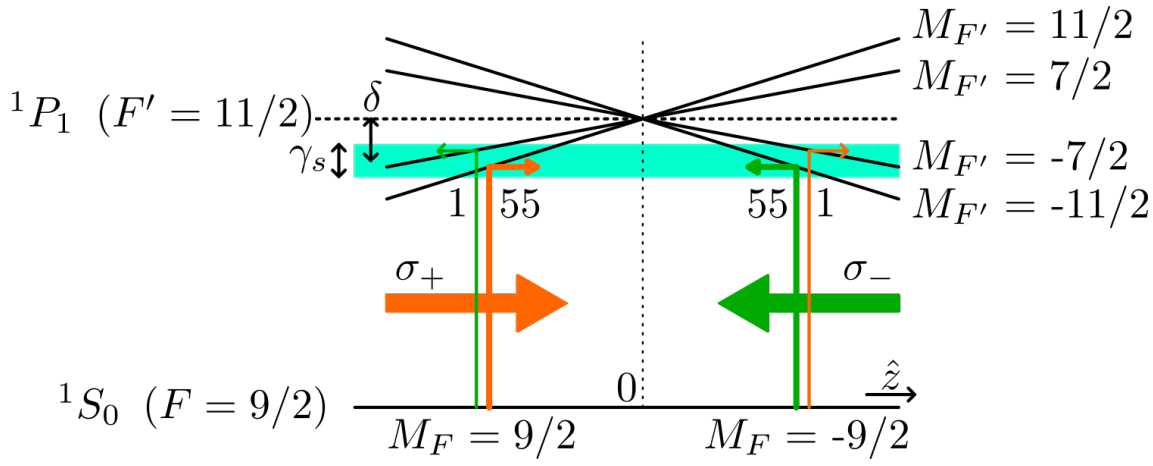


Figure 2.17: The MOT generates a restoring force for a ${}^{87}$Sr atom assuming a positive field gradient when the atom is in magnetic sublevel $M_F = 9/2$ at $z < 0$ and when the atom is in magnetic sublevel $M_F = -9/2$ at $z > 0$. The transitions that result in a restoring force towards the trap center are stronger by a factor 55 : 1 compared to the transitions that would expel the atoms from the center, which is due to the transition probabilities. Figure adapted from [106].

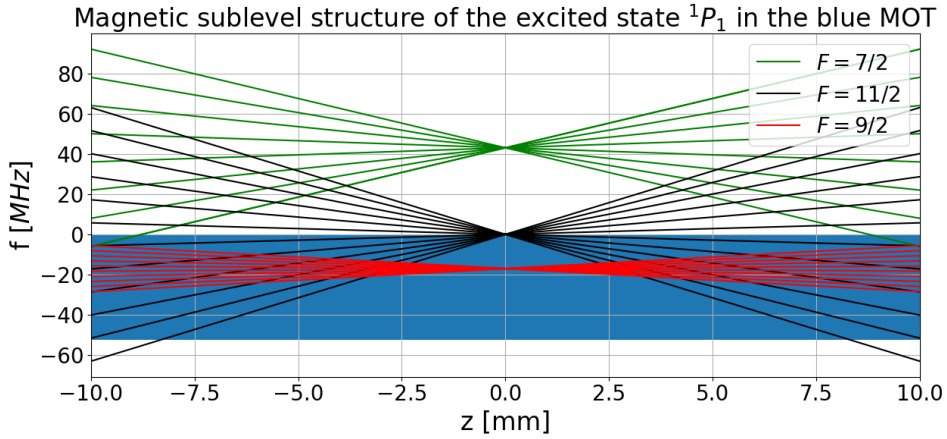


Figure 2.18: Magnetic sublevel structure of the hyperfine levels $F' = 7/2$ (green), $F' = 11/2$ (black) and $F' = 9/2$ (red) inside the blue MOT for the excited state ${}^1P_1$ for a magnetic field gradient of 45 G/cm. In this figure the blue MOT operates at a detuning of $\delta = -\gamma_s/2$ with a power broadened linewidth of $\gamma_s = \sqrt{3}\gamma$ (blue rectangle). The magnetic sublevels are optically pumped through the $F' = 9/2$ hyperfine level due to the broad linewidth of the blue transition and the close proximity of $F' = 9/2$ to $F' = 11/2$. The atoms are trapped and cooled via the ${}^1S_0\,(F = 9/2,\ M_F = \pm 9/2) \leftrightarrow {}^1P_1\,(F' = 11/2,\ M_{F'} = \pm 11/2)$ transitions that generate a net restoring force towards the trap center.

#### Repumping the Magnetic Sublevels of $^{87}$Sr

Some modifications to the repumping scheme are needed for $^{87}$Sr, because atoms are lost to all five hyperfine levels of the metastable $^3P_2$ state. However, roughly 80% of the atoms are lost to the hyperfine levels $F = 13/2$ and $F = 11/2$ of $^3P_2$, therefore it is sufficient to perform repumping only on the $^3P_2\,(F = 11/2) \leftrightarrow {}^3D_2\,(F' = 13/2)$ and $^3P_2\,(F = 13/2) \leftrightarrow {}^3D_2\,(F' = 13/2)$ transitions [101], which lie 1349.6 MHz apart (Tab. A.2). An electro-optic modulator (EOM) is used to generate two sidebands that are resonant with the $^3P_2\,(F = 11/2) \leftrightarrow {}^3D_2\,(F' = 13/2)$ and $^3P_2\,(F = 13/2) \leftrightarrow {}^3D_2\,(F' = 13/2)$ transitions, which repumps all magnetic sublevels due to the large linewidth of the transition. The EOM allows for rapid switching between $^{87}$Sr and $^{88}$Sr cooling.

### 2.5.2 Blue Laser System at 461 nm

The blue laser system [126] produces 461 nm light in order to provide cooling, trapping and imaging on the $^1S_0 \leftrightarrow {}^1P_1$ transition (Fig. 2.19). The ECDL master laser is frequency stabilised 146 MHz below resonance by a wavemeter (HighFinesse WS-U), which provides feedback on the piezoelectric transducer of the ECDL grating. The stabilised master injects the slave laser, a Fabry-Pérot cavity is used to check the injection of the slave laser. The light for the magneto-optical trap (MOT) is tuned 31 MHz below atomic resonance. The light for the Zeeman slower (ZS) is tuned 481 MHz below atomic resonance. The light for absorption imaging (Img) is on resonance with the $^1S_0 \leftrightarrow {}^1P_1$ transition.

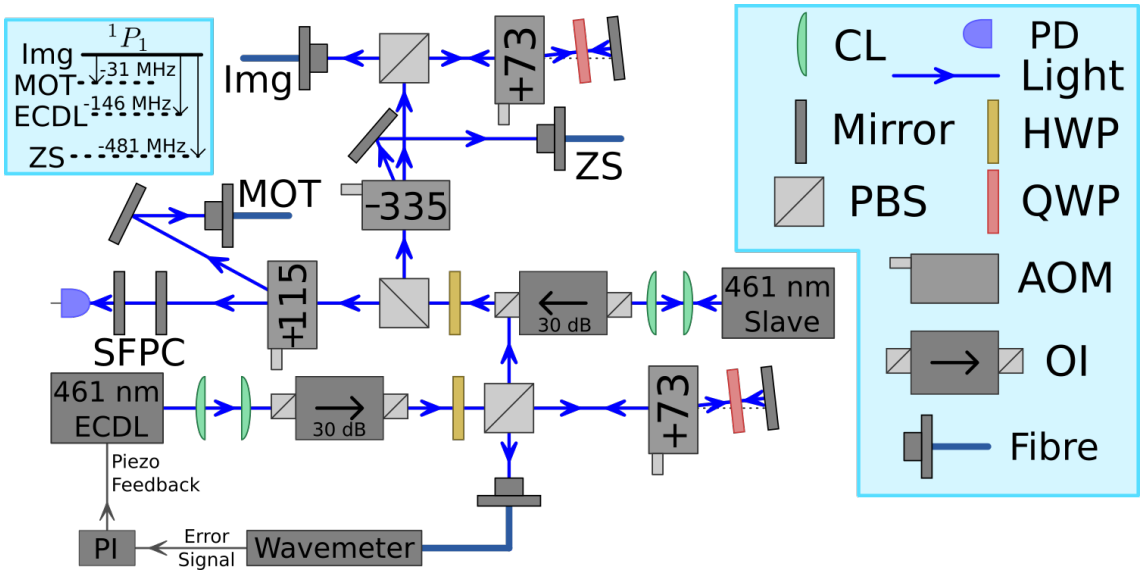


Figure 2.19: Schematic representation of the blue laser system in master-slave configuration. The abbreviated symbols indicate a cylindrical lens (CL), photodiode (PD), polarising beamsplitter cube (PBS), half waveplate (HWP), quarter waveplate (QWP), acousto-optic modulator (AOM) and an optical isolator (OI). The master laser is frequency stabilised 146 MHz below atomic resonance by a wavemeter (HighFinesse WS-U), which provides an error signal that is fed back to a PI-controller that acts on the piezoelectric transducer of the ECDL grating. The master injects the slave via the output port of an optical isolator. The transmission of the scanning Fabry-Pérot cavity (SFPC) is observed with a photodiode to check if the slave laser is injected. The light for the magneto-optical trap (MOT), Zeeman slower (ZS) and absorption imaging (Img) is transported to the vacuum chamber through optical fibres. The energy level diagram inset shows the detuning from the $^1S_0 \leftrightarrow {}^1P_1$ transition.

#### Blue Laser System Improvements

The imaging setup can be improved by stabilising the intensity of the light used in absorption spectroscopy, because two consecutive images are taken (the atoms are imaged, then a reference image is taken without atoms) and the intensities are compared. Fluctuations in intensity between these two images lead to an uncertainty in atom number. The intensity of the light can be stabilised by modulating the amplitude of the radio frequency signal that drives the imaging AOM [147]. Currently the absorption imaging is pulsed, therefore a slight modification to the setup is necessary, because the intensity feedback needs to be on all the time. Two single pass AOMs at 73 MHz will be used instead of one double pass AOM at 73 MHz to get the imaging beam on resonance. The first AOM will provide the intensity stabilisation, the second AOM will be used to pulse the light to take the images. If the second AOM is placed after the optical fiber then it is possible to compensate for polarisation noise as an added bonus (compared to having the second AOM before the optical fiber). The proposed setup is similar to figure 2.41. A polarising beamsplitter cube will be placed after the fiber, a small part of the beam will be picked off by placing a piece of glass after the cube. The second AOM (for the pulses) will be placed such that it acts on the light transmitted through the piece of glass. The light reflected from the piece of glass is observed with a photodiode, which generates a signal for the amplitude modulation of the AOM before the fiber. A PID-controller will be used to provide an intensity set point and to lock the feedback loop.

The cooling system can be improved by implementing transverse cooling on the atomic beam inside the cube between the oven and the Zeeman slower (Fig. 2.4), which will narrow the atomic cone that exits the oven. This leads to a higher atomic flux entering the Zeeman slower and thus an effective increase in the atomic flux loading the MOT. This will lead to a higher MOT loading rate and a larger final atom number in the blue MOT. Transverse cooling is currently not implemented due to a lack in laser power. The blue laser system is currently being expended with a second slave laser in order to increase the optical power output. In the current setup the master laser injects the slave with $\sim 10$ mW of optical power, this can be split into two beams of $\sim 5$ mW to inject both slaves with the same master. The optical power of the slaves needs to be divided among the Zeeman slower beam, MOT beams, transverse cooling and absorption imaging. One slave will be dedicated to the Zeeman slower beam, because the increase in optical power also opens up the use of higher oven temperatures, which also increases the atomic flux. When operating at higher oven temperatures a longer stopping distance is necessary, but the full length of the installed Zeeman slower is currently not utilised. It is convenient to use the light coming from the $0^{\text{th}}$ order of the Zeeman slower AOM for imaging as in the current setup, because otherwise it goes to waste. The $0^{\text{th}}$ order will also be used to check the injection of the slave laser with a scanning Faby-Pérot cavity. The other slave laser will be dedicated to the MOT beams and to the transverse cooling. A scanning Fabry-Pérot cavity will be placed on one of the unused beam paths to check the injection of the second slave laser.

### 2.5.3 Repumping Laser System at 497 nm

The repumping laser system produces 497 nm light in order to repump atoms that get lost to the metastable $^3P_2$ level during the blue MOT stage (Fig. 2.20). The repumping is performed on the $^3P_2 \leftrightarrow {}^3D_2$ transition. The ECDL master laser (EYP-RWE-1060) is frequency stabilised at double the atomic resonance frequency ($\lambda = 994$ nm) by a wavemeter (HighFinesse WS-U), which provides feedback on the piezoelectric transducer of the ECDL grating. The infrared light gets amplified by a tapered amplifier (TA) and then it is frequency doubled by a fiber coupled waveguide frequency doubler (NTT Electronics) through second harmonic generation (SHG). The electro-optic modulator (EOM) allows for rapid switching between $^{87}$Sr and $^{88}$Sr cooling. Sidebands are generated at $\pm 674.8$ MHz for $^{87}$Sr, such that the sidebands are on resonance with the two most important repump transitions [101].

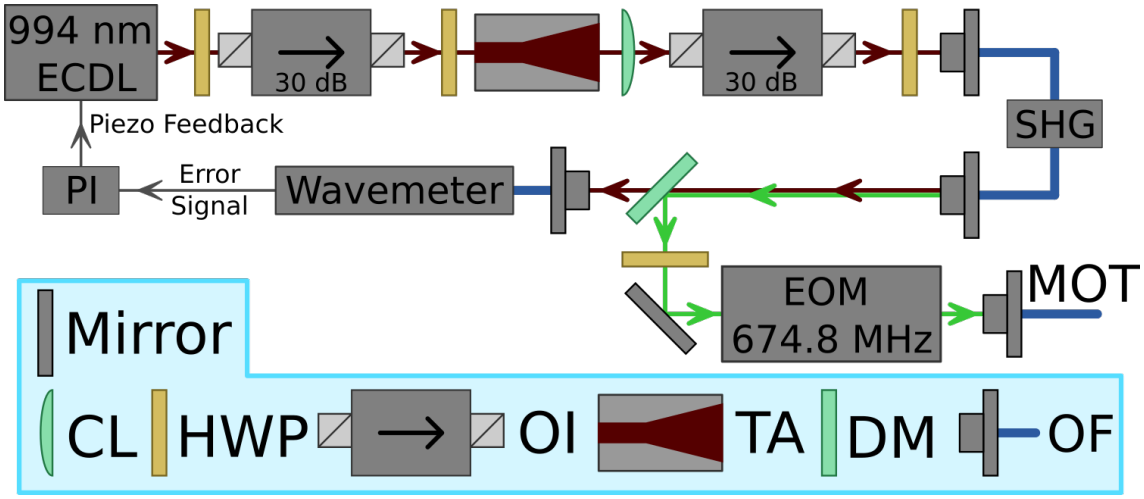


Figure 2.20: Schematic representation of the repumping laser system, with the master frequency doubled from 994 nm to 497 nm. The abbreviated symbols indicate a cylindrical lens (CL), half waveplate (HWP), optical isolator (OI), tapered amplifier (TA), dichroic mirror (DM) and an optical fibre (OF). The master laser is frequency stabilised at double the atomic resonance frequency by a wavemeter (HighFinesse WS-U), which provides an error signal that is fed back to a PI-controller that acts on the piezoelectric transducer of the ECDL grating. The master is amplified by a tapered amplifier and then frequency doubled by a fiber coupled waveguide through second harmonic generation (SHG). The frequency doubled light is picked off using a dichroic mirror (DM). The electro-optic modulator (EOM) generates sidebands in order to repump the two most important hyperfine levels of $^{87}$Sr. With the EOM switched off the system repumps $^{88}$Sr atoms. The light for the magneto-optical trap (MOT) is transported to the vacuum chamber through an optical fibre.

#### Repumping Laser System Improvements

The frequency doubled master provides only a couple milliwatt of light at 497 nm, so in order to improve the power a new diode (RWLD-495-80m-1) has been ordered which has a maximal output power of 80 mW. An upgrade to reduce the complexity of the system would be to have a master ECDL at 497 nm, which is frequency stabilised by the wavemeter. However, initial tests show that getting the laser diode to emit at a single frequency at 497 nm requires heating this particular diode model to 53 °C, which is considered not ideal. When the 495 nm diode is used inside a slave laser it requires less heating, roughly 30 °C is enough for the slave to become injected and follow the frequency doubled master. The master-slave configuration is currently still under construction, but will be able to provide tens of milliwatts, which is more than enough.

### 2.5.4 Red MOT

The second MOT stage operates on the red $^1S_0 \leftrightarrow {}^3P_1$ transition, because lower temperatures can be reached due to the narrow linewidth. The Doppler cooling limit [69] of the red MOT is $T_D = \hbar\gamma_s/(2k_B) = 180$ nK, which is smaller than the recoil temperature $T_{recoil} = \hbar^2k^2/(mk_B) =$ 464 nK. The narrow linewidth also means that the maximum deceleration $a_{max}$ is lower compared to the blue MOT, $a_{max}$ is of the same order of magnitude as the gravitational acceleration for the red MOT. The low $a_{max}$ for the red MOT leads to a low capture velocity, hence the need for a special loading procedure to efficiently transfer atoms from the blue MOT into the red MOT [105]. The magnetic field gradient drops substantially from 45 G/cm to 3 G/cm when switching from the blue MOT to the red MOT. The frequency of the red MOT beams is broadened in order to cover the Doppler shift of the atoms in the blue MOT, meanwhile the magnetic field gradient is changed adiabatically to compress the cloud size (typically from 3 G/cm to 10 G/cm), this is known as the broadband red MOT. The frequency modulation of the red MOT beams is turned off after the atoms are transferred successfully from the blue MOT to the broadband red MOT, such that the

red MOT operates at a single frequency. The detuning and intensities are ramped down in order to reach close to the Doppler cooling limit in the single frequency red MOT. A $^{88}$Sr red MOT of about $5 \cdot 10^6$ atoms and a temperature of about $T \approx 1$ $\mu$K has been generated in the experimental setup, when using the broadband MOT method to capture the atoms from the blue MOT.

### Stirring the Magnetic Sublevels of $^{87}$Sr

Operating the red MOT successfully for $^{87}$Sr has even more requirements than those discussed for the blue MOT in subsection 2.5.1, because the linewidth is narrower and the hyperfine levels of $^3P_1$ are spaced further apart. The hyperfine level $^3P_1$ ($F' = 11/2$) is used to cool and trap the atoms, which relies on the relative transition probabilities between the magnetic sublevels like in the blue MOT (Fig. 2.17). The net restoring force towards the trap center is generated by the $^1S_0$ ($F = 9/2,\ M_F = \pm 9/2$) $\leftrightarrow$ $^3P_1$ ($F' = 11/2,\ M_{F'} = \pm 11/2$) transitions for atoms in $M_F = 9/2$ at $z < 0$ and $M_F = -9/2$ at $z > 0$. A stirring laser stirs the magnetic sublevels of the atoms via the hyperfine level $^3P_1$ ($F' = 9/2$), such that the atoms end up in the correct magnetic sublevel to satisfy the trapping conditions [106]. A dedicated laser is necessary because the transition linewidth $\gamma = 2\pi \cdot 7.5$ kHz and the frequency difference between $^3P_1$ ($F' = 9/2$) and $^3P_1$ ($F' = 11/2$) is 1463.2 MHz, thus the stirring of the sublevels does not come for free like in the blue MOT. The g-factor of $^3P_1$ ($F' = 11/2$) is $g_{F'} = 3/11$ and the g-factor of $^3P_1$ ($F' = 9/2$) is $g_{F'} = 2/33$, which is a factor 4.5 weaker, this means that the atoms have a larger position-dependent resonance area to get stirred when experiencing the magnetic field gradient of the red MOT. It is critical that the stirring laser does not provide any excess heating, because the recoil frequency $\omega_{recoil} = k v_{recoil} = 2\pi \cdot 9.66$ kHz is larger than the transition linewidth, otherwise the atom would be pushed out of the position-dependent resonance. The stirring laser has to stay on resonance with all magnetic sublevels inside the red MOT area, such that it can provide the stirring through absorption and stimulated emission.

### Sawtooth-Wave Adiabatic Passage Cooling Scheme

Recently a new cooling scheme has been proposed based on scanning the laser frequency adiabatically with a sawtooth-wave pattern [148]. This new scheme has been demonstrated to cool strontium on the narrow $^1S_0 \leftrightarrow {}^3P_1$ transition close to the recoil limit [149]. The sawtooth-wave adiabatic passage (SWAP) cooling scheme has also been used to create a MOT that provides a larger capture velocity and a higher transfer efficiency from the blue to the red MOT compared to the traditional broadband MOT [150, 151]. Combining the SWAP method with the standard narrow-line cooling method provides faster and more robust cooling [152], achieving $6 \cdot 10^7$ bosonic $^{88}$Sr atoms at 2 $\mu$K and $1 \cdot 10^7$ fermionic $^{87}$Sr atoms at 1.4 $\mu$K. The SWAP technique has also been used to generate a steady-state MOT of $8.4 \cdot 10^7$ fermionic $^{87}$Sr atoms at 12 $\mu$K, with a loading rate of $1.3 \cdot 10^7$ atoms/s [153].

The procedure of [152] is followed in order to create the red MOT, because it combines the higher transfer efficiency of the SWAP MOT (compared to the broadband MOT) with the low temperatures achieved by the standard single frequency MOT. The advantage of the SWAP MOT is that a larger frequency range can be covered compared to the broadband MOT, when the sweep duration $\Delta t$ and ramping rate are equal (Fig. 2.21). Therefore a higher transfer efficiency is possible, because in this way the capture velocity is enlarged. The sweep parameters $\Delta_1$, $\Delta_2$ and $\Delta t$ can be optimised to operate with a smaller sweep duration $\Delta t$, such that the atoms have less time off-resonance, thus less time to escape. Turning the MOT beams off during the downward sweep of the sawtooth-shape is the second advantage of the SWAP MOT compared to the broadband MOT, because it prevents stimulated emission caused by the downward sweep. The MOT operates with counterpropagating polarised beams ($\sigma_+$ and $\sigma_-$), therefore the stimulated emission event would originate from the same beam as the absorption event, which eliminates the heat extraction. The SWAP MOT can therefore operate with a smaller sweep duration $\Delta t$ compared to the broadband MOT, which is required to have a 'long' sweep duration $\Delta t$, such that the atom has enough time to spontaneously emit the photon in order to cool down.

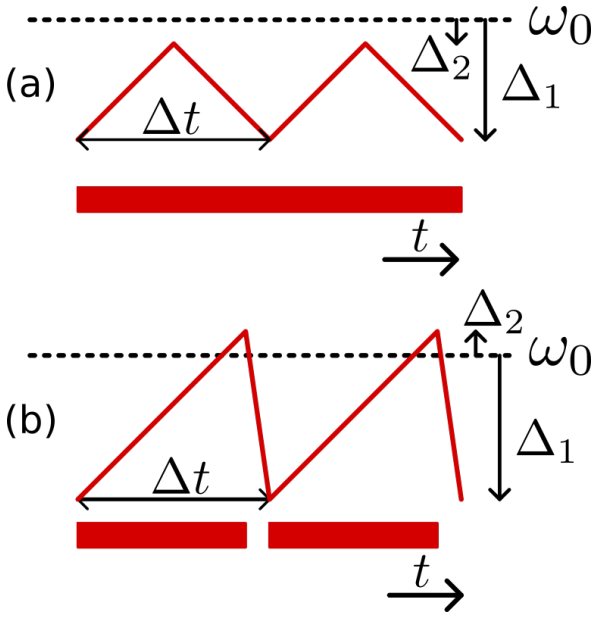


Figure 2.21: Frequency modulation of the red MOT beams with laser start detuning $\Delta_1$, stop detuning $\Delta_2$ and sweep duration $\Delta t$. (a) For the broadband MOT the frequency is swept below atomic resonance $\omega_0$ with a triangular wave and the MOT beams are always on (solid red bar). (b) For the SWAP MOT the frequency is swept across atomic resonance $\omega_0$ with a sawtooth-wave. The MOT beams are on during the upward sweep and they are turned off during the downward sweep of the sawtooth-shape (dashed red bar). Figure adapted from [153].

Using the SWAP technique on all three axes (SWAP-3) initially captures and cools the atoms efficiently, but after a time $t_{switch}$ the axes operate individually (SWAP-1), because of the faster cooling speed at low temperatures. When operating on all three axes simultaneously it is possible to have an unwanted stimulated emission process between different axes, which is avoided by operating the axes individually, such that heat is extracted due to spontaneous emission. The MOT beams are switched on and off by controlling the radio frequency to the MOT beam AOMs with an Arduino microcontroller (Sec. 2.5.4). Then at time $t_{ramp} > t_{switch}$ the MOT is operated traditionally at a single frequency with a negative detuning $\delta$, which is ramped down linearly (Fig. 2.22). The power in the MOT beams is ramped down polynomially in order to reach a lower steady state temperature.

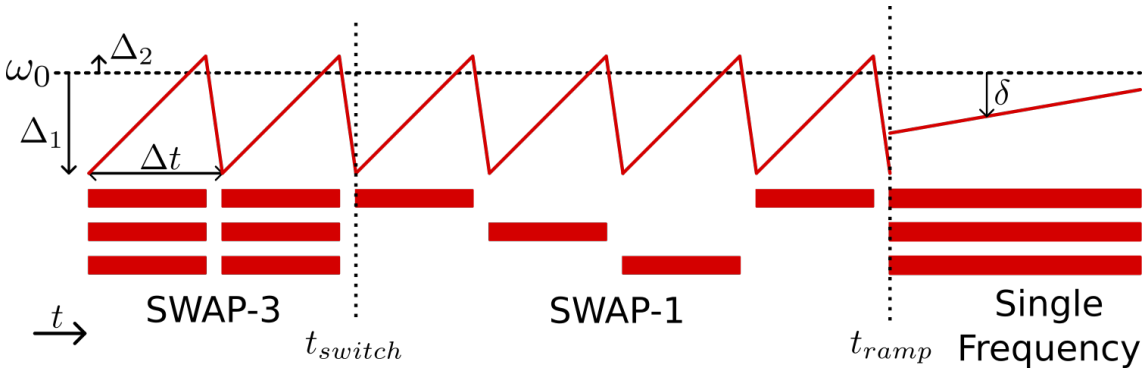


Figure 2.22: The red MOT sequence starts with the SWAP-3 MOT to efficiently capture the atoms. At time $t_{switch}$ the MOT beams (red bars) are operated individually to increase the cooling speed at low temperatures using the SWAP-1 MOT. At time $t_{ramp}$ the single frequency MOT is started, where the negative detuning $\delta$ is ramped down linearly. Figure adapted from [152].

The SWAP technique is ideal when working with $^{87}$Sr, because more of the magnetic sublevels are passed, still the stirring laser is used to stir the magnetic sublevels that are not crossed to provide stable trapping. Note that the $^{87}$Sr and $^{88}$Sr isotopes require different parameters and timings for the SWAP-3, SWAP-1 and single frequency MOT sequences [152].

### Sawtooth-Wave Adiabatic Passage Controller

The red magneto optical trap (MOT) sawtooth-wave adiabatic passage (SWAP) cooling scheme requires the ability to switch the MOT beams on and off individually at high speeds. The fast and individual switching is realised by using three fast radio frequency (RF) switches (Mini-Circuits ZASWA-2-50DRA+), which have a typical switching time of 20 ns, in order to turn the MOT beams on and off individually (Fig. 2.23). The SWAP controller powers the RF switches with ±5 V and provides triggers to determine the state of the RF switch. The RF switches have one input port and two output ports, the input signal is transmitted through one of the two output ports, which is controlled by the switch state. The SWAP controller synchronises the switching with the sawtooth-wave pattern, such that the MOT beams are on and off at the appropriate time for the SWAP-3 and SWAP-1 sequence (Fig. 2.22).

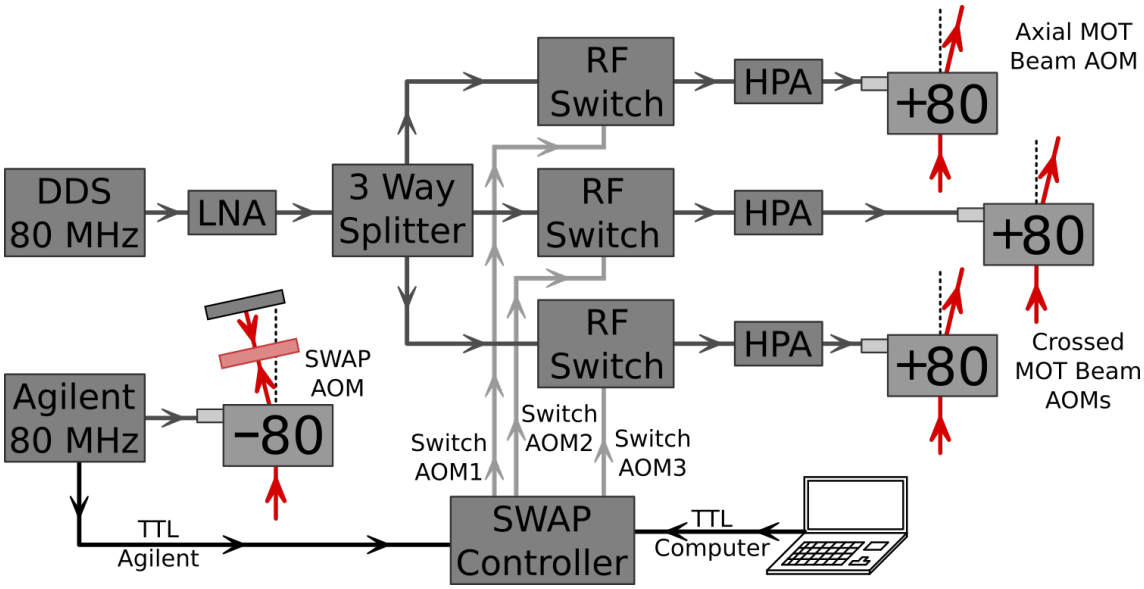


Figure 2.23: The DDS generates an 80 MHz radio frequency (RF) signal, which gets amplified by a low noise amplifier (LNA). The RF signal is split into three, each path is connected to the input port of an RF switch. Each RF switch has two output ports, one is terminated with a 50 Ω RF terminator (off path), the other port is connected (on path) to a high power amplifier (HPA). If the RF switch is 'closed' (on path), then the HPA amplifies the RF signal, which drives the acousto-optic modulator (AOM) to create the magneto-optical trap (MOT) beam. The SWAP controller receives triggers from the computer (TTL Computer) and the Agilent source (TTL Agilent), in order to start the SWAP sequence and to synchronise to the sawtooth-wave pattern respectively. The SWAP AOM generates the sawtooth-wave modulated light that injects the MOT slave, see figure 2.26 for the complete optical layout.

The printed circuit board (PCB) of the SWAP controller (Sec. B.2) is designed to act as a shield for the Arduino DUE microcontroller and to generate the ±5 V in order to power the RF switches. The Arduino microcontroller is programmed to handle the timing of the switches. During the SWAP-3 sequence the light is on for 40 $\mu$s and off for 5 $\mu$s. During the SWAP-1 sequence only a single MOT beam illuminates the atoms at a time for 40 $\mu$s. All three RF switches are 'closed' constantly during the single frequency red MOT.

## 2.6 Loading the Optical Lattice

The optical lattice is a tool to trap neutral atoms for prolonged periods of time based on the optical dipole force exerted by the trapping light, it is used extensively in optical lattice clocks [13, 6] and quantum simulation platforms [154]. The optical lattice is generated at $\lambda = 813$ nm, which is the magic wavelength [109, 110, 111] for the strontium optical clock transition ${}^1S_0 \leftrightarrow {}^3P_0$. The magic wavelength lattice exerts equal light shifts on the optical clock states, these states are used during the entanglement generation sequence (Ch. 3).

The purpose of the lattice in this work is collecting cold atoms from the red MOT and bringing them to the focal point of the optical ring cavity for maximum cavity-enhanced atom-light interaction. The lattice is coupled to the optical ring cavity using the Pound-Drever-Hall (PDH) technique [127, 128, 129], such that the optical lattice is created inside the plane of the optical ring cavity. The optical lattice potential formed by two counter-propagating beams is given by [69]

$$U_{lattice} \approx \frac{\hbar\Omega^2}{4\delta} 4\cos^2(kz) = \frac{\hbar\gamma^2}{2\delta}\frac{I}{I_{sat}}\cos^2(kz), \tag{2.19}$$

with $I$ the intensity of a single lattice beam and $\delta = 2\pi c\,(1/\lambda_{lattice} - 1/\lambda_{blue})$. The linewidth $\gamma$ and saturation intensity $I_{sat}$ are related to the ${}^1S_0 \leftrightarrow {}^1P_1$ transition at $\lambda_{blue} = 461$ nm, while the wavevector $k = 2\pi/\lambda_{lattice}$ is related to the wavelength of the lattice light at $\lambda_{lattice} = 813$ nm.

A frequency difference can be applied between the two lattice beams (Sec. 2.6.1) in order to create a movable lattice, such that atoms can be transported towards the focus of the optical ring cavity [155, 156, 157]. Note that a frequency difference needs to be applied that is smaller than the cavity linewidth ($\delta f < \kappa/(2\pi)$), otherwise one of the lattice beams is off-resonance with the optical ring cavity, which leads to losing the optical lattice (only an optical dipole trap would remain). The cavity linewidth $\kappa = 2\pi \cdot 637$ kHz at 813 nm due to the higher transmission coefficients of the mirrors at 813 nm compared to 689 nm [118].

The cavity finesse $\mathcal{F} = 2.2 \cdot 10^3$ at 813 nm, the transmission coefficient of mirror 1 at 813 nm is $T_1 = 1396$ ppm and the transmission coefficient of mirror 4 at 813 nm is $T_4 = 1012$ ppm [118]. The optical ring cavity amplifies the power of the optical lattice beams by a factor 517 and 714 [Eq. (2.3)] for lattice beam 1 and 2 respectively. The intensity of the individual lattice beams is adjusted to be equal by tuning the $\lambda/2$ waveplates, which also compensate differences in coupling efficiency to the cavity $\mathrm{TEM}_{00}$ mode. The strongest atom-light interaction happens at the focus of the cavity with the smaller waist of $w_0 = 30.7$ $\mu$m. The intensity of each lattice beam $I = 48$ kW/cm$^2$ at the small waist, when both the lattice beams couple 5 mW each into the cavity. This creates a lattice potential with a depth of 465 $\mu$K [Eq. (2.19)] at the small focus. The larger focus has a waist of $w_0 = 164$ $\mu$m, which means that the lattice potential has a depth of 16.2 $\mu$K. The lattice is sufficiently deep to load atoms from the red MOT, which are cooled down to microkelvin temperatures.

Fluctuations in the intensity of the lattice beams lead to heating of the atoms trapped inside the lattice [158, 159], therefore a stable PDH lock is of importance. Feedback can be provided on the intensity when necessary by modulating the power of the radio frequency signal driving the acousto-optic modulators.

### 2.6.1 Lattice Laser System at 813 nm

The lattice laser system produces 813 nm light in order to trap the atoms at the magic wavelength [109, 110, 111]. Both lattice beams are frequency modulated by an acousto-optic modulator in double pass configuration (Fig. 2.24). This enables operation of the lattice beams at a frequency difference, such that atoms can be transported in a moving lattice [155, 156, 157].

The diode of the ECDL laser has recently been replaced by a new diode (L820P100) which does not have an anti-reflection coating (the old diode did). Without the anti-reflection coating there is less competition between modes, which makes the laser less prone to mode hops and therefore easier to lock to the optical ring cavity.

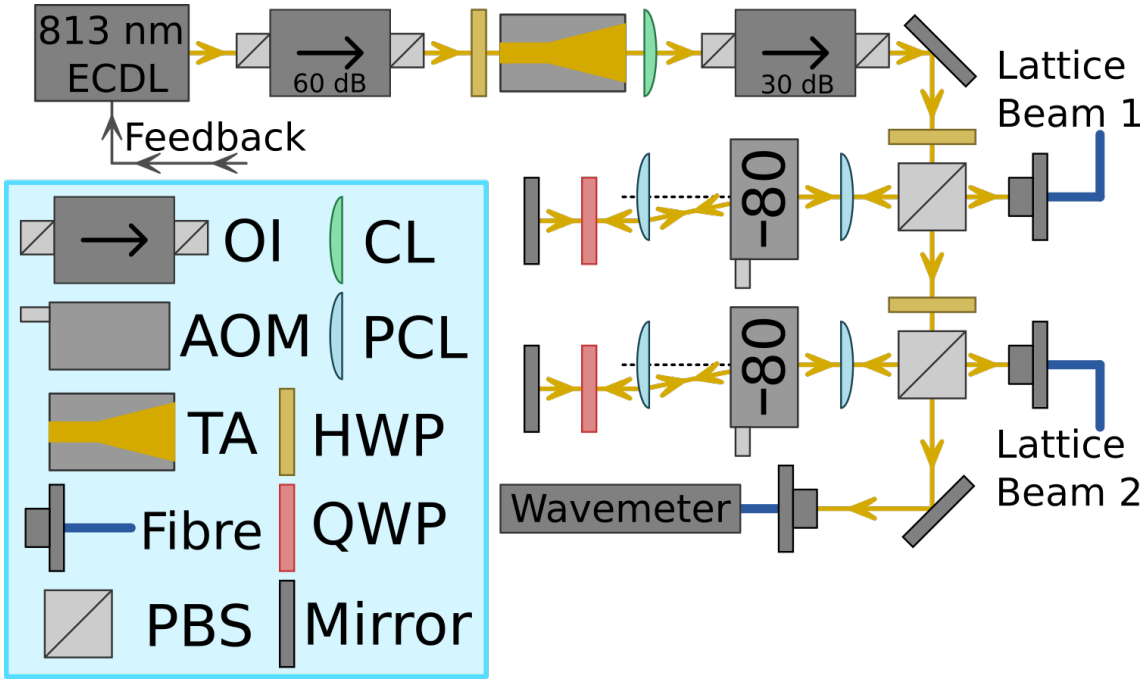


Figure 2.24: Schematic representation of the lattice laser system. The abbreviated symbols indicate an optical isolator (OI), acousto-optic modulator (AOM), tapered amplifier (TA), polarising beamsplitter cube (PBS), cylindrical lens (CL), plano convex lens (PCL), half waveplate (HWP) and a quarter waveplate (QWP). The master is locked to the optical ring cavity (Fig. 2.8) by providing feedback using the Pound-Drever-Hall technique [127, 128, 129]. The light is amplified by a tapered amplifier and split into two lattice beams. Both lattice beams pass twice through an AOM, such that a moving lattice can be created by driving the AOMs of the two lattice beams with a frequency difference.

#### First-Generation Lattice Laser System as an Inspiration for the Long ECDL Lasers

The current lattice laser system is using a 25 cm long ECDL laser, which enables locking to the optical ring cavity due to the narrow laser linewidth. A first-generation system was built before the realisation of the 25 cm long ECDL laser, the optical setup was similar, but the ECDL had only a 2 cm external cavity instead of 25 cm. The linewidth of the 2 cm long ECDL was too broad for locking to the cavity. After many tries it was possible to lock the first-generation system to the optical cavity by applying optical feedback with external optics. A second cavity was formed by picking of a small part of the beam with a piece of glass, the light was back reflected towards the ECDL by a mirror mounted on a piezoelectric transducer, such that the external cavity could be scanned. A polarising beamsplitter cube and a $\lambda/4$ waveplate were used to provide power tunability for the back reflected light. The external cavity created outside the laser box needed to be on resonance with the external cavity inside the laser box (the cavity between the laser diode and grating), such that there was constructive interference of the light inside the two cavities. Having the external cavity created with the optics in open air and roughly 20 cm long made the system very prone to mode hops, therefore the system was very unreliable when trying to create a lock to the optical ring cavity. However, the experience was an inspiration for developing the long ECDL lasers in order to benefit from a single extended cavity (Sec. 2.4.1). Indeed with the implementation of the 25 cm long ECDL the system is very reliable with easy locking to the optical ring cavity and a very good passive stability lasting several hours.

#### Lattice Laser System Improvements

Intensity noise on the lattice beams leads to parametric heating of the atoms inside the lattice [158, 159], this leads to atoms escaping from the trap when they get 'too hot' compared

to the trap depth. The intensity of the lattice beams can be stabilised by modulating the amplitude of the radio frequency signal driving the acousto-optic modulators (AOMs). Two intensity stabilisation feedback loops need to be realised [147], one per lattice beam. The light is already focussed close to the transducer of the AOMs with the plano convex lenses (PCLs), such that a high bandwidth can be achieved for the two intensity feedback loops. The point where the light is picked off is important, this light will be used to generate the error signal for the stabilisation loop. The intracavity intensity is the only intensity that matters for the intensity stability of the lattice. It is convenient to observe the transmitted light that exits the cavity, which is proportional to the intracavity light.

## 2.7 Red Laser System at 689 nm for Cooling and Squeezing

The red laser system produces 689 nm light in order to provide cooling, trapping and probing on the ${}^1S_0 \leftrightarrow {}^3P_1$ transition (Fig. 2.25 and fig. 2.26). The master is frequency stabilised to an intermediate finesse Fabry-Pérot cavity (FPC) using the Pound-Drever-Hall (PDH) technique [127, 128, 129]. The generated error signal is used to narrow the linewidth of the laser by providing feedback directly to the laser current (compensating high-frequency current noise), to the laser diode driver (compensating low-frequency current noise) and to the piezoelectric transducer controlling the ECDL grating (compensating low-frequency noise and drift). The ECDL master is stabilised in a second step to the high-finesse ultra-low expansion (ULE) Fabry-Pérot cavity using the PDH technique by double phase modulation through the fiber EOM. The double phase modulation bridges the gap between the atomic resonance frequency and the ULE cavity frequency (see the inset of fig. 2.25). The generated error signal is used to narrow the linewidth of the master laser even further by providing feedback to the piezoelectric transducer controlling the length of the intermediate finesse FPC.

The frequency stabilised light from the ECDL master is coupled into an optical fiber, which injects the slave lasers (Fig. 2.26). The slave lasers provide the necessary optical power for cooling (MOT slave) and for squeezing (probe slave) the atoms. The MOT slave and the stirring laser generate the MOT beams for the red MOT. The probe slave generates the probe and local oscillator (LO) beams for the homodyne detection system (Sec. 2.8). Furthermore, the probe slave generates the cavity reference beam, which is used to stabilise the cavity length (Fig. 2.8).

A new red master based on the cat eye design [133, 134] is being developed. A new powerful diode (HL69001DG, 210 mW) will be used as a slave, which will replaces the MOT slave and probe slave in the future. A small box is currently being designed and realised with a small pre-stabilisation cavity and two fiber coupled outputs: one towards the fiber EOM for the ULE cavity and one for the slave laser output.

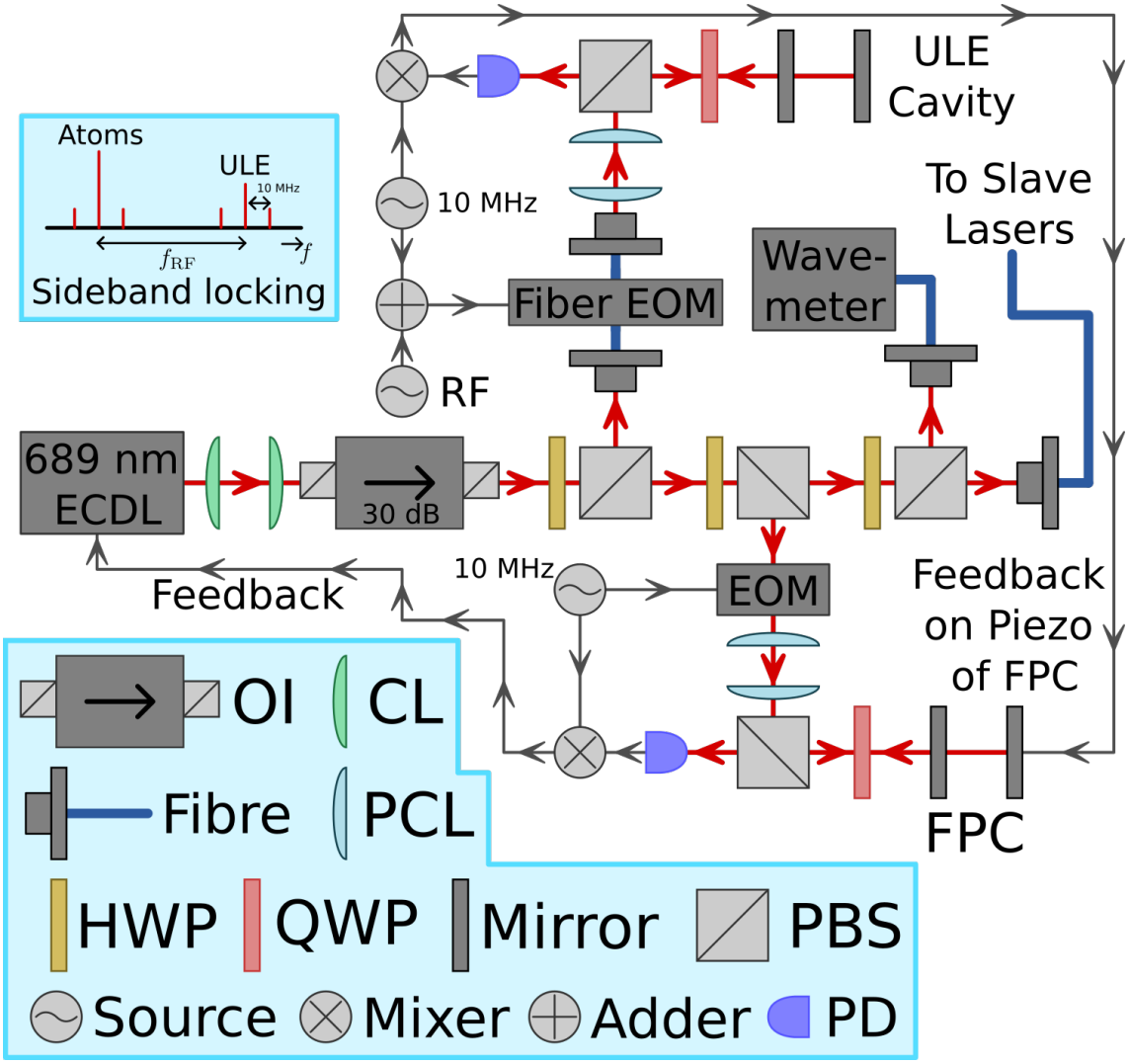


Figure 2.25: Schematic representation of the red laser system showing the stabilisation of the ECDL master laser. The abbreviated symbols indicate an optical isolator (OI), cylindrical lens (CL), plano convex lens (PLC), half waveplate (HWP), quarter waveplate (QWP), polarising beamsplitter cube (PBS) and a photodiode (PD). The ECDL is locked to a Fabry-Pérot cavity (FPC) using the Pound-Drever-Hall (PDH) technique [127, 128, 129] as a pre-stabilisation step. A sideband of the master laser is frequency stabilised to an ultra-low expansion (ULE) Fabry-Pérot cavity also using the PDH technique by double phase modulation through the fiber EOM. The frequency diagram inset shows the frequency spectrum of the master laser for sideband locking. The light from the ECDL master is coupled into an optical fiber, which transports the light to the other optical table in order to inject the slave lasers (Fig. 2.26).

The light at 689 nm from the frequency stabilised ECDL master laser injects the probe slave via an output port of an optical isolator (Fig. 2.26). The probe slave injection is checked by observing the transmission of a scanning Fabry-Pérot cavity (SFPC) with a photodiode. The probe slave generates the probe beam and the local oscillator (LO) of the homodyne detection system (Sec. 2.8). The phase-locked loop (PLL) stabilises the phase between the probe and LO beam (Fig. 2.39). The probe slave also generates the cavity reference beam, which is used to stabilise the frequency/length of the optical ring cavity. The cavity mode one free spectral range below atomic resonance ($^1S_0 \leftrightarrow {}^3P_1$) is locked to the cavity reference beam, see the energy level diagram inset for the relevant transitions for all beams.

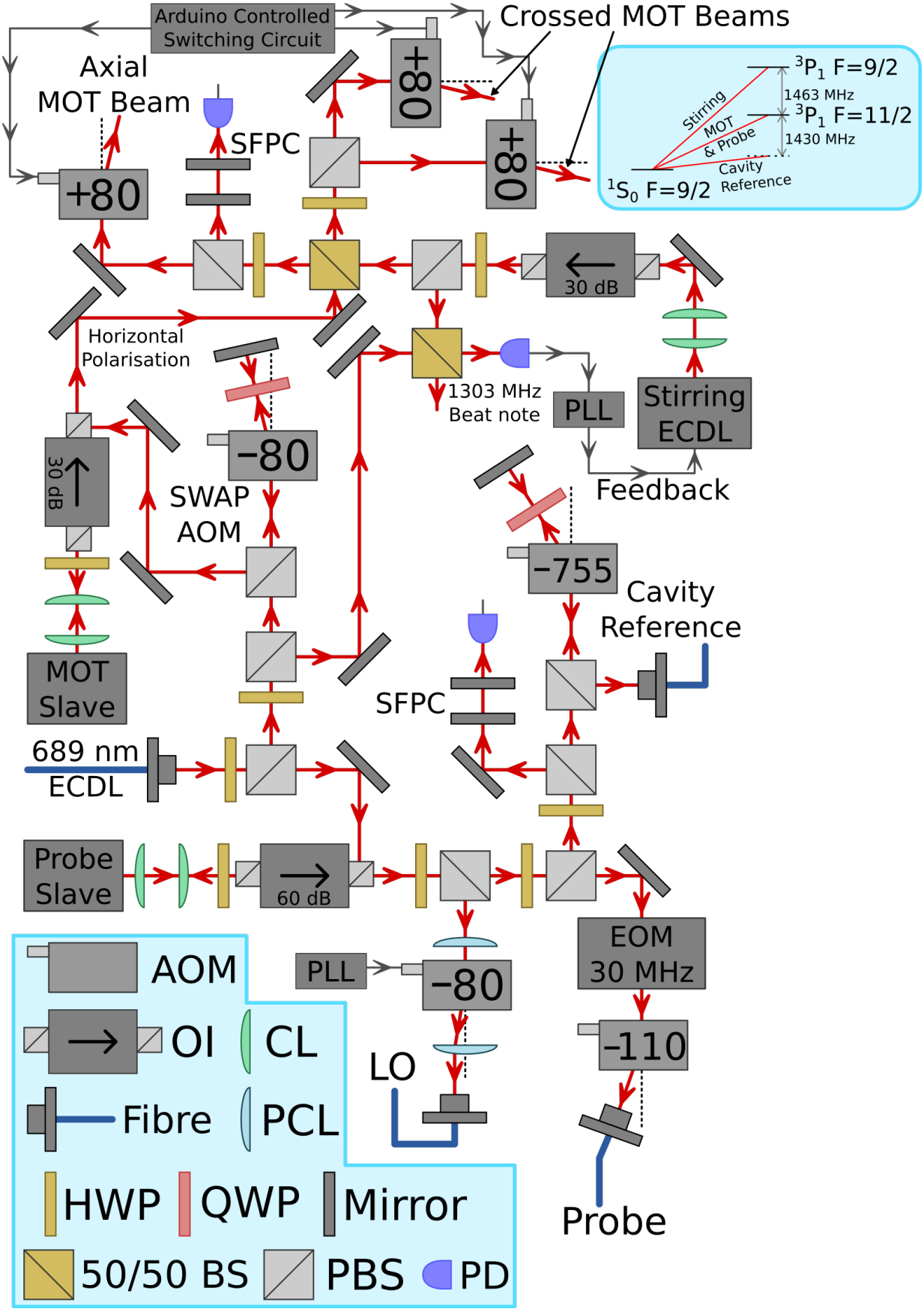


Figure 2.26: Schematic representation of the red laser system slave lasers and stirring ECDL. The full caption is shown on the next page.

Caption of figure 2.26: Schematic representation of the red laser system slave lasers and stirring ECDL. The abbreviated symbols indicate an acousto-optic modulator (AOM), optical isolator (OI), cylindrical lens (CL), plano convex lens (PLC), half waveplate (HWP), quarter waveplate (QWP), 50/50 beamsplitter cube (50/50 BS), polarising beamsplitter cube (PBS) and a photodiode (PD).

The magneto-optical trap (MOT) slave is also injected via an output port of an optical isolator (Fig. 2.26). The injected light is modulated by the SWAP AOM in order to generate the sawtooth-wave in frequency for the SWAP MOT (Subsec. 2.5.4). The system benefits from a higher power in the red MOT beams, because the SWAP AOM modulates the injection light from the 689 nm ECDL instead of the light generated by the MOT slave. The light from the MOT slave is split into three MOT beams (1 axial beam and 2 crossed beams), the beams can be switched on and off individually by the arduino controlled switching circuit (Subsec. 2.5.4) in order to realise the SWAP-3 MOT and SWAP-1 MOT (Fig. 2.22). The injection of the MOT slave is checked by observing the transmission of a scanning Fabry-Pérot cavity (SFPC) with a photodiode, the transmission peaks are moving when properly injected due to the frequency modulation provided by the SWAP AOM.

A stirring ECDL is needed to stir the hyperfine levels in $^{87}$Sr for efficient cooling in a red MOT (Subsec. 2.5.4). The stirring laser is superimposed with the red MOT beams generated by the MOT slave (Fig. 2.26). Part of the stirring laser is also superimposed with the 689 nm ECDL master, which creates a beat note at 1303 MHz. A phase-locked loop (PLL) provides feedback to the stirring laser in order to phase lock it to the 689 nm ECDL master.

The optical layout shown in figure 2.26 is complete apart from a scanning Fabry-Pérot cavity (SFPC), currently only one is available. The SFPC is shared between the probe slave and MOT slave, thus only a single injection can be checked at a time. A second SFPC will be constructed shortly when the necessary materials will be available. The phase-locked loop (PLL) of the stirring laser still needs to be realised, see figure 2.27 for the design.

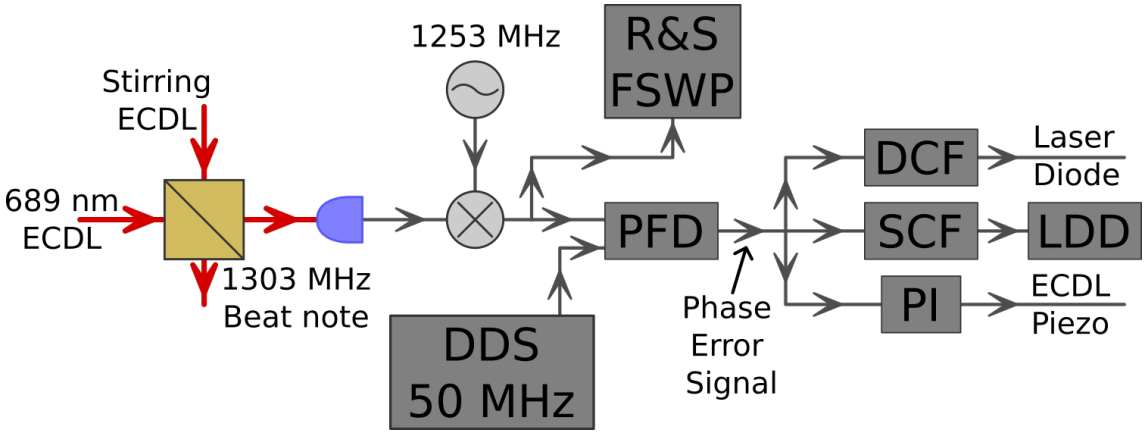


Figure 2.27: Schematic representation of the stirring laser phase-locked loop (PLL). The 1303 MHz beat note is downconverted to 50 MHz. The phase frequency detector (PFD) compares the 50 MHz signal to a 50 MHz reference from a DDS and generates a phase error signal. The direct current feedback (DCF) and slow current feedback (SCF) circuit will have some type of lead filter depending on the laser diode response. A voltage divider will also be included in both circuits in order to regulate the amount of feedback. Other filters will be added if necessary.

## 2.8 Homodyne Detection System

A low power is required when probing the optical ring cavity in the dispersive regime (Subsec. 3.1) during the quantum non-demolition measurement. As a consequence the optical signal is very weak. Therefore the signal is measured using balanced homodyne detection [160] in order to optically amplify the signal with a strong local oscillator (LO). The homodyne detection system is inspired by the system of the Thompson group [85, 161, 56].

### 2.8.1 Balanced Homodyne Detection

The weak optical signal is the probe field $\vec{E}_{probe} = E_{probe}\cos(\omega_{probe}t - \phi_{probe})\,\hat{\epsilon}_{probe}$ and the optical amplifier is the strong local oscillator (LO) field $\vec{E}_{LO} = E_{LO}\cos(\omega_{LO}t - \phi_{LO})\,\hat{\epsilon}_{LO}$. The two fields are combined and superimposed, for example by a 50/50 non-polarising beamsplitter cube (Fig. 2.28). The superimposed field $\vec{E}_{LO} + \vec{E}_{probe}$ interferes when the spatial modes and polarisations of the individual fields match. The interference term becomes meaningful when looking at the intensity of the superimposed field [160]

$$\begin{aligned} I &= cn_{air}\epsilon_0\left|\vec{E}_{LO} + \vec{E}_{probe}\right|^2 \\ &= cn_{air}\epsilon_0\left(\frac{|E_{LO}|^2}{2} + \frac{|E_{probe}|^2}{2} + |E_{LO}E_{probe}|\cos\left((\omega_{LO} - \omega_{probe})\,t - (\phi_{LO} - \phi_{probe})\right)\right. \\ &\qquad \left. + |E_{LO}E_{probe}|\cos\left((\omega_{probe} + \omega_{LO})\,t - (\phi_{probe} + \phi_{LO})\right)\right), \end{aligned}$$

with $n_{air}$ the refractive index of air. The average intensities of the individual fields are $I_{LO} = cn_{air}\epsilon_0|E_{LO}|^2/2$ and $I_{probe} = cn_{air}\epsilon_0|E_{probe}|^2/2$. The other two terms are the interference terms, one oscillates very fast at $\omega_{probe} + \omega_{LO}$, the other oscillates slow at $\omega_{probe} - \omega_{LO}$.

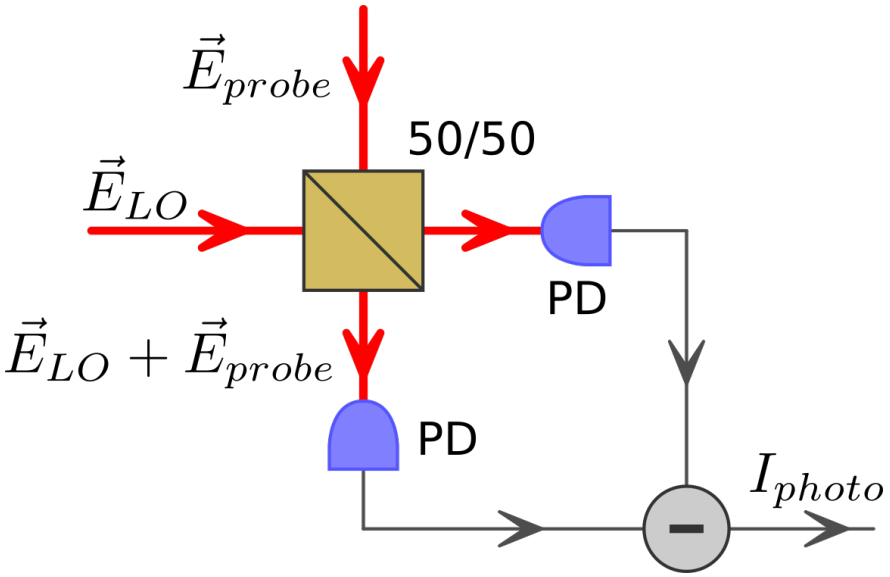


Figure 2.28: Balanced Homodyne detector schematic. The electric field of the probe $\vec{E}_{probe}$ and the local oscillator $\vec{E}_{LO}$ are combined and superimposed by a 50/50 non-polarising beamsplitter cube. The superimposed fields $\left(\vec{E}_{LO} + \vec{E}_{probe}\right)$ interfere after the cube when their spatial mode and polarisation matches. Both superimposed fields are detected by a photodiode (PD), which transforms the light into a photocurrent. The photodiodes are connected in a differential mode, such that the difference in photocurrent $I_{photo}$ is measured.

The superimposed field is incident on the photodiode, which converts the light into a photocur-

rent $I_{photo} = SP$, with $S$ the photosensitivity of the photodiode and $P$ the power of the light incident on the photodiode. The average intensities of the individual fields $I_{LO}$ and $I_{probe}$ are converted into DC signals. The interference term oscillating at the optical frequency $\omega_{probe} + \omega_{LO}$ is not detected, because of the limited photodiode bandwidth. The other interference term at $\omega_{LO} - \omega_{probe}$ is inside the bandwidth of the photodiode when the LO and probe field frequencies are close. In the case of a homodyne detection system the LO field and probe field have the same frequency $\omega_{LO} = \omega_{probe}$.

The two photodiodes are connected in a differential mode, such that the difference in photocurrent is measured. A balanced homodyne detection system operates with equal intensities hitting the photodiodes. Therefore the DC signals of the average intensities cancel and only the slowly oscillating interference term remains in the photocurrent difference

$$\begin{aligned} I_{photo} &\propto 2|E_{LO}E_{probe}| \cos\left(\left(\omega_{LO} - \omega_{probe}\right)t - \left(\phi_{LO} - \phi_{probe}\right)\right) \\ &\propto 2|E_{LO}E_{probe}| \cos\left(\phi_{LO} - \phi_{probe}\right), \end{aligned} \tag{2.20}$$

where the factor two comes from measuring the difference in photocurrent between the two photodiodes and $\omega_{LO} = \omega_{probe}$ in a homodyne detection system. Note that the photocurrent depends on the strength of the LO field $E_{LO}$, which provides optical amplification.

#### In-phase and Quadrature Components

The in-phase or the quadrature component of the photocurrent [Eq. (2.20)] is selected by tuning the phase of the local oscillator $\phi_{LO}$. When using a balanced homodyne detection system it is important to stabilise the LO phase $\phi_{LO}$, such that the correct component is selected and measured. When $\phi_{LO} = \phi_{probe}$ the in-phase component of the photocurrent is measured

$$I_{photo}(t) \propto 2|E_{LO}||E_{probe}(t)|,$$

which is sensitive to changes in the probe field amplitude $E_{probe}(t)$ and is therefore a measure of the probe field intensity $I_{probe}(t)$.

When $\phi_{LO} = \pi/2 + \phi_{probe}$ the quadrature component of the photocurrent is measured

$$I_{photo}(t) \propto 2|E_{LO}E_{probe}| \sin\left(\delta\phi_{probe}(t)\right), \tag{2.21}$$

which is sensitive to changes in the phase of the probe field $\delta\phi_{probe}(t)$ and is therefore a measure of the phase of the probe field $\phi_{probe}(t) = \phi_{probe} + \delta\phi_{probe}(t)$. For small phase shifts $\delta\phi_{probe}(t)$ the small angle approximation can be made resulting in a linear relation between the photocurrent $I_{photo}(t)$ and the phase shifts of the probe field $\delta\phi_{probe}(t)$.

### 2.8.2 Optical Layout to Stabilise the Phase Difference between the Probe and Local Oscillator

It is convenient to measure the probe light in reflection, such that the phase difference $\phi_{diff} = \phi_{LO} - \phi_{probe}$ between the LO beam and the probe beam can easily be stabilised in order to read out the quadrature field. The balanced homodyne detector (Sec. B.3) is designed to measure an AC beat note signal to stabilise the phase difference $\phi_{diff}$ and to measure a DC beat note signal in order to observe the quadrature field of the probe light. The DC beat note signal is amplified by a transimpedance amplifier (Sec. B.3). The output voltage of the homodyne detector

$$\begin{aligned} V_{HD}(t) &= R_f I_{photo}(t) = R_f SP(t) \\ &= 2R_f S\sqrt{P_{LO}P_{probe}} \sin\left(\delta\phi_{probe}(t)\right), \end{aligned} \tag{2.22}$$

with $R_f = 1$ MΩ the feedback resistance, $S = 0.45$ A/W the photo sensitivity of the photodiodes, $P_{LO}$ the power of the LO beam, $P_{probe}$ the power of the probe beam sideband and $I_{photo}$ the differential photo current of the homodyne detector when reading out the quadrature component.

Sidebands are created on the probe path by the electro-optic modulator (EOM), the carrier reflects of cavity input mirror M1 and is used in a scheme to stabilise the phase difference $\phi_{diff} = \phi_{LO} -$

$\phi_{probe}$ between the LO beam and the probe beam (Fig. 2.29). The +1 sideband acts as the probe, it is used to scan the cavity resonance with a very low power. The phase difference $\phi_{diff}$ is stabilised by creating a phase-locked loop (PLL) at 30 MHz between the probe carrier and LO tones (Fig. 2.30). The phase difference $\phi_{diff}$ is stabilised by the PLL to $\phi_{diff} = \pi/2$ by providing feedback on the LO acousto-optic modulator (AOM). The LO AOM is placed between two lenses that focus the light close to the transducer of the AOM, such that a 100 kHz modulation bandwidth is realised. The homodyne system will be used to measure the dispersion line shape of the cavity resonance (Fig. 3.5) by sweeping the frequency of the LO AOM and the EOM sideband simultaneously across cavity resonance.

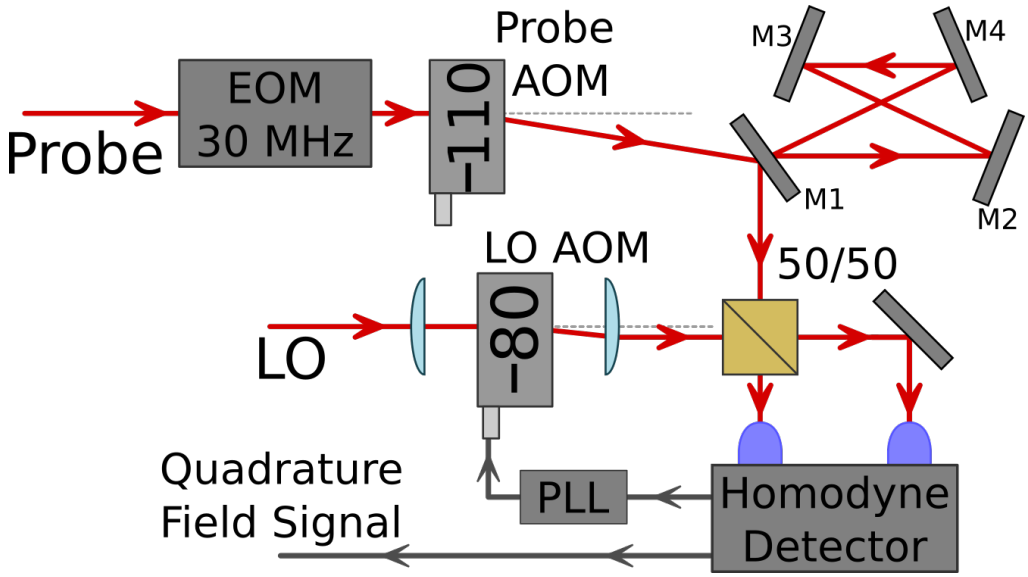


Figure 2.29: Simplified schematic of the balanced homodyne detection system, for the frequency diagram see figure 2.30. The phase difference $\phi_{diff} = \phi_{LO} - \phi_{probe}$ between the LO and probe beams is stabilised through a phase-locked loop (PLL). The PLL acts on the LO acousto-optic modulator (AOM) at 80 MHz, which is located between two lenses. The probe beam passes through an electro-optic modulator (EOM) that generates sidebands at ±30 MHz. Then the probe beam AOM shifts the frequency by −110 MHz, the $0^{\text{th}}$ order is blocked. The carrier and −1 sideband get reflected of the cavity input mirror M1, however the +1 sideband probes the cavity resonance. The LO and the probe are combined and superimposed on a 50/50 beamsplitter cube. The balanced homodyne detector measures the beat note between the probe carrier and LO tone, which is the input signal for the PLL and it measures the quadrature field of the probe +1 sideband. The full schematic of the homodyne detection system is shown in figure 2.8 and figure 2.26.

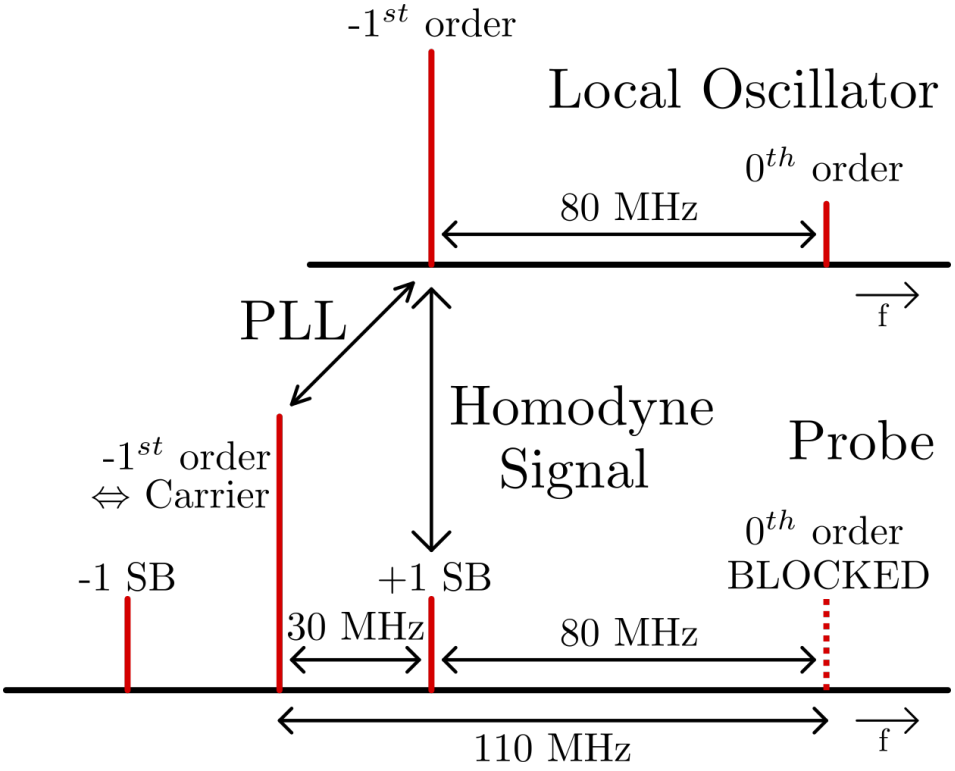


Figure 2.30: Frequency diagram of the balanced homodyne detection setup, for the simplified schematic see figure 2.29. The local oscillator (LO) is shifted by −80 MHz by the LO acousto-optic modulator (AOM), which diffracts the light into the $-1^{\text{st}}$ order. The probe light passes an electro-optic modulator (EOM), which creates sidebands (SB) at ±30 MHz. The probe is shifted by −110 MHz by the probe AOM, which diffracts the light into the $-1^{\text{st}}$ order. The $0^{\text{th}}$ order of the probe is blocked. The probe carrier and the LO $-1^{\text{st}}$ order form a beat note at 30 MHz, which is used to stabilise the phase difference $\phi_{diff} = \phi_{LO} - \phi_{probe}$ through a phase-locked loop (PLL) that acts on the LO AOM. The probe +1 sideband interferes with the LO tone, which are at the same frequency and the phase difference is stabilised to $\phi_{diff} = \pi/2$, such that the homodyne signal measures the quadrature field.

### 2.8.3 Low-Frequency Noise Leaking into the Homodyne Signal

In principle it is possible to design a similar balanced homodyne detection system without the probe AOM of figure 2.29. Then it is necessary to generate the EOM sidebands at 80 MHz, which means the PLL operates at 80 MHz (Fig. 2.31). This was how the first version of the homodyne detection system was designed, this was the Thompson group version. However, during testing the homodyne signal was not stable when the probe sideband was off-resonance with the cavity. After investigating the intensity stability, polarisation stability and other tests it became clear that a small part of the local oscillator $0^{\text{th}}$ order leaks into an optical fiber that is used to transport the light to the second story optical board, which hosts the homodyne detector and access to cavity mirror M1. The $0^{\text{th}}$ order of the LO AOM is 'blocked', but apparently only partially. Instead, the probe spectrum is shifted by implementing the AOM at 110 MHz on the probe path. This choice was made in order to strongly suppress the low-frequency noise, which is achieved by blocking the $0^{\text{th}}$ order of the probe path. No lenses are used around the probe AOM, because modulation is not necessary, thus the $0^{\text{th}}$ order and $-1^{\text{th}}$ order keep diverging, which makes it easy to completely block the $0^{\text{th}}$ order 'far' away from the probe AOM.

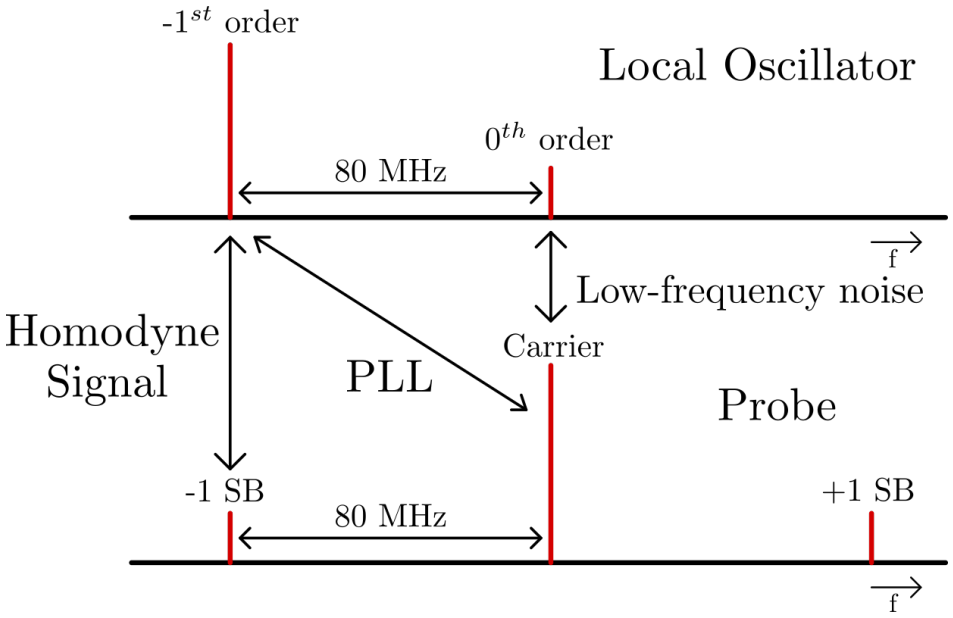


Figure 2.31: Frequency diagram of the balanced homodyne detection setup without the acousto-optic modulator (AOM) on the probe path, the Thompson group setup. This setup can read out the homodyne signal by stabilising the phase difference $\phi_{diff} = \phi_{LO} - \phi_{probe}$ using a phase-locked loop (PLL) at 80 MHz. However, the LO $0^{\text{th}}$ order partially leaks into an optical fiber that transports the light. The LO $0^{\text{th}}$ order causes a beat note with the carrier, this is picked up by the homodyne detector as low-frequency noise that gets added to the homodyne signal. Therefore the AOM on the probe path is crucial to circumvent this.

### 2.8.4 Phase-Locked Loop between the Probe and Local Oscillator

A phase-locked loop (PLL) stabilises the phase of an output signal to the phase of a reference signal. A simple electronic PLL [162] consists of a voltage controlled oscillator (VCO), a phase frequency detector (PFD) and a loop filter (Fig. 2.32). The PFD compares the two signals $V_{in}$ and $V_{out}$ by looking at the difference in the amount of zero crossings (frequency difference) and by looking which signal has its zero crossing first (phase difference). The PFD generates an error signal based on this comparison, which is fed to the loop filter and then to the VCO in order to adjust its frequency.

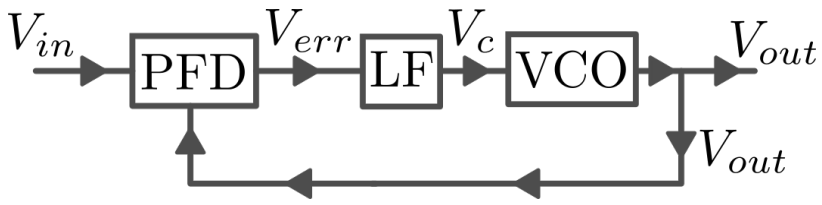


Figure 2.32: Schematic representation of a phase-locked loop (PLL) consisting of a phase frequency detector (PDF), a loop filter (LF) and a voltage controlled oscillator (VCO). The PFD compares the two signals $V_{in}$ and $V_{out}$ and generates an error signal $V_{err}$. The loop filter converts the error signal in a control voltage $V_c$ to regulate the VCO frequency. The phase of the VCO output signal $V_{out}$ is stabilised to the phase of the reference input signal $V_{in}$ when the PLL is engaged.

It is more convenient to consider the PLL in terms of phase (Fig. 2.33) since this is the quantity that needs to be stabilised. The VCO frequency $\omega = K_{VCO}V_c$ is regulated by the control voltage $V_c$. In terms of phase $\omega = d\phi/dt$, thus $\phi = \int \omega dt = \int K_{VCO}V_c dt$, which leads to the division by $s$ in Laplace space. The VCO can be seen as an integrator of the control voltage in the phase picture.

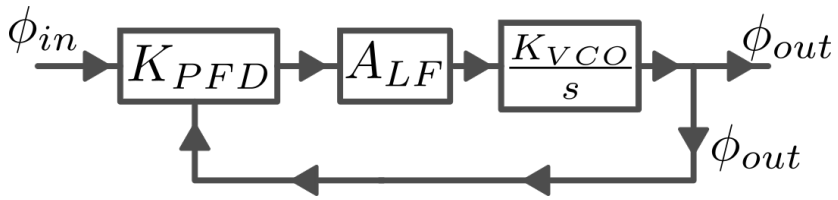


Figure 2.33: Schematic representation of the phase-locked loop (PLL) transfer functions with respect to phase $\phi$ in the Laplace domain. $K_{PFD}$ is the gain of the phase frequency detector, $A_{LF}$ is the transfer function of the loop filter. The voltage controlled oscillator with gain $K_{VCO}$ acts as an integrator, hence the division by $s$ in the Laplace domain.

The type of loop filter circuit (Fig. 2.34) depends on the output of the PFD, the ones used in the experimental setup give a voltage output. (See [162] for an alternative circuit if a current output PFD is used.) The loop filter is an integrator with a lag and a lead filter, it lags 90° in phase due to the integrator when the filters are not active (Fig. 2.35). The lead filter boosts the phase towards 0° until the lag filter kicks in. The lag filter makes the phase drop towards −90° again.

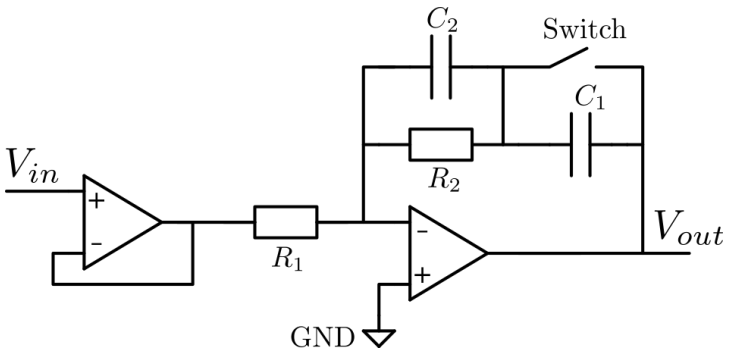


Figure 2.34: Schematic representation of the loop filter (LF) circuit. The input voltage $V_{in}$ is buffered. The second part of the loop filter consists of an integrator with a lag and lead filter. The switch can be closed to disable the low-frequency integrator stage.

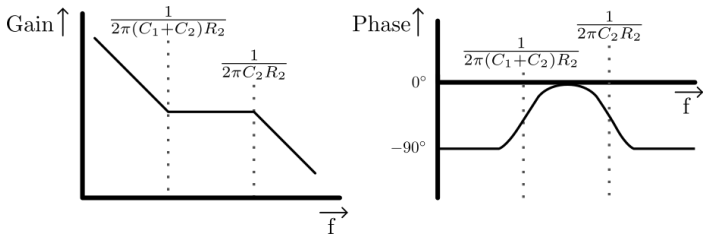


Figure 2.35: Bode plot of the loop filter transfer function $A_{LF}$. The frequency corners of the lag and lead filter are indicated by the dotted lines.

The full open loop transfer function (Fig. 2.36) acts like a double integrator with a lag and lead filter. Proper design of the lag and lead filter corner frequencies is crucial, because a double integrator lags phase by 180°, which leads to an unstable PLL at unity gain. The goal of the lead filter is to raise the phase around unity gain towards −90°. Past unity gain the lag filter kicks in, which returns the system back to the double integrator configuration. It is advised to have two decades between the lag and lead filter corner frequencies, such that the lead filter can gain the necessary amount of phase while keeping the integrator gain as large as possible. The loop filter

frequencies for a stable PLL are [162]

$$\begin{aligned} f_c &= \frac{K_{VCO}\,(C_1 + C_2)\,R_2}{2\pi C_1 R_1} \\ f_2 &= \frac{1}{2\pi\,(C_1 + C_2)\,R_2} \\ f_3 &= \frac{1}{2\pi C_2 R_2}, \end{aligned} \tag{2.23}$$

with $C_1 \approx 100 C_2$ to span approximately two decades between $f_2$ and $f_3$, with $f_c$ one decade away from both $f_2$ and $f_3$.

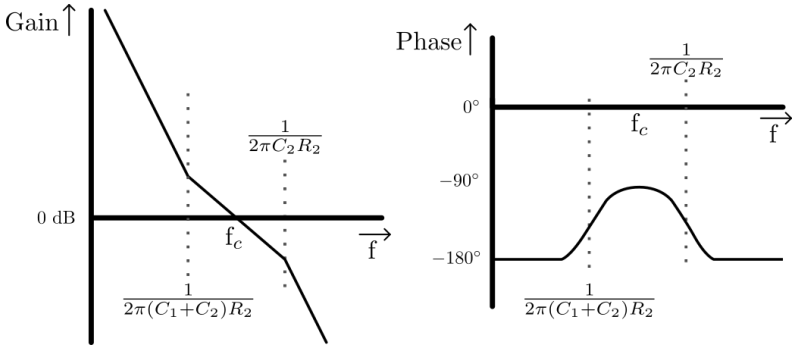


Figure 2.36: Bode plot of the open loop transfer function. The frequency corners of the lag and lead filter are indicated by the dotted lines. The amplitude decreases by −40 dB/decade and the phase lags by 180° due to the VCO and loop filter integrator. When the lead filter kicks in the amplitude decreases by −20 dB/decade and the phase increases towards −90°. At high frequencies the lag filter also acts, which brings the phase back down towards −180° and also causes the amplitude to decrease again at −40 dB/decade. The critical frequency $f_c$ at unity gain (0 dB) lies at the center in between the corner frequencies of the lag and lead filter. The open loop transfer function has a phase of −90° at unity gain, which ensures the stability of the PLL.

### Homodyne Detection System PLL Design

The homodyne detection system makes use of an optical phase-locked loop (PLL), the local oscillator (LO) phase is locked to the phase of the probe beam (Fig. 2.39). The bandwidth of the homodyne PLL is limited by the modulation bandwidth of the acousto-optic modulator (AOM), not by the VCO that is driving it. The modulation bandwidth of an AOM is typically on the order of 100 kHz, while the VCO (ROS-80-7119+) has a modulation bandwidth of 6 MHz. The optical PLL of the homodyne detection system therefore has a much smaller modulation bandwidth compared to a fully electronic PLL. The bandwidth is determined by measuring the phase noise of the PLL without the lag and lead filter installed. Oscillations occur at the critical frequency $f_c$ with only the double integrator active, which leads to an unstable PLL (Fig. 2.37). The oscillation occurs around $f_c = 150$ kHz, which means that the AOM is performing slightly better than expected.

With $f_c = 150$ kHz the lag and lead filter are targeted at $f_2 = 15$ kHz and $f_3 = 1.5$ MHz. For the lag filter $R_2 = 100\ \Omega$ and $C_2 = 1$ nF are chosen, which sets $f_3 = 1.59$ MHz [Eq. 2.23]. For the lead filter $C_1 = 100$ nF is chosen in order to span approximately two decades between the filters with $f_2 = 15.8$ kHz [Eq. 2.23]. The VCO has a gain (tuning sensitivity) of $K_{VCO} = 2\pi \cdot 3$ MHz/V, which leads to the choice of $R_1 = 2$ kΩ, such that $f_c = 151.5$ kHz [Eq. 2.23]. A loop filter (Fig. 2.34) is constructed with the mentioned values: $R_1 = 2$ kΩ, $R_2 = 100\ \Omega$, $C_1 = 100$ nF and $C_2 = 1$ nF. The PLL including the lag and lead filter does not show oscillations due to instability and it drastically lowers the phase noise with the PLL engaged (Subsec. 2.8.4).

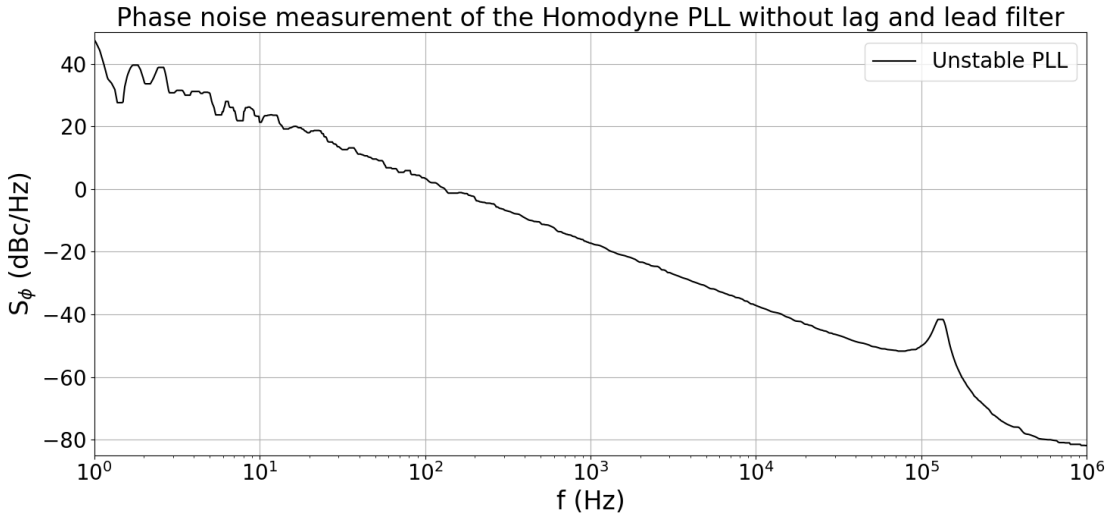


Figure 2.37: Phase noise measurement of the PLL without the lag and lead filter in the loop filter. The PLL becomes unstable around 150 kHz due to the double integrator causing positive feedback at unity gain, which causes the peak in the phase noise.

### Phase Noise of the Local Oscillator

Fluctuations in the local oscillator (LO) phase $\phi_{LO}$ lead to an uncertainty in the measured phase of the probe field. Therefore the phase noise of the beat note between the LO and probe carrier is measured with a Rohde & Schwarz phase noise analyser (Fig. 2.38), in order to determine the phase stability achieved by the phase-locked loop (PLL) (Fig. 2.39). The phase noise analyser (R&S FSWP) measures the single sideband power spectral density $\mathcal{L}(f)$ in units of dBc/Hz, this is converted to the phase power spectral density [163, 164]

$$S_\phi\left(\frac{\text{rad}^2}{\text{Hz}}\right) = \left(1\ \text{rad}^2\right) 10^{(\mathcal{L}(f)+3dB)/10}.$$

It is important that the slave laser, which generates the probe and LO fields, is injected by the master laser (Sec. 2.7) such that both fields are at a single frequency. A stable PLL is realised by the careful design of the loop filter (LF) as discussed in the previous subsection. The phase of the VCO gets locked to the phase of the Agilent reference with a bandwidth of roughly 100 kHz. The stable PLL reduces the phase noise to $S_\phi \approx 1 \cdot 10^{-9}$ rad$^2$/Hz from 100 Hz to 100 kHz. The phase stability of the 30 MHz reference signal sets the lower limit of the PLL phase noise. The phase noise of the 30 MHz reference signal is measured by connecting the Agilent source to the R&S FSWP. The second channel of the Agilent supplies a 30 MHz signal to the electro-optic modulator (EOM) in order to generate the sidebands of the probe field. The phase difference between the two Agilent channels is set such that the phase difference is stabilised at $\phi_{diff} = \phi_{LO} - \phi_{probe} = \pi/2$ by the PLL.

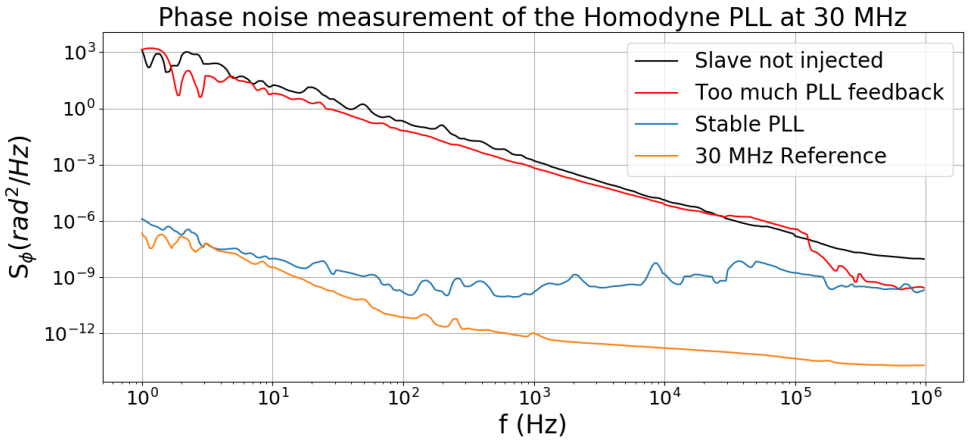


Figure 2.38: Phase noise power spectral density (PSD) measurement of the phase-locked loop (PLL) (Fig. 2.39) that is used to stabilise the phase difference $\phi_{diff} = \phi_{LO} - \phi_{probe}$ between the probe and LO fields. The probe and LO are not at a single frequency when the slave laser is not injected by the master (black). When the PLL applies to much feedback to the voltage controlled oscillator (VCO), then the LO is not at a single frequency. With appropriate feedback and loop filter design the PLL is stable, the phase of the VCO is locked to the phase of the reference, which reduces the phase noise (blue). The phase noise of the 30 MHz reference (orange) is the limit of the PLL.

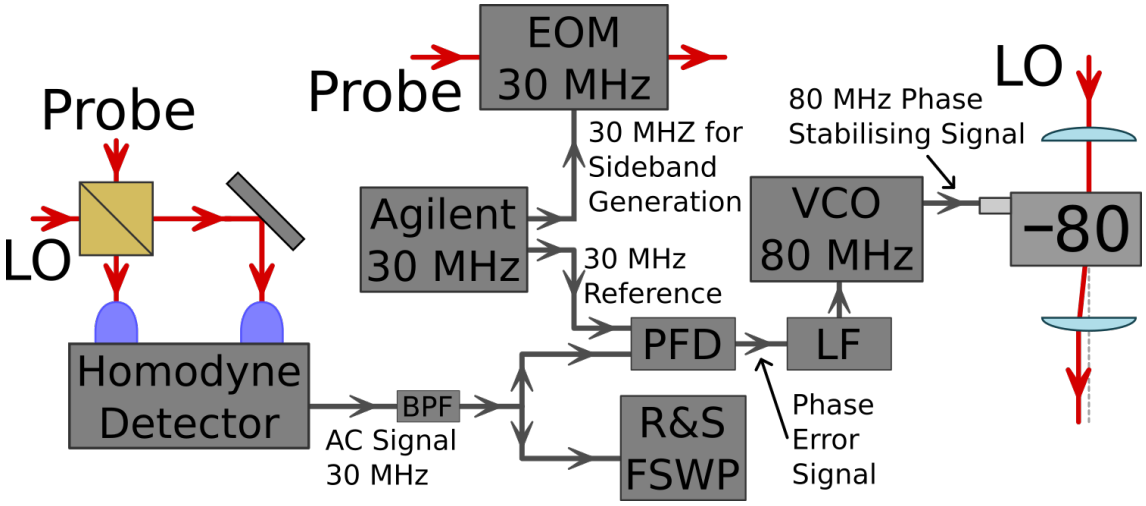


Figure 2.39: Schematic of the phase-locked loop (PLL). The homodyne detector measures a beat note between the probe and local oscillator (LO), which creates a 30 MHz AC signal. The AC signal is filtered by a band pass filter (BPF) with a range from 27 to 33 MHz. The filtered signal is split into two, one part goes to the phase frequency detector (PFD), the other part goes to the Rhode & Schwarz phase noise analyser (R&S FSWP). The PFD generates a phase error signal by comparing the frequency and phase of the 30 MHz beat note and the 30 MHz reference signal from the Agilent source. The phase error signal is integrated by the loop filter (LF), which is then used to provide feedback to the voltage controlled oscillator (VCO) at 80 MHz. The VCO generates the 80 MHz phase stabilising signal for the acousto-optic modulator (AOM) of the LO. The PLL locks the phase of the VCO to the phase of the Agilent reference. The second channel of the Agilent supplies a 30 MHz signal to the electro-optic modulator (EOM) in order to generate the sidebands of the probe field. The phase difference between the two Agilent channels is set such that the phase difference is stabilised at $\phi_{diff} = \phi_{LO} - \phi_{probe} = \pi/2$ by the PLL.

### 2.8.5 Photon Shot Noise Limited Detection

The components of the homodyne detector (Sec. B.3) are chosen to produce a low electrical noise when amplifying the detected photocurrent, such that low power optical signals can be measured. The background noise of the homodyne signal port is measured with the photodiodes of the detector blocked (Fig. 2.40). The tape blocking the photodiodes is removed and the measurement is repeated at various local oscillator (LO) powers $P_{LO}$ incident on the photodiodes. The measured voltage power spectral density $S_V$ is converted to the optical noise equivalent power (NEP) by

$$\mathrm{NEP}\,(f) = \frac{S_V\,(f)}{S^2 R_f^2},$$

with $R_f = 1$ MΩ the transimpedance gain and $S = 0.45$ A/W the photosensitivity of the photodiodes. The photon shot noise (PSN) limit is given by

$$S_P\,(f) = \frac{2hc}{\lambda} P. \tag{2.24}$$

For $P_{LO} < 70$ $\mu$W the measured NEP traces show a $1/f$ behaviour at low-frequencies followed by a constant value, which indicates that the homodyne detector is PSN limited at these LO powers. At higher optical powers ($P_{LO} > 70$ $\mu$W) spikes appear that probably originate from the power supply (multiples of 50 Hz). Noise from the power supply could cause a noise on the signal through the laser diode driver. The noise added by the laser diode driver depends on optical power. The LO power is chosen such that the detector is PSN limited while maximising the optical amplification, therefore a LO power of $P_{LO} = 70$ $\mu$W is chosen.

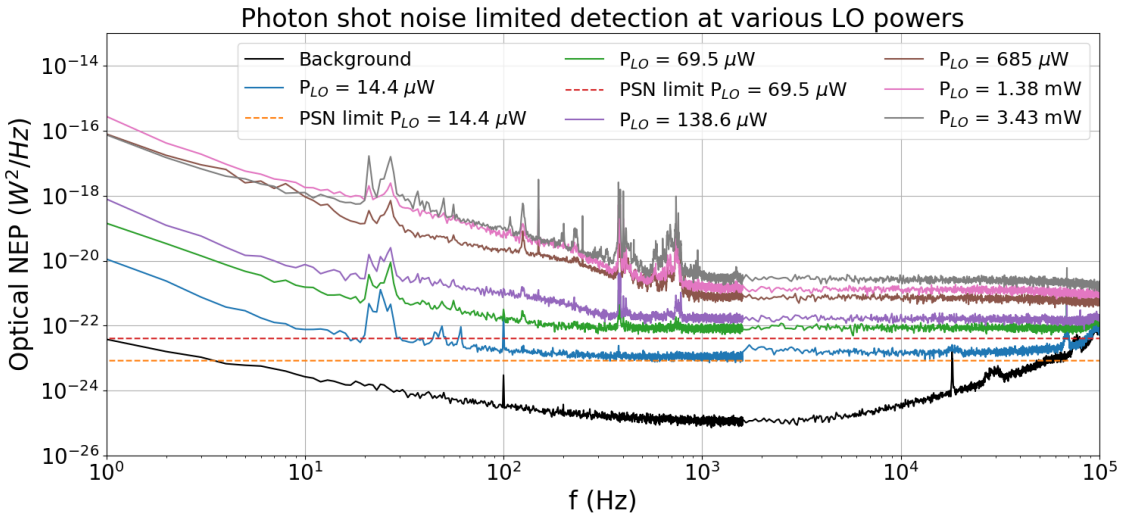


Figure 2.40: Optical noise equivalent power (NEP) of the homodyne signal port at various local oscillator (LO) powers $P_{LO}$. The background is measured by blocking the photodiodes of the detector. The flat optical NEP indicate that the detector is photon shot noise (PSN) limited for $P_{LO} < 70$ $\mu$W. The spikes between 100 Hz and 1 kHz for $P_{LO} > 70$ $\mu$W are at multiples of 50 Hz.

### 2.8.6 Stabilising the Local Oscillator Intensity

An intensity stabilising feedback loop is built with the goal of reaching photon shot noise (PSN) limited detection at high local oscillator (LO) powers $P_{LO} > 70$ $\mu$W, in order to increase the optical amplification of the homodyne system. A small part of the LO beam is picked off by placing a piece of glass after the polarising beamsplitter cube and it is focussed onto a photodiode (Fig. 2.41). The stabilising setup also compensates fluctuations in polarisation induced by the optical fiber, because the fluctuations in polarisation get transformed into intensity fluctuations by the polarising

beamsplitter (PBS) cube. The average LO power $P_{LO}$ can be set by changing the offset on a PID-controller when the intensity stability feedback loop is engaged [147]. Note that it is important to operate the feedback loop in the linear regime of the acousto-optic modulator.

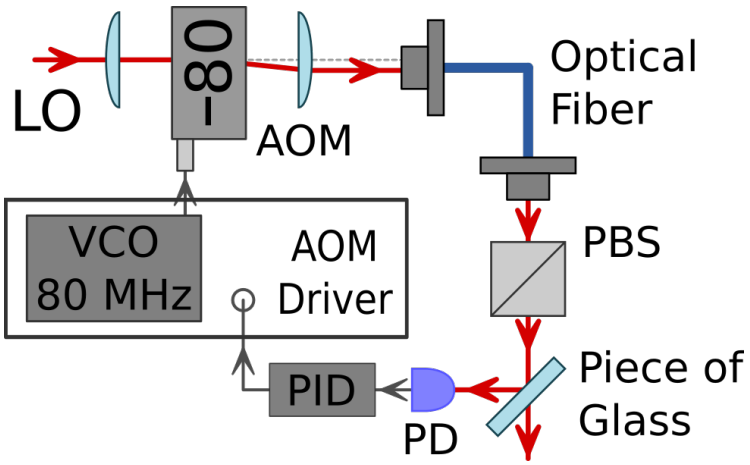


Figure 2.41: Local oscillator (LO) intensity stabilisation setup. The $-1^{\text{st}}$ order of the acousto-optic modulator (AOM) is coupled into the optical fiber. The output of the fiber is filtered by a polarising beamsplitter (PBS) cube, which transforms polarisation fluctuations into intensity fluctuations. A small part of the LO beam is picked off by a piece of glass and is focussed onto a photodiode (PD). The photodiode signal is fed to a PID-controller, which feeds back onto the amplitude modulation port of the AOM driver. The LO intensity is stabilised by the amplitude modulated radio frequency signal at 80 MHz that drives the AOM.

The intensity stability of the LO is verified by measuring the LO field with another photodiode outside of the stabilisation feedback loop, in this case the homodyne detector is used to observe the LO field. The measured voltage power spectral density $S_V$ is converted to a relative intensity noise (RIN) by

$$\text{RIN}\,(f) = \frac{S_V\,(f)}{\overline{P}^2 S^2 R_f^2},$$

with $R_f = 1$ MΩ the transimpedance gain, $S = 0.45$ A/W the photosensitivity of the photodiodes and $\overline{P}$ the average measured power.

The LO intensity stabilisation has no effect on the RIN (Fig. 2.42). The balanced homodyne detection setup already cancels a large part of the intensity fluctuations, which are common-mode before the 50/50 beamsplitter cube. Furthermore, it is probable that the noise from the power supply is transferred to intensity noise in the light through the laser diode driver and/or it is transferred into an electrical noise in the signal measured by the homodyne detector and/or by the photodetector inside the stabilisation loop. Therefore it is hard to compensate the noise that is attributed to the power supply, because all electronic systems in the laboratory are powered by the same electrical grid.

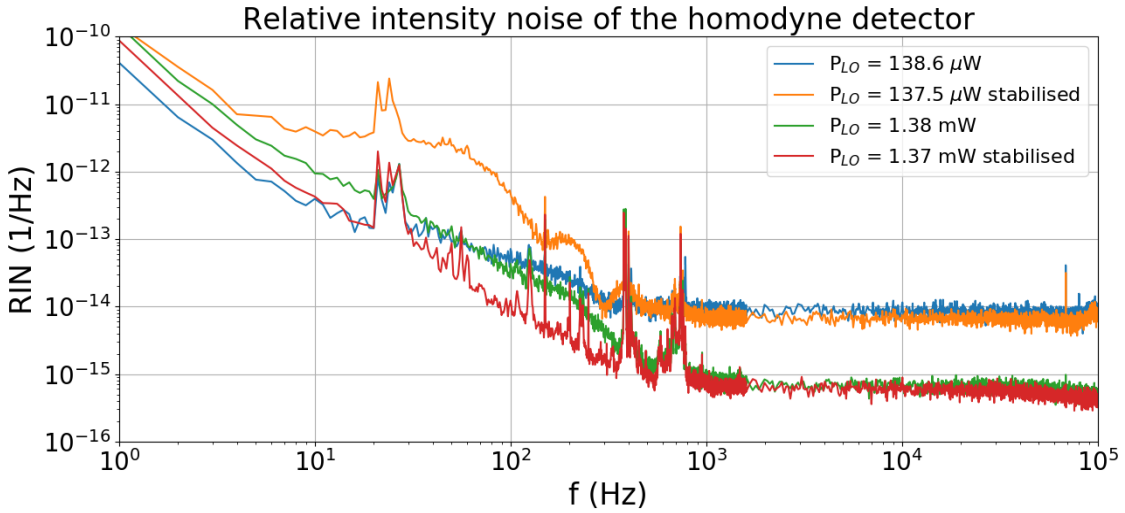


Figure 2.42: Relative intensity noise (RIN) of the homodyne signal port with and without stabilisation of the local oscillator (LO) intensity. Applying intensity stabilisation to the LO has no effect on the RIN of the homodyne detection system. The spikes between 100 Hz and 1 kHz at multiples of 50 Hz are still present.

### 2.8.7 Optically Balanced Homodyne Detection System Improvement

The current optical design (Fig. 2.8) creates a balanced homodyne detection system using a half waveplate (HWP) in combination with a polarising beamsplitter cube (PBS). However system tests show that the probe and local oscillator (LO) beam require a different rotation angle of the HWP for balanced detection due to imperfect reflection and transmission coefficients of the PBS. The imperfections of the PBS are visible with the homodyne detector due to the large sensitivity caused by the large transimpedance gain $R_f = 1$ MΩ. The homodyne detection system operates in a balanced configuration when both the probe beam and LO beam hit the detector, but this requires the rotation angle of the HWP to be somewhere between the balanced detection angles of the individual beams.

A small modification (Fig. 2.43) can be made in order to create a balanced homodyne detection setup for the individual beams and consequently the optimal angles for balancing remain the same when both beams hit the photodiode simultaneously. The LO polarisation needs to be changed to vertical (V), such that both the probe and LO have a vertical polarisation. The probe and LO beam are superimposed using a 50/50 beamsplitter cube (50/50 BS), however the transmission is slightly larger than the reflection due to imperfections in the 50/50 BS. The idea is to maximise the detected signal from the probe beam, therefore it is important to create an optical balance with the highest amount of signal. A HWP is used in combination with a PBS in order to reduce the optical power of the probe light hitting the homodyne detector, which leads to a negligible loss of probed signal. Balancing the probe leads to an unbalance in the LO beam hitting the homodyne detector, therefore a second HWP is used to optically balance the LO as well. The loss of LO light is not important, because there is enough optical power available for the LO.

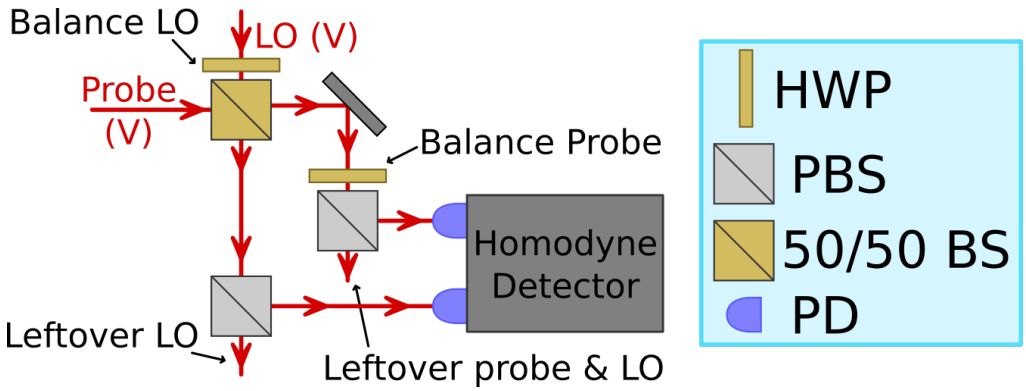


Figure 2.43: Schematic representation of the improved design for an optically balanced homodyne detection system. The abbreviated symbols indicate a half waveplate (HWP), polarising beamsplitter cube (PBS), 50/50 beamsplitter cube (50/50 BS) and a photodiode (PD). The designed optical system compensates for the imperfections in the beamsplitter cubes, such that an optically balanced homodyne detector will be realised with minimal signal loss from the probe beam.

# Chapter 3

# Using Atom-Cavity Interactions for Entanglement Generation

When reading out an atomic sensor with two energy levels the state of each atom is projected into one of two states. Correlations between the atoms can be created, which entangles them, this can lead to a readout surpassing the standard quantum limit (SQL) [50, 51, 52]. One of the tools used to generate entanglement is an optical cavity, which enhances the atom-light interaction in cavity quantum-electrodynamics (QED) systems [165, 83, 166, 167, 168, 84, 85, 169, 55]. The largest amounts of squeezing that have been generated are 20.1(3) dB [84] and 17.7(6) dB [85], both demonstrated between the internal states of $^{87}$Rb using atom-cavity interactions. Entanglement between many particles is used to enhance the sensitivity of quantum metrology systems [12], like in an entangled atomic clock [73, 170, 57] or in an entangled atom interferometer [82, 171, 78, 56, 57].

In this work the focus is on generating entanglement between atoms through quantum non-demolition (QND) measurements [83, 84, 85, 56, 172, 86, 57], which has many similarities to creating entanglement in qubit systems [173, 174, 175]. Another possibility to generate entanglement in cavity QED systems is using one-axis twisting (OAT) [166, 170, 78, 56], but it will not be discussed here.

The model of an atom located at the focus of an optical cavity is explored, in order to derive the cavity-enhanced atom-light interactions (Sec. 3.1). The principle of the ground state population measurement is explained (Sec. 3.2). The atoms located at the focus of the optical ring cavity are prepared in a single state, followed by the QND measurement sequence (Sec. 3.3) that generates the entanglement between the atoms. The attainable levels of squeezing are estimated (Sec. 3.4).

## 3.1 Cavity-Enhanced Atom-Light Interactions

When an atom is placed inside a cavity the atom-light interactions are enhanced, because a photon makes many round trips when the light is on resonance with the cavity, therefore passing the atom multiple times. The Hamiltonian describing the atom-cavity system [121]

$$\begin{aligned} H &= H_A + H_C + H_I \\ &= \frac{\hbar\omega_0}{2}\sigma_z + \hbar\omega_c a^\dagger a + H_I, \end{aligned}$$

where the atom is considered as a two-level system with $\omega_0$ the angular frequency of the atomic transition. The Pauli spin operator $\sigma_z$ describes the state of the atom when mapping the two-level system to a spin along the $\hat{z}$-direction: $|g\rangle = |\downarrow\rangle$ and $|e\rangle = |\uparrow\rangle$. The cavity Hamiltonian $H_C$ is described by the angular cavity resonance frequency $\omega_c$ and the photon creation and annihilation operators $a^\dagger$ and $a$, with commutation relation $[a, a^\dagger] = 1$. The interaction $H_I = -\vec{D}\cdot\vec{E}_c$ is described by the interaction between the cavity electric field operator $\vec{E}_c$ [Eq. 2.6] and the electric

dipole operator of the atom $\vec{D} = \vec{d}(|e\rangle\langle g| + |g\rangle\langle e|) = \vec{d}(\sigma_+ + \sigma_-)$, with $\sigma_+$ and $\sigma_-$ the Pauli raising and lowering operator and $\vec{d} = -e\vec{r}$ the electric dipole moment of the atom [69]. The fast oscillating terms average to zero in the rotating wave approximation (RWA) resulting in [121]

$$H_I = i\mathcal{E}_0\left(-\vec{d}\cdot\hat{\epsilon}_c\right)\left(f(\vec{r})\,a\sigma_+ e^{i(\omega_0-\omega_c)t} - f^*(\vec{r})\,a^\dagger\sigma_- e^{-i(\omega_0-\omega_c)t}\right) \tag{3.1}$$

$$= \frac{i\hbar\Omega_0}{2}\left(a\sigma_+ e^{i(\omega_0-\omega_c)t} - a^\dagger\sigma_- e^{-i(\omega_0-\omega_c)t}\right), \tag{3.2}$$

which leads to the Jaynes-Cummings Hamiltonian [176] in the RWA, with the assumption that the atom is at the focal point of the cavity where $f(\vec{r}) = 1$. The interaction oscillates at the vacuum Rabi frequency [121]

$$\Omega_0 = \frac{2\mathcal{E}_0}{\hbar}\left(-\vec{d}\cdot\hat{\epsilon}_c\right). \tag{3.3}$$

If the field polarisation is chosen such that it is parallel to the dipole moment, then $\vec{d}\cdot\hat{\epsilon}_c = d$. The size of the dipole moment $d$ can be related to the linewidth of the transition $\gamma$ with the help of the Einstein coefficients: $\gamma = \omega^3 d^2/\left(3\pi\epsilon_0\hbar c^3\right)$ [69]. Combining this with the expression for $\mathcal{E}_0$ [Eq. (2.8)] and $\mathcal{V}$ [Eq. 2.13] leads to

$$\begin{aligned}\Omega_0^2 &= \left(\frac{2}{\hbar}\sqrt{\frac{\hbar\omega_c}{2\epsilon_0\mathcal{V}}}\right)^2\left(-\vec{d}\cdot\hat{\epsilon}_c\right)^2 = \frac{2\omega_c}{\hbar\epsilon_0\mathcal{V}}d^2 \\ &= \frac{2\omega_c}{\hbar\epsilon_0\mathcal{V}}\frac{3\pi\epsilon_0\hbar\gamma c^3}{\omega_c^3} = \frac{6\pi\gamma c^3}{\mathcal{V}\omega_c^2} = \frac{6\pi\gamma c}{\mathcal{V}k^2} \\ &= \frac{12\pi\gamma c}{\pi L w_{0x} w_{0y} k^2} = \frac{6\gamma\kappa\mathcal{F}}{\pi w_{0x} w_{0y} k^2},\end{aligned} \tag{3.4}$$

where the cavity length $L = 2\pi c/(\kappa\mathcal{F})$. An important parameter is related to the coupling strength $\Omega_0$, it is called the single-atom cooperativity and it is defined as [165, 86]

$$\eta = \frac{\Omega_0^2}{\kappa\gamma} = \frac{6\mathcal{F}}{\pi w_{0x} w_{0y} k^2}, \tag{3.5}$$

when the atom is at the focal point of the cavity. The single-atom cooperativity (and also the vacuum Rabi frequency $\Omega_0$) can be computed at other positions $\vec{r}$ in the cavity mode by evaluating the spatial mode profile $f(\vec{r})$ at the desired location [121]

$$\eta(\vec{r}) = \eta|f(\vec{r})|^2. \tag{3.6}$$

### Ladder of Doublets

The 'uncoupled' eigenstates of $H_A + H_C$ are the bare atom-cavity states $|g,n\rangle$ and $|e,n\rangle$) with an energy of $\hbar(-\omega_0/2 + n\omega_c)$ and $\hbar(\omega/2 + n\omega_c)$ respectively, where $n = a^\dagger a$ describes the number of intracavity photons. When the detuning between the atom and the cavity is small compared to the cavity frequency ($|\Delta_c| = |\omega_0 - \omega_c| \ll \omega_c$), then a ladder of doublets is formed (Fig. 3.1). The $n^{\text{th}}$ excited doublet has $n+1$ excitations, either $n$ intracavity photons plus the atomic excitation for $|e,n\rangle$ or $n+1$ intracavity photons and no atomic excitation for $|g,n+1\rangle$. The full Hamiltonian can be split into separate two-level system Hamiltonians, with the $n^{\text{th}}$ excited doublet described by [121]

$$H_n = \hbar\omega_c\left(n + \frac{1}{2}\right)\begin{bmatrix}1 & 0\\ 0 & 1\end{bmatrix} + \frac{\hbar}{2}\begin{bmatrix}\Delta_c & -i\Omega_n\\ i\Omega_n & -\Delta_c\end{bmatrix},$$

with $\Omega_n = \sqrt{n+1}\Omega_0$ the $n$-photon Rabi frequency. The eigenenergies of $H_n$ are [121]

$$E_n^\pm = \hbar\omega_c(n+1) \pm \frac{\hbar}{2}\sqrt{\Delta_c^2 + \Omega_n^2}. \tag{3.7}$$

The corresponding eigenstates are [121]

$$|+,n\rangle = \cos(\theta_n/2)\,|e,n\rangle + i\sin(\theta_n/2)\,|g,n+1\rangle$$
$$|-,n\rangle = \sin(\theta_n/2)\,|e,n\rangle - i\cos(\theta_n/2)\,|g,n+1\rangle,$$

with $\theta_n = \arctan(\Omega_n/\Delta_c)$. They are called the 'dressed states' of the atom-cavity system. There are two interesting regimes, the resonant case $\Delta_c = 0$ and the far detuned regime $|\Delta_c| \gg \Omega_n$. At resonance there is an avoided crossing between $|+,n\rangle$ and $|-,n\rangle$, where Rabi oscillations can be observed.

### Dispersive Regime

A consequence of the large detuning is that the probability to make an atomic transition due to absorption or emission of a photon is small in the dispersive regime. Assuming a large and positive detuning $\Delta_c \gg \Omega_n$, then the energies of the doublet [Eq. (3.7)] can be expanded to the lowest order in $\Omega_0^2/\Delta_c^2$ [121]

$$\begin{aligned} E_n^{\pm} &= \hbar\omega_c(n+1) \pm \frac{\hbar\Delta_c}{2}\sqrt{1+\frac{\Omega_n^2}{\Delta_c^2}} \\ &\approx \hbar\omega_c(n+1) \pm \hbar\left(\frac{\Delta_c}{2} + \frac{\Omega_n^2}{4\Delta_c}\right). \end{aligned} \tag{3.8}$$

The uncoupled eigenenergies are [121]

$$E_n = \hbar\omega_c(n+1) \pm \frac{\hbar\Delta_c}{2}. \tag{3.9}$$

For large detunings $|\Delta_c| \gg \Omega_n$ the energy levels of the dressed states [Eq. (3.8)] lie close to the energy levels of the uncoupled states [Eq. (3.9)], but they differ slightly. The dressed energy levels get shifted by [121]

$$\Delta_{e,n} = \frac{\hbar\Omega_n^2}{4\Delta_c} = \frac{\hbar(n+1)\Omega_0^2}{4\Delta_c}$$
$$\Delta_{g,n} = -\frac{\hbar\Omega_{n-1}^2}{4\Delta_c} = -\frac{\hbar n\Omega_0^2}{4\Delta_c},$$

which leads to a shift in the cavity resonance frequency [121]

$$\begin{aligned} \delta_e\omega_c &= \frac{\Delta_{e,n+1} - \Delta_{e,n}}{\hbar} = \frac{\Omega_0^2}{4\Delta_c} \\ \delta_g\omega_c &= \frac{-\Delta_{g,n+2} + \Delta_{g,n+1}}{\hbar} = -\frac{\Omega_0^2}{4\Delta_c} \end{aligned} \tag{3.10}$$

that depends on the state of the atom. The shift in the dressed energy levels can also be regarded as a shift in the atomic transition frequency [121]

$$\delta\omega_0 = \frac{\Delta_{e,n} - \Delta_{g,n}}{\hbar} = \frac{(2n+1)\Omega_0^2}{4\Delta_c}.$$

The effect of the cavity-enhanced atom-light interaction can be regarded in two ways: 1. In the atomic frame it is as if the atom experiences an enhanced light shift that depends on the amount of intracavity photons $n$. 2. In the cavity frame there is a shift in cavity frequency, which depends on the state of the atom. The atom acts as a piece of transparent dielectric with a state-dependent refraction index. The atomic refraction index changes the effective cavity length, hence the cavity frequency changes.

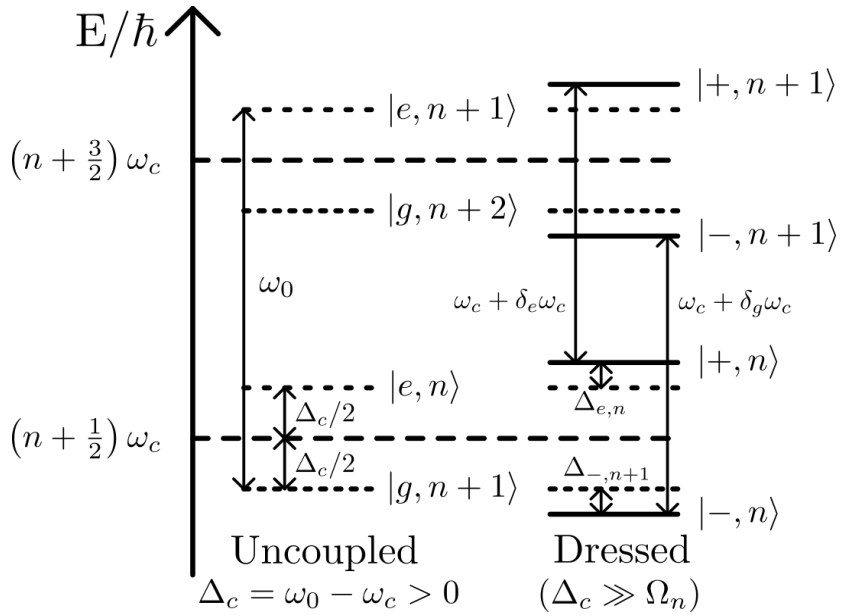


Figure 3.1: Energy level diagram of the $n^{\text{th}}$ and $(n+1)^{\text{th}}$ excited doublets in the atom-cavity model for a positive detuning $\Delta_c > 0$. On the left the uncoupled states of $H_A + H_C$ are shown and on the right the dressed states of $H_n$ are shown in the dispersive regime ($\Delta_c \gg \Omega_n$). In the dispersive regime the energy levels are shifted by $\Delta_{e,n}$ and $\Delta_{g,n}$, which leads to a shift in the cavity resonance frequency of $\delta_g\omega_c$ when the atom is in the ground state $|g\rangle$ and $\delta_e\omega_c$ when the atom is in the excited state $|e\rangle$. Figure adapted from [121].

The shift of the energy levels in the dispersive regime can be exploited to perform quantum measurements on either the cavity or the atom, where the other system is used as the detector. It is easier to see by rewriting the system in terms of the states $|+, n\rangle$ (the shifted state $|e, n\rangle$) and $|-, n-1\rangle$ (the shifted state $|g, n\rangle$) with corresponding energies [121]

$$E_n^+ = E_{e,n}^{shift} = \frac{\hbar\omega_0}{2} + n\hbar\omega_c + (n+1)\,\hbar\frac{\Omega_0^2}{4\Delta_c}$$
$$E_{n-1}^- = E_{g,n}^{shift} = -\frac{\hbar\omega_0}{2} + n\hbar\omega_c - n\hbar\frac{\Omega_0^2}{4\Delta_c},$$

which are the eigenstates and eigenenergies of the effective Hamiltonian [121]

$$H_{eff} = \hbar\omega_c a^\dagger a + \frac{\hbar}{2}\sigma_z\omega_0 + \hbar\frac{\Omega_0^2}{4\Delta_c}\sigma_z a^\dagger a + \hbar\frac{\Omega_0^2}{4\Delta_c}\sigma_+\sigma_-.$$

By grouping the terms with $\sigma_z$ to regard the interaction as a light shift on the atom or group the terms with $a^\dagger a$ to regard the interaction as a shift in the cavity frequency [121]

$$H_{eff} = \begin{cases} \hbar\omega_c a^\dagger a + \frac{\hbar}{2}\sigma_z\left(\omega_0 + 2\frac{\Omega_0^2}{4\Delta_c}a^\dagger a\right) + \hbar\frac{\Omega_0^2}{4\Delta_c}\sigma_+\sigma_- & \text{"Atom light shift"} \\ \hbar\left(\omega_c + \frac{\Omega_0^2}{4\Delta_c}\sigma_z\right)a^\dagger a + \frac{\hbar}{2}\sigma_z\omega_0 + \hbar\frac{\Omega_0^2}{4\Delta_c}\sigma_+\sigma_- & \text{"Cavity frequency shift".} \end{cases} \tag{3.11}$$

Thus the intracavity photon number can be measured in a non-destructive way by measuring the light shifted atomic resonance frequency. Or the state of the atom can be measured in a non-destructive way by measuring the shift in the cavity frequency. This approach is only valid in the dispersive regime when $\Delta_c \gg \Omega_n = \sqrt{n+1}\Omega_0$. Thus the intracavity photon number must be small compared to the ratio between the detuning and the vacuum Rabi frequency [121]

$$n \ll \frac{\Delta_c^2}{\Omega_0^2} = \frac{\Delta_c^2}{\eta\kappa\gamma} \tag{3.12}$$

in order to operate in the dispersive regime, where equation (3.5) was used in the final step.

**Extending the Picture to $N$ Atoms**

The atom-cavity picture described in this section can be extended to $N$ atoms coupled to a cavity, with each individual atomic state in a superposition. The state of each individual atom induces a shift in the cavity resonance frequency, which contributes to the total shift in cavity resonance frequency. Thus observing the total shift in resonance frequency is a collective measurement of the quantum state of the ensemble of $N$ atoms. The collective measurement creates entanglement between the $N$ atoms (forming an ensemble), because knowledge about the collective state is extracted without gaining knowledge about the individual atomic states.

## 3.2 Probing the Ground State Population

In this work one of the goals is to generate entanglement forming an ensemble of $N$ strontium atoms, which can then be injected into an atom interferometer that operates on the optical clock transition ${}^1S_0 \leftrightarrow {}^3P_0$ (Ch. 4). Therefore it is convenient to generate entanglement between atoms that are in a superposition between the ground state ${}^1S_0$ and the excited state ${}^3P_0$. The principle of probing the ground state population with a single QND measurement is highlighted below, which is a part of the full QND measurement sequence (Sec. 3.3) necessary to entangle the atoms.

The optical clock states of a single strontium atom can be considered as a spin-1/2 system, with ${}^1S_0\,(F = 9/2, M_F = -9/2) = |\downarrow\rangle$ and ${}^3P_0\,(F' = 9/2, M_{F'} = -9/2) = |\uparrow\rangle$, where the magnetic sublevels are resolved by a small bias field $\vec{B}_{bias}$ of 2 Gauss that is applied perpendicular to the cavity axis in the xz-plane. Thus for a cloud of $N$ atoms a collective spin-$N/2$ system can be defined, where $N_\downarrow$ and $N_\uparrow$ indicate the corresponding state populations (Fig. 3.2). The cloud is located at the focus of the optical ring cavity, with cavity resonance frequency $\omega_c$. The probe light circulating inside the optical ring cavity is vertically polarised (along the $\hat{y}$-axis), which decomposes into an equal superposition of $\sigma_+$ and $\sigma_-$ light because of the magnetic field $\vec{B}_{bias}$ in the xz-plane. As described in the previous section cavity-enhanced atom-light interactions only occur when the field polarisation is parallel to the dipole moment [Eq. (3.1)]. The dipole moment $\vec{d}$ points along the magnetic field direction due to the applied bias field $\vec{B}_{bias}$. Vertically polarised light propagating inside the cavity is perpendicular to the dipole moment, but it decomposes into driving $\sigma_+$ and $\sigma_-$ transitions that do couple the the dipole moment. The states $|\downarrow\rangle$ and ${}^3P_1\,(F' = 11/2, M_{F'} = -11/2) = |e\rangle$ couple to the cavity modes via the $\sigma_-$ transition. Furthermore, the $\sigma_+$ transition couples the states $|\downarrow\rangle$ and ${}^3P_1\,(F' = 11/2, M_{F'} = -7/2) = |e'\rangle$ to the cavity modes. The bias field of $B_{bias} = 2$ G results in a detuning of $\Delta_B = 2\pi \cdot 1.5$ MHz between the magnetic sublevels $M_{F'} = -11/2$ and $M_{F'} = -7/2$ of the ${}^3P_1\,(F' = 11/2)$ level. Both magnetic sublevels contribute to the shift in cavity resonance frequency.

The cavity resonance frequency experiences a state-dependent shift [Eq. (3.10)] from each individual atom when operating in the dispersive regime. The excited levels $|e\rangle$ and $|e'\rangle$ are unpopulated, thus only the population of the ground state $N_\downarrow$ contributes to the shift in cavity resonance frequency when probing the cavity. Therefore the shift in cavity resonance frequency

$$\delta\omega_c = -N_\downarrow \left( \frac{1}{2} \frac{\Omega_0^2}{4\Delta_c} + \frac{1}{2} \frac{\Omega_0^2}{4\,(\Delta_c + \Delta_B)} \right) = -N_\downarrow \left( \frac{\eta\kappa\gamma}{8\Delta_c} + \frac{\eta\kappa\gamma}{8\,(\Delta_c + \Delta_B)} \right) = -N_\downarrow \chi, \tag{3.13}$$

with $\eta$ the single-atom cooperativity [Eq. 3.5], $\kappa$ the linewidth of the cavity, $\gamma$ the linewidth of the ${}^1S_0 \leftrightarrow {}^3P_1$ transition and $\chi$ the cavity shift induced by a single atom. The $\sigma_-$ probe transition contributes $\eta\kappa\gamma/\,(8\Delta_c)$ to $\chi$ and the $\sigma_+$ probe transition contributes $\eta\kappa\gamma/\,(8\,(\Delta_c + \Delta_B))$ to $\chi$. Thus the ground state population $N_\downarrow$ is determined in a non-destructive way by measuring the total shift in resonance frequency $\delta\omega_c$.

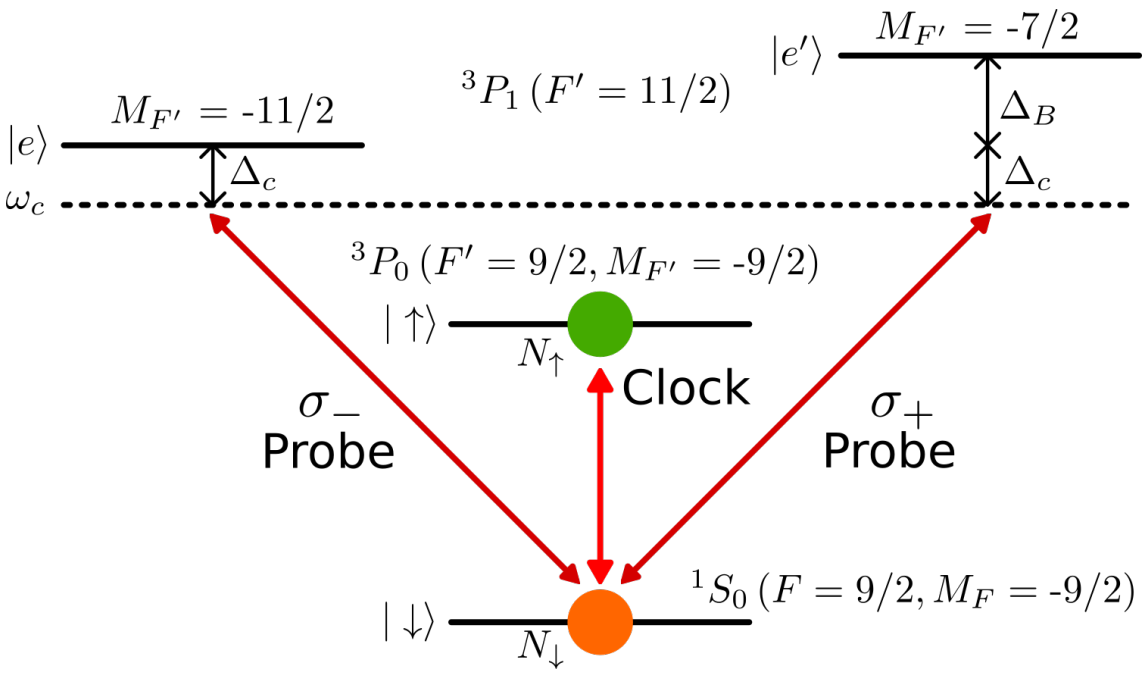


Figure 3.2: Energy level diagram of a cloud of $N$ strontium atoms located at the focus of the optical ring cavity. The cavity resonance frequency $\omega_c$ is detuned below the excited state $|e\rangle = {}^3P_1\,(F=11/2, M_{F'}=-11/2)$ by $\Delta_c$. A small bias field $B_{bias}$ is applied perpendicular to the cavity axis to resolve the magnetic sublevels. A spin-1/2 system is defined by the optical clock states with ${}^1S_0\,(F=9/2, M_F=-9/2) = |\downarrow\rangle$ and ${}^3P_0\,(F'=9/2, M_{F'}=-9/2) = |\uparrow\rangle$. A cloud of $N$ atoms forms a collective spin-$N/2$ system, where $N_\downarrow$ and $N_\uparrow$ indicate the corresponding state populations. The probe light circulating inside the optical ring cavity is vertically polarised, which decomposes into an equal superposition of $\sigma_+$ and $\sigma_-$ light. The probe light couples to the dipole moment via $\sigma_+$ and $\sigma_-$ transitions, which leads to cavity-enhanced atom-light interactions. The $N_\downarrow$ state population is probed in the dispersive regime by observing the shift in cavity resonance frequency. The excited state $|e'\rangle = {}^3P_1\,(F'=11/2, M_{F'}=-7/2)$ contributes less towards the shift in cavity resonance frequency compared to the excited state $|e\rangle = {}^3P_1\,(F'=11/2, M_{F'}=-11/2)$, because of the applied bias field $B_{bias}$, which detunes the two magnetic sublevels by $\Delta_B$.

The optical ring cavity has a finesse of $\mathcal{F} = 24(2)\cdot 10^3$, a free spectral range (FSR) of $f_{\mathrm{FSR}} = 1.43136(3)$ GHz and a linewidth of $\kappa = 2\pi\cdot 57.6(1)$kHz [120], which leads to a single-atom cooperativity of $\eta = 0.56$ at the small waist. ($w_{0x} = 32.0$ $\mu$m and $w_{0y} = 29.4$ $\mu$m, see Subsec. 2.2.1 and Fig. 2.3.) The cavity resonance shift per atom $\chi$ depends on the chosen detuning $\Delta_c$, which also influences the individual contribution of the $\sigma_+$ and $\sigma_-$ polarised probe light (Fig. 3.3). For $\Delta_c < 2\pi\cdot 1$ MHz the cavity shift $\chi$ is mainly determined by the contribution from magnetic sublevel $M_{F'} = -11/2$. For $\Delta_c > 2\pi\cdot 10$ MHz both magnetic sublevels contribute almost equally to the cavity shift $\chi$.

An important point to consider is that the $\sigma_-$ probe transition is closed, while the $\sigma_+$ probe transition is open. Additional losses occur on the open transition compared to the closed transition, this limits the amount of squeezing that can be created and will be discussed in more detail in section 3.4. The contribution to $\chi$ from probing on magnetic sublevel ${}^3P_1\,(F'=11/2, M_{F'}=-7/2) = |e'\rangle$ depends on the ratio between $\Delta_B$ and $\Delta_c$. Increasing the bias field $B_{bias}$ will increase the detuning $\Delta_B$.

Operating in the dispersive regime requires a small intracavity photon number $n$ [Eq. (3.12)]. Therefore it is crucial to probe the cavity with a low power $P_{PSB}$ in the +1 sideband of the probe beam. This reduces saturation of the probing transition and scattering into free space. The rate of photons that enter the cavity is $P_{PSB}/E_{photon}$. The energy of a single photon is $E_{photon} = hc/\lambda$, with $\lambda = 689.4$ nm for the probe transition $\left({}^1S_0 \leftrightarrow {}^3P_1\right)$. The intracavity probe field is

enhanced by a factor of $T_1\mathcal{F}^2/\pi^2 = 13 \cdot 10^3$ [Eq. 2.3] due to the power build up inside the cavity, with $T_1 = 240$ ppm the power transmission coefficient of mirror 1 at $\lambda = 689.4$ nm [120]. A photon takes $t = L/c = 1/f_{\mathrm{FSR}}$ to complete a round trip in the ring cavity, thus the number of intracavity photons

$$n = \frac{P_{PSB}}{E_{photon}} \frac{T_1\mathcal{F}^2}{\pi^2} \frac{1}{f_{\mathrm{FSR}}}. \tag{3.14}$$

The intracavity photon number $n$ can not exceed the upper limit of $\Delta_c^2/(\eta\kappa\gamma)$ [Eq. 3.12] in order to stay within the dispersive regime (Fig. 3.4), therefore the choice of $\Delta_c$ is very important.

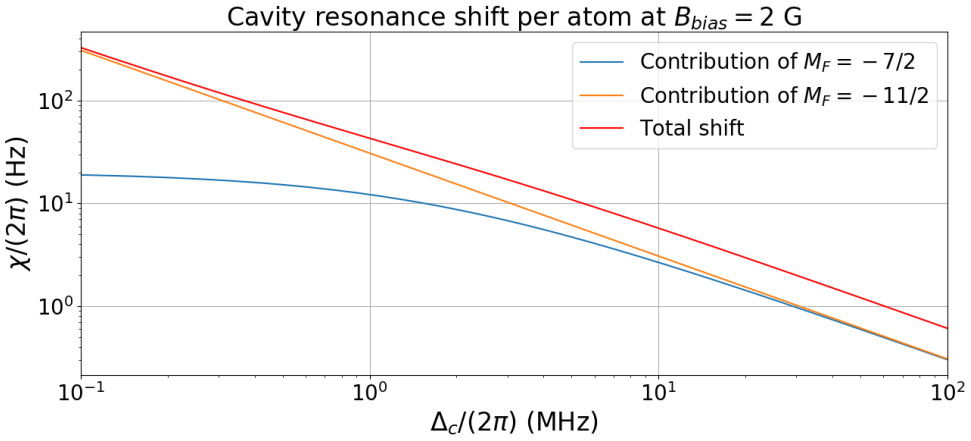


Figure 3.3: The cavity resonance shift per atom $\chi$ versus the cavity detuning $\Delta_c$ is shown at a bias field of $B_{bias} = 2$ G. The individual contribution of the two magnetic sublevels of $^3P_1$ ($F' = 11/2$) are also shown. For $\Delta_c < 2\pi \cdot 1$ MHz the cavity shift $\chi$ is mainly determined by the contribution from magnetic sublevel $M_{F'} = -11/2$. For $\Delta_c > 2\pi \cdot 10$ MHz both magnetic sublevels contribute almost equally to the cavity shift $\chi$.

A trade-off has to be made when choosing the cavity detuning $\Delta_c$, ideally $\Delta_c$ is chosen such that the best atom number resolution possible is realised. Having a small detuning $\Delta_c$ leads to a large shift per atom $\chi$, which causes a stronger signal in terms of cavity shift $\delta\omega_c$. However, a small detuning $\Delta_c$ requires operation with a low intracavity photon number $n$, which leads to a weaker signal in terms of optical power.

Initial tests will be performed at a cavity detuning of $\Delta_c = 2\pi \cdot 1$ MHz, which leads to a cavity resonance shift per atom of $\chi = 2\pi \cdot 43$ Hz. The contribution of magnetic sublevel $M_{F'} = -11/2$ to $\chi$ is $2\pi \cdot 31$ Hz and the contribution of magnetic sublevel $M_{F'} = -7/2$ is $2\pi \cdot 12$ Hz. However, the choice of $\Delta_c = 2\pi \cdot 1$ MHz poses a strict limit on the probe sideband power. Using a power of $P_{PSB} \approx 10$ pW allows for operation in the dispersive regime. The homodyne detection system (Sec. 2.8) is used to amplify the weak optical signal in the probe sideband.

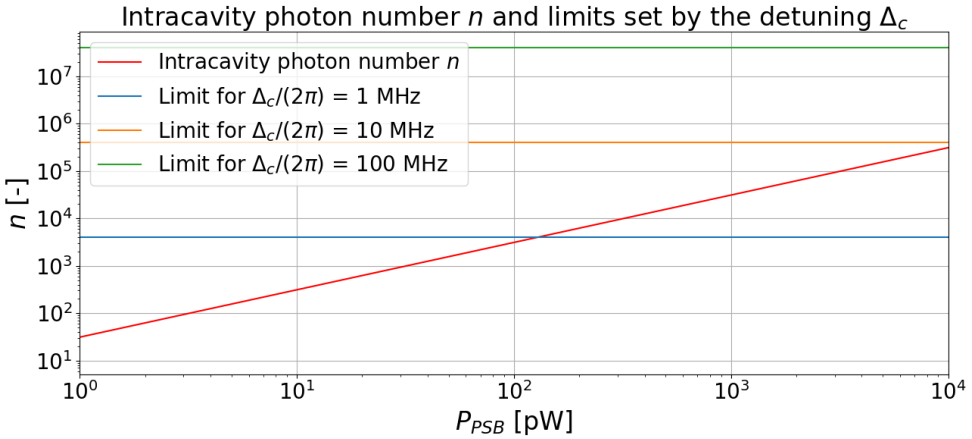


Figure 3.4: Intracavity photon number $n$ [Eq. (3.14)] versus probe sideband power $P_{PSB}$ (red). The upper limits on the intracavity photon number for operating in the dispersive regime [Eq. 3.12] are shown at a cavity detuning of $\Delta_c = 2\pi{\cdot}1$ MHz (blue), $2\pi{\cdot}10$ MHz (orange) and $2\pi{\cdot}100$ MHz (green).

### 3.2.1 Frequency Scan across Cavity Resonance

Knowledge about the bare cavity resonance frequency $\omega_c$ is needed in order to determine the shift in cavity resonance frequency $\delta\omega_c$ [Eq. (3.13)]. The method of choice to determine the cavity resonance frequency is scanning the frequency of the probe beam across cavity resonance. The frequency scan is performed twice, once to determine the bare cavity resonance frequency $\omega_c$ and then a second time when the cavity is loaded with atoms to determine the shifted cavity resonance frequency $\omega_c + \delta\omega_c$. The probe field $\vec{E}_{probe}$ is measured in reflection by the homodyne detection system, either the in-phase or the quadrature field (Fig. 3.5) can be read out. The in-phase component holds information about the intracavity intensity $I_c$, which has a Lorentzian line shape [Eq. (2.4)] of the form $f(x) = 1/(1+x^2)$, with $x = 2(\omega - \omega_c)/\kappa$, where $\kappa$ is the cavity linewidth. The quadrature component of the probe field holds the information about the phase, it has a dispersion line shape $g(x)$, which follows from the Kramers-Kronig relations [119]:

$$g(x) = \mathcal{H}\left[\frac{1}{1+x^2}\right] = -\frac{x}{1+x^2}, \tag{3.15}$$

with $\mathcal{H}$ the Hilbert transform. The zero crossing of the dispersion line shape is more sensitive to the cavity resonance frequency $\omega_c$ compared to the maximum of the absorption line shape, therefore the quadrature component of the probe field is measured during the frequency scan.

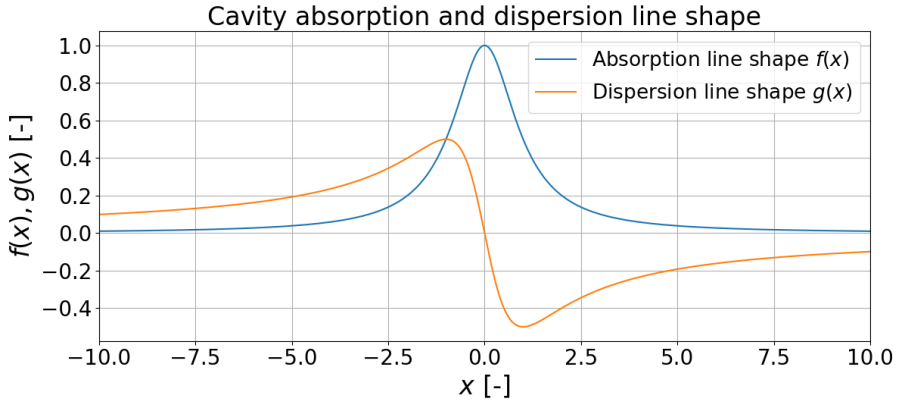


Figure 3.5: Absorption and dispersion line shape when scanning the probe across cavity resonance ($x = 0$). The absorption line shape is the in-field component and the dispersion line shape is the quadrature component of the probe light field.

**Converting Phase Noise of the Local Oscillator to an Uncertainty in the Ground State Population $N_\downarrow$**

The homodyne detector measures the quadrature component of the probe sideband light field when scanning across cavity resonance. The phase of the probe sideband $\phi_{probe}(\omega)$ follows a dispersion line shape, but it gets distorted due to the phase noise introduced by the local oscillator (LO). A model is developed in order to estimate the uncertainty introduced by the LO phase noise (Subsec. 2.8.4) when determining the ground state population $N_\downarrow$.

The dispersion line shape (Fig. 3.5) is non-linear in phase except for a region close to cavity resonance. The phase of the probe sideband changes from $-\pi$ rad to $\pi$ rad when scanning through the cavity resonance, which can be described as $\phi_{probe}(\omega) = \phi_{probe} + \delta\phi_{probe}(\omega)$, where $\delta\phi_{probe}(\omega) \in [0, 2\pi]$ and $\phi_{probe} = -\pi$ rad is the phase of the reflected carrier. The output signal of the homodyne detector $V_{HD} \propto \sin(\delta\phi_{probe}(\omega))$ [Eq. (2.22)], which means that there is a change of $\pi$ rad between the maximum and minimum of the dispersion line shape (Fig. 3.5). Furthermore, the displacement in frequency between the maximum and minimum of the dispersion line shape is equal to the cavity linewidth $\kappa$. This dispersive line shape is linear in phase in this regime, which enables the conversion of phase into frequency.

The frequency scan across cavity resonance is recorded on an oscilloscope, which takes traces of $10^4$ points. Consider that a single frequency scan takes 100 ms, such that the time between two measurement points on the oscilloscope is 10 $\mu$s. The variance in phase introduced by the frequency scan is estimated by integrating the measured phase noise power spectral density $S_\phi(f)$ (Fig. 2.38) from 10 Hz to 100 kHz (the oscilloscope measurement window)

$$\mathrm{Var}(\phi) = \int_{10\ \mathrm{Hz}}^{100\ \mathrm{kHz}} S_\phi(f)\, df = 3.09 \cdot 10^{-4}\ \mathrm{rad}^2,$$

which leads to a phase uncertainty of $\sigma_\phi = \sqrt{\mathrm{Var}(\phi)} = 17.6$ mrad. The phase uncertainty is converted to an uncertainty in the determined cavity frequency

$$\sigma_{\omega_c} = \frac{\kappa}{\pi\ \mathrm{rad}}\sigma_\phi = \frac{2\pi \cdot 57.6\ \mathrm{kHz}}{\pi\ \mathrm{rad}} 17.6\ \mathrm{mrad} = 2\pi \cdot 322\ \mathrm{Hz}.$$

Multiple scans will be performed across the bare cavity resonance $\omega_c$ in order to verify this phase noise conversion model. Each scan will be fit with the dispersion line shape in order to determine the bare cavity resonance frequency $\omega_c$. From the collection of measurements the uncertainty in the measured bare cavity resonance $\sigma_{\omega_c}$ is determined, which will also include the uncertainty from the fitting. The measured uncertainty in $\sigma_{\omega_c}$ will be compared to the uncertainty $\sigma_{\omega_c} = 2\pi \cdot 322$ Hz obtained using this model in order to determine the model validity.

The shift in cavity frequency is determined from two frequency scans $\delta\omega_c = \omega_c' - \omega_c$, with $\omega_c'$ the shifted cavity resonance frequency and $\omega_c$ the bare cavity resonance frequency. Thus the LO phase noise leads to an uncertainty in cavity resonance shift of

$$\sigma_{\delta\omega_c} = \sqrt{2}\sigma_{\omega_c} = 2\pi \cdot 456\ \mathrm{Hz}.$$

When using a detuning of $\Delta_c = 1$ MHz, then the cavity shift per atom $\chi = 2\pi \cdot 43$ Hz, thus the LO phase noise leads to an uncertainty of

$$\sigma_{N_\downarrow} = \sigma_{\delta\omega_c}/\chi = 10.6\ \mathrm{atoms}$$

when determining the atom number $N_\downarrow$.

### 3.2.2 Bare Cavity Resonance Frequency Measurement

The experimental setup is still under construction, at this point in time making a scan of the bare cavity resonance frequency $\omega_c$ is possible within a month. The probe light is coupled to the cavity, but the polarisation still needs to be optimised. Cavity mirror 1 has two optical access points, one along the $\hat{z}$-axis and one along the $\hat{y}$-axis via a small mirror that is angled at 45°. The small angled

mirror introduces a polarisation-dependent power loss, the loss is near zero for s-polarised light, but high for p-polarised light. Therefore the choice was made to have the probe incident on mirror 1 via the optical access along the $\hat{y}$-axis. In this way the full signal is extracted from the optical access along the $\hat{z}$-axis, compared to a loss in signal due to the angled mirror if the access points are switched. The angled mirror also changes the polarisation angle, but this can be compensated with a $\lambda/2$ waveplate. The probe light circulating inside the cavity should be vertically polarised, because a higher finesse $\mathcal{F}$ is achieved compared to using horizontally polarised light.

The angle of the $\lambda/2$ waveplate still needs to be determined in order to couple all light of the probe sideband into the cavity with a vertical polarisation. The transmission of the cavity is observed with a camera and a photodiode by splitting the transmitted light with a 50/50 beamsplitter cube. The coupling to the $\text{TEM}_{00}$ mode with a vertical polarisation will be maximised by tuning a pair of mirrors that couple the probe beam to the optical ring cavity. The polarisation of the beam incident onto the angled mirror will be checked with a polarising beamsplitter cube and/or with a polarisation meter from another laboratory in order to verify that the light transmitted into the cavity is vertically polarised.

Furthermore, the cavity frequency needs to be stabilised to the cavity reference beam (Fig. 2.8), otherwise the detuning $\Delta_c$ is not constant during the frequency scan. A Pound-Drever-Hall (PDH) setup [127, 128, 129] has been constructed to allow for the cavity frequency stabilisation. The polarisation of the cavity reference beam needs to be optimised in order to stabilise to the correct $\text{TEM}_{00}$ mode corresponding to a horizontal polarisation inside the cavity. When the polarisation optimisation of the probe beam will be completed, then it is easy to achieve the correct polarisation of the cavity reference beam as well, because a 90° difference in polarisation angle needs to be realised between the cavity reference beam and probe beam.

Bare cavity resonance scans can be performed after completing the mentioned adjustments to the experimental setup. Multiple scans will be performed across the bare cavity resonance $\omega_c$. Each scan will be fit with the dispersion line shape in order to determine the bare cavity resonance frequency $\omega_c$. The bare resonance scans can be performed at a higher photon number, because there are no atoms inside the cavity. From the collection of measurements the uncertainty in the measured bare cavity resonance $\sigma_{\omega_c}$ is determined, which will also include the uncertainty from the fitting. The measured uncertainty in $\sigma_{\omega_c}$ will be compared to the uncertainty $\sigma_{\omega_c} = 2\pi \cdot 322$ Hz obtained from the local oscillator phase noise model, described in the previous subsection, in order to determine the model validity.

### 3.2.3 Shifted Cavity Resonance Frequency Measurement

A cloud of cold atoms trapped at the focus of the optical ring cavity is necessary in order to induce a shift in cavity resonance frequency. A $^{88}$Sr red magneto-optical trap (MOT) was realised using the broadband MOT method (Subsec. 2.5.4), but at a later point in time the optical layout was changed to implement the sawtooth-wave adiabatic passage (SWAP) MOT scheme. The timings of the SWAP controller need to be optimised for the SWAP MOT sequence (Fig. 2.22). However, the current layout is still able to create a broadband MOT by modulating the double-pass acousto-optic modulator (AOM) that injects the MOT slave (Fig. 2.26) and having the MOT beam AOMs always on. Therefore the setup is able to create a $^{88}$Sr red MOT and to load it into the optical lattice. This has not yet been demonstrated, because currently the cavity frequency stabilisation is being worked on first (as described in the previous subsection), such that the cavity resonance scans can be performed.

The phase-locked loop (PLL) for the stirring laser (Fig. 2.27) still needs to be realised before a red MOT of $^{87}$Sr can be created. But $^{88}$Sr can be used in the meantime for preliminary tests, such as determining the ground state population by measuring the atom-induced shift in cavity resonance frequency.

Assuming $N = 10^4$ atoms are loaded into the lattice from the red MOT and $\Delta_c = 1$ MHz, then $\delta\omega_c = -N\chi = -430$ kHz. The predicted shift in cavity resonance frequency lies within the sweeping range of the homodyne detection system of 5 MHz. Initial frequency sweeps of 1 MHz will be performed in 100 ms, but the sweeping range and sweep time can be adjusted. The sweep

rate of 10 MHz/s is slow enough for the probe sideband to be on resonance for a decent amount of time, such that enough photons that interacted with the atoms can be collected by the homodyne detector.

## 3.3 Quantum Non-Demolition Measurement Sequence

Experiments using $^{87}$Rb that define a spin-1/2 system in the hyperfine ground states $|F = 1, M_F = 0\rangle = |\downarrow\rangle$ and $|F = 2, M_F = 0\rangle = |\uparrow\rangle$ can generate entanglement with a single quantum non-demolition (QND) measurement [83, 84, 57], which measures the shift in cavity resonance frequency based on the population difference $N_\uparrow - N_\downarrow$ between the levels $|\uparrow\rangle$ and $|\downarrow\rangle$. Note that in practice a spin-echo sequence is still used to cancel for example the light shifts induced by the probing. The $|\uparrow\rangle$ and $|\downarrow\rangle$ level have an equal but opposite atom-cavity detuning $\Delta_c$, such that the atoms in the two levels cause opposite shifts of the cavity resonance frequency. For $^{87}$Sr the spin-1/2 system is defined by the optical clock states (Fig. 3.2). The approach for a single QND measurement is not feasible for $^{87}$Sr, because the atom-cavity detuning $\Delta_c$ would be in the optical domain, which means that the cavity induced shift $\delta\omega_c$ would be negligible.

Two consecutive QND measurements are performed instead of a single QND measurement in order to read out the state populations $N_\uparrow$ and $N_\downarrow$ independently (Subsec. 3.3.2). A variation of this sequence is used to compare two squeezed optical clocks [178]. The sequence with two consecutive QND measurements is also used in rubidium [56] and it is possible to use the sequence with any other alkali or alkaline earth atom where a transition can be induced between two (meta)stable states.

### 3.3.1 State Preparation

The atomic state needs to be prepared first in either $|\downarrow\rangle$ or in $|\uparrow\rangle$ before performing the QND measurement sequence (Fig. 3.6), a similar procedure as described in [178] is followed, but for $M_F = -9/2$ instead of $M_F = 9/2$ and the bias field $\vec{B}_{bias}$ will be applied perpendicular to the cavity axis instead of along the cavity axis. A cloud of cold $^{87}$Sr will be trapped at the focus of the cavity in the 813 nm magic wavelength optical lattice described in section 2.6, the atoms are in the ground state $^1S_0|F = 9/2\rangle$, which is degenerate with respect to the magnetic sublevels $M_F$. The atoms are optically pumped into magnetic sublevel $|F = 9/2, M_F = -9/2\rangle$ by a low-intensity free space $\sigma_-$ polarised beam at 689 nm, such that the atoms do not get kicked out of the lattice. The lattice trap depth is ramped down in order to let the hot atoms escape, then it is ramped up again to the operational trap depth. A bias magnetic field of $B_{bias} = 2$ G is applied perpendicular to the cavity axis (the axis on which the focus with the smaller waist is located) in the xz-plane, in order to lift the degeneracy of the magnetic sublevels. The atoms are shelved by applying a $\pi$ pulse on the $^1S_0|F = 9/2, M_F = -9/2\rangle \leftrightarrow {}^3P_0|F' = 9/2, M_{F'} = -9/2\rangle$ transition. The atoms that remain in the ground state due to not being pumped into $M_F = -9/2$ or due to an imperfect $\pi$ pulse are blown away from the lattice by a strong light pulse on the $^1S_0 \leftrightarrow {}^1P_1$ transition. The state preparation procedure achieves a high spin state purity, all atoms inside the lattice are prepared in the $|\uparrow\rangle = {}^3P_0|F' = 9/2, M_{F'} = -9/2\rangle$ state.

### 3.3.2 Spin Echo Sequence

The quantum non-demolition (QND) measurement sequence (Fig. 3.6) consists of two QND measurements that form a spin echo sequence [179, 180]. The first $\pi/2$ pulse puts each atom into a superposition of $|\uparrow\rangle$ and $|\downarrow\rangle$. In the first QND measurement a frequency sweep across the cavity resonance determines the state population $N_\downarrow$. Then a $\pi$ pulse is applied, the state populations are flipped, therefore the state population $N_\uparrow$ is known form the first QND measurement. The second QND measurement determines the new state population $N_\downarrow$. Both state populations are now known without getting information of individual atoms or destroying the quantum state, therefore entanglement is created between the atoms. The quantum state becomes squeezed along the state population axis, which reduces the state population uncertainty, but increases the phase uncertainty. Therefore a final $\pi/2$ pulse is applied with a phase of 90° with respect to the first $\pi/2$

pulse, which rotates the quantum state on the Bloch sphere by 90°. The final state is squeezed in phase and can then be injected into an atom interferometer. The spin echo sequence cancels dephasing errors induced by light shifts during the two QND measurements, which is an advantage over the single QND measurement.

Note that the coupling of the clock pulses depends on the orientation of the polarisation. A $\lambda/2$ wave-plate is used to rotate the polarisation along the $\hat{x}$-axis for maximum coupling. The coupling efficiency is $\cos(2\theta) = \cos(23°) = 92\%$, because the angle of incidence on cavity mirror M1 is $\theta = 11.5°$. The coupling efficiency of a clock pulse can be increased to 100% by adiabatically changing the magnetic field angle to point completely along the $\hat{x}$-axis during the clock pulse. Changing the magnetic field has to be done slowly compared to the Larmor precession. The magnetic field angle then has to be restored to its original position perpendicular to the cavity axis in order to achieve the maximal coupling for the probe light during the QND measurement.

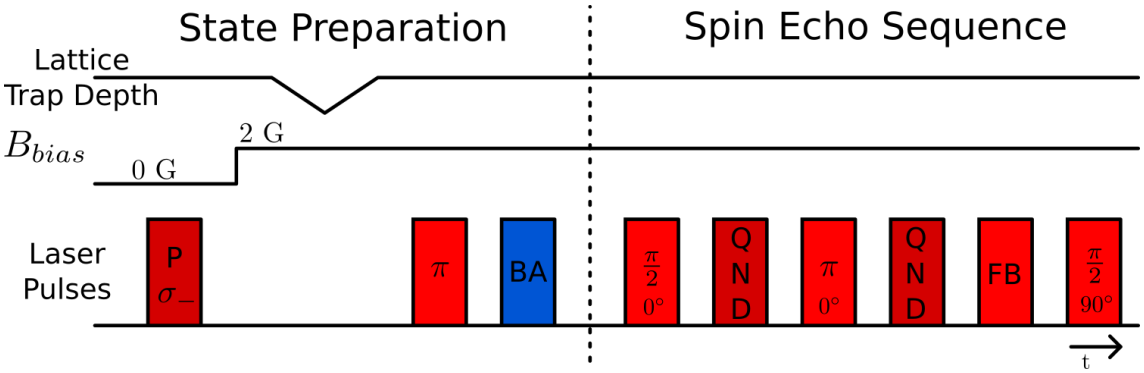


Figure 3.6: The state preparation sequence (Subsec. 3.3.1) prepares the atoms in the $|\uparrow\rangle = {}^3P_0|F' = 9/2, M_{F'} = -9/2\rangle$ state. The spin echo sequence (Subsec. 3.3.2) generates entanglement between the $|\uparrow\rangle$ and $|\downarrow\rangle = {}^1S_0|F = 9/2, M_F = -9/2\rangle$ states. The $\sigma_-$ polarised optical pump (P) and quantum non-demolition (QND) measurements are at $\lambda = 689$ nm (dark red). The blow away (BA) pulse is at $\lambda = 461$ nm (blue). The $\pi$ and $\pi/2$ clock pulses are at $\lambda = 698$ nm (red), the phase of pulses is indicated for the spin echo sequence. An optional feedback (FB) clock pulse at $\lambda = 698$ nm (red) can be applied to rotate the squeezed state onto the equator of the Bloch sphere (Subsec. 3.3.3).

### 3.3.3 Applying Feedback to the Squeezed State

The collective measurement of $J_z$ [Eq. 1.4] projects the squeezed state around the equator of the Bloch sphere, with the probability given by the initial coherent spin state. Thus the created squeezed state can be a bit above or below the equator of the Bloch sphere after the second QND measurement, while ideally the squeezed state is located on the equator. A feedback protocol has been demonstrated in $^{87}$Rb [85] by driving a microwave source at 6.8 GHz in order to drive a feedback transition between the $|\uparrow\rangle$ and $|\downarrow\rangle$ levels, which rotates the squeezed state over the Bloch sphere by a polar angle of [85]

$$\theta_{FB} = \frac{N_\uparrow - N_\downarrow}{NC}, \tag{3.16}$$

with $N = N_\uparrow + N_\downarrow$ the total atom number and $C$ the contrast of the state that remains after the two QND measurements. Since for $^{87}$Sr the optical clock states are used for the spin-1/2 system it is possible to drive the feedback transition optically (Fig. 3.6). The magnitude of the feedback rotation $|\theta_{FB}|$ is determined by the pulse duration $\tau_{FB}$. The sign of the rotation $\theta_{FB}$ is set by applying the feedback pulse in phase with respect to the first $\pi/2$ and $\pi$ pulse or by applying the feedback pulse 180° out of phase. Very accurate feedback pulses can be applied by decreasing the Rabi frequency of the clock transition by using lower intensities. Note that using lower intensities requires longer feedback pulse times $\tau_{FB}$, which might not be ideal depending on the fragility/lifetime of the squeezed state. Also the temperature of the atomic cloud is important, because the efficiency of the clock pulses is severely affected by Doppler broadening.

## 3.4 Estimates of the Attainable Squeezing

Using squeezed states is only useful if they provide a metrological gain over uncorrelated atoms. The cloud of $N$ atoms is again considered as a spin-$N/2$ system. The collective spin can be visualised on the Bloch sphere, see subsection 1.1 for an intuitive example. The collective Bloch vector projection along the $\hat{z}$-axis is $J_z = (N_\uparrow - N_\downarrow)/2$ [Eq.(1.4)]. The idea behind squeezing is to reduce the variance along one direction with respect to a coherent spin state (CSS) in order to create a squeezed spin state (SSS), see subsection 1.2.1 for an example of the population and phase squeezed states. The metric for determining how much squeezing has been created is defined by the metrological gain [52, 82, 86]

$$\xi = \left( \frac{\mathrm{Var}\left(J_{z,CSS}\right)}{\mathrm{Var}\left(J_z\right)} \right)^2 \mathcal{C}^2, \tag{3.17}$$

with $\mathrm{Var}\left(J_{z,CSS}\right) = N/4$ the variance of a CSS, $\mathrm{Var}\left(J_z\right)$ the variance of the created SSS and $\mathcal{C}$ the contrast of the SSS after the squeezing operation. The created SSS is only metrologically useful if $\xi > 0$ dB, therefore it is important that the squeezing operation does not drastically affect the contrast $\mathcal{C}$ of the created SSS, while reducing the variance $\mathrm{Var}\left(J_z\right)$ of the SSS as much as possible.

An extensive model for cavity-aided quantum non-demolition (QND) measurements for atom counting and spin squeezing is described in [86] for $^{87}$Rb. Furthermore, a model is described in [82] for squeezing momentum states in a Bragg interferometer for $^{88}$Sr using the optical ring cavity described in this work. The main points from these models are applied to describe the SSS that will be created between the optical clock levels $^1S_0$ and $^3P_0$ using the setup described in this work.

#### Loss of Contrast due to Free-Space Scattering

The contrast $\mathcal{C}$ is reduced due to photons scattering into free-space. A detailed description of cavity quantum electrodynamics is given in [181], which describes the relations between scattering into free-space and scattering into the cavity mode. The QND measurements are performed in the dispersive regime of the atom-cavity system. The atoms act as a piece of dielectric when interacting with the probe light inside the cavity. Photons are scattered during the atom-light interactions, they are either emitted back into the cavity mode or they are emitted into free-space. A scattered photon can be considered as a relaxation event from one of the excited probe levels $|e\rangle$ and $|e'\rangle$ (Fig. 3.2). If the photon is scattered into free-space, then by observing this photon it is possible to retrace its origin, therefore locating the atom that had a relaxation event. The photon scattered into free-space is an observable that projects the quantum state of the atom that emitted the photon into the ground state $|\downarrow\rangle$, therefore destroying the atomic superposition $(|\uparrow\rangle + |\downarrow\rangle)/2$. The projection of a single atom into state $|\downarrow\rangle$ shortens the Bloch vector of the collective spin-$N/2$ system, which leads to the loss in contrast $\mathcal{C}$. If the scattered photon is emitted back into the cavity mode, then it is indistinguishable from other intracavity photons. Therefore the atom that emitted the photon cannot be located when the photons are observed by the homodyne detector, which means that the superposition of the atomic state is not destroyed.

Two types of scattering occur during the QND measurements: Raman scattering and Rayleigh scattering. After a Rayleigh scattering event the atom returns to the ground state $|\downarrow\rangle$. When a Raman scattering event occurs the atom makes a transition to another level, which is detrimental to the quantum state, because this level lies outside the spin-1/2 system that describes the atomic state superposition between $|\uparrow\rangle$ and $|\downarrow\rangle$. Notice that the Rayleigh scattering event only reduces the contrast when the photon is emitted into free-space, meanwhile the Raman scattering event always reduces the contrast, also when the photon is emitted back into the cavity mode. If the Raman scattered photon is emitted into the cavity mode it will be observed by the homodyne detector, which will result in an unfair representation of the probed state. The contrast of the SSS is given by [86]

$$\mathcal{C} = \mathrm{e}^{-(n_{Ray}+n_{Ram})}, \tag{3.18}$$

with $n_{Ray}$ the number of Rayleigh scattered photons into free-space and $n_{Ram}$ the number of Raman scattered photons. Note that in certain cases Rayleigh scattering into free-space does not

lead to the collapse of the atomic superposition, this requires indistinguishability in the scattering process [182]. In general $n_{Ray}$ and $n_{Ram}$ are kept low, which leads to a high contrast $\mathcal{C} \approx 1$ [82, 86].

There are two probing transitions in the QND measurement: the closed probing transition to state $|e\rangle$ and the open probing transition to state $|e'\rangle$ (Fig. 3.2). Atoms probed on the $|e\rangle$ state always return to $|\downarrow\rangle$, thus photons are only Rayleigh scattered. Probing on the open transition to state $|e'\rangle$ can lead to a Rayleigh scattering event when the atom decays back to $|\downarrow\rangle$, but it can also lead to a Raman scattering event when the atom decays back to ${}^1S_0\,(F = 9/2, M_F = -7/2)$ or ${}^1S_0\,(F = 9/2, M_F = -5/2)$.

An interesting measurement to perform is determining the achievable metrological gain $\xi$ at different ratios of $\Delta_B/\Delta_c$, since Raman scattering is so detrimental to the quantum state. A different ratio of $\Delta_B/\Delta_c$ can be achieved by picking a different value for $\Delta_c$ (Fig. 3.3) or by changing the strength of the bias field $\vec{B}_{bias}$.

### Collective Cooperativity and Quantum Efficiency

The important parameter in the QND measurements is the collective cooperativity $N\eta$ [82, 86], which is the product of the atom number $N$ and the single-atom cooperativity $\eta$ [Eq. (3.5)]. It determines the optimal metrological gain [86]

$$\xi^{\text{opt}} \propto \begin{cases} q_{probe} N\eta & \text{for small atom number } N, \\ \sqrt{q_{probe} N\eta} & \text{for large atom number } N, \end{cases} \tag{3.19}$$

with $q_{probe}$ the quantum efficiency of the detected probe photons. The atom number $N$ for which the scaling changes from $\xi^{\text{opt}} \propto N$ to $\xi^{\text{opt}} \propto \sqrt{N}$ depends on the cavity finesse $\mathcal{F}$, the rate of Raman scattering and the broadening of the cavity linewidth $\kappa$. When operating in the dispersive atom-cavity regime the linewidth broadening is negligible [86]. The Raman scattering can be controlled by changing the ratio of $\Delta_B/\Delta_c$, the optimal detuning to maximise $\xi^{\text{opt}}$ depends only on the atomic properties and the quantum efficiency [86]. It might therefore be possible to prolong the $\xi^{\text{opt}} \propto N$ scaling to large atom numbers $N$ by limiting and potentially eliminating the Raman scattering, but this needs to be verified experimentally.

The homodyne detection system is based on the system realised by the Thompson group, their quantum efficiency $q_{probe} = 0.37\,(5)$ [85, 161]. The main takeaways that raised their quantum efficiency to 37% are using a single-ended cavity, reducing losses on cavity mirrors and using homodyne detection [85]. In this work a homodyne detection system has been developed and implemented (Sec. 2.8), the experimental ring cavity [60] is single-ended and uses high-reflectivity mirrors, therefore a similar quantum efficiency $q_{probe}$ is expected. However, two probing levels are used in this setup, with the level $|e'\rangle$ contributing less compared to the level $|e\rangle$. For $\Delta_c = 2\pi{\cdot}1$ MHz and $B_{bias} = 2$ G a cavity resonance shift per atom of $\chi = 2\pi \cdot 43$ Hz is achieved, where the level $|e\rangle$ contributes 31 Hz and the level $|e'\rangle$ contributes 12 Hz (Sec. 3.2). This means that the quantum efficiency needs to be multiplied by $43/62 = 69\%$ to account for the reduced strength of the $|e'\rangle$ probe level. Making the contribution of the level $|e'\rangle$ negligible by operating with $\Delta_B \gg \Delta_c$ would eliminate the Raman scattering at the cost of multiplying the quantum efficiency by $31/62 = 50\%$. The decrease in quantum efficiency is outweighed by the potential prolonged scaling of $\xi^{\text{opt}} \propto N$ towards higher atom numbers $N$, therefore it is worth to investigate experimentally.

The optical ring cavity has a single-atom cooperativity of $\eta = 0.56$ at the small waist. Assuming the realised homodyne detection system reaches a similar quantum efficiency as the Thompson group, then $q_{probe} = 0.37 \cdot 0.69 = 0.25$ to account for the reduced strength of the $|e'\rangle$ probe level for $\Delta_c = 2\pi{\cdot}1$ MHz and $B_{bias} = 2$ G. Assuming that $N = 10^4$ atoms will be trapped at the focus of the cavity during the QND measurement sequence, then in the worst case $\xi^{\text{opt}} \propto \sqrt{q_{probe} N\eta} = 15.7$ dB and in the best case $\xi^{\text{opt}} \propto q_{probe} N\eta = 31.5$ dB depending on the amount of Raman scattering. This prospect is very promising since the largest amounts of generated squeezing are 20.1(3) dB [84] and 17.7(6) dB [85].

# Chapter 4

# Using Entangled Atoms in Interferometry on the Clock Transition

Interferometers with entangled atoms have been demonstrated using $^{171}$Yb [55] and $^{87}$Rb [56, 57], but either the atom number $N$ or the interrogation time $T$ was limited due to the fragility of the squeezed states. The entangled interferometer technology needs to be developed further in order to become metrologically useful, otherwise there is no reason to switch from using large ensembles of uncorrelated atoms with large interrogation times. Entangling large atomic ensembles is hard, but the most challenging part is creating entanglement that persist for a long period of time, such that future atom interferometers and gravimeters benefit from operating with entangled atoms.

Using entangled strontium atoms in an atom interferometer operating on the optical clock transition combines two concepts that improve the accuracy, single-photon transitions (Sec. 4.1) and squeezed states. Two schemes are discussed to create an entangled interferometer, one scheme transfers entanglement from an internal state superposition to a momentum state superposition (Sec. 4.2) and the other scheme generates entanglement between free-falling atoms in a momentum state superposition (Sec. 4.3). Both schemes can be extended to an entangled gradiometer configuration (Sec. 4.4).

## 4.1 Advantage of Operating on the Clock Transition

An atom interferometer uses a superposition of two (meta)stable momentum states. In general the superposition of the momentum states is created using two-photon transitions like in Raman [65] or Bragg [70] interferometry, but an atom interferometer operating on the optical clock transition [58, 59] makes use of single-photon transitions. The difference between single- and two-photon transitions becomes more apparent when using a long baseline. Two-photon transitions are driven by counter-propagating laser beams that are created by retroreflecting the beams of a mirror. As a result the reflected beam is delayed compared to the other beam when making the two-photon transition. This delay affects the phase that is imprinted onto the atoms during the atom-light interaction [183, 184], because the phase noise of the laser accumulates during the delayed round trip. A longer baseline leads to a longer delay and therefore more accumulation of phase noise that gets imprinted onto the atoms. On the contrary single-photon transitions have the laser phase set at the moment the light is emitted, therefore phase noise can be precisely determined. The phase noise is cancelled in a gradiometer operating with single-photon transitions, this allows for long baseline experiments [185, 140]. Single-photon transitions also open up the possibility of transferring a large momentum by employing multiple pulses [185, 140], like in multiphoton Bragg diffraction [186, 70].

The laser phase noise only cancels in a gradiometer scheme, not in the regular atom interferometer configuration. However, the most important point is that only small amounts of phase noise are imprinted onto the atoms when operating on the clock transition. This is due to the narrow-linewidth clock laser having a low phase noise (Subsec. 2.4.2), which is necessary to drive the ultra-narrow optical clock transition.

## 4.2 Transferring Entanglement to a Momentum State Superposition

The quantum non-demolition (QND) measurement sequence described in section 3.3 generates entanglement between atoms that are trapped at the focus of the optical ring cavity, therefore they do not have momentum. The entanglement needs to be transferred from an internal state superposition to a momentum state superposition. A scheme consisting of microwave and optical pulses has been demonstrated to transfer entanglement from internal states to momentum states in a similar setup using $^{87}$Rb creating an entangled interferometer [57]. In this work the clock states of $^{87}$Sr will be used for the interferometer, therefore only optical pulses are available.

The idea of the scheme is to transfer the entanglement from an internal state superposition to a momentum state superposition, therefore the first interferometer pulse has to be a $\pi$ pulse in order to transfer the complete state population from an internal state to a momentum state. Opening the interferometer with a $\pi$ pulse leads to the choice of using a double-diffraction scheme consisting of four $\pi$ pulses in order to create an entangled atom interferometer (Fig. 4.1). The double-diffraction configuration has been studied for inertial sensing application [187] where the relation between the interferometer phase $\phi$ and the measured inertial field has been determined. The first two clock pulses are applied from below, then the second two clock pulses have to be applied from above in order to close the interferometer. The second and the fourth pulse need to incorporate two frequency tones to account for the Doppler effect, since the wave packets in the upper and lower arm are moving with different velocities. The acousto-optic modulator that generates the clock pulses can be driven at two radio frequency tones, like it was done in [59]. When the double-diffraction interferometer closes the atoms are retrapped in an optical lattice. A $\pi/2$ pulse is applied with a 90° phase compared to the previous pulses in order to rotate the quantum state to become population squeezed, such that the gained interferometer phase $\phi$ is read out with increased sensitivity.

The state rotating operation with the final $\pi/2$ pulse cannot be performed with free-falling atoms, because the transfer of momentum to half of the wave packets would lead to four different quantum states $|^1S_0, p = 0\rangle$, $|^1S_0, p = \hbar k\rangle$, $|^3P_0, p = 0\rangle$ and $|^3P_0, p = \hbar k\rangle$. The atoms are retrapped by an optical lattice after closing the interferometer, such that the lattice absorbs the transferred momentum during the final $\pi/2$ pulse. This means that at the end of the interferometer the entanglement is transferred back to the internal state superposition. In a microgravity environment the interferometer is closed at the starting point in space, therefore the wave packets can be trapped using the magic wavelength lattice that is coupled to the optical ring cavity. However, this is not an option for an experiment performed on the surface of the Earth. Therefore it is necessary to generate an optical lattice along the gravitational direction. Assuming an interrogation time of $T = 100$ ms the atoms will fall a distance of $2gT^2 = 20$ cm with a final velocity of $v_{fall} = 2gT = 2$ m/s, which is equivalent to a temperature of $mv_{fall}^2/(2k_B) = 20$ mK. A moving optical lattice is recommended in order to efficiently catch/retrap the atoms in order to relax the intensity requirements of the lattice. A lattice moving at a similar velocity to the falling atoms is created by applying a frequency difference of $\Delta f = (2v_{fall})/\lambda_{lattice} = 4.8$ MHz [156] between the counter-propagating lattice beams for $\lambda_{lattice} = 813$ nm. Such a moving optical lattice can be realised by a laser system with acousto-optic modulators in a double-pass configuration, similar to the system realised in this work (Subsec. 2.6.1). Since the retrapping lattice is created in free-space it does not benefit from the optical amplification of a cavity. Furthermore, the whole atomic cloud needs to be trapped, therefore a waist of $w_0 = 5$ mm is desired for the moving lattice. This means that high laser powers are required, therefore a Ti:Sapphire laser is recommended for the generation of the moving lattice system.

The interferometer phase is read out by determining the state populations $N_\downarrow$ and $N_\uparrow$ of the states $|^1S_0\rangle$ and $|^3P_0\rangle$ respectively. With the atoms trapped in the moving lattice along the gravitational axis it is possible transport them to a location for absorption imaging or fluorescence detection. The strong $^1S_0 \leftrightarrow ^1P_1$ transition can be used for the imaging/detection. First the state population $N_\downarrow$ is measured, then a $\pi$ pulse is applied with the clock laser to invert the state populations, which is followed by the measurement of $N_\uparrow$.

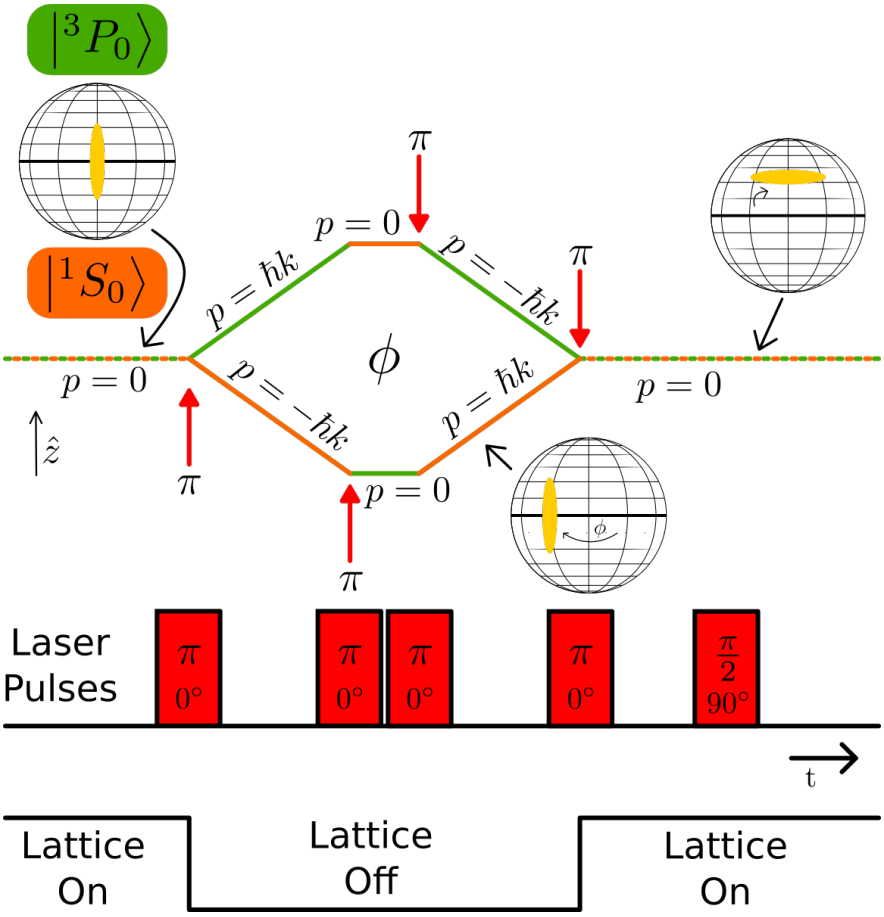


Figure 4.1: Entangled atom interferometer in a double-diffraction scheme, where the entanglement is transferred from an internal state superposition to a momentum state superposition. The trajectories of the wave packets are visualised in the absence of gravity, the laser pulse sequence is shown below the trajectories at the accompanying moment in time. The atoms are prepared in a phase squeezed superposition of internal states as described in section 3.3. The quantum state of the spin-N/2 system is depicted on the Bloch sphere at various points during the sequence, the yellow shape indicates the uncertainty distribution of the Bloch vector. The atom interferometer gains a phase $\phi$ with an increased sensitivity due to the phase squeezed state. The first two clock pulses are applied from below, the second two clock pulses are applied form above in order to close the interferometer. The atoms are retrapped in an optical lattice at the end of the double-diffraction interferometer sequence, because a population squeezed state is necessary for readout. The final clock pulse rotates the quantum state to become population squeezed in order to have an increased sensitivity during state readout.

Since the atoms are trapped inside the moving lattice along the gravitational axis it is also possible to transport them back to the focus of the optical ring cavity. The quantum non-demolition (QND) measurement sequence described in section 3.3 can also be used to read out the interferometer phase, since both state populations $N_\uparrow$ and $N_\downarrow$ are measured. Note that the additional transport time requires relatively long coherence times for the entangled states. However, in the case of

microgravity the atoms can be retrapped immediately in the lattice coupled to the optical ring cavity as stated before. Therefore it is possible to readout the interferometer phase using the optical ring cavity after applying the final $\pi/2$ pulse of the entangled interferometer sequence.

Note that the double-diffraction configuration does not create a spin-echo sequence like the Mach-Zehnder configuration. Implementing a spin-echo improves the life time of phase squeezed states [80]. For this reason microwave pulses that created a spin-echo sequence were applied in the scheme using $^{87}$Rb [57]. Since the optical clock states of $^{87}$Sr are used in the scheme described in figure 4.1 it is not possible to implement a spin-echo sequence with microwave pulses. However, the lifetime of the phase squeezed states needs to be measured experimentally before excluding this scheme.

## 4.3 Generating Entanglement with Free-Falling Atoms

It is possible to directly generate entanglement between free-falling atoms in a momentum states superposition, instead of transferring entanglement to a momentum state superposition. A scheme has been demonstrated using free-falling $^{87}$Rb atoms in order to create an entangled atom interferometer [56]. This scheme can be adapted for $^{87}$Sr, where the optical clock transition enables the creation of a superposition between the momentum states $|^1S_0, p = 0\rangle$ and $|^3P_0, p = \hbar k\rangle$.

The idea of the scheme is to generate entanglement between momentum states by performing quantum non-demolition (QND) measurements inside a mini atom interferometer configuration. The entangled momentum state superposition is then injected into an atom interferometer (Fig. 4.2). The state preparation sequence is the same as described in subsection 3.3.1, atoms from the red magneto-optical trap are loaded into the magic wavelength lattice, then they are prepared in the magnetic sublevel $^3P_0|F' = 9/2, M_{F'} = -9/2\rangle$. The scheme with free-falling atoms starts with turning off the lattice, such that the atoms are subjected to gravity. A momentum state superposition is created between $|\downarrow\rangle = |^1S_0\,(F = 9/2, M_F = -9/2)\,, p = 0\rangle$ and $|\uparrow\rangle = |^3P_0\,(F' = 9/2, M_{F'} = -9/2)\,, p = \hbar k\rangle$ by the first $\pi/2$ pulse. The first QND measurement determines the ground state population $N_\downarrow$. The $\pi$ pulse redirects the trajectories of the wave packets while switching the momentum state populations. The second QND measurement determines the new ground state population $N_\downarrow$. The knowledge about the state populations $N_\downarrow$ and $N_\uparrow$ generates a population squeezed state. A $\pi/2$ pulse with a 90° phase compared to the previous pulses is applied in order to rotate the squeezed state on the Bloch sphere to become squeezed in phase. This pulse completes the mini interferometer, which acts as a spin-echo sequence [179, 180] with free-falling atoms. This $\pi/2$ pulse also acts as the first pulse of the entangled atom interferometer. The entangled interferometer has an increased sensitivity to phase due to operating with the phase squeezed state, it gains a phase $\phi$ during the interferometer sequence. The final $\pi/2$ pulse in the interferometer sequence is applied with a phase of 90° compared to the previous pulse in order to rotate the squeezed state on the Bloch sphere to become population squeezed for an increased sensitivity during state readout.

The pulse timing of the scheme is important in order to realise homogeneous coupling between the atoms and the cavity during the QND measurements, because the cloud expands due to temperature and falls due to gravity. It is possible to close the mini interferometer at the same height as the starting point, if the interrogation time of the mini interferometer $T_{mini} = v_{rec}/\left(2g\right) = 336$ $\mu$s. Then also the initial velocity is zero when injecting the squeezed state into the entangled interferometer. This means that a single QND measurement should be performed within $T_{mini} = 336$ $\mu$s, the cloud falls only $\left(gT_{mini}^2\right)/2 = 0.55$ $\mu$m during the QND measurement. Therefore the coupling to the cavity remains homogeneous with respect to the vertical displacement, since the geometric mean of the small cavity waist $w_0 = 30.7$ $\mu$m [60]. The demonstrated atom interferometer [56] performed a QND measurement sweep typically in 150 $\mu$s, the homodyne detection system realised in this work is similar to the one used in [56], therefore the QND measurement can be performed within $T_{mini} = 336$ $\mu$s. The cloud size and expansion due to temperature are more important for the homogeneous coupling, because if the cloud size is larger than the geometric mean of the small cavity waist $w_0 = 30.7$ $\mu$m [60] the coupling is inhomogeneous. The initial cloud size depends on the final temperature of the red magneto-optical trap (MOT), on the number of atoms $N$ inside the cloud and on the optical lattice potential. The initial cloud size, temperature and atom number

will be determined experimentally when the red MOT is completed and is able to load the magic wavelength lattice.

At the end of the interferometer the states can be read out simultaneously by using the scheme from [59] consisting of a push pulse on $|^1S_0, \hbar k\rangle$ to separate the trajectories and a clock pulse to bring the $|^3P_0, \hbar k\rangle$ state to $^1S_0$. Both trajectories are spatially separated and can be detected on the strong $^1S_0 \leftrightarrow ^1P_1$ transition using fluorescence detection.

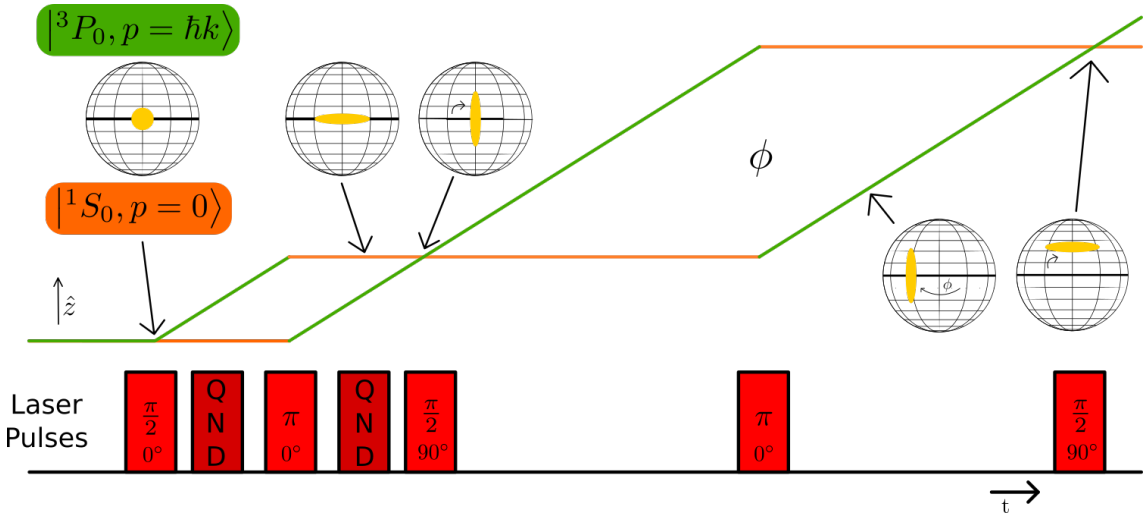


Figure 4.2: Entangled atom interferometer in a Mach-Zehnder scheme, where the entanglement is created between momentum states of free-falling atoms. The trajectories of the wave packets are visualised in the absence of gravity, the laser pulse sequence is shown below the trajectories at the accompanying moment in time. The atoms are prepared in magnetic sublevel $^3P_0|F' = 9/2, M_{F'} = -9/2\rangle$. The mini interferometer acts as a spin-echo sequence for the quantum non-demolition (QND) measurements that generate the entanglement. The quantum state of the spin-$N/2$ system is depicted on the Bloch sphere at various points during the sequence, the yellow shape indicates the uncertainty distribution of the Bloch vector. The atom interferometer operates with a phase squeezed state, resulting in an increased sensitivity towards the gained phase $\phi$. The final interferometer pulse rotates the quantum state to become population squeezed in order to have an increased sensitivity during state readout.

## 4.4 Entangled Gradiometer

A gradiometer performs measurements in a differential configuration, this allows for the cancellation of common-mode effects. Several long baseline instruments are being developed around the world: Matter wave-laser based Interferometer Gravitation Antenna (MIGA) [188], Matter wave Atomic Gradiometer Interferometric Sensor (MAGIS) [189], Atom Interferometer Observatory and Network (AION) [190] and Zhaoshan long baseline Atom Interferometer Gravitation Antenna (ZAIGA) [191]. Two of these instruments (MIGA and MAGIS) make use of interferometry on the clock transition in strontium like the instrument described in this work. A gradiometer gains sensitivity using a long baseline, another way to increase its sensitivity is using entangled atoms.

The gradiometer needs two displaced clouds of atoms at the start of the measurement. In a small baseline experiment it is possible to generate two atomic clouds from a single magneto-optical trap (MOT) using a double MOT launch technique [192]. For long baseline experiments it is more convenient to have two atomic sources, such that two separate MOTs are created. The gradiometer requires two cavities to perform the quantum non-demolition (QND) measurements in order to create entanglement atoms. Two atomic clouds will be prepared and trapped at the focal point of their respective cavity during the gradiometer state preparation sequence. The baseline of the

gradiometer is determined by the distance between the focal points of the two cavities, therefore the baseline should be chosen carefully, otherwise a redesign of the vacuum system is required.

The two proposed entangled interferometer schemes (Sec. 4.2 and sec. 4.3) can both be extended to a gradiometer configuration. The entanglement transfer scheme described in section 4.2 offers more control and maximum atom-cavity coupling, since the atoms are trapped inside an optical lattice during the QND measurement sequence. However, retrapping the atoms at the end of the sequence adds a layer of complexity. The entanglement generation scheme for free-falling atoms described in section 4.3 is less complex, but requires the ability to perform fast QND measurements. Both entangled atom interferometer schemes should be tested experimentally before deciding on the scheme to use in a first-generation entangled gradiometer.

# Chapter 5

# Roadmap towards a Future Space Mission

My PhD is co-funded by the European Space Agency (ESA), which I am very grateful for. In particular I would like to thank Oliver Carraz and Eamonn Murphy for supervising me during my five month stay at the European Space Research and Technology Center (ESTEC) in the first year of my PhD. I learned a great deal about atom interferometry in microgravity and about space missions in general. Over the last decades multiple atomic space missions have been proposed: Atomic Clock Ensemble in Space (ACES) [193], Mass Observation with Cold Atom Sensors in Space (MOCASS) [194], Space Atomic Gravity Explorer (SAGE) [195], Atomic Experiment for Dark Matter and Gravity Exploration in space (AEDGE) [196] and Space Time Explorer and QUantum Equivalence principle Space Test (STE-QUEST) [197]. These space missions make use of atomic clocks and atom interferometers to measure the Earth gravity field, test the equivalence principle, observe gravitational waves, search for dark matter and many other scientific goals that push the boundaries of our understanding of the Universe.

Atom interferometry is considered by ESA for a future gravity mission (Sec. 5.1). A roadmap towards a future gravity mission in space using an entangled atom interferometer operating on the clock transition is presented. A terrestrial mission (Sec. 5.2) should be performed first, but a preliminary design for a future space instrument is presented in section 5.3.

## 5.1 Next-Generation Gravity Mission

The microgravity environment is especially beneficial to atom interferometry, because it allows for long interrogation times on the order of multiple seconds, which will provide a better performance compared to any experiment performed on the ground [45]. Atom interferometry in space needs to outperform previous space gravity missions, the Gravity Recovery And Climate Experiment (GRACE) [42] and the Gravity field and steady-state Ocean Current Explorer (GOCE) [43], in order to be a viable candidate for a future gravity mission. Currently the ESA next-generation gravity mission (NGGM) [198] is based on laser interferometry between two satellites for a mission in the near future. However, many studies of gravity gradiometer mission concepts are being performed, a gravity mission based on atom interferometry offers an interesting perspective for a NGGM in the far future [198].

The apparatus described in this work is not space ready, the technology readiness level (TRL) needs to be developed further before a space mission based on an entangled atom interferometer operating on the clock transition can be considered. I recommend a roadmap consisting of a two-stage approach towards space implementation. The TRL of the quantum gravity sensor needs to be developed further, therefore my advice is to build a second-generation device that is tested in a terrestrial setup. In this way the apparatus is tested in the field with characteristics that resemble the challenges of a space mission. The design of the second-generation device can be improved

based on the difficulties that I faced in the implementation of the first-generation device during my PhD. The second stage of the roadmap would be dedicated to the realisation of a space mission. A preliminary design for a future space mission instrument is discussed in section 5.3.

## 5.2 Terrestrial Mission with a Second-Generation Device

For a transportable device it is important to realise miniaturised laser systems and a compact design of the vacuum chamber. Recently two transportable strontium optical lattice clocks have been demonstrated outside the laboratory with an uncertainty level of $10^{-18}$ [22], where a single clock including all electronics occupies 0.92 $m^3$ and weighs 370 kg. The laser architecture and vacuum chamber design of the transportable clocks provides a good starting point for developing a compact physics package for a second-generation device outside of the laboratory environment. The vacuum system design has to be adapted to allow for a gradiometer separation of at least 30 cm for a meaningful demonstration, but aiming for a larger separation of 50 cm [45] would be even better.

In the current setup the magneto-optical trap (MOT) is formed inside the cavity plane on the interferometer axis. The cycle time of the experiments can be improved in a second-generation device by moving the cavity to a separate chamber. In this way a new cloud can be prepared in the MOT chamber, while in the meantime the entangled gradiometer is performed in the cavity chamber. The MOT cloud would need to be transported towards the cavity chamber, this can be performed with a moving optical lattice [155, 156, 157]. The possibility of using a zoom lens [199] needs to be investigated. The concept of the zoom lens is to change the effective focal point while keeping the image plane position constant. An 89% transfer efficiency has been achieved while transporting $\sim 1.5 \cdot 10^6$ $^{174}$Yb atoms in an optical dipole trap over a distance of 600 mm, with a typical transport time of 3.6 s.

### Cavity Considerations

The most critical part of the entangled gradiometer are the two high-finesse cavities that are needed for the quantum non-demolition (QND) measurements.

- The two cavities could be connected in the form of a network [57, 200] sharing a common QND measurement. This would lead to even higher degrees of entanglement, since the upper and lower cloud would be entangled. But realistically this is a bit outside the scope of this work, there are still many challenges to face in order to realise an entangled interferometer with a large atom number $N$ and a long interrogation time $T$.
- Having a ring cavity configuration is crucial, because it leads to homogeneous atom-light interactions during the QND measurements, because the light passes the atoms only one-way. Probing atoms located inside a Fabry-Pérot cavity leads to inhomogeneous atom-light interactions, because the probe light forms an optical lattice inside the Fabry-Pérot cavity leading to bright and dark nodes. Every demonstrated entangled interferometer/clock [55, 56, 57, 178] so far uses a Fabry-Pérot cavity, because it is simpler to work with compared to a ring cavity. The Fabry-Pérot cavity would allow probing with $\sigma_-$ polarised light in order to eliminate Raman scattering, but this does not outweigh the inhomogeneous coupling to the atoms. Therefore it is recommended to stick to the cavity geometry according to the design described in [60], which is used in this work.
- The ring cavity used in this work has a high-finesse of $\mathcal{F} = 24(2) \cdot 10^3$ [120], which is the critical parameter for realising high degrees of squeezing through a high single-atom cooperativity $\eta$ [Eq. 3.5]. The cooperativity could be raised by creating a very small cavity waist, but this would mean that only a few amount of atoms can interact with the light to become entangled. The cavity waist needs to be large enough in order to interact with the full atomic cloud. The goal is to operate the gradiometer with a large ensemble of entangled atoms. Lowering the temperature of the prepared sample by additional cooling leads to smaller cloud sizes, such that a larger atom number can be used in order to create a larger ensemble of entangled atoms.

- The only meaningful improvement to the cavity finesse can be reached by using mirrors with an even higher reflectivity compared to the first version. It is recommended to stick to the cavity geometry according to the design described in [60]. The cavity has two focal points, one with a small waist $w_0 = 30.7$ $\mu$m and one with a large waist $w_0 = 164$ $\mu$m. The larger waist can be used when working with large clouds containing a large atom number $N$, if the atom-cavity coupling would be inhomogeneous when using the small waist.
- The current experimental setup suffers from vibrations, which make it difficult to stabilise the frequency of the optical ring cavity. An improved vibration isolation system for the optical ring cavity would be very useful for improving the cavity frequency stability.
- The final point to consider concerning the cavity is the orientation. The coupling efficiency of the clock laser pulses is 92% due to the angle of the required bias field $\vec{B}_{bias}$ compared to the cavity axis. The angle of the magnetic field can be adiabatically sweeped between clock pulses and QND measurements to improve the clock pulse coupling efficiency. The magnetic field needs to be in the xz-plane, while the polarisation of the probe light inside the cavity is along the $\hat{y}$-axis. The polarisation of the clock pulses is in the xy-plane, therefore the coupling efficiency to the atomic dipole moment is optimal when the polarisation of the clock pulses is along the $\hat{x}$-axis. To achieve the maximum coupling efficiency the bias field $\vec{B}_{bias}$ needs to point along the $\hat{x}$-axis as well. The cavity axis on which the focus is located needs to be along the magnetic field direction or perpendicular to the magnetic field direction. Having the cavity axis perpendicular to the field would block the clock pulses, therefore it is recommended to rotate the cavity such that the cavity axis points along the $\hat{x}$-axis as well. Note that the rotated configuration the horizontal velocity needs to be along the $\hat{y}$-axis, while in the first-generation setup the horizontal velocity can be along the $\hat{x}$ or $\hat{y}$-axis.

## 5.3 Entangled Gradiometer Space Mission Concept

A gradiometer space mission concept for $^{87}$Rb has been described in [45]. Squeezing can be implemented to this space gradiometer concept by using one of the entangled atom interferometer schemes (entangling free-falling atoms [56] or entanglement transfer [57]) that were first demonstrated using $^{87}$Rb. Since $^{87}$Sr is used in this work the gradiometer space mission concept is adapted for an entangled gradiometer operating on the clock transition in strontium.

### 5.3.1 Quantum Non-Demolition Measurements in Space

The entanglement transfer scheme (Sec. 4.2) and the entanglement generation scheme using free-falling atoms (Sec. 4.3) both benefit from microgravity, because it allows for longer interrogation times. Furthermore, the entanglement transfer scheme can use the lattice coupled to the cavity for retrapping of the atoms when the interferometer closes. There is no need for an additional lattice along the gravitational axis like for an experiment performed on the surface of the Earth.

One important point to consider is the repetition rate of the instrument. A transverse velocity is applied in order to have multiple clouds inside the instrument at once, since an interrogation time of $T = 5$ s is targeted [45]. The transverse velocity complicates the entanglement transfer scheme, because entanglement is created between the atoms when they are trapped at the focus of the cavity. Therefore the transverse velocity has to be added after creating the entangled state. The transverse velocity needs to be applied via $\pi$ pulses on the clock transition, such that the entanglement is preserved. A complication arises when it comes to reading out the interferometer phase, because the atoms need to be retrapped in order to rotate the quantum state to become population squeezed. The atom interferometer no longer closes at the focal point of the cavity due to the applied transverse velocity, thus the complication of realising additional trapping arises like for experiments on the surface of the Earth. This makes the entanglement transfer scheme less suited for a space mission when a transverse velocity is involved.

The scheme that creates entanglement between free-falling atoms can be adapted to work with a transverse velocity. Since the atoms are prepared in $^3P_0\,(F' = 9/2, M_{F'} = -9/2)$ by the state

preparation sequence (Subsec. 3.3.1) it is beneficial to generate the transverse velocity using the clock transition. Otherwise applying a $\pi$ pulse brings the atoms to the ${}^1S_0\,(F' = 9/2, M_{F'} = -9/2)$ level, then Bragg pulses can be used to give the atoms a transverse velocity. Two cavities per atom interferometer are needed due to the transverse velocity, thus a total of four cavities are needed for the entangled gradiometer configuration in space (Fig. 5.1). The atoms pass the small waist of $w_0 = 30$ $\mu$m in a time on the order of a millisecond assuming a transverse velocity of four photon recoils. The QND measurement therefore needs to be performed quickly and at a precise moment in time such that the wave packets interact homogeneously with the cavity and to achieve a strong atom-cavity coupling. The setup described in [56] was able to perform a scan in a typical time of 150 $\mu$s, thus a strong and homogeneous atom-cavity coupling can be achieved with proper timing of the scan. Another possibility is to have the probe at a fixed detuning from bare cavity resonance and to observe the effect on the signal when the wave packets pass the cavity focus. An optimum detuning can be selected based on the average atom number $N$ per cloud. (Note that for ${}^{87}$Rb a scheme can be created with a single cavity per interferometer, the probe on resonance with the cavity and detuned precisely halfway the atomic transitions [83, 166].)

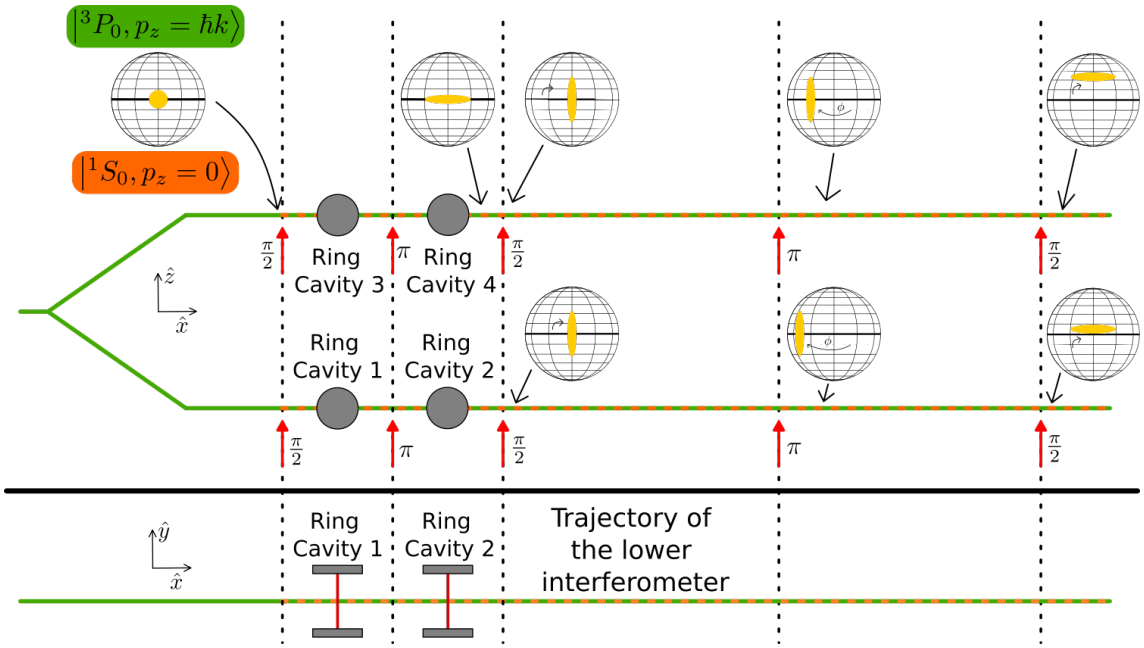


Figure 5.1: Entangled gradiometer in space concept (not drawn to scale). The dimensions of the entangled gradiometer in space concept depend on the satellite size, the chosen transverse velocity and the chosen gradiometer baseline. The atoms are moving along the $\hat{x}$-axis due to their transverse velocity. The quantum state of the spin-$N/2$ system is depicted on the Bloch sphere at various points during the sequence, the yellow shape indicates the uncertainty distribution of the Bloch vector. A cold atomic cloud is divided into two, one cloud is moved towards the upper interferometer axis, the other cloud is moved towards the lower interferometer axis. The free-falling atoms are entangled by the quantum non-demolition (QND) measurement sequence described in section 4.3. Note that the separation between the wave packets is small relative to the gradiometer baseline and therefore not visualised in this figure. (The green-orange dotted lines represent the locations where the wave packets are in a momentum state superposition.) Two cavities are used per interferometer axis due to the transverse velocity. The atoms cross the waist of the ring cavities sequentially. The interferometers gain phase with an increased sensitivity due to the phase squeezed state. The gradiometer phase is determined by measuring the phase difference between the upper and lower interferometer.

### 5.3.2 On-Board Readout using a Dual Species Gradiometer

A stationary gradiometer reads out its phase by fitting a Lissajous curve to the data that is obtained over multiple measurements by plotting the interferometry signal of the upper interferometer versus the lower interferometer [5]. A gradiometer aboard a satellite orbiting the Earth can not use this method, the phase needs to be extracted from a single interferometry measurement. A concept of a dual species atom interferometer configuration has been proposed for on-board applications [201]. The dual species configuration operates two interferometers simultaneously with a difference of 90° in phase quadrature, such that at least one interferometer is operating in the linear regime. Still the fringe index of the interference pattern needs to be determined, which can be achieved by using a priori data from the GOCE mission, an on-board classical accelerometer or by using a third species in an interferometer with a shorter interrogation time [201]. The concept proposes the combination $^{85}$Rb and $^{87}$Rb, with $^{133}$Cs for the optional third species. Other alkali atoms could be used as well, like $^{41}$K.

For a gradiometer operating on the clock transition the choice of atomic species is limited to alkaline earth(-like) atoms. An interferometer based on the strontium (Sr) optical clock transition has been demonstrated by our group [58, 59]. In another laboratory in Florence researchers are working on a dual species atom interferometer that operates on the clock transition in strontium and cadmium (Cd) [140]. Another good candidate is ytterbium (Yb), which is used extensively in optical lattice clocks [170, 202] and has also been demonstrated in an atom interferometer configuration [78, 55, 203]. Considering the TRL of the necessary laser systems a combination of $^{87}$Sr and $^{171}$Yb is recommended. But a combination of $^{87}$Sr and $^{111}$Cd should not be excluded, since the transition frequencies of cadmium are roughly twice the transition frequencies of strontium, this might lead to a design of a compact laser package when choosing to combine strontium and cadmium.

#### Quantum Non-Demolition Measurements when Working with Two Atomic Species

Entanglement needs to be created for both atomic species in order to create a dual species entangled gradiometer. It is important that the entanglement creation process for one species does not influence the quantum state of the other species. Entanglement generation through quantum non-demolition (QND) measurements by cavity-aided probing satisfies this requirement. The probing of one species is far off-resonant for the other species, due to the difference in transition frequencies. Each atomic species needs two cavities per atom interferometer due to the transverse velocity, thus a total of eight cavities are needed to create entanglement for a dual species gradiometer (Fig. 5.2). The cavities for ytterbium (Yb)/cadmium (Cd) can use the same geometry as the cavities for strontium (Sr) [60], but note that different mirror coatings are required based on the ytterbium/cadmium transition frequencies.

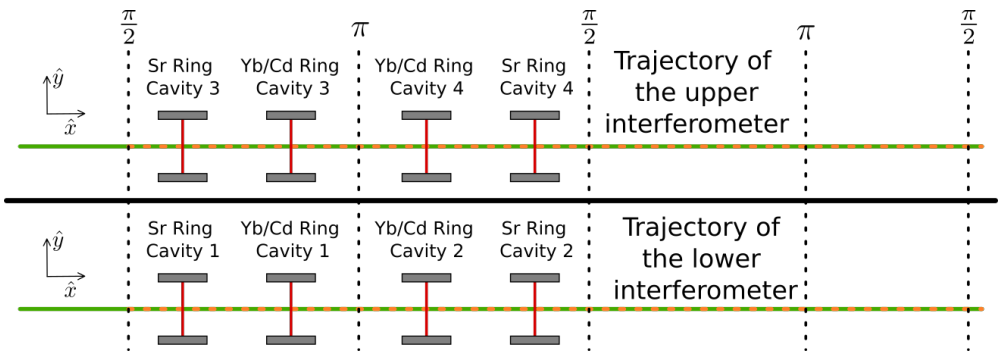


Figure 5.2: Cavity placement for an entangled gradiometer in space concept using two atomic species (not drawn to scale). The dimensions of the entangled gradiometer in space concept depend on the satellite size, the chosen transverse velocity and the chosen gradiometer baseline. The overall layout is similar to the one shown in figure 5.1, but with four additional cavities. The cavity order for the different isotopes (Sr and Yb/Cd) is chosen to fit the spin-echo sequence.

# Chapter 6

# Conclusions and Outlook

In this thesis an experimental setup has been described, which aims towards improving the sensitivity of an atom interferometer operating on the clock transition in strontium through the use of entangled atoms. A scheme for creating entanglement between strontium atoms through cavity-aided probing has been designed. The implementation of injecting entangled atoms into an interferometer has been studied. Finally a roadmap was laid out towards a future gravity mission in space using an entangled atom interferometer operating on the clock transition.

The majority of the work was spent on constructing various parts of the experimental setup described in chapter 2. An optical ring cavity with a finesse of $\mathcal{F} = 24\,(2) \cdot 10^3$ has been constructed for performing quantum non-demolition (QND) measurements by cavity-aided probing. A vacuum system has been constructed for the cooling and trapping of strontium. The optical ring cavity was mounted vertically inside the vacuum science chamber to allow for interferometry along the gravitational axis. A home-built clock laser has been realised, with an estimated linewidth on the order of 1 Hz. Interferometry pulses on the clock transition in $^{87}$Sr can be driven at a Rabi frequency of $\Omega = 2\pi \cdot 5$ kHz with a beam waist of $w_0 = 0.5$ mm. A magneto optical trap (MOT) operating on the blue $^1S_0 \leftrightarrow {}^1P_1$ transition has been created. A cloud of $1.4 \cdot 10^7$ $^{88}$Sr atoms was cooled down to a temperature of $9.7 \pm 1.3$ mK with a MOT loading time of 106.6 ms. The second MOT stage operating on the red $^1S_0 \leftrightarrow {}^3P_1$ transition was realised using the broadband MOT method to capture the atoms from the blue MOT, about $5 \cdot 10^6$ $^{88}$Sr atoms were cooled down to a temperature of about 1 $\mu$K. The red MOT setup has been modified for the implementation of a cooling scheme based on sawtooth-wave adiabatic passage (SWAP) in order to increase the transfer efficiency from the blue to the red MOT. A home-built laser has been constructed at $\lambda = 813$ nm, which is the magic wavelength for the strontium optical clock states. A lattice laser system was developed (twice) and coupled to the optical ring cavity, such that an optical lattice is formed inside the cavity plane. With the lattice beams each coupling 5 mW into the cavity a lattice potential is created with a depth of 465 $\mu$K at the small focus of the cavity and a depth of 16.2 $\mu$K at the large focus. The optical lattice is deep enough to be loaded with cold atoms from the red MOT. A balanced homodyne detection system inspired by the Thompson group has been created. A phase-locked loop was created in order to stabilise the phase difference between the probe beam and local oscillator (LO). The realised homodyne detector is photon shot noise (PSN) limited for local oscillator powers $P_{LO} < 70$ $\mu$W. An intensity stabilising feedback loop was built for the LO in order to compensate the observed increase in noise when operating at powers $P_{LO} > 70$ $\mu$W. Unfortunately the intensity stabilising feedback loop had no effect on the increase in noise at higher LO powers, therefore the power limit for PSN limited detection could not be raised. An imbalance due to imperfect transmission and reflection coefficients of the optical elements was observed for the probe and LO beams. An improved optical layout has been proposed that allows for optical balancing of the probe and LO beams individually, while minimising signal loss. Further system improvements are being developed. The realisation of an injection-locked titanium:sapphire laser will be explored in order to increase the laser power of the clock laser system. Clock pulses that have a large beam waist with respect to the atomic cloud size will increase the visibility of the

interferometer. The designed fiber phase noise cancellation scheme is to be implemented, such that the narrow linewidth of the clock laser is maintained when transporting the light via an optical fiber to the vacuum chamber. The SWAP pulse timings need to be optimised in order to realise a red MOT using the SWAP technique. An additional stirring laser is necessary for the creation of a $^{87}$Sr red MOT, the designed phase-locked loop still needs to be realised.

Chapter 3 described the atom-cavity interactions for entanglement generation in QND measurements. Two magnetic sublevels of the optical clock states in strontium are considered as a spin-1/2 system ($|\uparrow\rangle$ and $|\downarrow\rangle$). A concept is presented of probing the ground state population $N_\downarrow$ of strontium atoms located at the focus of an optical ring cavity. The concept operates in the dispersive regime of the atom-cavity system. A QND measurement sequence for entangling strontium atoms was proposed, which consisted of probing the ground state population twice inside a spin-echo sequence. Initial experiments with $N = 10^4$ atoms are estimated to attain a squeezing of 15.7 dB and potentially reaching up to 31.5 dB depending on the amount of Raman scattering. By changing the atom-cavity detuning with respect to the Zeeman splitting it is possible to operate the proposed QND measurement sequence with a reduced amount of Raman scattering. It needs to be investigated experimentally, but potentially prolonging the Heisenberg scaling to larger atom numbers is a very promising prospect.

Chapter 4 described how to inject entangled atoms into an atom interferometer that operates on the clock transition. A scheme was proposed to transfer entanglement from an internal state superposition to a momentum state superposition, with the interferometer operating in a double-diffraction configuration. After closing the interferometer the atoms will need to be retrapped in a moving optical lattice in order to prepare the quantum state for readout. A second scheme was proposed to generate entanglement between free-falling atoms in a momentum state superposition, with the interferometer operating in a Mach-Zehnder configuration. Homogenous atom-cavity coupling requires fast QND measurements, this was demonstrated in a similar system by the Thompson group, which inspired the realised homodyne detection system. Both interferometer schemes can be extended to an entangled gradiometer configuration.

Chapter 5 discussed space applications for atom interferometry. The entangled atom interferometer technology readiness level needs to be raised before it can be considered space ready, therefore a roadmap was laid out towards a future gravity mission in space using an entangled atom interferometer operating on the clock transition. The scheme creating entanglement between free-falling atoms is more suited to be implemented compared to the entanglement transfer scheme when a transverse velocity is used to increase the instrument's repetition rate. A preliminary design was made for a future space instrument using two atomic species for reading out the gradiometer phase in the linear regime.

An entangled atom interferometer operating with a large number of entangled atoms $N$ and an interrogation time $T$ surpassing a few milliseconds has not yet been demonstrated, because a large amount of entanglement is fragile. The entangled atom interferometer setup is not yet completed, but it is expected that the QND sequence can be performed in the coming months, which will be the first test of the amount of squeezing that the setup described in this work can generate. A fully functioning entangled interferometer on the clock transition is a bit further on the horizon, but the prospect of the increase in sensitivity compared to using uncorrelated atoms is promising.

# Appendix A

# Experimentally Useful Strontium Transition Frequencies

The listed transition frequencies aid in tuning the respective laser systems to the desired transitions for cooling, trapping, probing and interferometer pulses.

### $^{88}$Sr Transition Frequencies

| | | |
|---|---|---|
| $^1S_0 \leftrightarrow {}^1P_1$ | 650.506 18 THz | 460.860 28 nm in vacuum |
| $^1S_0 \leftrightarrow {}^3P_0$ | 429.228 066 418 009 THz | 698.445 608 419 379 nm in vacuum |
| $^1S_0 \leftrightarrow {}^3P_1$ | 434.829 121 311 THz | 689.448 896 836 nm in vacuum |
| $^3P_2 \leftrightarrow {}^3D_2$ | 603.287 8 THz | 496.931 1 nm in vacuum |

Table A.1: $^{88}$Sr transition frequencies and the corresponding wavelength in vacuum. $^1S_0 \leftrightarrow {}^1P_1$ and $^3P_2 \leftrightarrow {}^3D_2$ data from [116], $^1S_0 \leftrightarrow {}^3P_0$ data from [204] and $^1S_0 \leftrightarrow {}^3P_1$ data from [205].

### $^{87}$Sr Transition Frequencies

| $^1S_0 \leftrightarrow {}^1P_1$ | |
|---|---|
| $F = 9/2 \leftrightarrow F' = 9/2$ | 650.506 11 THz |
| $F = 9/2 \leftrightarrow F' = 11/2$ | 650.506 13 THz |
| $F = 9/2 \leftrightarrow F' = 7/2$ | 650.506 17 THz |
| $^1S_0 \leftrightarrow {}^3P_0$ | |
| $F = 9/2 \leftrightarrow F' = 9/2$ | 429.228 004 229 873 65 THz |
| $^1S_0 \leftrightarrow {}^3P_1$ | |
| $F = 9/2 \leftrightarrow F' = 11/2$ | 434.827 879 860 THz |
| $F = 9/2 \leftrightarrow F' = 9/2$ | 434.829 343 010 THz |
| $F = 9/2 \leftrightarrow F' = 7/2$ | 434.830 473 270 THz |

| $^3P_2 \leftrightarrow {}^3D_2$ | |
|---|---|
| $F = 13/2 \leftrightarrow F' = 13/2$ | 603.287 021 1 THz |
| $F = 13/2 \leftrightarrow F' = 11/2$ | 603.287 485 6 THz |
| $F = 11/2 \leftrightarrow F' = 13/2$ | 603.285 671 5 THz |
| $F = 11/2 \leftrightarrow F' = 11/2$ | 603.286 133 1 THz |
| $F = 11/2 \leftrightarrow F' = 9/2$ | 603.286 530 8 THz |
| $F = 9/2 \leftrightarrow F' = 11/2$ | 603.284 969 3 THz |
| $F = 9/2 \leftrightarrow F' = 9/2$ | 603.285 358 5 THz |
| $F = 9/2 \leftrightarrow F' = 7/2$ | 603.285 670 6 THz |
| $F = 7/2 \leftrightarrow F' = 9/2$ | 603.284 381 8 THz |
| $F = 7/2 \leftrightarrow F' = 7/2$ | 603.284 694 0 THz |
| $F = 7/2 \leftrightarrow F' = 5/2$ | Not observed. |
| $F = 5/2 \leftrightarrow F' = 7/2$ | 603.283 927 0 THz |
| $F = 5/2 \leftrightarrow F' = 5/2$ | 603.284 178 9 THz |

Table A.2: $^{87}$Sr transition frequencies between hyperfine levels $F$ and $F'$. $^1S_0 \leftrightarrow {}^3P_0$ data from [206], $^1S_0 \leftrightarrow {}^3P_1$ data from [207], $^3P_2 \leftrightarrow {}^3D_2$ data from [208] and $^1S_0 \leftrightarrow {}^1P_1$ data from [116] calculated using the isotope shifts from [208].

**$^{87}$Sr Hyperfine Structure**

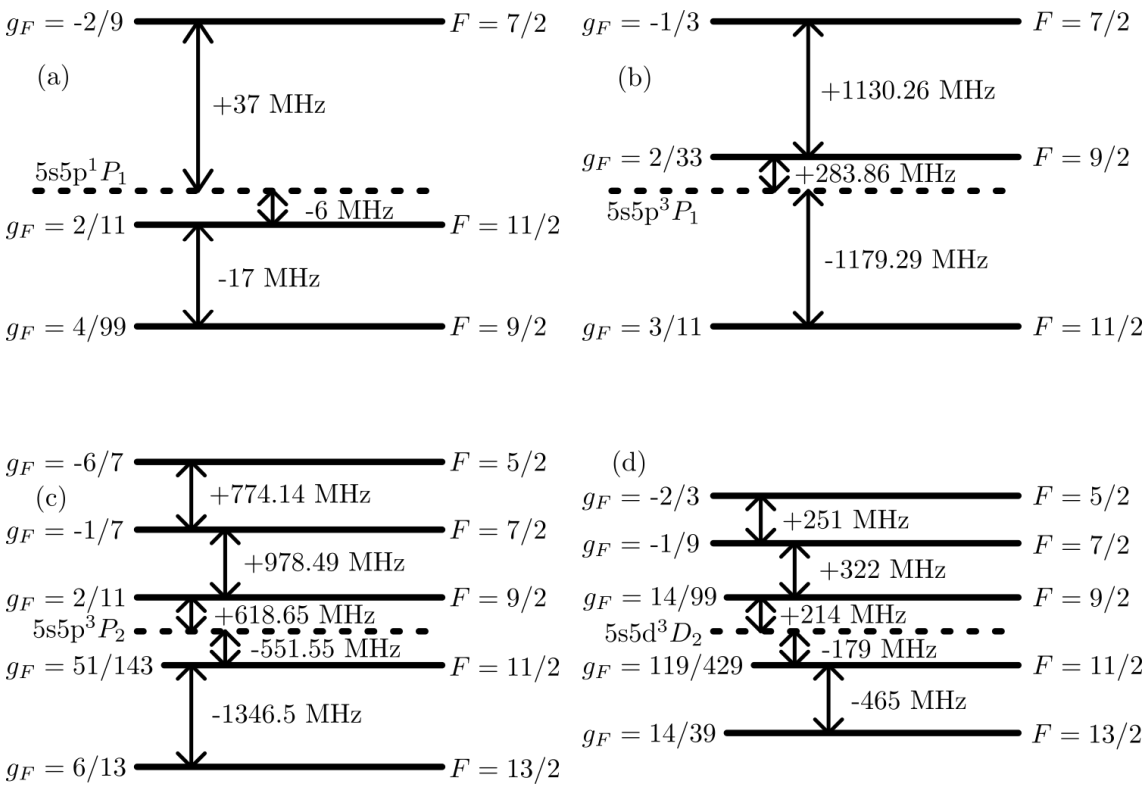


Figure A.1: The hyperfine level structure of $^{87}$Sr is shown for the levels (a) 5s5p$^1P_1$, (b) 5s5p$^3P_1$, (c) 5s5p$^3P2$ and (d) 5s5d$^3D_2$, with the respective g-factors $g_F$. The dotted lines represent the energy levels of $^{87}$Sr if the hyperfine structure would be absent. Figure adapted from [208].

# Appendix B

# Printed Circuit Board Designs

The majority of the electronics in the lab has been designed by the LENS electronic workshop, the various projects are available on their website [209]. Constructing and soldering a variety of their projects gave me a great insight in circuit design, which helped a lot when using the home-built electronics. Even though many project designs are available, some applications require a custom design, therefore I designed a few printed circuit boards (PCBs) myself. I would like to thank Roberto Concas for teaching me how to make PCB designs and layouts in Eagle, for his tips during the circuit design process of the projects described in this chapter and for checking the final PCB layouts before printing.

## B.1 Cavity Temperature Controller Schematic

The Eagle circuit design, which includes the names and values of the used components, is shown on the last four pages of this section.

#### Cavity TC V8 Sheet 1/4

The PT100 resistance is read out in a voltage divider configuration (R1 and PT100), the voltage is low pass filtered (R43 and C36) and amplified (IC3), with a gain of $G = 9$ ($G$ = R3/R2). It is important that R1, R2 and R3 have a low temperature coefficient (TCR < 15 ppm/°C). It is also important to use a low drift voltage reference (IC1 is a REF102 with 2.5 ppm/°C drift.)

The temperature set point is created by reading out the voltage V_SET of a 10 kΩ trimmer potentiometer (R_SET), which is placed between two resistances (R4 and R5) in order to limit the set point voltage to a range corresponding to temperatures between 25°C and 45°C. The set point voltage is buffered (IC4) in order to be read out by the LCD display.

The ±15 V supply is filtered (L1, L2, C1 and C2). A voltage regulator (IC2 = LM317) is used to supply the Arduino DUE with 9 V.

#### Cavity TC V8 Sheet 2/4

A coarse error signal (ERROR_COARSE) is created by comparing the measured voltage V_MEAS with the set point voltage V_SET using an instrumentation amplifier (IC6) with a gain of $G_{coarse} = 62$. The coarse error signal is used when the measured temperature is far away from its set point. The coarse error signal has a sensitivity of 4.55 mK/bit.

A fine error signal (ERROR_FINE) is created for when the measured temperature is close the set point, because the analog to digital input ports of the Arduino DUE are limited to 12 bits. The INA114 (IC5) that generates the fine error signal has a gain of $G_{fine} = 5001$. The fine error signal has a sensitivity of 56.3 $\mu$K/bit.

Negative error signals pose a problem since the Arduino DUE only handles voltages between 0 V and 3.3 V on its input and output ports. Therefore the error signal is split into the absolute error signal and the sign of the error signal. The circuit around IC7A and IC8 creates the absolute value of the coarse error signal (ERROR_ABS_COARSE). The circuit around IC7B and IC9 creates the absolute value of the fine error signal (ERROR_ABS_FINE). The Arduino input ports are protected by 3.3 V Zener diodes (D3 and D6), this is especially necessary for the fine error signal input port, since ERROR_ABS_FINE is close to the saturation voltage of the operational amplifiers when the measured temperature is far from the set point due to the large gain of $G_{fine} = 5001$.

**Cavity TC V8 Sheet 3/4**

The sign of the error signal (ERR_SGN) is generated by the circuit around IC10. The fine error signal (ERROR_FINE) is chosen as an input, since it is the relevant error signal when the temperature is close to the set point. Far away from the set point the sign of the fine and coarse error signal are equal, thus there is no need to read out the sign of the coarse error signal.

The Arduino performs the task of the digital PID controller and outputs a voltage on the digital to analog (DAC) ports. Both DAC ports, DAC_FINE and DAC_COARSE, are used and added together by IC11A with a gain of 1/100 (R20/R18) and 1 (R20/R19) respectively. Combining the two DAC channels in this way creates an effective DAC of 14 bits, while the individual DAC channels are limited to 12 bits. The output voltage is inverted by IC11B in order to become positive again. The output voltage is turned into a current by the PA75 power amplifier (IC12) configured as a Howland pump with a gain of 1/10 (R26/R25). Make sure the sensing resistor $R_s$ =R42 is a high power resistor, such that it does not burn! The current supplied to the load/heaters

$$I_{heat} = I_{load} = \frac{1}{\mathrm{R42}} \frac{\mathrm{R26}}{R25} \mathrm{V\_ADD\_INV} = \frac{\mathrm{V\_ADD\_INV}}{30}$$

is independent of the load. The heaters are connected via a BNC cable that is connected to V_HEAT.

A switch on the front panel can be flipped to turn the integrator function of the Arduino on and off. The switch controls the voltage (INT_SWITCH) to the integrator pin (digital pin 29). R24 is a pull down resistor in order to set the pin to 0 V in the off state. A LED is also installed on the front panel to indicate if the integrator is on or off, it is connected between INT-2 and INT-3, hence the resistor R23 to ground.

An offset to the heater current can be added through a 10 kΩ trimmer potentiometer. The voltage (MANUAL) is low pass filtered and read out by an analog port of the Arduino. The measured input voltage is then added to the DAC_COARSE output port.

An LCD screen (LASCAR DPM 1AS-BL) is mounted on the front panel in order to visualise the various voltages. A rotating switch (also mounted on the front panel) is used to select the voltage to display on the LCD screen. Voltage dividers are necessary since the LCD screen has a 200 mV full scale reading.

**Cavity TC V8 Sheet 4/4**

The Arduino DUE is inserted onto the PCB, which acts as an Arduino shield. The Arduino is powered by 9 V (V_ARDUINO) on the VIN pin. The ground (GND) pins of the Arduino are connected with the ground (GND) plane of the PCB. The Arduino supplies 3.3 V to create a small 3.3 V power plane on the board that is used for the sign of the error signal, the integrator switch and the manual input.

The coarse absolute error signal is read out with analog pin A2, the fine absolute error signal is read out with analog pin A4, the manual voltage is read out with analog pin A6, the sign of the error signal is read out with digital pin 23 and the state of the integrator switch is read out with digital pin 29.

The Arduino outputs the voltage for the Howland pump on its two digital to analog (DAC) channels, which are located on analog pin A12 and A13.

### Arduino PID-Controller Software

The Arduino DUE is programmed to act as a PID-controller with proportional gain $K_P = 25$, integral gain $K_I = 0.15\ \mathrm{s}^{-1}$ and derivative gain $K_D = 125$ s. The derivative component is digitally low pass filtered with a time constant of $\tau_{LF} = 1$ s, which is chosen at $T_D/5 = K_D/(5K_P)$. The output voltage of the PID-controller is updated every 100 ms. The measured input voltages are averaged over the 100 ms step size. The Arduino uses the coarse error signal when the measured voltage is far from the set point and it switches to using the fine error signal when close to the set point. The switching between the coarse and fine error signal occurs when the fine error voltage $< 3$ V, such that it is in range of the analog output port (0 V to 3.3 V) with a small margin. The integrator switch can be turned off in order to disable the integrator, which resets the value of the integral component to the output voltage.

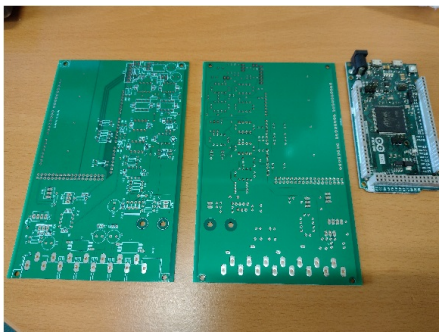

Figure B.1: Cavity temperature controller bare printed circuit board (front and back), which acts as a shield for the Arduino DUE.

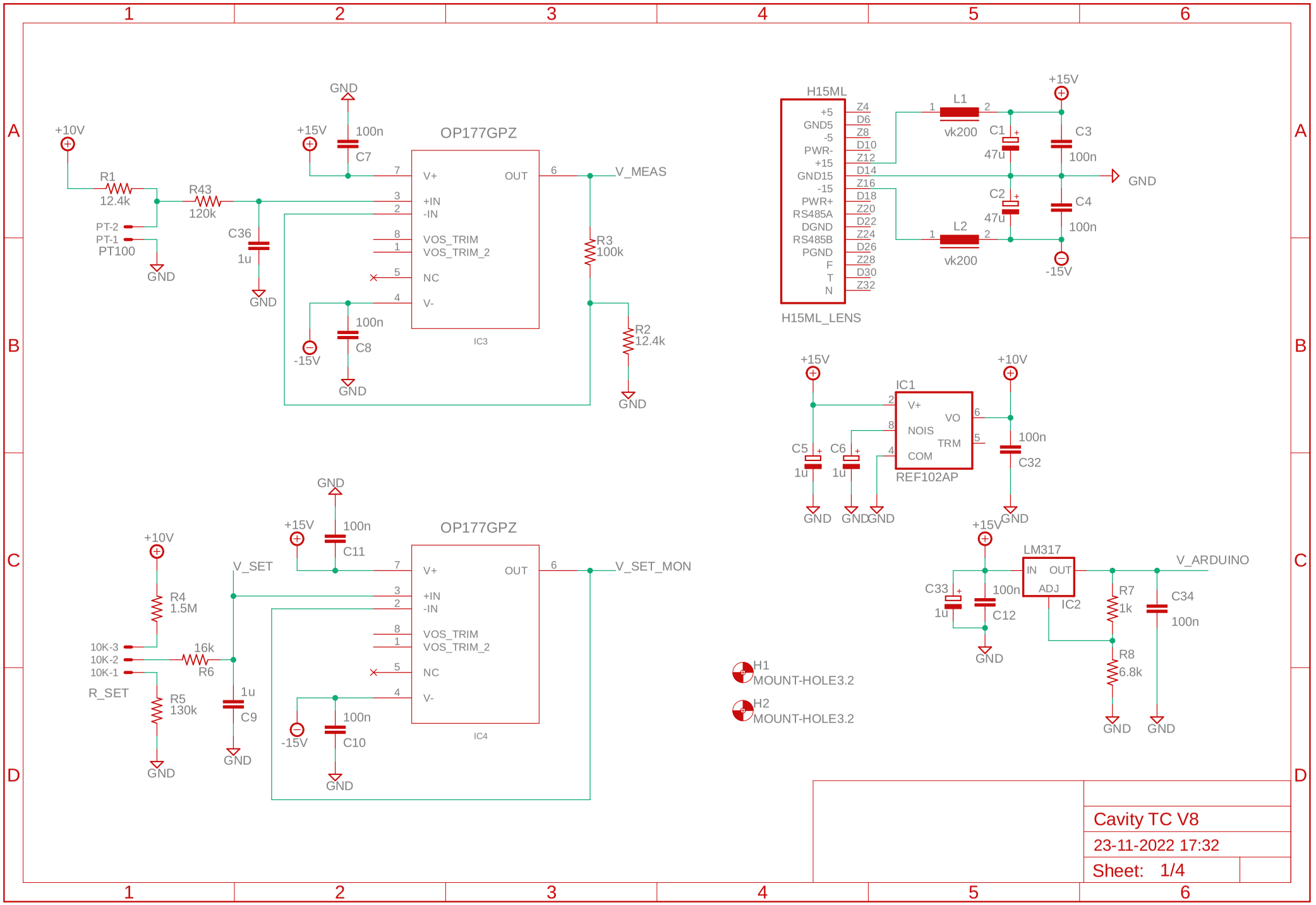
OP177GPZ
IC3
OP177GPZ
IC4
H15ML
H15ML_LENS
REF102AP
IC1
LM317
IC2
V_MEAS
V_SET_MON
V_ARDUINO
V_SET
R_SET
PT100
MOUNT-HOLE3.2
MOUNT-HOLE3.2
Cavity TC V8
23-11-2022 17:32
Sheet: 1/4

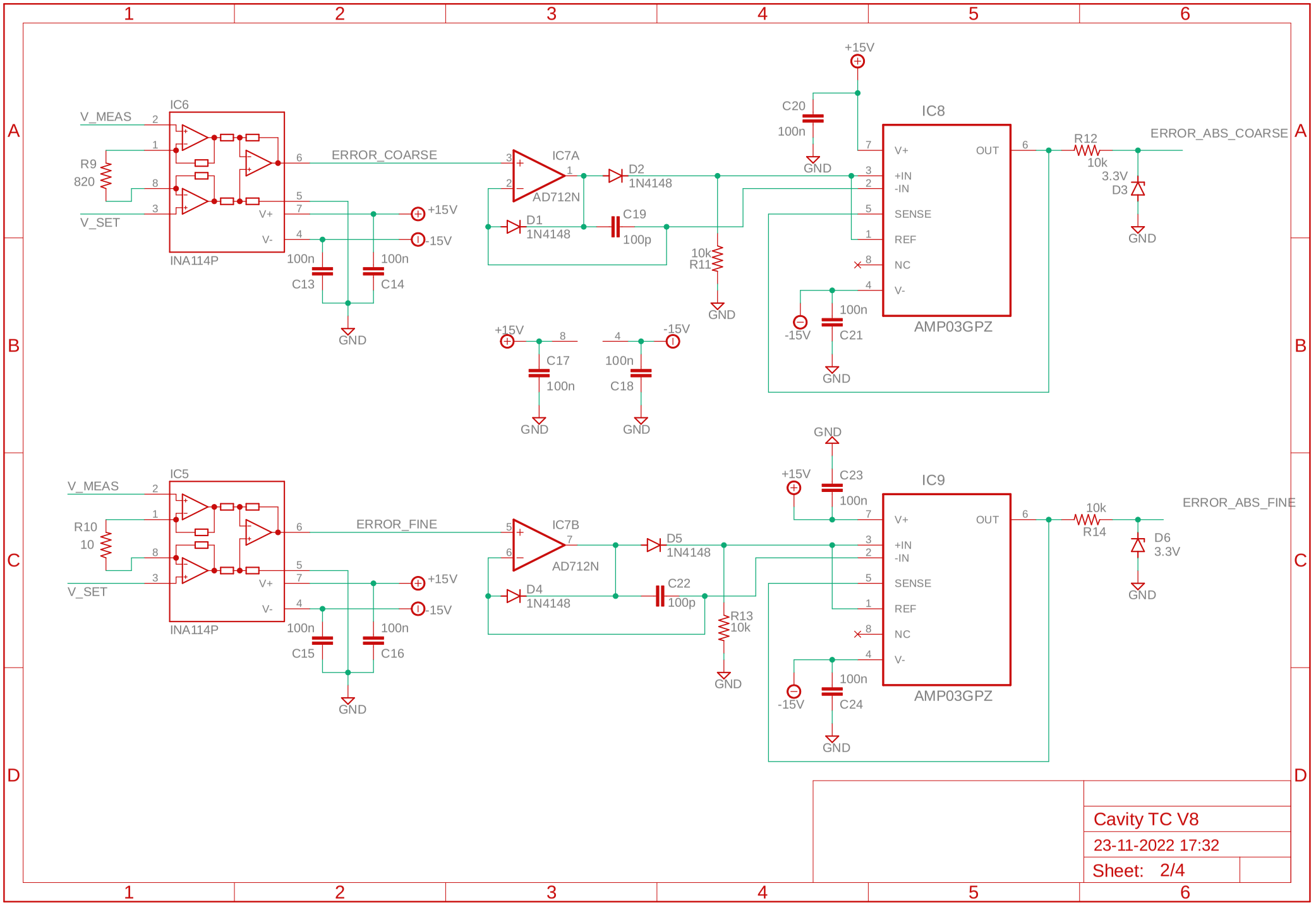
1
2
3
4
5
6
A
B
C
D
V_MEAS
V_SET
IC6
INA114P
R9
820
ERROR_COARSE
+15V
-15V
V+
V-
100n
C13
C14
GND
IC7A
AD712N
D1
1N4148
D2
1N4148
C19
100p
10k
R11
IC8
AMP03GPZ
V+
OUT
+IN
-IN
SENSE
REF
NC
V-
C20
C21
R12
10k
3.3V
D3
ERROR_ABS_COARSE
C17
C18
IC5
R10
10
ERROR_FINE
IC7B
D4
1N4148
D5
1N4148
C22
100p
R13
10k
IC9
C23
C24
R14
D6
3.3V
ERROR_ABS_FINE
Cavity TC V8
23-11-2022 17:32
Sheet: 2/4

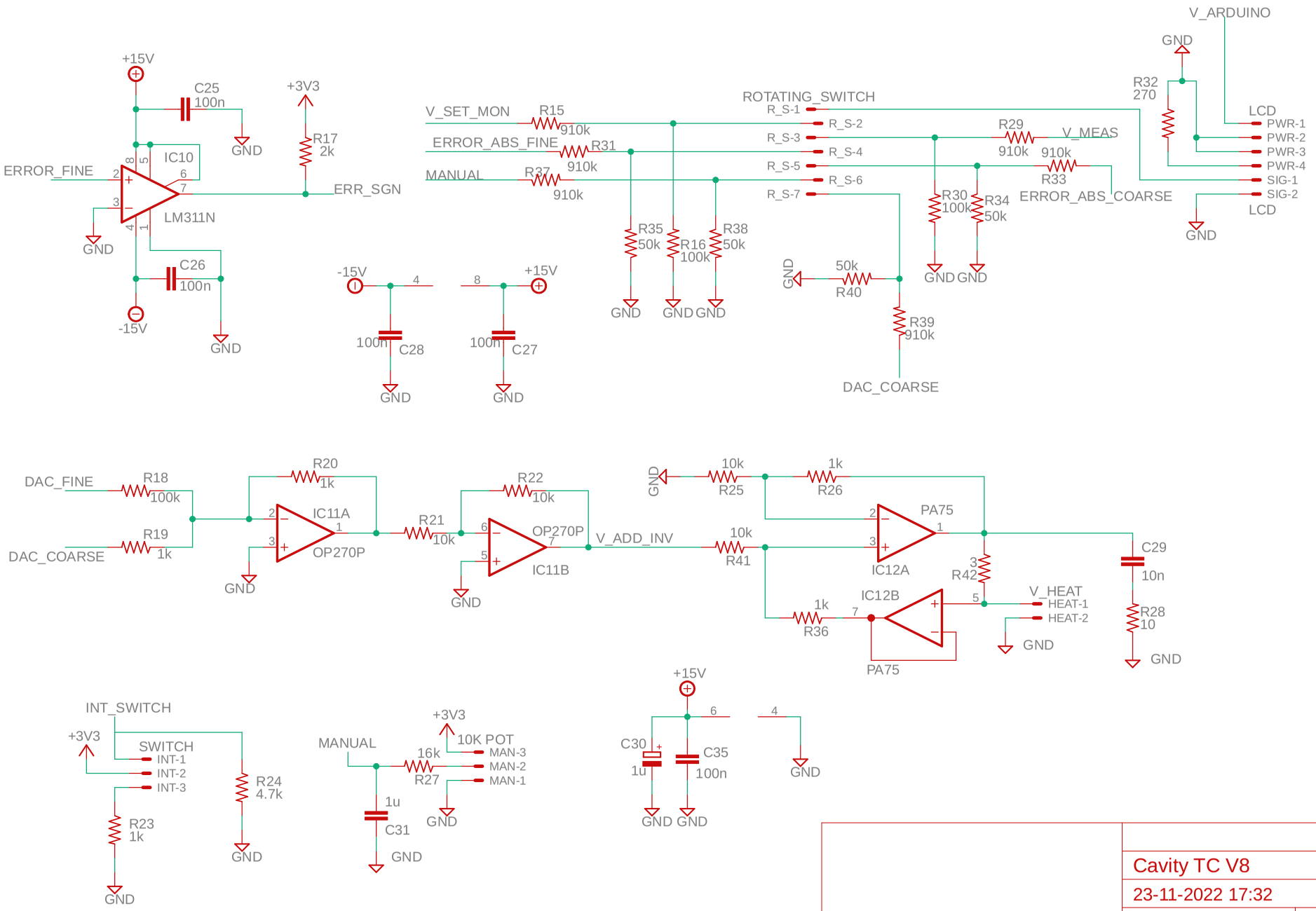
+15V
C25
100n
GND
+3V3
R17
2k
ERR_SGN
ERROR_FINE
IC10
LM311N
GND
C26
100n
-15V
GND
V_SET_MON
R15
910k
ERROR_ABS_FINE
R31
910k
MANUAL
R37
910k
ROTATING_SWITCH
R_S-1
R_S-2
R_S-3
R_S-4
R_S-5
R_S-6
R_S-7
R29
910k
V_MEAS
910k
R33
ERROR_ABS_COARSE
R30
100k
R34
50k
GND GND
R35
50k
R16
100k
R38
50k
GND GND GND
-15V
100n
C28
GND
+15V
100n
C27
GND
GND
50k
R40
R39
910k
DAC_COARSE
V_ARDUINO
GND
R32
270
LCD
PWR-1
PWR-2
PWR-3
PWR-4
SIG-1
SIG-2
LCD
GND
DAC_FINE
R18
100k
DAC_COARSE
R19
1k
GND
R20
1k
IC11A
OP270P
R21
10k
R22
10k
OP270P
IC11B
GND
V_ADD_INV
GND
10k
R25
1k
R26
10k
R41
PA75
IC12A
R42
3
IC12B
1k
R36
PA75
V_HEAT
HEAT-1
HEAT-2
GND
C29
10n
R28
10
GND
INT_SWITCH
+3V3
SWITCH
INT-1
INT-2
INT-3
R24
4.7k
R23
1k
GND
MANUAL
+3V3
16k
R27
10K POT
MAN-3
MAN-2
MAN-1
GND
1u
C31
GND
+15V
C30
1u
C35
100n
GND GND
GND
Cavity TC V8
23-11-2022 17:32
Sheet: 3/4

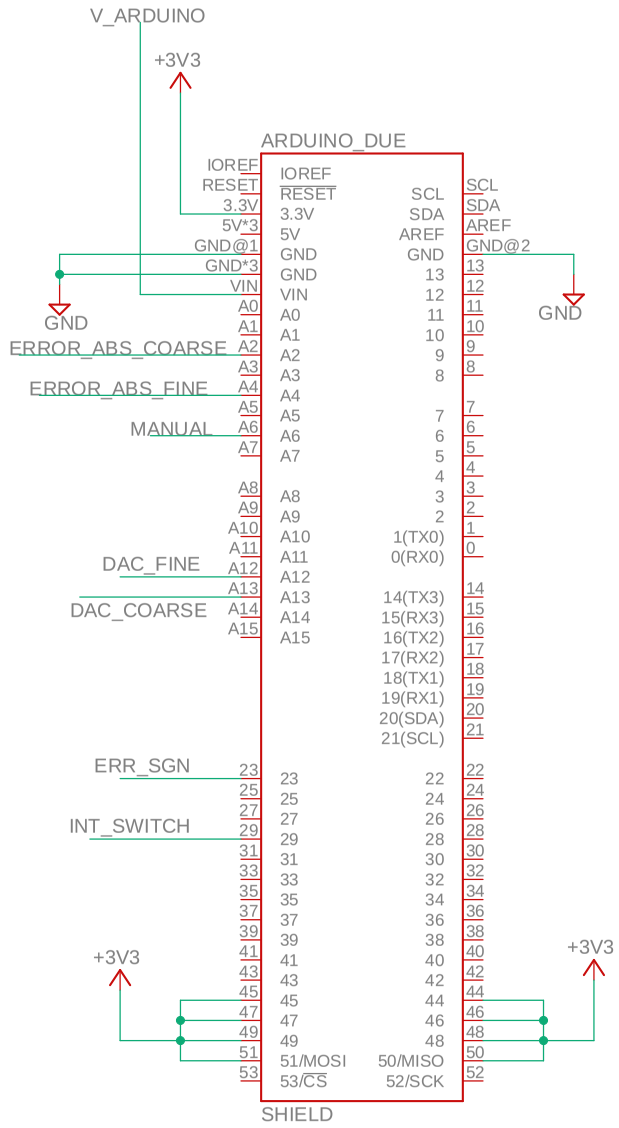


| | |
|---|---|
| Cavity TC V8 | |
| 23-11-2022 17:32 | |
| Sheet: 4/4 | |

## B.2 SWAP Controller Schematic

The Eagle circuit design, which includes the names and values of the used components, is shown on the next page.

### SWAP Switch Controller V3 Sheet 1/1

The ±15 V supply is filtered (L1, L2, C1 and C2). A voltage regulator (IC2 = LM317) is used to supply the Arduino DUE with 9 V. A second voltage regulator (IC3) is used to generate 5 V. IC1 is used to invert the 5 V into −5 V. The ±5 V is used to power the RF switches.

The trigger from the computer (TTL-COMP) and the trigger from the Agilent source (TTL-AGILENT) are read out on Arduino digital pins 29 and 35 respectively. The input pins are protected with 3.3 V Zener diodes (D1 and D2).

The Arduino outputs triggers to control the three RF switches via ditigal pins 27, 25 and 23 for AOM1, AOM2 and AOM3 respectively.

The switch on the front panel is read out with digital pin 40. The switch is used to turn of the SWAP controller in case a manual reset is necessary. Flip the switch on and off like a button to reset, turn the switch on in order to turn off the SWAP controller if desired.

The Arduino DUE is inserted onto the PCB, which acts as an Arduino shield. The Arduino is powered by 9 V (V_ARDUINO) on the VIN pin. The ground (GND) pins of the Arduino are connected with the ground (GND) plane of the PCB. The Arduino supplies 3.3 V to create a small 3.3 V power plane on the board that is used for the reset switch.

### Arduino SWAP Controller Software

The Arduino DUE is programmed to wait until it receives the trigger from the computer (TTL-COMPUTER) to start the red MOT SWAP sequence (Fig. 2.22). The controller needs to wait a little longer after receiving the trigger from the computer in order to be synchronised to the sawtooth-waves. The SWAP AOM is constantly powered by the sawtooth-wave radio frequency signals from the Agilent source, the trigger of the agilent (TTL-AGILENT) is used to synchronise the RF switching with the sawtooth-wave pattern. When the Arduino has received both triggers it starts the RF switching sequence, first excecuting SWAP-3, followed by SWAP-1. When the single frequency red MOT starts, then the RF switches remain closed.

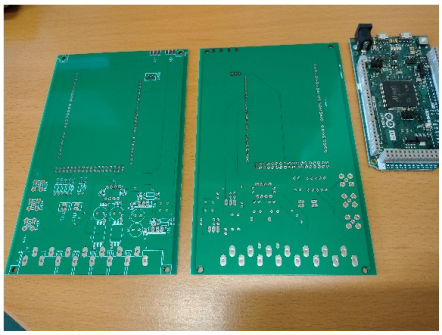

Figure B.2: SWAP controller bare printed circuit board (front and back), which acts as a shield for the Arduino DUE.

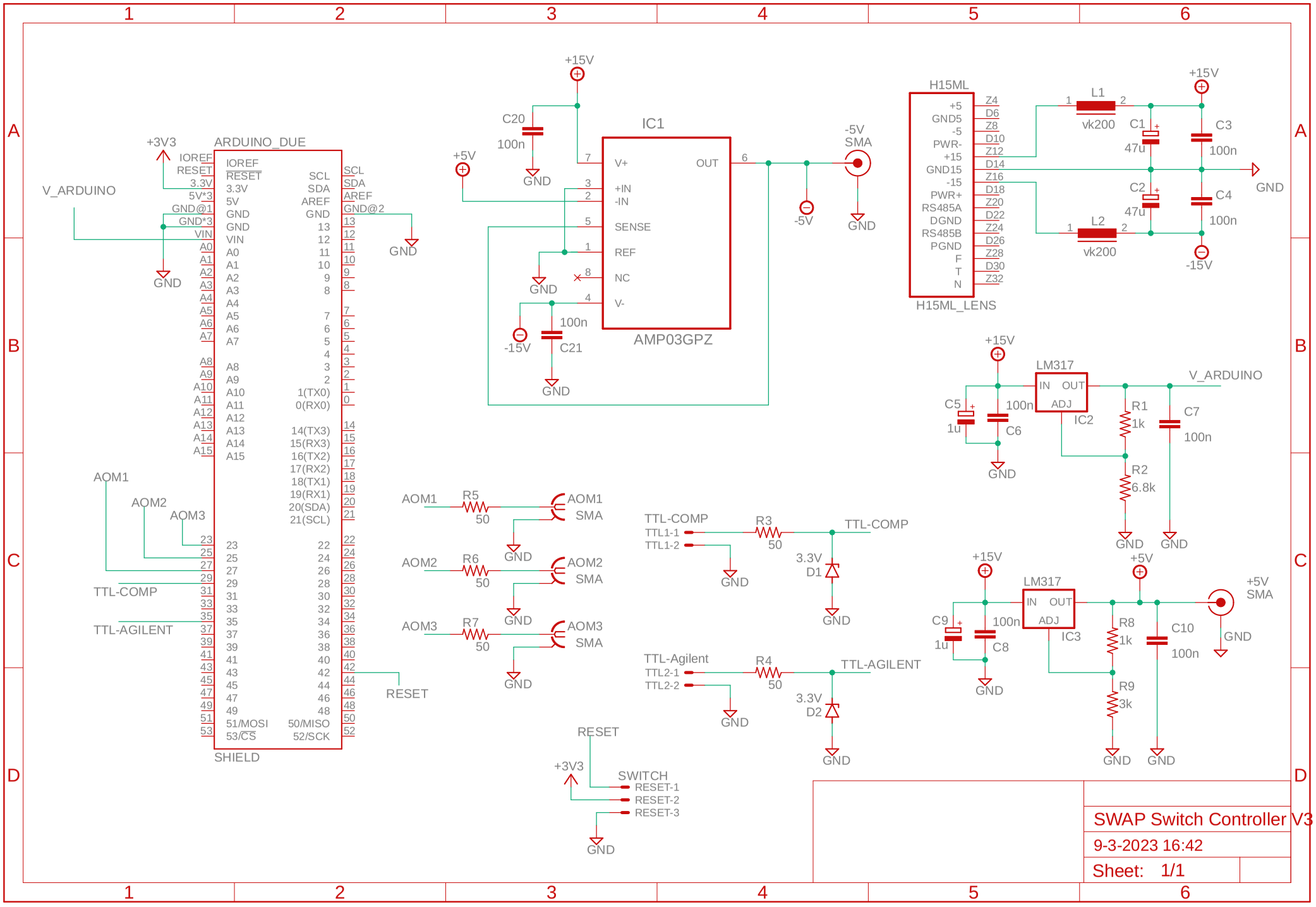
ARDUINO_DUE
SHIELD
V_ARDUINO
+3V3
GND
AOM1
AOM2
AOM3
TTL-COMP
TTL-AGILENT
RESET
IC1
AMP03GPZ
C20
100n
C21
+15V
-15V
+5V
-5V
SMA
H15ML
H15ML_LENS
L1
L2
vk200
C1
C2
47u
C3
C4
LM317
IC2
IC3
C5
C6
C7
C8
C9
C10
1u
R1
1k
R2
6.8k
R3
R4
R5
R6
R7
R8
R9
50
3k
D1
D2
3.3V
TTL-COMP
TTL-Agilent
SWITCH
RESET-1
RESET-2
RESET-3
SWAP Switch Controller V3
9-3-2023 16:42
Sheet: 1/1

## B.3 Homodyne Detector Schematic

The homodyne detector needs to measure the beat notes between the probe and local oscillator (LO) in order to read out the phase of the optical ring cavity and to stabilise the LO phase, the design is based on the homodyne detector of the Thompson group [161]. The Eagle circuit design, which includes the names and values of the used components, is shown on the next page.

### Homodyne V2.5 Sheet 1/1

Two photodiodes (PD1 and PD2) are placed in a differential configuration in order to suppress common mode signals. The photocurrent difference is split into a direct current (DC) and alternating current (AC) part by using two capacitors (C3 and C4).

The AC coupled signal contains the beat note signal between the LO and probe carrier, which is at 30 MHz (Fig. 2.30). The beat note signal is amplified by IC1, which is a wideband transimpedance amplifier (AD8015). The amplified output signal AC_OUT is bandpass filtered and send to the phase frequency detector (PFD) of the phase-locked loop (PLL), see figure 2.39 for the complete PLL schematic.

For the DC output two separate amplification chains are available: amplifying the differential photocurrent or amplifying the individual photocurrents. The amplification chain is chosen by shorting the pads: for the differential signal pads R5 and R8 are shorted and pads R6 and R7 are left open, for the individual signals pads R6 and R7 are shorted and pads R5 and R8 are left open. The differential photocurrent amplification chain is used in the experimental setup.

The differential signal I_DIFF_DC is amplified by IC7, a low noise high gain-bandwidth transimpedance amplifier (OPA657). A feedback resistor (R3) of $R_f = 1$ MΩ is used. The output signal DC_OUT is observed on an oscilloscope. The output voltage of the homodyne signal

$$\begin{aligned} V_{HD}(t) &= R_f I_{photo}(t) = R_f S P(t) \\ &= 2R_f S \sqrt{P_{LO} P_{probe}} \sin\left(\delta\phi_{probe}(t)\right), \end{aligned}$$

with $R_f$ the feedback resistance, $S$ the photo sensitivity of the photodiodes, $I_{photo}$ the differential photo current of the homodyne detector when reading out the quadrature component [Eq. (2.21)].

The individual photocurrents are amplified by IC5 and IC6, both are low noise high gain-bandwidth transimpedance amplifiers (OPA656). The amplified photocurrents are added to create the sum (IC4) and difference (IC3). The added photocurrents can be electrically balanced by varying the trimmer potentiometer (R17). The choice was made to use the differential signal instead of the individual signals, because the differential signal is not limited by saturation of the operational amplifiers due to the LO intensity.

The ±15 V supply gets filtered (L4, L5, C17 and C18) and low noise voltage regulators (IC2 and IC3) are used to power the operational amplifiers.

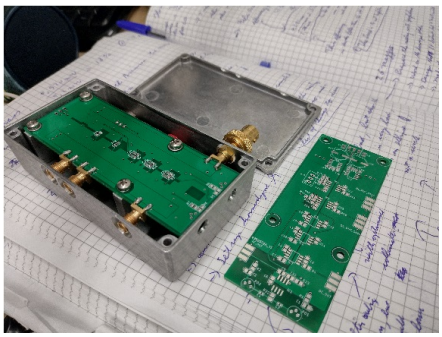

Figure B.3: Mounted homodyne detector and bare printed circuit board.

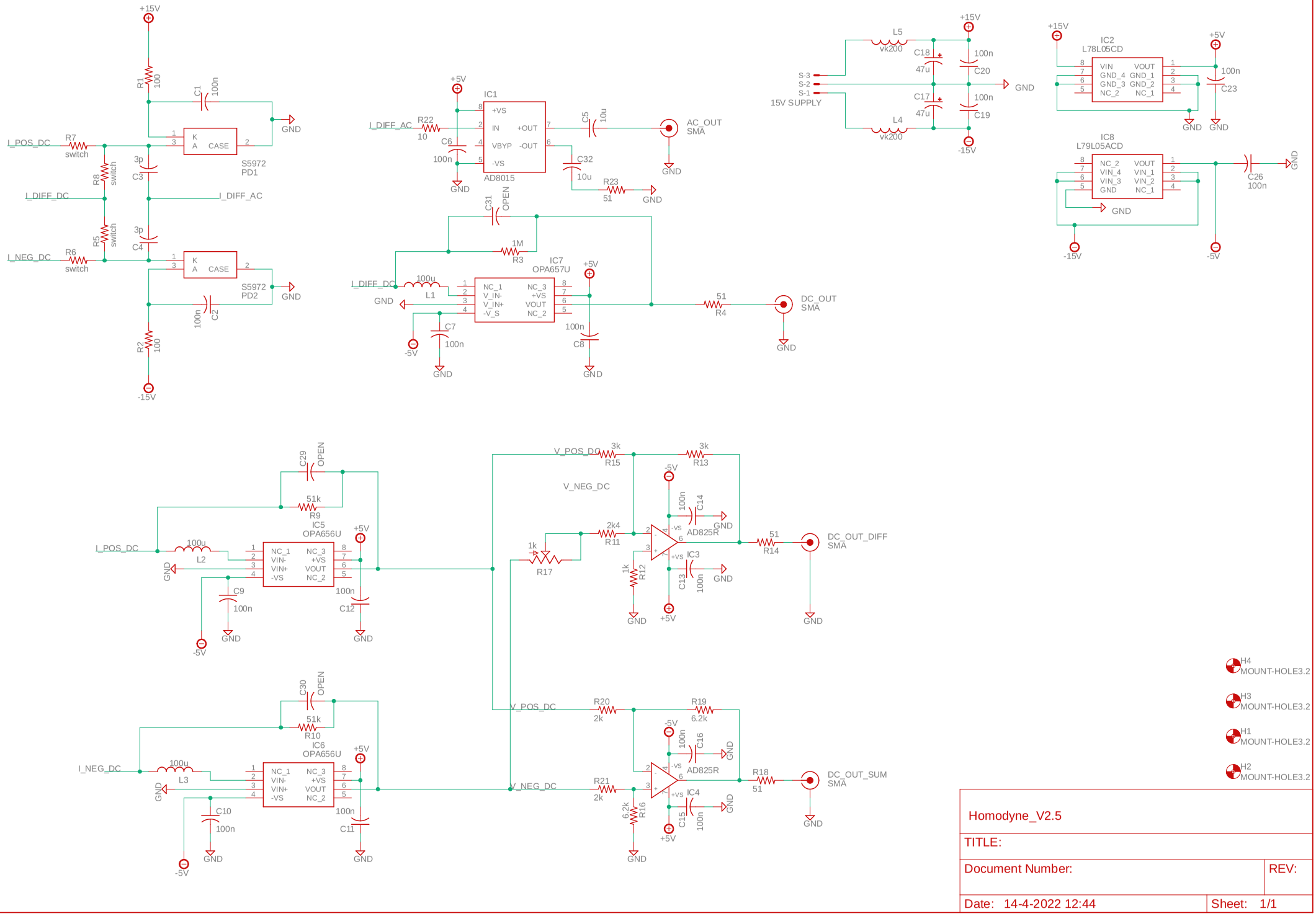
+15V
R1
100
C1
100n
GND
I_POS_DC
R7
switch
K
A
CASE
S5972
PD1
R8
switch
3p
C3
I_DIFF_DC
I_DIFF_AC
R5
switch
3p
C4
I_NEG_DC
R6
switch
S5972
PD2
100n
C2
R2
100
-15V
+5V
IC1
+VS
IN
+OUT
VBYP
-OUT
-VS
AD8015
I_DIFF_AC
R22
10
C6
100n
C5
10u
AC_OUT
SMA
C32
10u
R23
51
C31
OPEN
1M
R3
IC7
OPA657U
I_DIFF_DC
100u
L1
NC_1
V_IN-
V_IN+
-V_S
NC_3
+VS
VOUT
NC_2
C7
100n
C8
100n
51
R4
DC_OUT
SMA
L5
vk200
C18
47u
100n
C20
S-3
S-2
S-1
15V SUPPLY
C17
47u
100n
C19
L4
vk200
IC2
L78L05CD
VIN
GND_4
GND_3
NC_2
VOUT
GND_1
GND_2
NC_1
100n
C23
IC8
L79L05ACD
NC_2
VIN_4
VIN_3
GND
VOUT
VIN_1
VIN_2
NC_1
C26
100n
C29
OPEN
51k
R9
IC5
OPA656U
I_POS_DC
100u
L2
C9
100n
100n
C12
V_POS_DC
3k
R15
3k
R13
V_NEG_DC
2k4
R11
1k
R17
1k
R12
AD825R
IC3
C14
100n
C13
100n
51
R14
DC_OUT_DIFF
SMA
C30
OPEN
51k
R10
IC6
OPA656U
I_NEG_DC
100u
L3
C10
100n
100n
C11
V_POS_DC
2k
R20
6.2k
R19
V_NEG_DC
2k
R21
6.2k
R16
AD825R
IC4
C16
100n
C15
100n
R18
51
DC_OUT_SUM
SMA
H4
MOUNT-HOLE3.2
H3
MOUNT-HOLE3.2
H1
MOUNT-HOLE3.2
H2
MOUNT-HOLE3.2
Homodyne_V2.5
TITLE:
Document Number:
REV:
Date: 14-4-2022 12:44
Sheet: 1/1

# Bibliography


[1] J. P. Dowling and G. J. Milburn, "Quantum technology: the second quantum revolution," *Philosophical Transactions of the Royal Society of London. Series A: Mathematical, Physical and Engineering Sciences*, vol. 361, no. 1809, pp. 1655–1674, Jun. 2003. [Online]. Available: https://doi.org/10.1098/rsta.2003.1227

[2] L. Jaeger, *The second quantum revolution*, 1st ed. Cham, Switzerland: Springer International Publishing, Jan. 2019, ISBN: 978-3-319-98824-5.

[3] L. Essen and J. V. L. Parry, "An atomic standard of frequency and time interval: A cæsium resonator," *Nature*, vol. 176, no. 4476, pp. 280–282, Aug. 1955. [Online]. Available: https://doi.org/10.1038/176280a0

[4] W. Markowitz, R. G. Hall, L. Essen, and J. V. L. Parry, "Frequency of cesium in terms of ephemeris time," *Phys. Rev. Lett.*, vol. 1, pp. 105–107, Aug 1958. [Online]. Available: https://link.aps.org/doi/10.1103/PhysRevLett.1.105

[5] G. Rosi, F. Sorrentino, L. Cacciapuoti, M. Prevedelli, and G. M. Tino, "Precision measurement of the newtonian gravitational constant using cold atoms," *Nature*, vol. 510, no. 7506, pp. 518–521, Jun. 2014. [Online]. Available: https://doi.org/10.1038/nature13433

[6] T. Bothwell, D. Kedar, E. Oelker, J. M. Robinson, S. L. Bromley, W. L. Tew, J. Ye, and C. J. Kennedy, "JILA SrI optical lattice clock with uncertainty of 2.0e-18," *Metrologia*, vol. 56, no. 6, p. 065004, oct 2019. [Online]. Available: https://dx.doi.org/10.1088/1681-7575/ab4089

[7] M. A. Nielsen and I. L. Chuang, *Quantum Computation and Quantum Information: 10th Anniversary Edition*. Cambridge University Press, 2010, ISBN: 9781107002173.

[8] E. National Academies of Sciences and Medicine, *Quantum Computing: Progress and Prospects*, E. Grumbling and M. Horowitz, Eds. Washington, DC: The National Academies Press, 2019, ISBN: 978-0-309-47969-1.

[9] T. M. Graham, Y. Song, J. Scott, C. Poole, L. Phuttitarn, K. Jooya, P. Eichler, X. Jiang, A. Marra, B. Grinkemeyer, M. Kwon, M. Ebert, J. Cherek, M. T. Lichtman, M. Gillette, J. Gilbert, D. Bowman, T. Ballance, C. Campbell, E. D. Dahl, O. Crawford, N. S. Blunt, B. Rogers, T. Noel, and M. Saffman, "Multi-qubit entanglement and algorithms on a neutral-atom quantum computer," *Nature*, vol. 604, no. 7906, pp. 457–462, Apr. 2022. [Online]. Available: https://doi.org/10.1038/s41586-022-04603-6

[10] D. Bluvstein, H. Levine, G. Semeghini, T. T. Wang, S. Ebadi, M. Kalinowski, A. Keesling, N. Maskara, H. Pichler, M. Greiner, V. Vuletić, and M. D. Lukin, "A quantum processor based on coherent transport of entangled atom arrays," *Nature*, vol. 604, no. 7906, pp. 451–456, Apr. 2022. [Online]. Available: https://doi.org/10.1038/s41586-022-04592-6

[11] K. Barnes, P. Battaglino, B. J. Bloom, K. Cassella, R. Coxe, N. Crisosto, J. P. King, S. S. Kondov, K. Kotru, S. C. Larsen, J. Lauigan, B. J. Lester, M. McDonald, E. Megidish, S. Narayanaswami, C. Nishiguchi, R. Notermans, L. S. Peng, A. Ryou, T.-Y. Wu, and M. Yarwood, "Assembly and coherent control of a register of nuclear spin qubits," *Nature Communications*, vol. 13, no. 1, May 2022. [Online]. Available: https://doi.org/10.1038/s41467-022-29977-z

[12] L. Pezzè, A. Smerzi, M. K. Oberthaler, R. Schmied, and P. Treutlein, "Quantum metrology with nonclassical states of atomic ensembles," *Rev. Mod. Phys.*, vol. 90, p. 035005, Sep 2018. [Online]. Available: https://link.aps.org/doi/10.1103/RevModPhys.90.035005

[13] A. D. Ludlow, M. M. Boyd, J. Ye, E. Peik, and P. O. Schmidt, "Optical atomic clocks," *Rev. Mod. Phys.*, vol. 87, pp. 637–701, Jun 2015. [Online]. Available: https://link.aps.org/doi/10.1103/RevModPhys.87.637

[14] G. M. Tino, "Testing gravity with cold atom interferometry: results and prospects," *Quantum Science and Technology*, vol. 6, no. 2, p. 024014, Mar. 2021. [Online]. Available: https://doi.org/10.1088/2058-9565/abd83e

[15] D. Budker and M. Romalis, "Optical magnetometry," *Nature Physics*, vol. 3, no. 4, pp. 227–234, Apr. 2007. [Online]. Available: https://doi.org/10.1038/nphys566

[16] G. Rosi, G. D'Amico, L. Cacciapuoti, F. Sorrentino, M. Prevedelli, M. Zych, Č. Brukner, and G. M. Tino, "Quantum test of the equivalence principle for atoms in coherent superposition of internal energy states," *Nature Communications*, vol. 8, no. 1, Jun. 2017. [Online]. Available: https://doi.org/10.1038/ncomms15529

[17] P. Asenbaum, C. Overstreet, M. Kim, J. Curti, and M. A. Kasevich, "Atom-interferometric test of the equivalence principle at the $10^{-12}$ level," *Phys. Rev. Lett.*, vol. 125, p. 191101, Nov 2020. [Online]. Available: https://link.aps.org/doi/10.1103/PhysRevLett.125.191101

[18] T. Bothwell, C. J. Kennedy, A. Aeppli, D. Kedar, J. M. Robinson, E. Oelker, A. Staron, and J. Ye, "Resolving the gravitational redshift across a millimetre-scale atomic sample," *Nature*, vol. 602, no. 7897, pp. 420–424, Feb. 2022. [Online]. Available: https://doi.org/10.1038/s41586-021-04349-7

[19] X. Zheng, J. Dolde, H. M. Lim, and S. Kolkowitz, "A lab-based test of the gravitational redshift with a miniature clock network," *arXiv*, 2022. [Online]. Available: https://arxiv.org/abs/2207.07145

[20] S. Kolkowitz, I. Pikovski, N. Langellier, M. D. Lukin, R. L. Walsworth, and J. Ye, "Gravitational wave detection with optical lattice atomic clocks," *Phys. Rev. D*, vol. 94, p. 124043, Dec 2016. [Online]. Available: https://link.aps.org/doi/10.1103/PhysRevD.94.124043

[21] K. Bongs, M. Holynski, J. Vovrosh, P. Bouyer, G. Condon, E. Rasel, C. Schubert, W. P. Schleich, and A. Roura, "Taking atom interferometric quantum sensors from the laboratory to real-world applications," *Nature Reviews Physics*, vol. 1, no. 12, pp. 731–739, Oct. 2019. [Online]. Available: https://doi.org/10.1038/s42254-019-0117-4

[22] N. Ohmae, M. Takamoto, Y. Takahashi, M. Kokubun, K. Araki, A. Hinton, I. Ushijima, T. Muramatsu, T. Furumiya, Y. Sakai, N. Moriya, N. Kamiya, K. Fujii, R. Muramatsu, T. Shiimado, and H. Katori, "Transportable strontium optical lattice clocks operated outside laboratory at the level of 10e-18 uncertainty," *Advanced Quantum Technologies*, vol. 4, no. 8, p. 2100015, May 2021. [Online]. Available: https://doi.org/10.1002/qute.202100015

[23] Y.-Y. Xu, J.-F. Cui, K. Qi, L.-L. Chen, X.-B. Deng, Q. Luo, H. Zhang, Y.-J. Tan, C.-G. Shao, M.-K. Zhou, X.-C. Duan, and Z.-K. Hu, "Evaluation of the transportable atom gravimeter HUST-QG," *Metrologia*, vol. 59, no. 5, p. 055001, Aug. 2022. [Online]. Available: https://doi.org/10.1088/1681-7575/ac8258

[24] Y. Tanaka and K. Heki, "Long- and short-term postseismic gravity changes of megathrust earthquakes from satellite gravimetry," *Geophysical Research Letters*, vol. 41, no. 15, pp. 5451–5456, Aug. 2014. [Online]. Available: https://doi.org/10.1002/2014gl060559

[25] I. Velicogna, T. C. Sutterley, and M. R. van den Broeke, "Regional acceleration in ice mass loss from greenland and antarctica using GRACE time-variable gravity data," *Geophysical Research Letters*, vol. 41, no. 22, pp. 8130–8137, Nov. 2014. [Online]. Available: https://doi.org/10.1002/2014gl061052

[26] D. Carbone, L. Zuccarello, A. Messina, S. Scollo, and H. Rymer, "Balancing bulk gas accumulation and gas output before and during lava fountaining episodes at mt. etna," *Scientific Reports*, vol. 5, no. 1, Dec. 2015. [Online]. Available: https://doi.org/10.1038/srep18049

[27] M. V. Camp, O. de Viron, and J. P. Avouac, "Separating climate-induced mass transfers and instrumental effects from tectonic signal in repeated absolute gravity measurements," *Geophysical Research Letters*, vol. 43, no. 9, pp. 4313–4320, May 2016. [Online]. Available: https://doi.org/10.1002/2016gl068648

[28] Y. Bidel, N. Zahzam, C. Blanchard, A. Bonnin, M. Cadoret, A. Bresson, D. Rouxel, and M. F. Lequentrec-Lalancette, "Absolute marine gravimetry with matter-wave interferometry," *Nature Communications*, vol. 9, no. 1, Feb. 2018. [Online]. Available: https://doi.org/10.1038/s41467-018-03040-2

[29] T. C. Sutterley, I. Velicogna, and C.-W. Hsu, "Self-consistent ice mass balance and regional sea level from time-variable gravity," *Earth and Space Science*, vol. 7, no. 3, Mar. 2020. [Online]. Available: https://doi.org/10.1029/2019ea000860

[30] N. Poli, R. Pašteka, and P. Zahorec, "Atomic changes can map subterranean structures," *Nature*, vol. 602, no. 7898, pp. 579–580, Feb. 2022. [Online]. Available: https://doi.org/10.1038/d41586-022-00464-1

[31] R. Bhatia and D. Geller, "Sensitivity analysis of precision inertial sensor-based navigation system (SAPIENS)," *NAVIGATION*, vol. 67, no. 4, pp. 795–822, Oct. 2020. [Online]. Available: https://doi.org/10.1002/navi.397

[32] M. A. Zaher, H. Saibi, J. Nishijima, Y. Fujimitsu, H. Mesbah, and S. Ehara, "Exploration and assessment of the geothermal resources in the hammam faraun hot spring, sinai peninsula, egypt," *Journal of Asian Earth Sciences*, vol. 45, pp. 256–267, Feb. 2012. [Online]. Available: https://doi.org/10.1016/j.jseaes.2011.11.007

[33] H. Yi and L. Wen, "Satellite gravity measurement monitoring terrestrial water storage change and drought in the continental united states," *Scientific Reports*, vol. 6, no. 1, Jan. 2016. [Online]. Available: https://doi.org/10.1038/srep19909

[34] W. Feng, C. Shum, M. Zhong, and Y. Pan, "Groundwater storage changes in china from satellite gravity: An overview," *Remote Sensing*, vol. 10, no. 5, p. 674, Apr. 2018. [Online]. Available: https://doi.org/10.3390/rs10050674

[35] K. Chavanidis, A. Stampolidis, P. Kirmizakis, M. Tranos, M. Fedi, R. Pasteka, K. Al-Ramadan, S. Kaka, G. N. Tsokas, and P. Soupios, "Gravity survey on the oil-bearing dammam dome (eastern saudi arabia) and its implications," *Remote Sensing*, vol. 14, no. 3, p. 735, Feb. 2022. [Online]. Available: https://doi.org/10.3390/rs14030735

[36] H. Fang, F. Bielsa, S. Li, A. Kiss, and M. Stock, "The BIPM kibble balance for realizing the kilogram definition," *Metrologia*, vol. 57, no. 4, p. 045009, Jul. 2020. [Online]. Available: https://doi.org/10.1088/1681-7575/ab860c

[37] X. Wu, Z. Pagel, B. S. Malek, T. H. Nguyen, F. Zi, D. S. Scheirer, and H. Müller, "Gravity surveys using a mobile atom interferometer," *Science Advances*, vol. 5, no. 9, Sep. 2019. [Online]. Available: https://doi.org/10.1126/sciadv.aax0800

[38] S. Cai, J. Tie, K. Zhang, J. Cao, and M. Wu, "Marine gravimetry using the strapdown gravimeter SGA-WZ," *Marine Geophysical Research*, vol. 38, no. 4, pp. 325–340, Jun. 2017. [Online]. Available: https://doi.org/10.1007/s11001-017-9312-9

[39] R. Geiger, V. Ménoret, G. Stern, N. Zahzam, P. Cheinet, B. Battelier, A. Villing, F. Moron, M. Lours, Y. Bidel, A. Bresson, A. Landragin, and P. Bouyer, "Detecting inertial effects with airborne matter-wave interferometry," *Nature Communications*, vol. 2, no. 1, Sep. 2011. [Online]. Available: https://doi.org/10.1038/ncomms1479

[40] B. Lu, F. Barthelmes, S. Petrovic, C. Förste, F. Flechtner, Z. Luo, K. He, and M. Li, "Airborne gravimetry of geohalo mission: Data processing and gravity field modeling," *Journal of Geophysical Research: Solid Earth*, vol. 122, no. 12, pp. 10,586–10,604, 2017. [Online]. Available: https://agupubs.onlinelibrary.wiley.com/doi/abs/10.1002/2017JB014425

[41] Y. Bidel, N. Zahzam, A. Bresson, C. Blanchard, M. Cadoret, A. V. Olesen, and R. Forsberg, "Absolute airborne gravimetry with a cold atom sensor," *Journal of Geodesy*, vol. 94, no. 2, Jan. 2020. [Online]. Available: https://doi.org/10.1007/s00190-020-01350-2

[42] B. D. Tapley, S. Bettadpur, J. C. Ries, P. F. Thompson, and M. M. Watkins, "GRACE measurements of mass variability in the earth system," *Science*, vol. 305, no. 5683, pp. 503–505, 2004. [Online]. Available: http://science.sciencemag.org/content/305/5683/503

[43] R. Floberghagen, M. Fehringer, D. Lamarre, D. Muzi, B. Frommknecht, C. Steiger, J. Piñeiro, and A. da Costa, "Mission design, operation and exploitation of the gravity field and steady-state ocean circulation explorer mission," *Journal of Geodesy*, vol. 85, no. 11, pp. 749–758, Nov 2011. [Online]. Available: https://doi.org/10.1007/s00190-011-0498-3

[44] F. Sorrentino, K. Bongs, P. Bouyer, L. Cacciapuoti, M. de Angelis, H. Dittus, W. Ertmer, A. Giorgini, J. Hartwig, M. Hauth, S. Herrmann, M. Inguscio, E. Kajari, T. T. Könemann, C. Lämmerzahl, A. Landragin, G. Modugno, F. P. dos Santos, A. Peters, M. Prevedelli, E. M. Rasel, W. P. Schleich, M. Schmidt, A. Senger, K. Sengstock, G. Stern, G. M. Tino, and R. Walser, "A compact atom interferometer for future space missions," *Microgravity Science and Technology*, vol. 22, no. 4, pp. 551–561, Sep. 2010. [Online]. Available: https://doi.org/10.1007/s12217-010-9240-7

[45] O. Carraz, C. Siemes, L. Massotti, R. Haagmans, and P. Silvestrin, "A spaceborne gravity gradiometer concept based on cold atom interferometers for measuring Earth's gravity field," *Microgravity Science and Technology*, vol. 26, no. 3, pp. 139–145, 2014. [Online]. Available: https://link.springer.com/article/10.1007/s12217-014-9385-x

[46] A. Trimeche, B. Battelier, D. Becker, A. Bertoldi, P. Bouyer, C. Braxmaier, E. Charron, R. Corgier, M. Cornelius, K. Douch, N. Gaaloul, S. Herrmann, J. Müller, E. Rasel, C. Schubert, H. Wu, and F. P. dos Santos, "Concept study and preliminary design of a cold atom interferometer for space gravity gradiometry," *Classical and Quantum Gravity*, vol. 36, no. 21, p. 215004, Oct. 2019. [Online]. Available: https://doi.org/10.1088/1361-6382/ab4548

[47] G. M. Tino, *Testing gravity with atom interferometry*, ser. Proceedings of the International School of Physics "Enrico Fermi". IOS Press, 2014, vol. 188, pp. 457–491. [Online]. Available: http://ebooks.iospress.nl/volumearticle/38101

[48] A. Sugarbaker, S. M. Dickerson, J. M. Hogan, D. M. S. Johnson, and M. A. Kasevich, "Enhanced atom interferometer readout through the application of phase shear," *Phys. Rev. Lett.*, vol. 111, p. 113002, Sep 2013. [Online]. Available: https://link.aps.org/doi/10.1103/PhysRevLett.111.113002

[49] M. Schilling, É. Wodey, L. Timmen, D. Tell, K. H. Zipfel, D. Schlippert, C. Schubert, E. M. Rasel, and J. Müller, "Gravity field modelling for the hannover 10 m atom interferometer," *Journal of Geodesy*, vol. 94, no. 12, Nov. 2020. [Online]. Available: https://doi.org/10.1007/s00190-020-01451-y

[50] M. Kitagawa and M. Ueda, "Squeezed spin states," *Phys. Rev. A*, vol. 47, pp. 5138–5143, Jun 1993. [Online]. Available: https://link.aps.org/doi/10.1103/PhysRevA.47.5138

[51] W. M. Itano, J. C. Bergquist, J. J. Bollinger, J. M. Gilligan, D. J. Heinzen, F. L. Moore, M. G. Raizen, and D. J. Wineland, "Quantum projection noise: Population fluctuations in two-level systems," *Phys. Rev. A*, vol. 47, pp. 3554–3570, May 1993. [Online]. Available: https://link.aps.org/doi/10.1103/PhysRevA.47.3554

[52] D. J. Wineland, J. J. Bollinger, W. M. Itano, and D. J. Heinzen, "Squeezed atomic states and projection noise in spectroscopy," *Phys. Rev. A*, vol. 50, pp. 67–88, Jul 1994. [Online]. Available: https://link.aps.org/doi/10.1103/PhysRevA.50.67

[53] J. Aasi, J. Abadie, B. P. Abbott, R. Abbott, T. D. Abbott, M. R. Abernathy, C. Adams, T. Adams, P. Addesso, R. X. Adhikari, C. Affeldt, O. D. Aguiar, P. Ajith, B. Allen, E. A. Ceron, D. Amariutei, S. B. Anderson, W. G. Anderson, K. Arai, M. C. Araya, C. Arceneaux, S. Ast, S. M. Aston, D. Atkinson, P. Aufmuth, C. Aulbert, L. Austin, B. E. Aylott, S. Babak, P. T. Baker, S. Ballmer, Y. Bao, J. C. Barayoga, D. Barker, B. Barr, L. Barsotti, M. A. Barton, I. Bartos, R. Bassiri, J. Batch, J. Bauchrowitz, B. Behnke, A. S. Bell, C. Bell, G. Bergmann, J. M. Berliner, A. Bertolini, J. Betzwieser, N. Beveridge, P. T. Beyersdorf, T. Bhadbhade, I. A. Bilenko, G. Billingsley, J. Birch, S. Biscans, E. Black, J. K. Blackburn, L. Blackburn, D. Blair, B. Bland, O. Bock, T. P. Bodiya, C. Bogan, C. Bond, R. Bork, M. Born, S. Bose, J. Bowers, P. R. Brady, V. B. Braginsky, J. E. Brau, J. Breyer, D. O. Bridges, M. Brinkmann, M. Britzger, A. F. Brooks, D. A. Brown, D. D. Brown, K. Buckland, F. Brückner, B. C. Buchler, A. Buonanno, J. Burguet-Castell, R. L. Byer, L. Cadonati, J. B. Camp, P. Campsie, K. Cannon, J. Cao, C. D. Capano, L. Carbone, S. Caride, A. D. Castiglia, S. Caudill, M. Cavaglià, C. Cepeda, T. Chalermsongsak, S. Chao, P. Charlton, X. Chen, Y. Chen, H.-S. Cho, J. H. Chow, N. Christensen, Q. Chu, S. S. Y. Chua, C. T. Y. Chung, G. Ciani, F. Clara, D. E. Clark, J. A. Clark, M. C. Junior, D. Cook, T. R. Corbitt, M. Cordier, N. Cornish, A. Corsi, C. A. Costa, M. W. Coughlin, S. Countryman, P. Couvares, D. M. Coward, M. Cowart, D. C. Coyne, K. Craig, J. D. E. Creighton, T. D. Creighton, A. Cumming, L. Cunningham, K. Dahl, M. Damjanic, S. L. Danilishin, K. Danzmann, B. Daudert, H. Daveloza, G. S. Davies, E. J. Daw, T. Dayanga, E. Deleeuw, T. Denker, T. Dent, V. Dergachev, R. DeRosa, R. DeSalvo, S. Dhurandhar, I. D. Palma, M. Díaz, A. Dietz, F. Donovan, K. L. Dooley, S. Doravari, S. Drasco, R. W. P. Drever, J. C. Driggers, Z. Du, J.-C. Dumas, S. Dwyer, T. Eberle, M. Edwards, A. Effler, P. Ehrens, S. S. Eikenberry, R. Engel, R. Essick, T. Etzel, K. Evans, M. Evans, T. Evans, M. Factourovich, S. Fairhurst, Q. Fang, B. F. Farr, W. Farr, M. Favata, D. Fazi, H. Fehrmann, D. Feldbaum, L. S. Finn, R. P. Fisher, S. Foley, E. Forsi, N. Fotopoulos, M. Frede, M. A. Frei, Z. Frei, A. Freise, R. Frey, T. T. Fricke, D. Friedrich, P. Fritschel, V. V. Frolov, M.-K. Fujimoto, P. J. Fulda, M. Fyffe, J. Gair, J. Garcia, N. Gehrels, G. Gelencser, L. Á. Gergely, S. Ghosh, J. A. Giaime, S. Giampanis, K. D. Giardina, S. Gil-Casanova, C. Gill, J. Gleason, E. Goetz, G. González, N. Gordon, M. L. Gorodetsky, S. Gossan, S. Goßler, C. Graef, P. B. Graff, A. Grant, S. Gras, C. Gray, R. J. S. Greenhalgh, A. M. Gretarsson, C. Griffo, H. Grote, K. Grover, S. Grunewald, C. Guido, E. K. Gustafson, R. Gustafson, D. Hammer, G. Hammond, J. Hanks, C. Hanna, J. Hanson, K. Haris, J. Harms, G. M. Harry, I. W. Harry, E. D. Harstad, M. T. Hartman, K. Haughian, K. Hayama, J. Heefner, M. C. Heintze, M. A. Hendry, I. S. Heng, A. W. Heptonstall, M. Heurs, M. Hewitson, S. Hild, D. Hoak, K. A. Hodge, K. Holt, M. Holtrop, T. Hong, S. Hooper, J. Hough, E. J. Howell, V. Huang, E. A. Huerta, B. Hughey, S. H. Huttner, M. Huynh, T. Huynh-Dinh, D. R. Ingram, R. Inta, T. Isogai, A. Ivanov, B. R. Iyer, K. Izumi, M. Jacobson, E. James, H. Jang, Y. J. Jang, E. Jesse, W. W. Johnson, D. Jones, D. I. Jones, R. Jones, L. Ju, P. Kalmus, V. Kalogera, S. Kandhasamy, G. Kang, J. B. Kanner, R. Kasturi, E. Katsavounidis, W. Katzman, H. Kaufer, K. Kawabe, S. Kawamura, F. Kawazoe, D. Keitel, D. B. Kelley, W. Kells, D. G. Keppel, A. Khalaidovski, F. Y. Khalili, E. A. Khazanov, B. K. Kim, C. Kim, K. Kim, N. Kim, Y.-M. Kim, P. J. King, D. L. Kinzel, J. S. Kissel, S. Klimenko, J. Kline, K. Kokeyama, V. Kondrashov, S. Koranda, W. Z. Korth, D. Kozak, C. Kozameh, A. Kremin, V. Kringel, B. Krishnan, C. Kucharczyk, G. Kuehn, P. Kumar, R. Kumar, B. J. Kuper, R. Kurdyumov, P. Kwee, P. K. Lam, M. Landry, B. Lantz, P. D. Lasky, C. Lawrie, A. Lazzarini, A. L. Roux, P. Leaci, C.-H. Lee, H. K. Lee, H. M. Lee, J. Lee, J. R. Leong, B. Levine, V. Lhuillier, A. C. Lin, V. Litvine, Y. Liu, Z. Liu, N. A. Lockerbie, D. Lodhia, K. Loew, J. Logue, A. L. Lombardi, M. Lormand, J. Lough, M. Lubinski, H. Lück, A. P. Lundgren, J. Macarthur, E. Macdonald, B. Machenschalk, M. MacInnis, D. M. Macleod, F. Magaña-Sandoval, M. Mageswaran, K. Mailand, G. Manca, I. Mandel, V. Mandic, S. Márka, Z. Márka, A. S. Markosyan,

E. Maros, I. W. Martin, R. M. Martin, D. Martinov, J. N. Marx, K. Mason, F. Matichard, L. Matone, R. A. Matzner, N. Mavalvala, G. May, G. Mazzolo, K. McAuley, R. McCarthy, D. E. McClelland, S. C. McGuire, G. McIntyre, J. McIver, G. D. Meadors, M. Mehmet, T. Meier, A. Melatos, G. Mendell, R. A. Mercer, S. Meshkov, C. Messenger, M. S. Meyer, H. Miao, J. Miller, C. M. F. Mingarelli, S. Mitra, V. P. Mitrofanov, G. Mitselmakher, R. Mittleman, B. Moe, F. Mokler, S. R. P. Mohapatra, D. Moraru, G. Moreno, T. Mori, S. R. Morriss, K. Mossavi, C. M. Mow-Lowry, C. L. Mueller, G. Mueller, S. Mukherjee, A. Mullavey, J. Munch, D. Murphy, P. G. Murray, A. Mytidis, D. N. Kumar, T. Nash, R. Nayak, V. Necula, G. Newton, T. Nguyen, E. Nishida, A. Nishizawa, A. Nitz, D. Nolting, M. E. Normandin, L. K. Nuttall, J. O'Dell, B. O'Reilly, R. O'Shaughnessy, E. Ochsner, E. Oelker, G. H. Ogin, J. J. Oh, S. H. Oh, F. Ohme, P. Oppermann, C. Osthelder, C. D. Ott, D. J. Ottaway, R. S. Ottens, J. Ou, H. Overmier, B. J. Owen, C. Padilla, A. Pai, Y. Pan, C. Pankow, M. A. Papa, H. Paris, W. Parkinson, M. Pedraza, S. Penn, C. Peralta, A. Perreca, M. Phelps, M. Pickenpack, V. Pierro, I. M. Pinto, M. Pitkin, H. J. Pletsch, J. Pöld, F. Postiglione, C. Poux, V. Predoi, T. Prestegard, L. R. Price, M. Prijatelj, S. Privitera, L. G. Prokhorov, O. Puncken, V. Quetschke, E. Quintero, R. Quitzow-James, F. J. Raab, H. Radkins, P. Raffai, S. Raja, M. Rakhmanov, C. Ramet, V. Raymond, C. M. Reed, T. Reed, S. Reid, D. H. Reitze, R. Riesen, K. Riles, M. Roberts, N. A. Robertson, E. L. Robinson, S. Roddy, C. Rodriguez, L. Rodriguez, M. Rodruck, J. G. Rollins, J. H. Romie, C. Röver, S. Rowan, A. Rüdiger, K. Ryan, F. Salemi, L. Sammut, V. Sandberg, J. Sanders, S. Sankar, V. Sannibale, L. Santamaría, I. Santiago-Prieto, G. Santostasi, B. S. Sathyaprakash, P. R. Saulson, R. L. Savage, R. Schilling, R. Schnabel, R. M. S. Schofield, D. Schuette, B. Schulz, B. F. Schutz, P. Schwinberg, J. Scott, S. M. Scott, F. Seifert, D. Sellers, A. S. Sengupta, A. Sergeev, D. A. Shaddock, M. S. Shahriar, M. Shaltev, Z. Shao, B. Shapiro, P. Shawhan, D. H. Shoemaker, T. L. Sidery, X. Siemens, D. Sigg, D. Simakov, A. Singer, L. Singer, A. M. Sintes, G. R. Skelton, B. J. J. Slagmolen, J. Slutsky, J. R. Smith, M. R. Smith, R. J. E. Smith, N. D. Smith-Lefebvre, E. J. Son, B. Sorazu, T. Souradeep, M. Stefszky, E. Steinert, J. Steinlechner, S. Steinlechner, S. Steplewski, D. Stevens, A. Stochino, R. Stone, K. A. Strain, S. E. Strigin, A. S. Stroeer, A. L. Stuver, T. Z. Summerscales, S. Susmithan, P. J. Sutton, G. Szeifert, D. Talukder, D. B. Tanner, S. P. Tarabrin, R. Taylor, M. Thomas, P. Thomas, K. A. Thorne, K. S. Thorne, E. Thrane, V. Tiwari, K. V. Tokmakov, C. Tomlinson, C. V. Torres, C. I. Torrie, G. Traylor, M. Tse, D. Ugolini, C. S. Unnikrishnan, H. Vahlbruch, M. Vallisneri, M. V. van der Sluys, A. A. van Veggel, S. Vass, R. Vaulin, A. Vecchio, P. J. Veitch, J. Veitch, K. Venkateswara, S. Verma, R. Vincent-Finley, S. Vitale, T. Vo, C. Vorvick, W. D. Vousden, S. P. Vyatchanin, A. Wade, L. Wade, M. Wade, S. J. Waldman, L. Wallace, Y. Wan, M. Wang, J. Wang, X. Wang, A. Wanner, R. L. Ward, M. Was, M. Weinert, A. J. Weinstein, R. Weiss, T. Welborn, L. Wen, P. Wessels, M. West, T. Westphal, K. Wette, J. T. Whelan, S. E. Whitcomb, A. G. Wiseman, D. J. White, B. F. Whiting, K. Wiesner, C. Wilkinson, P. A. Willems, L. Williams, R. Williams, T. Williams, J. L. Willis, B. Willke, M. Wimmer, L. Winkelmann, W. Winkler, C. C. Wipf, H. Wittel, G. Woan, R. Wooley, J. Worden, J. Yablon, I. Yakushin, H. Yamamoto, C. C. Yancey, H. Yang, D. Yeaton-Massey, S. Yoshida, H. Yum, M. Zanolin, F. Zhang, L. Zhang, C. Zhao, H. Zhu, X. J. Zhu, N. Zotov, M. E. Zucker, and J. Zweizig, "Enhanced sensitivity of the LIGO gravitational wave detector by using squeezed states of light," *Nature Photonics*, vol. 7, no. 8, pp. 613–619, Jul. 2013. [Online]. Available: https://doi.org/10.1038/nphoton.2013.177

[54] B. P. Abbott, R. Abbott, T. D. Abbott, M. R. Abernathy, F. Acernese, K. Ackley, C. Adams, T. Adams, P. Addesso, R. X. Adhikari, V. B. Adya, C. Affeldt, M. Agathos, K. Agatsuma, N. Aggarwal, O. D. Aguiar, L. Aiello, A. Ain, P. Ajith, B. Allen, A. Allocca, P. A. Altin, S. B. Anderson, W. G. Anderson, K. Arai, M. A. Arain, M. C. Araya, C. C. Arceneaux, J. S. Areeda, N. Arnaud, K. G. Arun, S. Ascenzi, G. Ashton, M. Ast, S. M. Aston, P. Astone, P. Aufmuth, C. Aulbert, S. Babak, P. Bacon, M. K. M. Bader, P. T. Baker, F. Baldaccini, G. Ballardin, S. W. Ballmer, J. C. Barayoga, S. E. Barclay, B. C. Barish, D. Barker, F. Barone, B. Barr, L. Barsotti, M. Barsuglia, D. Barta, J. Bartlett, M. A. Barton, I. Bartos, R. Bassiri, A. Basti, J. C. Batch, C. Baune, V. Bavigadda,

M. Bazzan, B. Behnke, M. Bejger, C. Belczynski, A. S. Bell, C. J. Bell, B. K. Berger, J. Bergman, G. Bergmann, C. P. L. Berry, D. Bersanetti, A. Bertolini, J. Betzwieser, S. Bhagwat, R. Bhandare, I. A. Bilenko, G. Billingsley, J. Birch, R. Birney, O. Birnholtz, S. Biscans, A. Bisht, M. Bitossi, C. Biwer, M. A. Bizouard, J. K. Blackburn, C. D. Blair, D. G. Blair, R. M. Blair, S. Bloemen, O. Bock, T. P. Bodiya, M. Boer, G. Bogaert, C. Bogan, A. Bohe, P. Bojtos, C. Bond, F. Bondu, R. Bonnand, B. A. Boom, R. Bork, V. Boschi, S. Bose, Y. Bouffanais, A. Bozzi, C. Bradaschia, P. R. Brady, V. B. Braginsky, M. Branchesi, J. E. Brau, T. Briant, A. Brillet, M. Brinkmann, V. Brisson, P. Brockill, A. F. Brooks, D. A. Brown, D. D. Brown, N. M. Brown, C. C. Buchanan, A. Buikema, T. Bulik, H. J. Bulten, A. Buonanno, D. Buskulic, C. Buy, R. L. Byer, M. Cabero, L. Cadonati, G. Cagnoli, C. Cahillane, J. C. Bustillo, T. Callister, E. Calloni, J. B. Camp, K. C. Cannon, J. Cao, C. D. Capano, E. Capocasa, F. Carbognani, S. Caride, J. C. Diaz, C. Casentini, S. Caudill, M. Cavaglià, F. Cavalier, R. Cavalieri, G. Cella, C. B. Cepeda, L. C. Baiardi, G. Cerretani, E. Cesarini, R. Chakraborty, T. Chalermsongsak, S. J. Chamberlin, M. Chan, S. Chao, P. Charlton, E. Chassande-Mottin, H. Y. Chen, Y. Chen, C. Cheng, A. Chincarini, A. Chiummo, H. S. Cho, M. Cho, J. H. Chow, N. Christensen, Q. Chu, S. Chua, S. Chung, G. Ciani, F. Clara, J. A. Clark, F. Cleva, E. Coccia, P.-F. Cohadon, A. Colla, C. G. Collette, L. Cominsky, M. Constancio, A. Conte, L. Conti, D. Cook, T. R. Corbitt, N. Cornish, A. Corsi, S. Cortese, C. A. Costa, M. W. Coughlin, S. B. Coughlin, J.-P. Coulon, S. T. Countryman, P. Couvares, E. E. Cowan, D. M. Coward, M. J. Cowart, D. C. Coyne, R. Coyne, K. Craig, J. D. E. Creighton, T. D. Creighton, J. Cripe, S. G. Crowder, A. M. Cruise, A. Cumming, L. Cunningham, E. Cuoco, T. D. Canton, S. L. Danilishin, S. D'Antonio, K. Danzmann, N. S. Darman, C. F. Da Silva Costa, V. Dattilo, I. Dave, H. P. Daveloza, M. Davier, G. S. Davies, E. J. Daw, R. Day, S. De, D. DeBra, G. Debreczeni, J. Degallaix, M. De Laurentis, S. Deléglise, W. Del Pozzo, T. Denker, T. Dent, H. Dereli, V. Dergachev, R. T. DeRosa, R. De Rosa, R. DeSalvo, S. Dhurandhar, M. C. Díaz, L. Di Fiore, M. Di Giovanni, A. Di Lieto, S. Di Pace, I. Di Palma, A. Di Virgilio, G. Dojcinoski, V. Dolique, F. Donovan, K. L. Dooley, S. Doravari, R. Douglas, T. P. Downes, M. Drago, R. W. P. Drever, J. C. Driggers, Z. Du, M. Ducrot, S. E. Dwyer, T. B. Edo, M. C. Edwards, A. Effler, H.-B. Eggenstein, P. Ehrens, J. Eichholz, S. S. Eikenberry, W. Engels, R. C. Essick, T. Etzel, M. Evans, T. M. Evans, R. Everett, M. Factourovich, V. Fafone, H. Fair, S. Fairhurst, X. Fan, Q. Fang, S. Farinon, B. Farr, W. M. Farr, M. Favata, M. Fays, H. Fehrmann, M. M. Fejer, D. Feldbaum, I. Ferrante, E. C. Ferreira, F. Ferrini, F. Fidecaro, L. S. Finn, I. Fiori, D. Fiorucci, R. P. Fisher, R. Flaminio, M. Fletcher, H. Fong, J.-D. Fournier, S. Franco, S. Frasca, F. Frasconi, M. Frede, Z. Frei, A. Freise, R. Frey, V. Frey, T. T. Fricke, P. Fritschel, V. V. Frolov, P. Fulda, M. Fyffe, H. A. G. Gabbard, J. R. Gair, L. Gammaitoni, S. G. Gaonkar, F. Garufi, A. Gatto, G. Gaur, N. Gehrels, G. Gemme, B. Gendre, E. Genin, A. Gennai, J. George, L. Gergely, V. Germain, A. Ghosh, A. Ghosh, S. Ghosh, J. A. Giaime, K. D. Giardina, A. Giazotto, K. Gill, A. Glaefke, J. R. Gleason, E. Goetz, R. Goetz, L. Gondan, G. González, J. M. G. Castro, A. Gopakumar, N. A. Gordon, M. L. Gorodetsky, S. E. Gossan, M. Gosselin, R. Gouaty, C. Graef, P. B. Graff, M. Granata, A. Grant, S. Gras, C. Gray, G. Greco, A. C. Green, R. J. S. Greenhalgh, P. Groot, H. Grote, S. Grunewald, G. M. Guidi, X. Guo, A. Gupta, M. K. Gupta, K. E. Gushwa, E. K. Gustafson, R. Gustafson, J. J. Hacker, B. R. Hall, E. D. Hall, G. Hammond, M. Haney, M. M. Hanke, J. Hanks, C. Hanna, M. D. Hannam, J. Hanson, T. Hardwick, J. Harms, G. M. Harry, I. W. Harry, M. J. Hart, M. T. Hartman, C.-J. Haster, K. Haughian, J. Healy, J. Heefner, A. Heidmann, M. C. Heintze, G. Heinzel, H. Heitmann, P. Hello, G. Hemming, M. Hendry, I. S. Heng, J. Hennig, A. W. Heptonstall, M. Heurs, S. Hild, D. Hoak, K. A. Hodge, D. Hofman, S. E. Hollitt, K. Holt, D. E. Holz, P. Hopkins, D. J. Hosken, J. Hough, E. A. Houston, E. J. Howell, Y. M. Hu, S. Huang, E. A. Huerta, D. Huet, B. Hughey, S. Husa, S. H. Huttner, T. Huynh-Dinh, A. Idrisy, N. Indik, D. R. Ingram, R. Inta, H. N. Isa, J.-M. Isac, M. Isi, G. Islas, T. Isogai, B. R. Iyer, K. Izumi, M. B. Jacobson, T. Jacqmin, H. Jang, K. Jani, P. Jaranowski, S. Jawahar, F. Jiménez-Forteza, W. W. Johnson, N. K. Johnson-McDaniel, D. I. Jones, R. Jones, R. J. G. Jonker, L. Ju, K. Haris, C. V. Kalaghatgi, V. Kalogera, S. Kandhasamy, G. Kang, J. B. Kanner, S. Karki, M. Kasprzack, E. Katsavounidis, W. Katzman, S. Kaufer,

T. Kaur, K. Kawabe, F. Kawazoe, F. Kéfélian, M. S. Kehl, D. Keitel, D. B. Kelley, W. Kells, R. Kennedy, D. G. Keppel, J. S. Key, A. Khalaidovski, F. Y. Khalili, I. Khan, S. Khan, Z. Khan, E. A. Khazanov, N. Kijbunchoo, C. Kim, J. Kim, K. Kim, N.-G. Kim, N. Kim, Y.-M. Kim, E. J. King, P. J. King, D. L. Kinzel, J. S. Kissel, L. Kleybolte, S. Klimenko, S. M. Koehlenbeck, K. Kokeyama, S. Koley, V. Kondrashov, A. Kontos, S. Koranda, M. Korobko, W. Z. Korth, I. Kowalska, D. B. Kozak, V. Kringel, B. Krishnan, A. Królak, C. Krueger, G. Kuehn, P. Kumar, R. Kumar, L. Kuo, A. Kutynia, P. Kwee, B. D. Lackey, M. Landry, J. Lange, B. Lantz, P. D. Lasky, A. Lazzarini, C. Lazzaro, P. Leaci, S. Leavey, E. O. Lebigot, C. H. Lee, H. K. Lee, H. M. Lee, K. Lee, A. Lenon, M. Leonardi, J. R. Leong, N. Leroy, N. Letendre, Y. Levin, B. M. Levine, T. G. F. Li, A. Libson, T. B. Littenberg, N. A. Lockerbie, J. Logue, A. L. Lombardi, L. T. London, J. E. Lord, M. Lorenzini, V. Loriette, M. Lormand, G. Losurdo, J. D. Lough, C. O. Lousto, G. Lovelace, H. Lück, A. P. Lundgren, J. Luo, R. Lynch, Y. Ma, T. MacDonald, B. Machenschalk, M. MacInnis, D. M. Macleod, F. Magaña Sandoval, R. M. Magee, M. Mageswaran, E. Majorana, I. Maksimovic, V. Malvezzi, N. Man, I. Mandel, V. Mandic, V. Mangano, G. L. Mansell, M. Manske, M. Mantovani, F. Marchesoni, F. Marion, S. Márka, Z. Márka, A. S. Markosyan, E. Maros, F. Martelli, L. Martellini, I. W. Martin, R. M. Martin, D. V. Martynov, J. N. Marx, K. Mason, A. Masserot, T. J. Massinger, M. Masso-Reid, F. Matichard, L. Matone, N. Mavalvala, N. Mazumder, G. Mazzolo, R. McCarthy, D. E. McClelland, S. McCormick, S. C. McGuire, G. McIntyre, J. McIver, D. J. McManus, S. T. McWilliams, D. Meacher, G. D. Meadors, J. Meidam, A. Melatos, G. Mendell, D. Mendoza-Gandara, R. A. Mercer, E. Merilh, M. Merzougui, S. Meshkov, C. Messenger, C. Messick, P. M. Meyers, F. Mezzani, H. Miao, C. Michel, H. Middleton, E. E. Mikhailov, L. Milano, J. Miller, M. Millhouse, Y. Minenkov, J. Ming, S. Mirshekari, C. Mishra, S. Mitra, V. P. Mitrofanov, G. Mitselmakher, R. Mittleman, A. Moggi, M. Mohan, S. R. P. Mohapatra, M. Montani, B. C. Moore, C. J. Moore, D. Moraru, G. Moreno, S. R. Morriss, K. Mossavi, B. Mours, C. M. Mow-Lowry, C. L. Mueller, G. Mueller, A. W. Muir, A. Mukherjee, D. Mukherjee, S. Mukherjee, N. Mukund, A. Mullavey, J. Munch, D. J. Murphy, P. G. Murray, A. Mytidis, I. Nardecchia, L. Naticchioni, R. K. Nayak, V. Necula, K. Nedkova, G. Nelemans, M. Neri, A. Neunzert, G. Newton, T. T. Nguyen, A. B. Nielsen, S. Nissanke, A. Nitz, F. Nocera, D. Nolting, M. E. N. Normandin, L. K. Nuttall, J. Oberling, E. Ochsner, J. O'Dell, E. Oelker, G. H. Ogin, J. J. Oh, S. H. Oh, F. Ohme, M. Oliver, P. Oppermann, R. J. Oram, B. O'Reilly, R. O'Shaughnessy, C. D. Ott, D. J. Ottaway, R. S. Ottens, H. Overmier, B. J. Owen, A. Pai, S. A. Pai, J. R. Palamos, O. Palashov, C. Palomba, A. Pal-Singh, H. Pan, Y. Pan, C. Pankow, F. Pannarale, B. C. Pant, F. Paoletti, A. Paoli, M. A. Papa, H. R. Paris, W. Parker, D. Pascucci, A. Pasqualetti, R. Passaquieti, D. Passuello, B. Patricelli, Z. Patrick, B. L. Pearlstone, M. Pedraza, R. Pedurand, L. Pekowsky, A. Pele, S. Penn, A. Perreca, H. P. Pfeiffer, M. Phelps, O. Piccinni, M. Pichot, M. Pickenpack, F. Piergiovanni, V. Pierro, G. Pillant, L. Pinard, I. M. Pinto, M. Pitkin, J. H. Poeld, R. Poggiani, P. Popolizio, A. Post, J. Powell, J. Prasad, V. Predoi, S. S. Premachandra, T. Prestegard, L. R. Price, M. Prijatelj, M. Principe, S. Privitera, R. Prix, G. A. Prodi, L. Prokhorov, O. Puncken, M. Punturo, P. Puppo, M. Pürrer, H. Qi, J. Qin, V. Quetschke, E. A. Quintero, R. Quitzow-James, F. J. Raab, D. S. Rabeling, H. Radkins, P. Raffai, S. Raja, M. Rakhmanov, C. R. Ramet, P. Rapagnani, V. Raymond, M. Razzano, V. Re, J. Read, C. M. Reed, T. Regimbau, L. Rei, S. Reid, D. H. Reitze, H. Rew, S. D. Reyes, F. Ricci, K. Riles, N. A. Robertson, R. Robie, F. Robinet, A. Rocchi, L. Rolland, J. G. Rollins, V. J. Roma, J. D. Romano, R. Romano, G. Romanov, J. H. Romie, D. Rosińska, S. Rowan, A. Rüdiger, P. Ruggi, K. Ryan, S. Sachdev, T. Sadecki, L. Sadeghian, L. Salconi, M. Saleem, F. Salemi, A. Samajdar, L. Sammut, L. M. Sampson, E. J. Sanchez, V. Sandberg, B. Sandeen, G. H. Sanders, J. R. Sanders, B. Sassolas, B. S. Sathyaprakash, P. R. Saulson, O. Sauter, R. L. Savage, A. Sawadsky, P. Schale, R. Schilling, J. Schmidt, P. Schmidt, R. Schnabel, R. M. S. Schofield, A. Schönbeck, E. Schreiber, D. Schuette, B. F. Schutz, J. Scott, S. M. Scott, D. Sellers, A. S. Sengupta, D. Sentenac, V. Sequino, A. Sergeev, G. Serna, Y. Setyawati, A. Sevigny, D. A. Shaddock, T. Shaffer, S. Shah, M. S. Shahriar, M. Shaltev, Z. Shao, B. Shapiro, P. Shawhan, A. Sheperd, D. H. Shoemaker, D. M. Shoemaker, K. Siellez, X. Siemens, D. Sigg, A. D. Silva, D. Simakov, A. Singer, L. P.

Singer, A. Singh, R. Singh, A. Singhal, A. M. Sintes, B. J. J. Slagmolen, J. R. Smith, M. R. Smith, N. D. Smith, R. J. E. Smith, E. J. Son, B. Sorazu, F. Sorrentino, T. Souradeep, A. K. Srivastava, A. Staley, M. Steinke, J. Steinlechner, S. Steinlechner, D. Steinmeyer, B. C. Stephens, S. P. Stevenson, R. Stone, K. A. Strain, N. Straniero, G. Stratta, N. A. Strauss, S. Strigin, R. Sturani, A. L. Stuver, T. Z. Summerscales, L. Sun, P. J. Sutton, B. L. Swinkels, M. J. Szczepańczyk, M. Tacca, D. Talukder, D. B. Tanner, M. Tápai, S. P. Tarabrin, A. Taracchini, R. Taylor, T. Theeg, M. P. Thirugnanasambandam, E. G. Thomas, M. Thomas, P. Thomas, K. A. Thorne, K. S. Thorne, E. Thrane, S. Tiwari, V. Tiwari, K. V. Tokmakov, C. Tomlinson, M. Tonelli, C. V. Torres, C. I. Torrie, D. Töyrä, F. Travasso, G. Traylor, D. Trifirò, M. C. Tringali, L. Trozzo, M. Tse, M. Turconi, D. Tuyenbayev, D. Ugolini, C. S. Unnikrishnan, A. L. Urban, S. A. Usman, H. Vahlbruch, G. Vajente, G. Valdes, M. Vallisneri, N. van Bakel, M. van Beuzekom, J. F. J. van den Brand, C. Van Den Broeck, D. C. Vander-Hyde, L. van der Schaaf, J. V. van Heijningen, A. A. van Veggel, M. Vardaro, S. Vass, M. Vasúth, R. Vaulin, A. Vecchio, G. Vedovato, J. Veitch, P. J. Veitch, K. Venkateswara, D. Verkindt, F. Vetrano, A. Viceré, S. Vinciguerra, D. J. Vine, J.-Y. Vinet, S. Vitale, T. Vo, H. Vocca, C. Vorvick, D. Voss, W. D. Vousden, S. P. Vyatchanin, A. R. Wade, L. E. Wade, M. Wade, S. J. Waldman, M. Walker, L. Wallace, S. Walsh, G. Wang, H. Wang, M. Wang, X. Wang, Y. Wang, H. Ward, R. L. Ward, J. Warner, M. Was, B. Weaver, L.-W. Wei, M. Weinert, A. J. Weinstein, R. Weiss, T. Welborn, L. Wen, P. Weßels, T. Westphal, K. Wette, J. T. Whelan, S. E. Whitcomb, D. J. White, B. F. Whiting, K. Wiesner, C. Wilkinson, P. A. Willems, L. Williams, R. D. Williams, A. R. Williamson, J. L. Willis, B. Willke, M. H. Wimmer, L. Winkelmann, W. Winkler, C. C. Wipf, A. G. Wiseman, H. Wittel, G. Woan, J. Worden, J. L. Wright, G. Wu, J. Yablon, I. Yakushin, W. Yam, H. Yamamoto, C. C. Yancey, M. J. Yap, H. Yu, M. Yvert, A. Zadrożny, L. Zangrando, M. Zanolin, J.-P. Zendri, M. Zevin, F. Zhang, L. Zhang, M. Zhang, Y. Zhang, C. Zhao, M. Zhou, Z. Zhou, X. J. Zhu, M. E. Zucker, S. E. Zuraw, and J. Zweizig, "Observation of gravitational waves from a binary black hole merger," *Phys. Rev. Lett.*, vol. 116, p. 061102, Feb 2016. [Online]. Available: https://link.aps.org/doi/10.1103/PhysRevLett.116.061102

[55] S. Colombo, E. Pedrozo-Peñafiel, A. F. Adiyatullin, Z. Li, E. Mendez, C. Shu, and V. Vuletić, "Time-reversal-based quantum metrology with many-body entangled states," *Nature Physics*, vol. 18, no. 8, pp. 925–930, Jul. 2022. [Online]. Available: https://doi.org/10.1038/s41567-022-01653-5

[56] G. P. Greve, C. Luo, B. Wu, and J. K. Thompson, "Entanglement-enhanced matter-wave interferometry in a high-finesse cavity," *Nature*, vol. 610, no. 7932, pp. 472–477, Oct. 2022. [Online]. Available: https://doi.org/10.1038/s41586-022-05197-9

[57] B. K. Malia, Y. Wu, J. Martínez-Rincón, and M. A. Kasevich, "Distributed quantum sensing with mode-entangled spin-squeezed atomic states," *Nature*, Nov. 2022. [Online]. Available: https://doi.org/10.1038/s41586-022-05363-z

[58] L. Hu, N. Poli, L. Salvi, and G. M. Tino, "Atom interferometry with the Sr optical clock transition," *Phys. Rev. Lett.*, vol. 119, p. 263601, Dec 2017. [Online]. Available: https://link.aps.org/doi/10.1103/PhysRevLett.119.263601

[59] L. Hu, E. Wang, L. Salvi, J. N. Tinsley, G. M. Tino, and N. Poli, "Sr atom interferometry with the optical clock transition as a gravimeter and a gravity gradiometer," *Classical and Quantum Gravity*, vol. 37, no. 1, p. 014001, Nov 2019. [Online]. Available: https://iopscience.iop.org/article/10.1088/1361-6382/ab4d18

[60] L. Salvi, "Towards atom interferometry beyond the Standard Quantum Limit with strontium atoms," Ph.D. dissertation, Università degli Studi di Firenze, Firenze, 2017.

[61] F. Riehle, T. Kisters, A. Witte, J. Helmcke, and C. J. Bordé, "Optical ramsey spectroscopy in a rotating frame: Sagnac effect in a matter-wave interferometer," *Phys. Rev. Lett.*, vol. 67, pp. 177–180, Jul 1991. [Online]. Available: https://link.aps.org/doi/10.1103/PhysRevLett.67.177

[62] M. Kasevich and S. Chu, "Measurement of the gravitational acceleration of an atom with a light-pulse atom interferometer," *Applied Physics B Photophysics and Laser Chemistry*, vol. 54, no. 5, pp. 321–332, May 1992. [Online]. Available: https://doi.org/10.1007/bf00325375

[63] A. Peters, "High precision gravity measurements using atom interferometry," Ph.D. dissertation, Stanford University, Stanford, May 1998. [Online]. Available: https://web.stanford.edu/group/kasevich/cgi-bin/wordpress/wp-content/uploads/2012/09/PachimsThesis.pdf

[64] A. Peters, K. Y. Chung, and S. Chu, "Measurement of gravitational acceleration by dropping atoms," *Nature*, vol. 400, no. 6747, pp. 849–852, Aug. 1999. [Online]. Available: https://doi.org/10.1038/23655

[65] ——, "High-precision gravity measurements using atom interferometry," *Metrologia*, vol. 38, no. 1, pp. 25–61, Feb. 2001. [Online]. Available: https://doi.org/10.1088/0026-1394/38/1/4

[66] C. J. Bordé, "Theoretical tools for atom optics and interferometry," *Comptes Rendus de l'Académie des Sciences - Series IV - Physics*, vol. 2, no. 3, pp. 509–530, 2001. [Online]. Available: http://www.sciencedirect.com/science/article/pii/S1296214701011866

[67] A. A. Michelson, "The relative motion of the earth and of the luminiferous ether," *American Journal of Science*, vol. s3-22, no. 128, pp. 120–129, Aug. 1881. [Online]. Available: https://doi.org/10.2475/ajs.s3-22.128.120

[68] A. A. Michelson and E. W. Morley, "On the relative motion of the earth and the luminiferous ether," *American Journal of Science*, vol. s3-34, no. 203, pp. 333–345, Nov. 1887. [Online]. Available: https://doi.org/10.2475/ajs.s3-34.203.333

[69] C. J. Foot, *Atomic Physics*, ser. Oxford Master Series in Physics. London, England: Oxford University Press, nov 2004, ISBN: 9780198506966.

[70] T. Mazzoni, X. Zhang, R. Del Aguila, L. Salvi, N. Poli, and G. M. Tino, "Large-momentum-transfer bragg interferometer with strontium atoms," *Phys. Rev. A*, vol. 92, p. 053619, Nov 2015. [Online]. Available: https://link.aps.org/doi/10.1103/PhysRevA.92.053619

[71] J. Bouman and M. J. Fuchs, "GOCE gravity gradients versus global gravity field models," *Geophysical Journal International*, vol. 189, no. 2, pp. 846–850, Mar. 2012. [Online]. Available: https://doi.org/10.1111/j.1365-246x.2012.05428.x

[72] F. Sorrentino, Y.-H. Lien, G. Rosi, L. Cacciapuoti, M. Prevedelli, and G. M. Tino, "Sensitive gravity-gradiometry with atom interferometry: progress towards an improved determination of the gravitational constant," *New Journal of Physics*, vol. 12, no. 9, p. 095009, Sep. 2010. [Online]. Available: https://doi.org/10.1088/1367-2630/12/9/095009

[73] L. Pezzè and A. Smerzi, "Heisenberg-limited noisy atomic clock using a hybrid coherent and squeezed state protocol," *Phys. Rev. Lett.*, vol. 125, p. 210503, Nov 2020. [Online]. Available: https://link.aps.org/doi/10.1103/PhysRevLett.125.210503

[74] A. Einstein, B. Podolsky, and N. Rosen, "Can quantum-mechanical description of physical reality be considered complete?" *Phys. Rev.*, vol. 47, pp. 777–780, May 1935. [Online]. Available: https://link.aps.org/doi/10.1103/PhysRev.47.777

[75] J. S. Bell, "On the einstein podolsky rosen paradox," *Physics Physique Fizika*, vol. 1, pp. 195–200, Nov 1964. [Online]. Available: https://link.aps.org/doi/10.1103/PhysicsPhysiqueFizika.1.195

[76] B. Hensen, H. Bernien, A. E. Dréau, A. Reiserer, N. Kalb, M. S. Blok, J. Ruitenberg, R. F. L. Vermeulen, R. N. Schouten, C. Abellán, W. Amaya, V. Pruneri, M. W. Mitchell, M. Markham, D. J. Twitchen, D. Elkouss, S. Wehner, T. H. Taminiau, and R. Hanson, "Loophole-free bell inequality violation using electron spins separated by 1.3 kilometres," *Nature*, vol. 526, no. 7575, pp. 682–686, Oct. 2015. [Online]. Available: https://doi.org/10.1038/nature15759

[77] W. Heisenberg, "Über den anschaulichen inhalt der quantentheoretischen kinematik und mechanik," *Zeitschrift für Physik*, vol. 43, no. 3-4, pp. 172–198, Mar. 1927. [Online]. Available: https://doi.org/10.1007/bf01397280

[78] B. Braverman, A. Kawasaki, E. Pedrozo-Peñafiel, S. Colombo, C. Shu, Z. Li, E. Mendez, M. Yamoah, L. Salvi, D. Akamatsu, Y. Xiao, and V. Vuletić, "Near-unitary spin squeezing in $^{171}$Yb," *Phys. Rev. Lett.*, vol. 122, p. 223203, Jun 2019. [Online]. Available: https://link.aps.org/doi/10.1103/PhysRevLett.122.223203

[79] A. André, A. S. Sørensen, and M. D. Lukin, "Stability of atomic clocks based on entangled atoms," *Phys. Rev. Lett.*, vol. 92, p. 230801, Jun 2004. [Online]. Available: https://link.aps.org/doi/10.1103/PhysRevLett.92.230801

[80] I. D. Leroux, M. H. Schleier-Smith, and V. Vuletić, "Orientation-dependent entanglement lifetime in a squeezed atomic clock," *Phys. Rev. Lett.*, vol. 104, p. 250801, Jun 2010. [Online]. Available: https://link.aps.org/doi/10.1103/PhysRevLett.104.250801

[81] M. O. Scully and M. S. Zubairy, *Quantum Optics*. Cambridge, England: Cambridge University Press, Jun. 2012, ISBN: 9780511813993.

[82] L. Salvi, N. Poli, V. Vuletić, and G. M. Tino, "Squeezing on momentum states for atom interferometry," *Physical Review Letters*, vol. 120, p. 033601, Jan 2018. [Online]. Available: https://link.aps.org/doi/10.1103/PhysRevLett.120.033601

[83] M. H. Schleier-Smith, I. D. Leroux, and V. Vuletić, "States of an ensemble of two-level atoms with reduced quantum uncertainty," *Phys. Rev. Lett.*, vol. 104, p. 073604, Feb 2010. [Online]. Available: https://link.aps.org/doi/10.1103/PhysRevLett.104.073604

[84] O. Hosten, N. J. Engelsen, R. Krishnakumar, and M. A. Kasevich, "Measurement noise 100 times lower than the quantum-projection limit using entangled atoms," *Nature*, vol. 529, no. 7587, pp. 505–508, Jan. 2016. [Online]. Available: https://doi.org/10.1038/nature16176

[85] K. C. Cox, G. P. Greve, J. M. Weiner, and J. K. Thompson, "Deterministic squeezed states with collective measurements and feedback," *Phys. Rev. Lett.*, vol. 116, p. 093602, Mar 2016. [Online]. Available: https://link.aps.org/doi/10.1103/PhysRevLett.116.093602

[86] Z. Chen, J. G. Bohnet, J. M. Weiner, K. C. Cox, and J. K. Thompson, "Cavity-aided nondemolition measurements for atom counting and spin squeezing," *Phys. Rev. A*, vol. 89, p. 043837, Apr 2014. [Online]. Available: https://link.aps.org/doi/10.1103/PhysRevA.89.043837

[87] I. S. Madjarov, J. P. Covey, A. L. Shaw, J. Choi, A. Kale, A. Cooper, H. Pichler, V. Schkolnik, J. R. Williams, and M. Endres, "High-fidelity entanglement and detection of alkaline-earth rydberg atoms," *Nature Physics*, vol. 16, no. 8, pp. 857–861, May 2020. [Online]. Available: https://doi.org/10.1038/s41567-020-0903-z

[88] R. C. Teixeira, A. Larrouy, A. Muni, L. Lachaud, J.-M. Raimond, S. Gleyzes, and M. Brune, "Preparation of long-lived, non-autoionizing circular rydberg states of strontium," *Phys. Rev. Lett.*, vol. 125, p. 263001, Dec 2020. [Online]. Available: https://link.aps.org/doi/10.1103/PhysRevLett.125.263001

[89] J. Rudolph, T. Wilkason, M. Nantel, H. Swan, C. M. Holland, Y. Jiang, B. E. Garber, S. P. Carman, and J. M. Hogan, "Large momentum transfer clock atom interferometry on the 689 nm intercombination line of strontium," *Phys. Rev. Lett.*, vol. 124, p. 083604, Feb 2020. [Online]. Available: https://link.aps.org/doi/10.1103/PhysRevLett.124.083604

[90] M. Yasuda, T. Kishimoto, M. Takamoto, and H. Katori, "Photoassociation spectroscopy of $^{88}$Sr: Reconstruction of the wave function near the last node," *Phys. Rev. A*, vol. 73, p. 011403, Jan 2006. [Online]. Available: https://link.aps.org/doi/10.1103/PhysRevA.73.011403

[91] T. Kurosu and F. Shimizu, "Laser cooling and trapping of calcium and strontium," *Japanese Journal of Applied Physics*, vol. 29, no. Part 2, No. 11, pp. L2127–L2129, Nov. 1990. [Online]. Available: https://doi.org/10.1143/jjap.29.l2127

[92] X. Xu, T. H. Loftus, J. L. Hall, A. Gallagher, and J. Ye, "Cooling and trapping of atomic strontium," *Journal of the Optical Society of America B*, vol. 20, no. 5, p. 968, May 2003. [Online]. Available: https://doi.org/10.1364/josab.20.000968

[93] F. Sorrentino, G. Ferrari, N. Poli, R. Drullinger, and G. M. Tino, "Laser cooling and trapping of atomic strontium for ultracold atoms physics, high-precision spectroscopy and quantum sensors," *Modern Physics Letters B*, vol. 20, no. 21, pp. 1287–1320, Sep. 2006. [Online]. Available: https://doi.org/10.1142/s0217984906011682

[94] L. R. Hunter, W. A. Walker, and D. S. Weiss, "Observation of an atomic stark–electric-quadrupole interference," *Phys. Rev. Lett.*, vol. 56, pp. 823–826, Feb 1986. [Online]. Available: https://link.aps.org/doi/10.1103/PhysRevLett.56.823

[95] C. W. Bauschlicher, S. R. Langhoff, and H. Partridge, "The radiative lifetime of the $^1D_2$ state of Ca and Sr: a core-valence treatment," *Journal of Physics B: Atomic and Molecular Physics*, vol. 18, no. 8, pp. 1523–1532, Apr. 1985. [Online]. Available: https://doi.org/10.1088/0022-3700/18/8/011

[96] M. Yasuda and H. Katori, "Lifetime measurement of the $^3P_2$ metastable state of strontium atoms," *Phys. Rev. Lett.*, vol. 92, p. 153004, Apr 2004. [Online]. Available: https://link.aps.org/doi/10.1103/PhysRevLett.92.153004

[97] T. P. Dinneen, K. R. Vogel, E. Arimondo, J. L. Hall, and A. Gallagher, "Cold collisions of $Sr^* - Sr$ in a magneto-optical trap," *Phys. Rev. A*, vol. 59, pp. 1216–1222, Feb 1999. [Online]. Available: https://link.aps.org/doi/10.1103/PhysRevA.59.1216

[98] D. S. Barker, B. J. Reschovsky, N. C. Pisenti, and G. K. Campbell, "Enhanced magnetic trap loading for atomic strontium," *Phys. Rev. A*, vol. 92, p. 043418, Oct 2015. [Online]. Available: https://link.aps.org/doi/10.1103/PhysRevA.92.043418

[99] N. Poli, R. E. Drullinger, G. Ferrari, J. Léonard, F. Sorrentino, and G. M. Tino, "Cooling and trapping of ultracold strontium isotopic mixtures," *Phys. Rev. A*, vol. 71, p. 061403, Jun 2005. [Online]. Available: https://link.aps.org/doi/10.1103/PhysRevA.71.061403

[100] N. Poli, G. Ferrari, M. Prevedelli, F. Sorrentino, R. Drullinger, and G. Tino, "Laser sources for precision spectroscopy on atomic strontium," *Spectrochimica Acta Part A: Molecular and Biomolecular Spectroscopy*, vol. 63, no. 5, pp. 981–986, Apr. 2006. [Online]. Available: https://doi.org/10.1016/j.saa.2005.10.024

[101] S. Stellmer and F. Schreck, "Reservoir spectroscopy of $5s5p\ ^3P_2$–$5snd\ ^3D_{1,2,3}$ transitions in strontium," *Phys. Rev. A*, vol. 90, p. 022512, Aug 2014. [Online]. Available: https://link.aps.org/doi/10.1103/PhysRevA.90.022512

[102] H. J. Andrä, H.-J. Plöhn, W. Wittmann, A. Gaupp, J. O. Stoner, and M. Gaillard, "Lifetimes of levels in neutral strontium (Sr I)*," *Journal of the Optical Society of America*, vol. 65, no. 12, p. 1410, Dec. 1975. [Online]. Available: https://doi.org/10.1364/josa.65.001410

[103] I. J. Ma, G. zu Putlitz, and G. Schütte, "Lebensdauer des $5s5p\ ^3P_1$-zustands von strontium," *Zeitschrift für Physik A Hadrons and nuclei*, vol. 208, no. 3, pp. 276–285, Jun. 1968. [Online]. Available: https://doi.org/10.1007/bf01379918

[104] R. Drozdowski, M. Ignaciuk, J. Kwela, and J. Heldt, "Radiative lifetimes of the lowest $^3P_1$ metastable states of Ca and Sr," *Zeitschrift für Physik D Atoms, Molecules and Clusters*, vol. 41, no. 2, pp. 125–131, Jul. 1997. [Online]. Available: https://doi.org/10.1007/s004600050300

[105] H. Katori, T. Ido, Y. Isoya, and M. Kuwata-Gonokami, "Magneto-optical trapping and cooling of strontium atoms down to the photon recoil temperature," *Phys. Rev. Lett.*,

vol. 82, pp. 1116–1119, Feb 1999. [Online]. Available: https://link.aps.org/doi/10.1103/PhysRevLett.82.1116

[106] T. Mukaiyama, H. Katori, T. Ido, Y. Li, and M. Kuwata-Gonokami, "Recoil-limited laser cooling of $^{87}$Sr atoms near the fermi temperature," *Phys. Rev. Lett.*, vol. 90, p. 113002, Mar 2003. [Online]. Available: https://link.aps.org/doi/10.1103/PhysRevLett.90.113002

[107] J. A. Muniz, D. J. Young, J. R. K. Cline, and J. K. Thompson, "Cavity-QED measurements of the $^{87}$Sr millihertz optical clock transition and determination of its natural linewidth," *Phys. Rev. Research*, vol. 3, p. 023152, May 2021. [Online]. Available: https://link.aps.org/doi/10.1103/PhysRevResearch.3.023152

[108] A. V. Taichenachev, V. I. Yudin, C. W. Oates, C. W. Hoyt, Z. W. Barber, and L. Hollberg, "Magnetic field-induced spectroscopy of forbidden optical transitions with application to lattice-based optical atomic clocks," *Phys. Rev. Lett.*, vol. 96, p. 083001, Mar 2006. [Online]. Available: https://link.aps.org/doi/10.1103/PhysRevLett.96.083001

[109] H. Katori, M. Takamoto, V. G. Pal'chikov, and V. D. Ovsiannikov, "Ultrastable optical clock with neutral atoms in an engineered light shift trap," *Phys. Rev. Lett.*, vol. 91, p. 173005, Oct 2003. [Online]. Available: https://link.aps.org/doi/10.1103/PhysRevLett.91.173005

[110] M. Takamoto and H. Katori, "Spectroscopy of the $^1S_0$–$^3P_0$ clock transition of $^{87}$Sr in an optical lattice," *Phys. Rev. Lett.*, vol. 91, p. 223001, Nov 2003. [Online]. Available: https://link.aps.org/doi/10.1103/PhysRevLett.91.223001

[111] H. Katori, K. Hashiguchi, E. Y. Il'inova, and V. D. Ovsiannikov, "Magic wavelength to make optical lattice clocks insensitive to atomic motion," *Phys. Rev. Lett.*, vol. 103, p. 153004, Oct 2009. [Online]. Available: https://link.aps.org/doi/10.1103/PhysRevLett.103.153004

[112] R. Rana, M. Höcker, and E. G. Myers, "Atomic masses of strontium and ytterbium," *Phys. Rev. A*, vol. 86, p. 050502, Nov 2012. [Online]. Available: https://link.aps.org/doi/10.1103/PhysRevA.86.050502

[113] J. R. de Laeter, J. K. Böhlke, P. D. Bièvre, H. Hidaka, H. S. Peiser, K. J. R. Rosman, and P. D. P. Taylor, "Atomic weights of the elements. review 2000 (IUPAC technical report)," *Pure and Applied Chemistry*, vol. 75, no. 6, pp. 683–800, Jan. 2003. [Online]. Available: https://doi.org/10.1351/pac200375060683

[114] L. Moore, T. Murphy, I. Barnes, and P. Paulsen, "Absolute isotopic abundance ratios and atomic weight of a reference sample of strontium," *Journal of Research of the National Bureau of Standards*, vol. 87, no. 1, p. 1, Jan. 1982. [Online]. Available: https://doi.org/10.6028/jres.087.001

[115] J. Emsley, *The Elements*, 3rd ed., ser. Oxford Chemistry Guides. London, England: Oxford University Press, Mar. 1998, ISBN: 0198558198.

[116] A. Kramida, Yu. Ralchenko, J. Reader, and and NIST ASD Team, NIST Atomic Spectra Database (ver. 5.9), National Institute of Standards and Technology, Gaithersburg, MD., 2021. [Online]. Available: https://physics.nist.gov/asd

[117] A. Antušek, P. Rodziewicz, D. Kędziera, A. Kaczmarek-Kędziera, and M. Jaszuński, "Ab initio study of NMR shielding of alkali earth metal ions in water complexes and magnetic moments of alkali earth metal nuclei," *Chemical Physics Letters*, vol. 588, pp. 57–62, Nov. 2013. [Online]. Available: https://doi.org/10.1016/j.cplett.2013.10.018

[118] E. Wang, "Cavity-enhanced measurement for the generation of spin squeezed states in strontium atom interferometry," Ph.D. dissertation, Università degli Studi di Firenze, Firenze, Jan 2021. [Online]. Available: https://flore.unifi.it/handle/2158/1234654

[119] D. A. Steck, *Classical and Modern Optics*, Jul. 2021. [Online]. Available: https://atomoptics.uoregon.edu/~dsteck/teaching/

[120] E. Wang, G. Verma, J. N. Tinsley, N. Poli, and L. Salvi, "Method for the differential measurement of phase shifts induced by atoms in an optical ring cavity," *Phys. Rev. A*, vol. 103, p. 022609, Feb 2021. [Online]. Available: https://link.aps.org/doi/10.1103/PhysRevA.103.022609

[121] S. Haroche and J. Raimond, *Exploring the Quantum: Atoms, Cavities, and Photons*. Oxford, England: Oxford University Press, 2006, ISBN: 9780198509141.

[122] K. J. Ross and B. Sonntag, "High temperature metal atom beam sources," *Review of Scientific Instruments*, vol. 66, no. 9, pp. 4409–4433, Sep. 1995. [Online]. Available: https://doi.org/10.1063/1.1145337

[123] M. Schioppo, N. Poli, M. Prevedelli, S. Falke, C. Lisdat, U. Sterr, and G. M. Tino, "A compact and efficient strontium oven for laser-cooling experiments," *Review of Scientific Instruments*, vol. 83, no. 10, p. 103101, Oct 2012. [Online]. Available: https://doi.org/10.1063/1.4756936

[124] S. Stellmer, R. Grimm, and F. Schreck, "Production of quantum-degenerate strontium gases," *Phys. Rev. A*, vol. 87, p. 013611, Jan 2013. [Online]. Available: https://link.aps.org/doi/10.1103/PhysRevA.87.013611

[125] W. D. Phillips and H. Metcalf, "Laser deceleration of an atomic beam," *Phys. Rev. Lett.*, vol. 48, pp. 596–599, Mar 1982. [Online]. Available: https://link.aps.org/doi/10.1103/PhysRevLett.48.596

[126] G. Verma, E. Wang, J. Assendelft, N. Poli, G. Rosi, G. M. Tino, and L. Salvi, "A scalable laser system at 461 nm for laser cooling and trapping of sr atoms," *Applied Physics B*, vol. 128, no. 6, May 2022. [Online]. Available: https://doi.org/10.1007/s00340-022-07815-w

[127] R. W. P. Drever, J. L. Hall, F. V. Kowalski, J. Hough, G. M. Ford, A. J. Munley, and H. Ward, "Laser phase and frequency stabilization using an optical resonator," *Applied Physics B Photophysics and Laser Chemistry*, vol. 31, no. 2, pp. 97–105, Jun 1983. [Online]. Available: https://doi.org/10.1007/bf00702605

[128] E. D. Black, "An introduction to Pound–Drever–Hall laser frequency stabilization," *American Journal of Physics*, vol. 69, no. 1, pp. 79–87, Jan 2001. [Online]. Available: https://doi.org/10.1119/1.1286663

[129] MOGLabs, "AN002: Pound-Drever-Hall locking with the FSC," 2022, accessed on 18 August 2022. [Online]. Available: https://www.moglabs.com/support/appnotes/an002-pdh-r2.pdf

[130] L. Ricci, M. Weidemüller, T. Esslinger, A. Hemmerich, C. Zimmermann, V. Vuletic, W. König, and T. Hänsch, "A compact grating-stabilized diode laser system for atomic physics," *Optics Communications*, vol. 117, no. 5-6, pp. 541–549, Jun. 1995. [Online]. Available: https://doi.org/10.1016/0030-4018(95)00146-y

[131] C. J. Hawthorn, K. P. Weber, and R. E. Scholten, "Littrow configuration tunable external cavity diode laser with fixed direction output beam," *Review of Scientific Instruments*, vol. 72, no. 12, pp. 4477–4479, Dec. 2001. [Online]. Available: https://doi.org/10.1063/1.1419217

[132] S. D. Saliba, M. Junker, L. D. Turner, and R. E. Scholten, "Mode stability of external cavity diode lasers," *Applied Optics*, vol. 48, no. 35, p. 6692, Dec. 2009. [Online]. Available: https://doi.org/10.1364/ao.48.006692

[133] X. Baillard, A. Gauguet, S. Bize, P. Lemonde, P. Laurent, A. Clairon, and P. Rosenbusch, "Interference-filter-stabilized external-cavity diode lasers," *Optics Communications*, vol. 266, no. 2, pp. 609–613, Oct. 2006. [Online]. Available: https://doi.org/10.1016/j.optcom.2006.05.011

[134] S. Palmer, A. Boes, G. Ren, T. G. Nguyen, S. J. Tempone-Wiltshire, N. Longhurst, P. M. Farrell, A. Steiner, C. D. Marciniak, T. Monz, A. Mitchell, and R. E. Scholten, "High bandwidth frequency modulation of an external cavity diode laser using an intracavity

lithium niobate electro-optic modulator as output coupler," *APL Photonics*, vol. 7, no. 8, p. 086106, Aug. 2022. [Online]. Available: https://doi.org/10.1063/5.0097880

[135] M. G. Tarallo, "Development of a strontium optical lattice clock," Ph.D. dissertation, Università degli Studi di Pisa, Pisa, 2009. [Online]. Available: https://etd.adm.unipi.it/t/etd-05182009-164852/

[136] M. G. Tarallo, N. Poli, M. Schioppo, D. Sutyrin, and G. M. Tino, "A high-stability semiconductor laser system for a $^{88}$Sr-based optical lattice clock," *Applied Physics B*, vol. 103, no. 1, p. 17–25, Sep 2010. [Online]. Available: http://dx.doi.org/10.1007/s00340-010-4232-2

[137] J. Assendelft, "Clock laser 698 nm datasheet," Feb 2022.

[138] G. D. Domenico, S. Schilt, and P. Thomann, "Simple approach to the relation between laser frequency noise and laser line shape," *Applied Optics*, vol. 49, no. 25, p. 4801, Aug. 2010. [Online]. Available: https://doi.org/10.1364/ao.49.004801

[139] M. A. Tran, D. Huang, and J. E. Bowers, "Tutorial on narrow linewidth tunable semiconductor lasers using Si/III-V heterogeneous integration," *APL Photonics*, vol. 4, no. 11, p. 111101, Nov. 2019. [Online]. Available: https://doi.org/10.1063/1.5124254

[140] M. Chiarotti, J. N. Tinsley, S. Bandarupally, S. Manzoor, M. Sacco, L. Salvi, and N. Poli, "Practical limits for large-momentum-transfer clock atom interferometers," *PRX Quantum*, vol. 3, p. 030348, Sep 2022. [Online]. Available: https://link.aps.org/doi/10.1103/PRXQuantum.3.030348

[141] T. Takano, H. Ogawa, C. Ohae, and M. Katsuragawa, "10 w injection-locked single-frequency continuous-wave titanium:sapphire laser," *Optics Express*, vol. 29, no. 5, p. 6927, Feb. 2021. [Online]. Available: https://doi.org/10.1364/oe.415583

[142] L.-S. Ma, P. Jungner, J. Ye, and J. L. Hall, "Delivering the same optical frequency at two places: accurate cancellation of phase noise introduced by an optical fiber or other time-varying path," *Optics Letters*, vol. 19, no. 21, p. 1777, Nov. 1994. [Online]. Available: https://doi.org/10.1364/ol.19.001777

[143] J. Ye, J.-L. Peng, R. J. Jones, K. W. Holman, J. L. Hall, D. J. Jones, S. A. Diddams, J. Kitching, S. Bize, J. C. Bergquist, L. W. Hollberg, L. Robertsson, and L.-S. Ma, "Delivery of high-stability optical and microwave frequency standards over an optical fiber network," *Journal of the Optical Society of America B*, vol. 20, no. 7, p. 1459, Jul. 2003. [Online]. Available: https://doi.org/10.1364/josab.20.001459

[144] E. L. Raab, M. Prentiss, A. Cable, S. Chu, and D. E. Pritchard, "Trapping of neutral sodium atoms with radiation pressure," *Phys. Rev. Lett.*, vol. 59, pp. 2631–2634, Dec 1987. [Online]. Available: https://link.aps.org/doi/10.1103/PhysRevLett.59.2631

[145] M. M. Boyd, "High precision spectroscopy of strontium in an optical lattice: Towards a new standard for frequency and time," Ph.D. dissertation, University of Colorado Boulder, Boulder, Oct 2007. [Online]. Available: https://jila.colorado.edu/bibcite/reference/1905

[146] P. Bouyer, P. Lemonde, M. B. Dahan, A. Michaud, C. Salomon, and J. Dalibard, "An atom trap relying on optical pumping," *Europhysics Letters (EPL)*, vol. 27, no. 8, pp. 569–574, Sep. 1994. [Online]. Available: https://doi.org/10.1209/0295-5075/27/8/003

[147] MOGLabs, "AN001: PID intensity-stabilisation with the ARF," 2022, accessed on 18 August 2022. [Online]. Available: https://www.moglabs.com/support/appnotes/an001-pid-r3.pdf

[148] J. P. Bartolotta, M. A. Norcia, J. R. K. Cline, J. K. Thompson, and M. J. Holland, "Laser cooling by sawtooth-wave adiabatic passage," *Phys. Rev. A*, vol. 98, p. 023404, Aug 2018. [Online]. Available: https://link.aps.org/doi/10.1103/PhysRevA.98.023404

[149] M. A. Norcia, J. R. K. Cline, J. P. Bartolotta, M. J. Holland, and J. K. Thompson, "Narrow-line laser cooling by adiabatic transfer," *New Journal of Physics*, vol. 20, no. 2, p. 023021, Feb. 2018. [Online]. Available: https://doi.org/10.1088/1367-2630/aaa950

[150] J. A. Muniz, M. A. Norcia, J. R. K. Cline, and J. K. Thompson, "A robust narrow-line magneto-optical trap using adiabatic transfer," *arXiv*, 2018. [Online]. Available: https://arxiv.org/abs/1806.00838v1

[151] J. P. Bartolotta and M. J. Holland, "Sawtooth-wave adiabatic passage in a magneto-optical trap," *Phys. Rev. A*, vol. 101, p. 053434, May 2020. [Online]. Available: https://link.aps.org/doi/10.1103/PhysRevA.101.053434

[152] S. Snigirev, A. J. Park, A. Heinz, I. Bloch, and S. Blatt, "Fast and dense magneto-optical traps for strontium," *Phys. Rev. A*, vol. 99, p. 063421, Jun 2019. [Online]. Available: https://link.aps.org/doi/10.1103/PhysRevA.99.063421

[153] R. González Escudero, C.-C. Chen, S. Bennetts, B. Pasquiou, and F. Schreck, "Steady-state magneto-optical trap of fermionic strontium on a narrow-line transition," *Phys. Rev. Research*, vol. 3, p. 033159, Aug 2021. [Online]. Available: https://link.aps.org/doi/10.1103/PhysRevResearch.3.033159

[154] S. Ebadi, T. T. Wang, H. Levine, A. Keesling, G. Semeghini, A. Omran, D. Bluvstein, R. Samajdar, H. Pichler, W. W. Ho, S. Choi, S. Sachdev, M. Greiner, V. Vuletić, and M. D. Lukin, "Quantum phases of matter on a 256-atom programmable quantum simulator," *Nature*, vol. 595, no. 7866, pp. 227–232, Jul. 2021. [Online]. Available: https://doi.org/10.1038/s41586-021-03582-4

[155] S. Kuhr, W. Alt, D. Schrader, M. Müller, V. Gomer, and D. Meschede, "Deterministic delivery of a single atom," *Science*, vol. 293, no. 5528, pp. 278–280, Jul. 2001. [Online]. Available: https://doi.org/10.1126/science.1062725

[156] D. Schrader, S. Kuhr, W. Alt, M. Müller, V. Gomer, and D. Meschede, "An optical conveyor belt for single neutral atoms," *Applied Physics B*, vol. 73, no. 8, pp. 819–824, Dec. 2001. [Online]. Available: https://doi.org/10.1007/s003400100722

[157] J. A. Sauer, K. M. Fortier, M. S. Chang, C. D. Hamley, and M. S. Chapman, "Cavity qed with optically transported atoms," *Phys. Rev. A*, vol. 69, p. 051804, May 2004. [Online]. Available: https://link.aps.org/doi/10.1103/PhysRevA.69.051804

[158] T. A. Savard, K. M. O'Hara, and J. E. Thomas, "Laser-noise-induced heating in far-off resonance optical traps," *Phys. Rev. A*, vol. 56, pp. R1095–R1098, Aug 1997. [Online]. Available: https://link.aps.org/doi/10.1103/PhysRevA.56.R1095

[159] M. E. Gehm, K. M. O'Hara, T. A. Savard, and J. E. Thomas, "Dynamics of noise-induced heating in atom traps," *Phys. Rev. A*, vol. 58, pp. 3914–3921, Nov 1998. [Online]. Available: https://link.aps.org/doi/10.1103/PhysRevA.58.3914

[160] D.-G. Welsch, W. Vogel, and T. Opatrný, "II homodyne detection and quantum-state reconstruction," in *Progress in Optics*. Elsevier, 1999, pp. 63–211. [Online]. Available: https://doi.org/10.1016/s0079-6638(08)70389-5

[161] G. Greve, "Entanglement-enhanced matter-wave interferometry," Ph.D. dissertation, University of Colorado Boulder, Boulder, Sep 2021. [Online]. Available: https://jila.colorado.edu/bibcite/reference/12711

[162] Mini-Circuits, "Phase locked loop fundamentals," 1999, accessed on 13 July 2022. [Online]. Available: https://www.minicircuits.com/app/VCO15-10.pdf

[163] J. R. Vig and E. S. Ferre-Pikal, "IEEE standard definitions of physical quantities for fundamental frequency and time metrology–random instabilities," *IEEE Std 1139-2008 (Revision of IEEE Std 1139-1999)*, pp. 1–50, 2009. [Online]. Available: https://doi.org/10.1109/IEEESTD.2009.6581834

[164] E. Rubiola, *Phase Noise and Frequency Stability in Oscillators*, ser. The Cambridge RF and Microwave Engineering Series. Cambridge University Press, 2008, ISBN: 9780511812798.

[165] M. H. Schleier-Smith, I. D. Leroux, and V. Vuletić, "Squeezing the collective spin of a dilute atomic ensemble by cavity feedback," *Phys. Rev. A*, vol. 81, p. 021804, Feb 2010. [Online]. Available: https://link.aps.org/doi/10.1103/PhysRevA.81.021804

[166] I. D. Leroux, M. H. Schleier-Smith, and V. Vuletić, "Implementation of cavity squeezing of a collective atomic spin," *Phys. Rev. Lett.*, vol. 104, p. 073602, Feb 2010. [Online]. Available: https://link.aps.org/doi/10.1103/PhysRevLett.104.073602

[167] M. H. Schleier-Smith, "Cavity-enabled spin squeezing for a quantum-enhanced atomic clock," Ph.D. dissertation, Massachusetts Institute of Technology, Cambridge, Jun 2011. [Online]. Available: https://dspace.mit.edu/handle/1721.1/68878

[168] Z. Chen, J. G. Bohnet, S. R. Sankar, J. Dai, and J. K. Thompson, "Conditional spin squeezing of a large ensemble via the vacuum rabi splitting," *Phys. Rev. Lett.*, vol. 106, p. 133601, Mar 2011. [Online]. Available: https://link.aps.org/doi/10.1103/PhysRevLett.106.133601

[169] B. K. Malia, J. Martínez-Rincón, Y. Wu, O. Hosten, and M. A. Kasevich, "Free space ramsey spectroscopy in rubidium with noise below the quantum projection limit," *Phys. Rev. Lett.*, vol. 125, p. 043202, Jul 2020. [Online]. Available: https://link.aps.org/doi/10.1103/PhysRevLett.125.043202

[170] E. Pedrozo-Peñafiel, S. Colombo, C. Shu, A. F. Adiyatullin, Z. Li, E. Mendez, B. Braverman, A. Kawasaki, D. Akamatsu, Y. Xiao, and V. Vuletić, "Entanglement on an optical atomic-clock transition," *Nature*, vol. 588, no. 7838, pp. 414–418, Dec. 2020. [Online]. Available: https://doi.org/10.1038/s41586-020-3006-1

[171] A. Shankar, L. Salvi, M. L. Chiofalo, N. Poli, and M. J. Holland, "Squeezed state metrology with bragg interferometers operating in a cavity," *Quantum Science and Technology*, vol. 4, no. 4, p. 045010, Oct. 2019. [Online]. Available: https://doi.org/10.1088/2058-9565/ab455d

[172] J. Appel, P. J. Windpassinger, D. Oblak, U. B. Hoff, N. Kjærgaard, and E. S. Polzik, "Mesoscopic atomic entanglement for precision measurements beyond the standard quantum limit," *Proceedings of the National Academy of Sciences*, vol. 106, no. 27, pp. 10 960–10 965, Jul. 2009. [Online]. Available: https://doi.org/10.1073/pnas.0901550106

[173] L. DiCarlo, M. D. Reed, L. Sun, B. R. Johnson, J. M. Chow, J. M. Gambetta, L. Frunzio, S. M. Girvin, M. H. Devoret, and R. J. Schoelkopf, "Preparation and measurement of three-qubit entanglement in a superconducting circuit," *Nature*, vol. 467, no. 7315, pp. 574–578, Sep. 2010. [Online]. Available: https://doi.org/10.1038/nature09416

[174] D. Ristè, M. Dukalski, C. A. Watson, G. de Lange, M. J. Tiggelman, Y. M. Blanter, K. W. Lehnert, R. N. Schouten, and L. DiCarlo, "Deterministic entanglement of superconducting qubits by parity measurement and feedback," *Nature*, vol. 502, no. 7471, pp. 350–354, Oct. 2013. [Online]. Available: https://doi.org/10.1038/nature12513

[175] Y. Zhong, H.-S. Chang, A. Bienfait, É. Dumur, M.-H. Chou, C. R. Conner, J. Grebel, R. G. Povey, H. Yan, D. I. Schuster, and A. N. Cleland, "Deterministic multi-qubit entanglement in a quantum network," *Nature*, vol. 590, no. 7847, pp. 571–575, Feb. 2021. [Online]. Available: https://doi.org/10.1038/s41586-021-03288-7

[176] E. Jaynes and F. Cummings, "Comparison of quantum and semiclassical radiation theories with application to the beam maser," *Proceedings of the IEEE*, vol. 51, no. 1, pp. 89–109, 1963. [Online]. Available: https://doi.org/10.1109/proc.1963.1664

[177] P. Grangier, J. A. Levenson, and J.-P. Poizat, "Quantum non-demolition measurements in optics," *Nature*, vol. 396, no. 6711, pp. 537–542, Dec. 1998. [Online]. Available: https://doi.org/10.1038/25059

[178] J. M. Robinson, M. Miklos, Y. M. Tso, C. J. Kennedy, T. Bothwell, D. Kedar, J. K. Thompson, and J. Ye, "Direct comparison of two spin squeezed optical clocks below the quantum projection noise limit," *arXiv*, 2022. [Online]. Available: https://arxiv.org/abs/2211.08621v2

[179] E. L. Hahn, "Spin echoes," *Phys. Rev.*, vol. 80, pp. 580–594, Nov 1950. [Online]. Available: https://link.aps.org/doi/10.1103/PhysRev.80.580

[180] H. Y. Carr and E. M. Purcell, "Effects of diffusion on free precession in nuclear magnetic resonance experiments," *Phys. Rev.*, vol. 94, pp. 630–638, May 1954. [Online]. Available: https://link.aps.org/doi/10.1103/PhysRev.94.630

[181] H. Tanji-Suzuki, I. D. Leroux, M. H. Schleier-Smith, M. Cetina, A. T. Grier, J. Simon, and V. Vuletić, "Chapter 4 - interaction between atomic ensembles and optical resonators: Classical description," in *Advances in Atomic, Molecular, and Optical Physics*, ser. Advances In Atomic, Molecular, and Optical Physics, E. Arimondo, P. Berman, and C. Lin, Eds. Academic Press, 2011, vol. 60, pp. 201 – 237. [Online]. Available: http://www.sciencedirect.com/science/article/pii/B9780123855084000048

[182] H. Uys, M. J. Biercuk, A. P. VanDevender, C. Ospelkaus, D. Meiser, R. Ozeri, and J. J. Bollinger, "Decoherence due to elastic rayleigh scattering," *Phys. Rev. Lett.*, vol. 105, p. 200401, Nov 2010. [Online]. Available: https://link.aps.org/doi/10.1103/PhysRevLett.105.200401

[183] J. M. McGuirk, G. T. Foster, J. B. Fixler, M. J. Snadden, and M. A. Kasevich, "Sensitive absolute-gravity gradiometry using atom interferometry," *Phys. Rev. A*, vol. 65, p. 033608, Feb 2002. [Online]. Available: https://link.aps.org/doi/10.1103/PhysRevA.65.033608

[184] J. L. Gouët, P. Cheinet, J. Kim, D. Holleville, A. Clairon, A. Landragin, and F. P. D. Santos, "Influence of lasers propagation delay on the sensitivity of atom interferometers," *The European Physical Journal D*, vol. 44, no. 3, pp. 419–425, Jun. 2007. [Online]. Available: https://doi.org/10.1140/epjd/e2007-00218-2

[185] P. W. Graham, J. M. Hogan, M. A. Kasevich, and S. Rajendran, "New method for gravitational wave detection with atomic sensors," *Phys. Rev. Lett.*, vol. 110, p. 171102, Apr 2013. [Online]. Available: https://link.aps.org/doi/10.1103/PhysRevLett.110.171102

[186] H. Müller, S.-w. Chiow, Q. Long, S. Herrmann, and S. Chu, "Atom interferometry with up to 24-photon-momentum-transfer beam splitters," *Phys. Rev. Lett.*, vol. 100, p. 180405, May 2008. [Online]. Available: https://link.aps.org/doi/10.1103/PhysRevLett.100.180405

[187] M. Cadoret, N. Zahzam, Y. Bidel, C. Diboune, A. Bonnin, F. Théron, and A. Bresson, "Phase shift formulation for n-light-pulse atom interferometers: application to inertial sensing," *Journal of the Optical Society of America B*, vol. 33, no. 8, p. 1777, Jul. 2016. [Online]. Available: https://doi.org/10.1364/josab.33.001777

[188] B. Canuel, A. Bertoldi, L. Amand, E. P. di Borgo, T. Chantrait, C. Danquigny, M. D. Álvarez, B. Fang, A. Freise, R. Geiger, J. Gillot, S. Henry, J. Hinderer, D. Holleville, J. Junca, G. Lefèvre, M. Merzougui, N. Mielec, T. Monfret, S. Pelisson, M. Prevedelli, S. Reynaud, I. Riou, Y. Rogister, S. Rosat, E. Cormier, A. Landragin, W. Chaibi, S. Gaffet, and P. Bouyer, "Exploring gravity with the MIGA large scale atom interferometer," *Scientific Reports*, vol. 8, no. 1, Sep. 2018. [Online]. Available: https://doi.org/10.1038/s41598-018-32165-z

[189] M. Abe, P. Adamson, M. Borcean, D. Bortoletto, K. Bridges, S. P. Carman, S. Chattopadhyay, J. Coleman, N. M. Curfman, K. DeRose, T. Deshpande, S. Dimopoulos, C. J. Foot, J. C. Frisch, B. E. Garber, S. Geer, V. Gibson, J. Glick, P. W. Graham, S. R. Hahn, R. Harnik, L. Hawkins, S. Hindley, J. M. Hogan, Y. Jiang, M. A. Kasevich, R. J. Kellett, M. Kiburg, T. Kovachy, J. D. Lykken, J. March-Russell, J. Mitchell, M. Murphy, M. Nantel, L. E. Nobrega, R. K. Plunkett, S. Rajendran, J. Rudolph, N. Sachdeva, M. Safdari, J. K. Santucci, A. G. Schwartzman, I. Shipsey, H. Swan, L. R. Valerio, A. Vasonis, Y. Wang, and T. Wilkason, "Matter-wave atomic gradiometer interferometric sensor (MAGIS-100)," *Quantum Science and Technology*, vol. 6, no. 4, p. 044003, Jul. 2021. [Online]. Available: https://doi.org/10.1088/2058-9565/abf719

[190] L. Badurina, E. Bentine, D. Blas, K. Bongs, D. Bortoletto, T. Bowcock, K. Bridges, W. Bowden, O. Buchmueller, C. Burrage, J. Coleman, G. Elertas, J. Ellis, C. Foot, V. Gibson, M. Haehnelt, T. Harte, S. Hedges, R. Hobson, M. Holynski, T. Jones, M. Langlois, S. Lellouch, M. Lewicki, R. Maiolino, P. Majewski, S. Malik, J. March-Russell, C. McCabe, D. Newbold, B. Sauer, U. Schneider, I. Shipsey, Y. Singh, M. Uchida, T. Valenzuela, M. van der Grinten, V. Vaskonen, J. Vossebeld, D. Weatherill, and I. Wilmut, "AION: an atom interferometer observatory and network," *Journal of Cosmology and Astroparticle Physics*, vol. 2020, no. 05, pp. 011–011, May 2020. [Online]. Available: https://doi.org/10.1088/1475-7516/2020/05/011

[191] M.-S. Zhan, J. Wang, W.-T. Ni, D.-F. Gao, G. Wang, L.-X. He, R.-B. Li, L. Zhou, X. Chen, J.-Q. Zhong, B. Tang, Z.-W. Yao, L. Zhu, Z.-Y. Xiong, S.-B. Lu, G.-H. Yu, Q.-F. Cheng, M. Liu, Y.-R. Liang, P. Xu, X.-D. He, M. Ke, Z. Tan, and J. Luo, "ZAIGA: Zhaoshan long-baseline atom interferometer gravitation antenna," *International Journal of Modern Physics D*, vol. 29, no. 04, p. 1940005, Jul. 2019. [Online]. Available: https://doi.org/10.1142/s0218271819400054

[192] R. P. del Aguila, T. Mazzoni, L. Hu, L. Salvi, G. M. Tino, and N. Poli, "Bragg gravity-gradiometer using the $^1S_0 - {}^3P_1$ intercombination transition of $^{88}Sr$," *New Journal of Physics*, vol. 20, no. 4, p. 043002, Apr. 2018. [Online]. Available: https://doi.org/10.1088/1367-2630/aab088

[193] P. Laurent, D. Massonnet, L. Cacciapuoti, and C. Salomon, "The ACES/PHARAO space mission," *Comptes Rendus Physique*, vol. 16, no. 5, pp. 540–552, Jun. 2015. [Online]. Available: https://doi.org/10.1016/j.crhy.2015.05.002

[194] F. Migliaccio, M. Reguzzoni, K. Batsukh, G. M. Tino, G. Rosi, F. Sorrentino, C. Braitenberg, T. Pivetta, D. F. Barbolla, and S. Zoffoli, "MOCASS: A satellite mission concept using cold atom interferometry for measuring the earth gravity field," *Surveys in Geophysics*, vol. 40, no. 5, pp. 1029–1053, Aug. 2019. [Online]. Available: https://doi.org/10.1007/s10712-019-09566-4

[195] G. M. Tino, A. Bassi, G. Bianco, K. Bongs, P. Bouyer, L. Cacciapuoti, S. Capozziello, X. Chen, M. L. Chiofalo, A. Derevianko, W. Ertmer, N. Gaaloul, P. Gill, P. W. Graham, J. M. Hogan, L. Iess, M. A. Kasevich, H. Katori, C. Klempt, X. Lu, L.-S. Ma, H. Müller, N. R. Newbury, C. W. Oates, A. Peters, N. Poli, E. M. Rasel, G. Rosi, A. Roura, C. Salomon, S. Schiller, W. Schleich, D. Schlippert, F. Schreck, C. Schubert, F. Sorrentino, U. Sterr, J. W. Thomsen, G. Vallone, F. Vetrano, P. Villoresi, W. von Klitzing, D. Wilkowski, P. Wolf, J. Ye, N. Yu, and M. Zhan, "SAGE: A proposal for a space atomic gravity explorer," *The European Physical Journal D*, vol. 73, no. 11, Nov. 2019. [Online]. Available: https://doi.org/10.1140/epjd/e2019-100324-6

[196] Y. A. El-Neaj, C. Alpigiani, S. Amairi-Pyka, H. Araújo, A. Balaž, A. Bassi, L. Bathe-Peters, B. Battelier, A. Belić, E. Bentine, J. Bernabeu, A. Bertoldi, R. Bingham, D. Blas, V. Bolpasi, K. Bongs, S. Bose, P. Bouyer, T. Bowcock, W. Bowden, O. Buchmueller, C. Burrage, X. Calmet, B. Canuel, L.-I. Caramete, A. Carroll, G. Cella, V. Charmandaris, S. Chattopadhyay, X. Chen, M. L. Chiofalo, J. Coleman, J. Cotter, Y. Cui, A. Derevianko, A. D. Roeck, G. S. Djordjevic, P. Dornan, M. Doser, I. Drougkakis, J. Dunningham, I. Dutan, S. Easo, G. Elertas, J. Ellis, M. E. Sawy, F. Fassi, D. Felea, C.-H. Feng, R. Flack, C. Foot, I. Fuentes, N. Gaaloul, A. Gauguet, R. Geiger, V. Gibson, G. Giudice, J. Goldwin, O. Grachov, P. W. Graham, D. Grasso, M. van der Grinten, M. Gündogan, M. G. Haehnelt, T. Harte, A. Hees, R. Hobson, J. Hogan, B. Holst, M. Holynski, M. Kasevich, B. J. Kavanagh, W. von Klitzing, T. Kovachy, B. Krikler, M. Krutzik, M. Lewicki, Y.-H. Lien, M. Liu, G. G. Luciano, A. Magnon, M. A. Mahmoud, S. Malik, C. McCabe, J. Mitchell, J. Pahl, D. Pal, S. Pandey, D. Papazoglou, M. Paternostro, B. Penning, A. Peters, M. Prevedelli, V. Puthiya-Veettil, J. Quenby, E. Rasel, S. Ravenhall, J. Ringwood, A. Roura, D. Sabulsky, M. Sameed, B. Sauer, S. A. Schäffer, S. Schiller, V. Schkolnik, D. Schlippert, C. Schubert, H. R. Sfar, A. Shayeghi, I. Shipsey, C. Signorini, Y. Singh, M. Soares-Santos, F. Sorrentino, T. Sumner, K. Tassis, S. Tentindo, G. M.

Tino, J. N. Tinsley, J. Unwin, T. Valenzuela, G. Vasilakis, V. Vaskonen, C. Vogt, A. Webber-Date, A. Wenzlawski, P. Windpassinger, M. Woltmann, E. Yazgan, M.-S. Zhan, X. Zou, and J. Zupan, "AEDGE: Atomic experiment for dark matter and gravity exploration in space," *EPJ Quantum Technology*, vol. 7, no. 1, Mar. 2020. [Online]. Available: https://doi.org/10.1140/epjqt/s40507-020-0080-0

[197] H. Ahlers, L. Badurina, A. Bassi, B. Battelier, Q. Beaufils, K. Bongs, P. Bouyer, C. Braxmaier, O. Buchmueller, M. Carlesso, E. Charron, M. L. Chiofalo, R. Corgier, S. Donadi, F. Droz, R. Ecoffet, J. Ellis, F. Estève, N. Gaaloul, D. Gerardi, E. Giese, J. Grosse, A. Hees, T. Hensel, W. Herr, P. Jetzer, G. Kleinsteinberg, C. Klempt, S. Lecomte, L. Lopes, S. Loriani, G. Métris, T. Martin, V. Martín, G. Müller, M. Nofrarias, F. P. D. Santos, E. M. Rasel, A. Robert, N. Saks, M. Salter, D. Schlippert, C. Schubert, T. Schuldt, C. F. Sopuerta, C. Struckmann, G. M. Tino, T. Valenzuela, W. von Klitzing, L. Wörner, P. Wolf, N. Yu, and M. Zelan, "Ste-quest: Space time explorer and quantum equivalence principle space test," *arXiv*, 2022. [Online]. Available: https://arxiv.org/abs/2211.15412v3

[198] R. Haagmans, C. Siemes, L. Massotti, O. Carraz, and P. Silvestrin, "ESA's next-generation gravity mission concepts," *Rendiconti Lincei. Scienze Fisiche e Naturali*, vol. 31, no. S1, pp. 15–25, Jan. 2020. [Online]. Available: https://doi.org/10.1007/s12210-020-00875-0

[199] J. H. Lee, H. Jung, J.-y. Choi, and J. Mun, "Transporting cold atoms using an optically compensated zoom lens," *Phys. Rev. A*, vol. 102, p. 063106, Dec 2020. [Online]. Available: https://link.aps.org/doi/10.1103/PhysRevA.102.063106

[200] E. S. Polzik and J. Ye, "Entanglement and spin squeezing in a network of distant optical lattice clocks," *Phys. Rev. A*, vol. 93, p. 021404, Feb 2016. [Online]. Available: https://link.aps.org/doi/10.1103/PhysRevA.93.021404

[201] A. Bonnin, C. Diboune, N. Zahzam, Y. Bidel, M. Cadoret, and A. Bresson, "New concepts of inertial measurements with multi-species atom interferometry," *Applied Physics B*, vol. 124, no. 9, Aug. 2018. [Online]. Available: https://doi.org/10.1007/s00340-018-7051-5

[202] T. Kobayashi, D. Akamatsu, K. Hosaka, Y. Hisai, M. Wada, H. Inaba, T. Suzuyama, F.-L. Hong, and M. Yasuda, "Demonstration of the nearly continuous operation of an $^{171}$Yb optical lattice clock for half a year," *Metrologia*, vol. 57, no. 6, p. 065021, Nov. 2020. [Online]. Available: https://doi.org/10.1088/1681-7575/ab9f1f

[203] D. Gochnauer, T. Rahman, A. Wirth-Singh, and S. Gupta, "Interferometry in an atomic fountain with ytterbium bose–einstein condensates," *Atoms*, vol. 9, no. 3, p. 58, Aug. 2021. [Online]. Available: https://doi.org/10.3390/atoms9030058

[204] X. Baillard, M. Fouché, R. L. Targat, P. G. Westergaard, A. Lecallier, Y. L. Coq, G. D. Rovera, S. Bize, and P. Lemonde, "Accuracy evaluation of an optical lattice clock with bosonic atoms," *Opt. Lett.*, vol. 32, no. 13, pp. 1812–1814, Jul 2007. [Online]. Available: http://opg.optica.org/ol/abstract.cfm?URI=ol-32-13-1812

[205] G. Ferrari, P. Cancio, R. Drullinger, G. Giusfredi, N. Poli, M. Prevedelli, C. Toninelli, and G. M. Tino, "Precision frequency measurement of visible intercombination lines of strontium," *Phys. Rev. Lett.*, vol. 91, p. 243002, Dec 2003. [Online]. Available: https://link.aps.org/doi/10.1103/PhysRevLett.91.243002

[206] G. K. Campbell, A. D. Ludlow, S. Blatt, J. W. Thomsen, M. J. Martin, M. H. G. de Miranda, T. Zelevinsky, M. M. Boyd, J. Ye, S. A. Diddams, T. P. Heavner, T. E. Parker, and S. R. Jefferts, "The absolute frequency of the Sr-87 optical clock transition," *Metrologia*, vol. 45, no. 5, pp. 539–548, sep 2008. [Online]. Available: https://doi.org/10.1088/0026-1394/45/5/008

[207] I. Courtillot, A. Quessada-Vial, A. Brusch, D. Kolker, G. D. Rovera, and P. Lemonde, "Accurate spectroscopy of sr atoms," *The European Physical Journal D*, vol. 33, no. 2, pp. 161–171, May 2005. [Online]. Available: https://doi.org/10.1140/epjd/e2005-00058-0

[208] S. Stellmer, "Degenerate quantum gases of strontium," Ph.D. dissertation, University of Innsbruck, Innsbruck, 2013. [Online]. Available: http://www.ultracold.at/theses/2013-stellmer.pdf

[209] LENS Electronic Workshop, "Electronic workshop projects," 2020, accessed on 22 September 2020. [Online]. Available: http://ew.lens.unifi.it/index.php?action=show&what=projects&title=Electronic%20Workshop%20Projects